CHIRAL SPECTROSCOPY:

A multidisciplinary approach to chiral structure determination of organic molecules

Ewoud De Gussem

Promotoren
Prof. Dr. Wouter Herrebout
Prof. Dr. Patrick Bultinck

Proefschrift voorgelegd tot het behalen van de graad van doctor in de Wetenschappen: chemie

Januari 2015

UNIVERSITEIT GENT

Universiteit Antwerpen

Faculteit Wetenschappen

CHIRAL SPECTROSCOPY: A MULTIDISCIPLINARY APPROACH TO CHIRAL STRUCTURE DETERMINATION OF ORGANIC MOLECULES

Ewoud De Gussem

Proefschrift voorgelegd tot het behalen van de graad van doctor in de wetenschappen: chemie.

2014

Promotor: Prof. Dr. W. Herrebout, Universiteit Antwerpen
Promotor: Prof. Dr. P. Bultinck, Universiteit Gent

Contents

List of Publications

The following papers were published as a result of the work performed by the author of this thesis. His own contributions are highlighted and where applicable a reference is made to the relevant chapter in this thesis.

- E. Debie, E. De Gussem, R. Dukor, W. Herrebout, L. Nafie, and P. Bultinck. "A Confidence Level Algorithm for the Determination of Absolute Configuration Using Vibrational Circular Dichroism or Raman Optical Activity". In: *Chemphyschem* 12.8 (2011), pp. 1542–1549
  This paper is reproduced in chapter 4 of this thesis. The results in this paper are a continuation of the research performed at the Ghent Quantum Chemistry Group and BioTools Inc. For the database, data from BioTools Inc. were used. The code of the algorithm was modified and corrected by the author of the thesis who also generated the data reported.

- E. De Gussem, P. Bultinck, M. Feledziak, J. Marchand-Brynaert, C. V. Stevens, and W. Herrebout. "Vibrational Circular Dichroism versus Optical Rotation Dispersion and Electronic Circular Dichroism for diastereomers: the stereochemistry of 3-(1 '-hydroxyethyl)-1-(3 '-phenylpropanoyl)-azetidin-2-one". In: *Physical Chemistry Chemical Physics* 14.24 (2012), pp. 8562–8571
  This paper is reproduced in chapter 5 of this thesis. In this paper organic synthesis was performed by co-authors M. Feledziak, J. Marchand-Brynaert and C. Stevens. All calculations, most measurements (except for NMR) and processing of the data were performed by the author of the thesis.

- F. Cherblanc, Y. P. Lo, E. De Gussem, L. Alcazar-Fuoli, E. Bignell, Y. A. He, N. Chapman-Rothe, P. Bultinck, W. A. Herrebout, R. Brown, H. S. Rzepa, and M. J. Fuchter. "On the Determination of the Stereochemistry of Semisynthetic

Natural Product Analogues using Chiroptical Spectroscopy: Desulfurization of Epidithiodioxopiperazine Fungal Metabolites". In: *Chemistry-A European Journal* 17.42 (2011), pp. 11868–11875
This paper is not reproduced in this thesis. All VCD related results in this paper were obtained by the author of this thesis.

- E. De Gussem, J. Cornelus, S. Pieters, D. Van den Bossche, J. Van der Eycken, W. Herrebout, and P. Bultinck. "Synthesis of the Natural Product Building Block 5-(3-Bromophenyl)-4-hydroxy-5-methylhexan-2-one and its Chiral Characterization by Using Chiroptical Spectroscopy". In: *ChemPhysChem* 14.14 (2013), pp. 3255–3262
This paper is reproduced in chapter 6 of this thesis. In this paper organic synthesis was performed by J. Cornelus, S. Pieters, D. Van den Bossche and J. Van der Eycken. All calculations, most measurements (except for NMR and ORD) and analysis of the data were performed by the author of this thesis.

- S. Qiu, E. De Gussem, K. A. Tehrani, S. Sergeyev, P. Bultinck, and W. Herrebout. "Stereochemistry of the Tadalafil Diastereoisomers: A Critical Assessment of Vibrational Circular Dichroism, Electronic Circular Dichroism, and Optical Rotatory Dispersion". In: *Journal of Medicinal Chemistry* 56.21 (2013), pp. 8903–8914
This paper is reproduced in chapter 7 of this thesis. In this paper most calculations and measurements were performed by S. Qiu. Processing of the data was performed for a large part by the author of this thesis.

- E. De Gussem, W. Herrebout, S. Specklin, C. Meyer, J. Cossy, and P. Bultinck. "Strength by Joining Methods: Combining Synthesis with NMR, IR, and Vibrational Circular Dichroism Spectroscopy for the Determination of the Relative Configuration in Hemicalide". In: *Chemistry A European Journal* (2014)
This paper is reproduced in chapter 8 of this thesis. The organic synthesis in this paper was performed by S. Specklin, C. Meyer and J. Cossy, as are the experimental NMR analyses linking the natural product with the model compounds. All calculations, most measurements (except for NMR) and analysis of the data were performed by the author of this thesis.

- The results of chapter 9 are the subject of a paper in preparation. All calculations, most measurements (except for NMR, Raman and ROA) and processing of the

data were performed by the author of this thesis.

Nomenclature

AAT	Atomic axial tensor
AC	Absolute configuration
API	Active pharmaceutical ingredient
APT	Atomic polar tensor
BO	Born-Oppenheimer approximation
BP	Birefringent plate
CB	Circular birefringence
CD	Circular dichroism
CDA	Chiral derivatizing agent
COSY	Correlation spectroscopy (NMR)
CPHF	Coupled perturbed Hartree-Fock
CPKS	Coupled perturbed Kohn-Sham
CPL	Circularly polarized light
DFT	Density functional theory
ECD	Electronic circular dichroism
EDTM	Electric dipole transition moment

FT-IR Fourier-transform infrared spectroscopy

IR Infrared

LB Linear birefringence

LCAO Linear combination of atomic orbitals

LD Linear dichroism

LIA Lock-in amplifier

MDTM Magnetic dipole transition moment

MFP Magnetic field perturbation

MO Molecular orbital

NMR Nuclear magnetic resonance

NOESY Nuclear Overhauser effect spectroscopy (NMR)

ORD Optical rotatory dispersion

PEM Photo-elastic modulator

PES Potential energy surface

RC Relative Configuration

ROA Raman optical activity

S/N Signal-to-noise ratio

SCP-ROA Scattered circular polarization Raman optical activity

TMS Tetramethylsilane

UV-VIS Ultraviolet and visible region of the spectrum of electromagnetic radiation

VCD Vibrational circular dichroism

XRC X-ray crystallography

XRD X-ray diffraction

Chapter 1

Chirality and its Chemical Implications

1.1 Introduction

At the very essence of this work lies a physical phenomenon called chirality, derived from the Greek word for hand, '$\chi\epsilon\iota\rho$'. Chirality is observed in almost every aspect of our universe, from vast galaxies with a certain handedness, down to the selective interaction of the electroweak force, which possibly lies at the basis of the homochirality of life.[7] An object is chiral if, as it was defined by Lord Kelvin in the 19$^{\text{th}}$ century, its image in a plane mirror, ideally realized, cannot be brought to coincide with itself.[8] The first observations of chirality in a chemical context date from the first half of the 19$^{\text{th}}$ century, when Pasteur observed that plane polarized light rotated in opposite directions when passed through mirror-image crystals of tartaric acid.[9]

At the molecular level, chirality can be defined by the lack of an improper rotation axis (S_n) of a molecular system. For organic molecules and natural products, which are the main subject of this thesis, this is most often caused by the presence of an asymmetric atom, called the chiral center. In all cases considered in this thesis, the chiral center is a tetrahedral (sp^3–hybridized) carbon atom, to which four different groups are attached.[10] Such a molecule and its mirror image are termed *enantiomers*. In chemistry, a unique system for identification of enantiomers was introduced by Cahn, Ingold and Prelog,[11] based on the atomic mass of the four substituents of the

chiral center. This way, the *absolute configuration* (AC) of each chiral center can be indicated by *R* (for 'rectus') or *S* (for 'sinister') in a unique way.

Having the same atoms and connectivity, enantiomers are completely equal as far as physical properties (such as thermodynamic properties, refractive index for unpolarized light, ...) are concerned. However, their behaviour differs when they interact with other chiral entities, such as polarized radiation or other chiral molecules. The different interaction of enantiomers with light of a certain handedness lies at the basis of all chiroptical techniques used in this thesis, such as circular dichroism or optical rotation. The fact that enantiomers interact differently with other chiral molecules is what gives purpose to the research in this thesis. Indeed, even in the human body chirality is prominent. DNA is composed of right-handed helices, enzymes and proteins are composed of L-amino acids and carbohydrates of D-monosaccharides in almost all living organisms.[12] On the other hand, numerous molecules in our environment are chiral, and thus act differently upon entry in our body. For example, (*R*)-(+)-limonene has a fresh citrus, orange-like smell, whereas its enantiomer (*S*)-(-)-limonene has a more turpentine-like lemon smell.[13]

For pharmaceutical molecules, the impact of chirality is more severe. It is often the case that the activity of an active pharmaceutical ingredient (API) can be attributed to only one enantiomer. Its mirror image can be inactive (but possibly with the same adverse effects), be an antagonist of the active enantiomer or could even have a completely different (desirable or undesirable) activity.[14,15] A well-known and dramatic example is the case of Thalidomide®. The (*R*)-enantiomer has sedative effects, and was for this reason given to pregnant women in the 1950's. The (*S*)-enantiomer, which can be obtained by enantiomerization from the (*R*)-enantiomer in aqueous conditions[16] proved to be teratogenic, with known consequences.[17] All this, together with commercial motives,[18] has spurred an increased interest of the pharmaceutical industry and regulatory authorities to market single-enantiomer drugs.[19]

1.2 Structure Determination of Chiral Molecules

1.2.1 Overview

A few techniques are predominant in the determination of the relative configuration (RC) or absolute configuration (AC) of organic molecules and natural products. A short overview of these techniques, together with their strengths and shortcomings,

will be given.

Single-crystal X-ray diffraction (XRD) is well known as a reliable technique for stereochemical structure determination.[20] The technique is based on the diffraction of X-rays by a crystal. The obtained diffraction pattern can be used to reconstruct the electron density, and thus the atomic coordinates. The reliability of an AC assignment using XRD can be quantified using the so-called Flack parameter.[21] However, XRD relies on the anomalous scattering effect, which requires heavy atoms, such as S, P, halogens, ... to be present, whereas natural products are mainly composed of C, H, N, O, ... with only minimal anomalous scattering.[22] This issue can be resolved by using Cu Kα radiation rather than Mo Kα, or by introducing heavy atoms into the sample by derivatization. Nonetheless, an XRD-analysis always depends on the availability of high-quality single crystals which is an important limitation. In this thesis, cases occur where high quality crystals cannot be obtained, for which solution state methods, such as chiroptical techniques, are highly preferable.

Nuclear magnetic resonance (NMR) is a well established method for identifying molecular structures but can also be applied to the assignment of the stereochemistry of a molecule. Enantiomers have exactly equal chemical shifts, but when they react with other chiral molecules, a pair of enantiomeric chiral derivatizing agents (CDA) such as Mosher's reagent, they form diastereoisomers which exhibit different chemical shifts. Drawbacks of this methodology however are that relatively large quantities of samples are needed. Also, for molecules with multiple functional groups, interpretation is not straightforward.[22]

The final techniques for the AC determination are collectively called chiroptical methods. This term comprises a collection of techniques, that all rely on the wavelength dependent interaction of radiation with molecules. Moreover, the mode of operation of these techniques is based on the fact that enantiomers interact differently with two chiral forms of radiation, namely left and right circularly polarized light (CPL).[23] Optical rotatory dispersion (ORD) measures the rotation of the plane of polarization of linearly polarized light, which is caused by the different refractive index for left and right CPL in chiral media. When a difference in absorbance between left and right CPL is measured as a function of the wavelength, a circular dichroism (CD) spectrum is observed. When the wavelength of the absorbed radiation is in the UV-Vis region of the spectrum, we speak of electronic circular dichroism (ECD) because electronic transitions are observed. In the case of infrared radiation (IR), vibrational transitions are induced, and the method is then called vibrational circular dichroism

(VCD). Both methods are frequently used for solution state AC assignment. However, ECD needs chromophores with low-lying electronic transition states, accessible in the UV-Vis region. Moreover, only few bands are available to make the assignment. VCD has the advantage that no chromophores are necessary, and that there are 3N-6 bands available to aid in the interpretation of the spectra, where N is the number of atoms in the molecule. The last chiroptical method, Raman optical activity (ROA) is based on the differential scattering of CPL by chiral molecules. An ROA spectrum has the same number of bands as VCD but has a different spectrum, which makes these techniques complementary.

1.2.2 Assigning the Stereochemistry with Chiroptical Spectroscopy

For all these chiroptical techniques, spectra of enantiomers are perfect mirror images. However, no direct information is given about the AC of the corresponding samples. Therefore, spectra need to be simulated for molecules of a predefined AC to act as a reference for comparison with the experimental spectra. A VCD analysis is usually conceived in the following manner:

- The structure of the molecule is drawn with a given AC. In the case that the molecule has multiple chiral centers (diastereoisomers), all possible combinations of configurations of the chiral centers need to be accounted for.
- Since a VCD (or any other chiroptical) spectrum depends on the molecular geometry, a conformational search is performed to find all stable conformers of the molecule, which are given as minima of the potential energy surface (PES). Usually, this is done by computer algorithms that gradually or randomly rotate all bonds in the molecule and re-optimize the energy of the obtained geometry. This is usually done at a low level of theory (molecular mechanics) to reduce computational cost.
- All minima found in the previous step are further optimized at a higher level of theory (using density functional theory). For the resulting conformers, vibrational frequencies are calculated, and the corresponding spectral quantities are calculated.
- This gives rise to single peaks at discrete frequencies for each conformer. To allow comparison with the experiment, these peaks are broadened (or 'smeared') to resemble the experimental spectrum as much as possible.

- A Boltzmann averaged spectrum is obtained by adding all conformer spectra with their respective Boltzmann weights.

- As a final step, this calculated spectrum is compared to the experimental one. If the signs of the calculated peaks are equal to their measured counterparts, the sample has the same AC as the one drawn in the first step. If the signs are opposite, and the experimental and calculated spectrum are thus mirror images, the sample is the enantiomer of the drawn AC.

For the other techniques the spectra can be obtained in a similar fashion, with the understanding that the corresponding physical quantities need to be used, which are discussed in the second chapter.

1.2.3 Vibrational Circular Dichroism: Exploring the Boundaries

At the beginning of my research period, back in 2009, VCD was already an established method for the AC determination of chiral molecules. Moreover, it was accepted by regulatory authorities as prove for the stereochemical characterization of new molecular entities in the pharmaceutical industry. Application of stereochemical characterization using VCD however was for a large part limited to small to medium-sized organic molecules.[24] On the other hand, a large number of drugs (about 40%) commercialized in the past few decades originates from natural products.[25] Very often, these molecules have a complexity that easily surpasses that of synthetic drugs. The scope for my research was to extend the use of this method to these complex and challenging, yet important molecules.

Algorithms were developed to facilitate an extensive conformational analysis, processing of calculated and measured data, and an objective and powerful comparison of these data. As the complexity of the research subjects was increasing, an interest in parallel, complementary methods such as ECD, ROA, ORD and NMR was gradually developed. As it turns out, and this is also the main conclusion of this research, it is the combination of these largely complementary techniques that gives the most conclusive results, or even the only satisfactory results.[2–5] Therefore, focus was diverted from VCD spectroscopy specifically to this multitude of techniques, which are collectively termed chiroptical spectroscopy (with the exception of NMR).[26,27]

The build-up of this thesis also reflects this gradual inclusion of new techniques. In chapter 2 an overview is given of all these techniques from a physics point of view.

Vibrational and electronic circular dichroism, optical rotatory dispersion, Raman optical activity and finally nuclear magnetic resonance are discussed. Only VCD is discussed in some detail, but I have tried to emphasize the similarities and differences of the other techniques with VCD. In chapter 3, only the measurement of VCD is discussed, both in a theoretical manner and also from a practical point of view. Chapter 4 embodies the transition from the theoretical part of this thesis to the discussion of my research results. An algorithm was developed which allows to ascribe a level of confidence to the AC assignment made when comparing calculated VCD spectra with their experimental counterparts. This algorithm will be used throughout the rest of this thesis (chapter 5 - chapter 9), where the stereochemical elucidation of a variety of natural products and chiral synthetic molecules is discussed. Only results that have been or will be published in peer–reviewed journals are presented in this thesis.

Chapter 2

Theoretical Background

In this thesis, a variety of methods are used to determine the absolute configuration of the molecules under study. In order to understand these techniques and their mutual relationships, a decent understanding of the physics behind these techniques is indispensable. Since this thesis focusses mainly on Vibrational Circular Dichroism (VCD), this phenomenon, together with its unpolarized counterpart infrared (IR) absorption, will comprise the main part of this chapter. Another chiroptical spectroscopic technique that also probes vibrational motion of a molecule is Raman Optical Activity (ROA) which was used in the last years of my research, when an ROA instrument had become available. Although vibrational spectroscopy yields superior detail and sensitivity, two methods in the UV-VIS region, being Electronic Circular Dichroism (ECD) and Optical Rotatory Disperson (ORD), are also investigated. Finally, NMR and its relation to VCD is described.

2.1 Molecules and Time-dependent Perturbations

Physical phenomena on a microscopic, atomic scale must be described using quantum mechanics.[28] For the description of the phenomena in this thesis, it suffices to treat only the molecules as quantum objects perturbed by classical electromagnetic fields as opposed to photons, thus avoiding the use of quantum electrodynamics.[29,30] In this section, the classical description of light and the quantum mechanical description of matter is reviewed. Then, the interaction between the two, which occurs through

interaction of the electromagnetic radiation field with the charged particles in the molecule is described.[31] This section is conceived with the theory of VCD in mind, but it is for a large part applicable to the other techniques in this thesis.

2.1.1 Circularly Polarized Light

We start with the description of circularly polarized light (CPL) which can, just as any form of electromagnetic radiation, be described as perpendicular electrical and magnetic fields $\vec{E}$ and $\vec{B}$, and perpendicular to the propagation direction $\vec{k}$ as expressed by Maxwell's equations.[32] Defining the z-axis as the propagation direction, the electric field may be described as a vector in the xy-plane as follows:

$$\vec{E}(\vec{r},t) = E_0 \vec{v}_e e^{i(kz-\omega t)} \tag{2.1}$$

The vector $\vec{v}_e$ is a normalized vector describing the polarization state of the electric field in the xy-plane, and is of the form $\cos(\alpha)\vec{e}_x + \sin(\alpha)\vec{e}_y$ for linearly polarized light at an angle α with the x-axis. For the magnetic field this becomes $\vec{v}_h = -\sin(\alpha)\vec{e}_x + \cos(\alpha)\vec{e}_y$. The angular frequency is given by $\omega = 2\pi\nu$ and the propagation vector as $\vec{k} = 2\pi\vec{n}/\lambda$ with $\vec{n}$ the refractive index in the propagation direction and λ/n the wavelength of the radiation.[10] For CPL, a phase shift of $\pm\pi/2$ is introduced between the x-component and y-component of the electric field.

$$\vec{v}_+ = \frac{1}{\sqrt{2}}(\vec{e}_x - i\vec{e}_y) \qquad \vec{v}_- = \frac{1}{\sqrt{2}}(\vec{e}_x + i\vec{e}_y) \tag{2.2}$$

where the relationship $i = e^{i\pi/2}$ is used to describe the $\pi/2$ phase shift between the x- and y-component. The + and - subscripts denote right and left CPL, respectively, where we use the convention that the electric field vector rotates clockwise for right CPL when viewed by an observer looking in the opposite direction of the propagation direction. Finally, inserting (2.2) into (2.1) and considering only the real part, we get an expression for left or right CPL.

$$\vec{E}_\pm = \frac{E_0}{\sqrt{2}}\left(\cos(kz-\omega t)\vec{e}_x \pm \sin(kz-\omega t)\vec{e}_y\right) \tag{2.3}$$

Similarly, we find for the magnetic field of CPL:

$$\vec{B}_\pm = \frac{B_0}{\sqrt{2}}\left(\mp\sin(kz-\omega t)\vec{e}_x + \cos(kz-\omega t)\vec{e}_y\right) \tag{2.4}$$

2.1.2 Molecules in Periodic Fields

To describe the effect of an oscillating electromagnetic field on a molecule, we consider the state of the molecule at time t as a superposition of time-dependent unperturbed states, forming a complete set.[33]

$$\Psi(\vec{r},t) = \sum_i a_i(t)\Psi_i^{(0)}(\vec{r},t) = \sum_i a_i(t)\psi_i^{(0)}(\vec{r})e^{-iE_it/\hbar} \tag{2.5}$$

where the $\psi_i^{(0)}(\vec{r})$ are the solutions to the unperturbed time-independent Schrödinger equation $H^{(0)}\psi_i = E_i\psi_i$. The probability of the molecule being in state i is given as $|a_i(t)|^2$. The Hamiltonian of the molecule interacting with the radiation can be interpreted as the Hamiltonian of the unperturbed molecule plus a perturbation Hamiltonian.

$$H = H^{(0)} + H^{(1)} \tag{2.6}$$

$H^{(0)}$ corresponds to the Hamiltonian of the molecular system, whereas the perturbation Hamiltonian $H^{(1)}$ signifies the interaction of the charged particles in the molecule with the oscillating electric and magnetic fields of the radiation. To illustrate this interaction we write down the classical expression of the Lorentz force of an electron moving in the electric and magnetic fields at velocity $\vec{v}$.

$$\vec{F}\,(\vec{r},t) = -e\left(\vec{E} + \vec{v}\times\vec{B}\right) \tag{2.7}$$

where $\vec{E}$ and $\vec{B}$ are given in equations (2.3) and (2.4). Usually, only the electric component of this force is considered, since it is approximately 2 orders of magnitude (v/c) larger than the magnetic force. Also, since the wavelengths considered in VCD spectroscopy (IR-region) are approximately 10^4 times larger than the size of a molecule, the fields can be considered uniform. Therefore, we can remove the position dependence of the electric field and its coupling with higher order multipoles.[29,34] This way:[35]

$$\vec{F}(t) = eE_0\vec{v}_e e^{-i\omega t} \tag{2.8}$$

Since the electric force is the gradient of a scalar potential W,[36] the potential associated with this Lorentz force becomes:

$$W = e\vec{E}\cdot\vec{r} = -\vec{E}\cdot\vec{\mu} \tag{2.9}$$

For the description of VCD however, the magnetic force cannot be ignored, and it can be shown in a similar fashion that the magnetic field interacts with the magnetic dipole moment of the molecule. The perturbation Hamiltonian to first order is the sum of the scalar potentials:

$$H^{(1)} = -\vec{E} \cdot \vec{\mu} - \vec{B} \cdot \vec{m} \tag{2.10}$$

In this equation, $\vec{\mu}$ and $\vec{m}$ are the electric and magnetic dipole moment operators, respectively. For a molecule with N atoms and n electrons, these are given by (in atomic units):

$$\vec{\mu} = \vec{\mu}^e + \vec{\mu}^n = -\sum_i^n e\vec{r}_i + \sum_J^N Z_\lambda e\vec{R}_J \tag{2.11}$$

$$\vec{m} = \vec{m}^e + \vec{m}^n = -\frac{e}{2mc}\sum_i^n \vec{r}_i \times \vec{p}_i + \sum_J^N \frac{Z_\lambda e}{2M_\lambda c}\vec{R}_J \times \vec{P}_J \tag{2.12}$$

Here, the spin magnetic moment of the nuclei and the electrons has been ignored. Combining equation (2.10) with (2.3) and (2.4) gives:

$$\begin{aligned} H_\pm^{(1)} &= -\frac{E_0}{\sqrt{2}}\left(\mu_x \cos(\omega t) \pm \mu_y \sin(\omega t)\right) - \frac{B_0}{\sqrt{2}}\left(\pm m_x \sin(\omega t) - m_y \cos(\omega t)\right) \\ H_\pm^{(1)} &= \underbrace{-\left(E_0\mu_x + B_0 m_y\right)}_{A}\left(e^{i\omega t} + e^{-i\omega t}\right) \pm \underbrace{i\left(-E_0\mu_y + B_0 m_x\right)}_{B}\left(e^{i\omega t} - e^{-i\omega t}\right) \end{aligned} \tag{2.13}$$

In the last equation, the time-independent parts of the perturbation Hamiltonian are indicated by the operators A and B. To calculate the influence of the oscillating part of the perturbation on the state function, we make use of time-dependent perturbation theory.[33] Inserting (2.10) in the time-dependent Schrödinger equation $H\Psi = i\hbar\frac{\partial\Psi}{\partial t}$ yields:

$$\begin{aligned} \sum_i a_i(t)[H^{(0)} + H^{(1)}(t)]\psi_i^{(0)} e^{-iE_i t/\hbar} = &\sum_i E_i a_i(t)\psi_i^{(0)} e^{-iE_i t/\hbar} \\ &+ i\hbar\sum_i \frac{\partial a_i(t)}{\partial t}\psi_i^{(0)} e^{-iE_i t/\hbar} \end{aligned} \tag{2.14}$$

Because the unperturbed time-independent Schrödinger equation $H^{(0)}\psi_i = E_i\psi_i$ holds, this becomes:

$$\sum_i a_i(t)H^{(1)}(t)\psi_i^{(0)}e^{-iE_it/\hbar} = i\hbar\sum_i \frac{\partial a_i(t)}{\partial t}\psi_i^{(0)}e^{-iE_it/\hbar} \tag{2.15}$$

Multiplying this expression to the left with $\psi_k^*(t)$ and integrating gives (in bra-ket notation):

$$\sum_i a_i(t)\left\langle k\right| H^{(1)}(t)\left|i\right\rangle e^{-iE_it/\hbar} = i\hbar\frac{\partial a_k(t)}{\partial t}e^{-iE_kt/\hbar} \tag{2.16}$$

The orthonormality of the eigenstates was used to remove the sum on the right hand side of (2.16). This equation can be further simplified by writing $\left\langle k\right| H^{(1)}(t)\left|i\right\rangle = H_{ki}^{(1)}(t)$ and defining $\hbar\omega_{ki} = E_k - E_i$.

$$\frac{\partial a_k(t)}{\partial t} = \frac{1}{i\hbar}\sum_i a_i(t)H_{ki}^{(1)}(t)e^{i\omega_{ki}t} \tag{2.17}$$

To integrate this set of simultaneous differential equations we need to determine the initial conditions. Consider a perturbation applied at $t = 0$ to a system that was in a stationary state n ($a_n(t \leqslant 0) = 1$. For a small perturbation, we can use the initial values of $a_k = \delta_{nk}$ as a viable approximation in the case of a weak and short perturbation.[37] With this, (2.17) becomes:

$$a_k(t) = \frac{1}{i\hbar}\int_0^t H_{kn}^{(1)}(t)e^{i\omega_{kn}t}dt \tag{2.18}$$

Inserting equation (2.13), the matrix elements $H_{kn}^{(1)}(t)$ can be written as:

$$H_{kn}^{(1)}(t) = A_{kn}\left(e^{i\omega t} + e^{-i\omega t}\right) \pm B_{kn}\left(e^{i\omega t} - e^{-i\omega t}\right) \tag{2.19}$$

Only the complex exponentials are time-dependent in these matrix elements. Inserting this in (2.18) gives:

$$\begin{aligned} a_k(t) =& \frac{1}{i\hbar}A_{kn}\int_0^t \left[e^{i(\omega_{kn}+\omega)t} + e^{i(\omega_{kn}-\omega)t}\right]dt \\ &\pm \frac{1}{i\hbar}B_{kn}\int_0^t \left[e^{i(\omega_{kn}+\omega)t} - e^{i(\omega_{kn}-\omega)t}\right]dt \end{aligned} \tag{2.20}$$

Grouping the two different exponential functions and integrating finally gives:

$$a_k(t) = \frac{1}{\hbar}\left[(A_{kn} \mp B_{kn})\frac{e^{i(\omega_{kn}+\omega)t}-1}{\omega_{kn}+\omega} + (A_{kn} \pm B_{kn})\frac{e^{i(\omega_{kn}-\omega)t}-1}{\omega_{kn}-\omega}\right] \tag{2.21}$$

Under the conditions of vibrational spectroscopy, the angular frequencies ω and ω_{kn} are of the order of 10^{13}, whereas the numerator in the above expression is of the order of 1. This means that the first term in (2.21) can safely be ignored in cases where $\omega \approx \omega_{kn}$.[38]

$$a_k(t) = \frac{1}{\hbar}H_{kn}^{(1)}\left[\frac{e^{i(\omega_{kn}-\omega)t}-1}{\omega_{kn}-\omega}\right] \tag{2.22}$$

where

$$H_{kn}^{(1)} = A_{kn} \pm B_{kn} = \langle k| - (E_0\mu_x + B_0 m_y) \pm i\,(E_0\mu_y - B_0 m_x)\,|n\rangle \tag{2.23}$$

The $\pm$ indicates the difference between right and left CPL for the matrix element $H_{kn}^{(1)}$. This way, the probability P_k to find the system in state $|k\rangle$ after the perturbation is given by:

$$P_k(t) = |a_k(t)|^2 = \frac{4|H_{kn}^{(1)}|^2}{\hbar^2\left(\omega_{kn}-\omega\right)^2}\sin^2\frac{1}{2}\left(\omega_{kn}-\omega\right)t \tag{2.24}$$

When interaction with a photon is involved, the final state, say $|f\rangle$, is actually a continuum of states. To account for this, the density of states $\rho_f(E_f)$, the number of states per energy interval dE_f is introduced.[33] To find the total transition probability to this continuum of states, we need to integrate 2.24 over the range of energies E_f:

$$P_f(t) = \int \frac{4|H_{fn}^{(1)}|^2}{\hbar^2}\frac{\sin^2\frac{1}{2}\left(E_f/\hbar-\omega\right)t}{\left(E_f/\hbar-\omega\right)^2}\rho(E_f)dE_f \tag{2.25}$$

where the transition frequency was written in terms of energy using the equation $\omega_{fn} = E/\hbar$. To simplify this expression, some approximations can be made. First of all, due to the sharpness of the function $\sin^2(x)/x^2$, we can assume that both $H_{fn}^{(1)}$ and $\rho(E_f)$ are constant over the small energy interval and thus can be brought outside the integral. This also incurs that the density of states $\rho(E_f)$ is to be evaluated at the radiation energy E_{fn}. Moreover, the form of this function allows us to extend the integration limits to infinity without incurring a substantial error. We thus get the

integral:

$$P_f(t) = \frac{|H_{fn}^{(1)}|^2}{\hbar^2}\rho(E_f)\int_{-\infty}^{\infty}\frac{\sin^2\frac{(E_f/\hbar-\omega)t}{2}}{\left(\frac{E_{fn}/\hbar-\omega)t}{2}\right)^2}dE_{fn} \tag{2.26}$$

Using the standard integral $\int_{-\infty}^{\infty}\frac{\sin^2(x)}{x^2}dx = \pi$ gives:

$$P_f(t) = \frac{2\pi}{\hbar}|H_{fn}^{(1)}|^2\rho(E_f)t \tag{2.27}$$

With this the transition rate, which is proportional to the spectral intensities, is given by:

$$w = \frac{dP}{dt} = \frac{2\pi}{\hbar}|H_{fn}^{(1)}|^2\rho(E_{fn}) \tag{2.28}$$

Equation 2.28 is known as 'Fermi's golden rule' (number 2).[33] It shows that the transition rate from the ground state to an excited state is proportional to the square modulus of the transition matrix element $\langle i|\, H^{(1)}\, |f\rangle$ of the perturbation Hamiltonian. In the following, this perturbation Hamiltonian will be specified to find the expression for the transition rate and thus the spectral intensities associated with IR and VCD.

2.2 Vibrational Circular Dichroism

2.2.1 IR and VCD Spectral Intensities

Having determined the time-dependent part of the transition probability (2.28), we now need to specify the time-independent part of the perturbation Hamiltonian to find the necessary expressions for IR and VCD spectroscopy. Writing $\mu^{\beta}_{fn} = \langle f| \mu^{\beta} |n\rangle$ and $m^{\beta}_{fn} = \langle f| m^{\beta} |n\rangle$, the square modulus of (2.23) becomes:

$$\begin{aligned} |H^{(1)}_{fn}|^2 = \quad & E_0^2 \left(|\mu^x_{fn}|^2 + |\mu^y_{fn}|^2 \right) + B_0^2 \left(|m^x_{fn}|^2 + |m^y_{fn}|^2 \right) \\ & \pm 2iE_0B_0 \left(\mu^x_{fn} m^x_{nf} + \mu^y_{fn} m^y_{nf} \right) \end{aligned} \tag{2.29}$$

Note that the wave functions $|n\rangle$ and $|f\rangle$ are real for a Hermitian Hamiltonian, just as the electric dipole moment operator $\vec{\mu}$. Looking at (2.11) and remembering that $\vec{p} = -i\hbar\vec{\nabla}$ in quantum mechanics,[35] one can see that $\vec{m}$ is purely imaginary, and also Hermitian. This way we have for the β-components of the dipole operators:

$$\langle k| (\vec{\mu})_{\beta} |n\rangle = \langle k| (\vec{\mu})_{\beta} |n\rangle^* = \langle n| (\vec{\mu})_{\beta} |k\rangle \qquad EDTM \tag{2.30}$$

$$\langle k| (\vec{m})_{\beta} |n\rangle = \langle k| (\vec{m})_{\beta} |n\rangle^* = -\langle n| (\vec{m})_{\beta} |k\rangle \qquad MDTM \tag{2.31}$$

where $\beta \in \{x, y, z\}$. Here we have defined $\langle n| \vec{\mu} |k\rangle$ as the Electric Dipole Transition Moment (EDTM) and $\langle n| \vec{m} |k\rangle$ as the Magnetic Dipole Transition Moment (MDTM) for the $n \to k$ transition. For an isotropic sample, we can take the average of the quantities $|\mu^{\alpha}_{fn}|^2$, $|m^{\alpha}_{fn}|^2$ and $\mu^{\alpha}_{fn} m^{\alpha}_{fn}$ as $\frac{1}{3}|\vec{\mu}_{fi}|^2$, $\frac{1}{3}|\vec{m}_{fi}|^2$ and $\frac{1}{3}(\vec{\mu}_{fi} \cdot \vec{m}_{fi})$ respectively. From classical electromagnetism, the field amplitudes E_0 and B_0 are related to the intensity I of the radiation. This can be calculated from the average value of the Poynting vector, which signifies the energy flux per unit time,[39] divided by the volume occupied by the radiation during that time.

$$I = \langle \vec{S} \rangle = \frac{cnE_0^2}{8\pi} = \frac{cB_0E_0}{8\pi} = \frac{cB_0^2}{n8\pi} \tag{2.32}$$

With this, the matrix element $|H^{(1)}_{fn}|^2$ is:

$$|H^{(1)}_{fn}|^2 = \frac{8\pi I}{3c} \left(|\vec{\mu}_{fi}|^2/n + n|\vec{m}_{fi}|^2 \pm 2i \left(\vec{\mu}_{fi}.\vec{m}_{if} \right) \right) \tag{2.33}$$

The transition rate is thus proportional to the radiation intensity. Inserting this equation in the expression for Fermi's golden rule (2.28) gives the transition rate in the case of CPL:

$$w_{\pm} = \frac{16\pi^2 I}{3\hbar c}\left(|\vec{\mu}_{fi}|^2/n + n|\vec{m}_{fi}|^2 \pm 2i\left(\vec{\mu}_{fi}\cdot\vec{m}_{if}\right)\right)\rho(E_{fn}) \tag{2.34}$$

We can now define the following quantities:

$$D_{if} = |\vec{\mu}_{fi}|^2 = \vec{\mu}_{if}\cdot\vec{\mu}_{fi} \qquad Electric\ Dipole\ Strength \tag{2.35}$$

$$G_{if} = |\vec{m}_{fi}|^2 = \vec{m}_{if}\cdot\vec{m}_{fi} \qquad Magnetic\ Dipole\ Strength \tag{2.36}$$

$$R_{if} = Im\left(\vec{m}_{if}\cdot\vec{m}_{fi}\right) \qquad Rotational\ Strength \tag{2.37}$$

Inserting this in (2.34), keeping in mind that $\vec{m}_{fi}$ is purely imaginary, we get:

$$w_{\pm} = \frac{16\pi^2 I}{3\hbar c}\left(D_{if}/n + nG_{if} \mp 2R_{if}\right)\rho(E_{fn}) \tag{2.38}$$

As a final step, we relate the transition rate to the observable molar extinction coefficient ϵ.[32] Consider a sample of concentration C and thickness dl. According to the Beer-Lambert law, the loss of radiation intensity through the sample is:

$$dI = -2.303\epsilon C I dl \tag{2.39}$$

On the other hand, the loss of intensity corresponds to the energy absorbed in the sample of thickness dl, which is the number of molecules CN_A times the average absorption rate $w_{\pm}$ and the energy per absorbed photon, $\hbar\omega_{fn}$.

$$dI = CN_A w_{\pm}\hbar\omega_{fn} dl \tag{2.40}$$

Comparing this with the Lambert-Beer law, we find the extinction coefficients for right and left CPL:

$$\epsilon_{\pm} = \frac{N_A\hbar\omega_{fn}w_{\pm}}{2.303I} \tag{2.41}$$

We can now express the macroscopic quantity ϵ in terms of the quantum mechanical quantity $w_{\pm}$. Equation (2.41) shows that the absorption of CPL differs in the sign of the rotational strength term in (2.38). Note that the intensity of the radiation in the denominator cancels the intensity in (2.38). First consider the case of absorption of

linearly polarized light (e.g. IR or UV spectroscopy). Linearly polarized light can be considered a superposition of left and right CPL of equal amplitude, with the same phase.[40]Also, the magnetic dipole strength, which is about 10^{-4} times smaller than its electric counterpart, can be ignored. The molar absorptivity for linearly polarized light then is:

$$\epsilon = \frac{N_A \hbar \omega_{fn}}{2.303I} \cdot \frac{w_+ + w_-}{2} = \frac{32\pi^2 N_A \nu}{3(2.303)\hbar c n} \cdot D_{if}\rho(\nu) \tag{2.42}$$

For circular dichroism, the difference between the extinction for left and right CPL is calculated. The electric and magnetic dipole strengths, which are equal for both forms of CPL, cancel and only the rotational strength remains.

$$\Delta\epsilon = \epsilon_+ - \epsilon_- = \frac{32\pi^2 N_A \nu}{3(2.303)\hbar c n} \cdot R_{if}\rho(\nu) \tag{2.43}$$

Equation (2.43) shows how the measurable differential molar extinction ϵ can be compared directly with theoretical expressions of CD intensity. Note that, since the nature of the state functions $|i\rangle$ and $|f\rangle$ is not yet specified, these equations are valid for both electronic (UV/ECD) and vibrational (IR/VCD) spectroscopy. Equation (2.43) is also intimately related to the Rosenfeld equation for optical rotation dispersion, as will be shown later in this chapter.[10]

A final factor that is not yet defined theoretically, is the form of the transition density $\rho(\omega)$, which was introduced because the transition occurs to a continuum of states with similar, but not equal energy. This corresponds to a broadening of the absorption peak, and is usually approximated with an empirical function.[32] For a transition for which the lifetime of the final state is assumed to decay exponentially, it can be shown that a Lorentzian band shape accounts for the energy uncertainty of the transition.[35] Therefore, when comparing theoretically derived transition intensities with experimental bands, the Lorentzian band shape superimposed on the absorption line is of the form:

$$\rho(\omega) = f_a(\omega) = \frac{1}{\pi}\left[\frac{\omega_{if} - \omega}{(\omega_{if} - \omega)^2 + \gamma_a^2}\right] \tag{2.44}$$

where γ_a is the exponential decay constant. The value for γ_a is usually chosen empirically as the one providing the best fit with the experiment.

Inspection of (2.43) shows that the differential molar absorption, and thus the VCD

signals, depend essentially on the rotational strength.

$$R_{if} = Im\left(\vec{m}_{if} \cdot \vec{m}_{fi}\right) = Im\left(\langle i|\,\vec{\mu}\,|f\rangle\,\langle f|\,\vec{m}\,|i\rangle\right) \tag{2.45}$$

In the following section, we clarify how the electric and magnetic dipole transition moments can be calculated ab initio for vibrational transitions, i.e. when the initial and final state of the molecule $|i\rangle$ and $|f\rangle$ represent vibrational states.

2.2.2 Vibrational Dipole Transitions Moments: Calculation of IR and VCD

In this section the framework in which the transition moments will be calculated is defined. It makes use of the Born-Oppenheimer (BO) approximation, which is widely used in quantum mechanics on molecular systems. Although useful for the calculation of the electric dipole transition moment, it turns out this approximation is invalid for the calculation of the magnetic dipole transition moment.[41]

2.2.2.1 Born-Oppenheimer Approximation

A molecular system is described by the (stationary) Schrödinger equation:

$$H\left(\vec{r},\vec{R}\right)\Psi_{Kk}\left(\vec{r},\vec{R}\right) = E_{Kk}\left(\vec{r},\vec{R}\right)\Psi_{Kk}\left(\vec{r},\vec{R}\right) \tag{2.46}$$

where $\vec{R}$ and $\vec{r}$ indicate the nuclear and electronic coordinates, respectively. The electronic and vibrational states of the molecules are indicated by the indices K and k. The Hamiltonian operator for a molecules with N nuclei of mass M_J and n electrons of mass m_e is defined as (in atomic units):

$$\begin{aligned} H\left(\vec{r},\vec{R}\right) = &\overbrace{-\sum_{J}^{N}\frac{\hbar^2}{2M_J}\nabla_J^2}^{T_N}\overbrace{-\frac{\hbar^2}{2m_e}\sum_{i}^{n}\nabla_i^2}^{T_E} \\ &\underbrace{+\frac{1}{2}\sum_{J\neq J'}^{N_J}\frac{Z_J Z_{J'} e^2}{r_{JJ'}} - \sum_{J}^{N}\sum_{i}^{n}\frac{Z_J e^2}{r_{Ji}} + \frac{1}{2}\sum_{i\neq j}^{n}\frac{e^2}{r_{ij}}}_{V} \end{aligned} \tag{2.47}$$

where T_N and T_E are the nuclear and electronic kinetic energy operators. The Coulombic potential energy is given by the terms combined in V. The indices i and J denote

electron and nucleus labels respectively. The Hamiltonian can thus be split up in an electronic Hamiltonian and a nuclear kinetic energy operator.

$$H\left(\vec{r},\vec{R}\right) = V(\vec{r},\vec{R}) + T_E(\vec{r}) + T_N(\vec{R}) = H_{el}(\vec{r},\vec{R}) + T_N(\vec{R}) \tag{2.48}$$

The Schrödinger equation (2.46) cannot be solved analytically for system with multiple electrons, causing the need for approximations. A wide-spread approximation is the so-called Born-Oppenheimer (BO) approximation, where the coupling of the movement of electrons and nuclei is ignored. This is justified because the electrons, being at least 3 orders of magnitude lighter, move much faster than the nuclei and can thus be considered to adapt instantaneously to changes in the nuclear geometry. Therefore, we can write the molecular wave function as the product of an electronic wave function $\psi_K(\vec{r};\vec{R})$ and a nuclear wave function $\chi_{Kk}(\vec{R})$.

$$\Psi_{Kk}(\vec{r},\vec{R}) = \psi_K(\vec{r};\vec{R})\chi_{Kk}(\vec{R}) \tag{2.49}$$

There is only a parametric dependence of the electronic wave function on the nuclear coordinates $\vec{R}$. Inserting this in (2.46) and using bra-ket notation gives:

$$(H_{el} + T_N)\,|\psi_K^A(\vec{r};\vec{R})\rangle\,|\chi_{Kk}^A(\vec{R})\rangle = E_{Kk}^A(\vec{r},\vec{R})\,|\psi_K^A(\vec{r};\vec{R})\rangle\,|\chi_{Kk}^A(\vec{R})\rangle \tag{2.50}$$

Here, the A superscript indicates that the wave function, and its corresponding energy are adiabatic, i.e. they change gradually and reversibly with nuclear coordinates. The operation of the electronic Hamiltonian H_{el} is governed by the electronic Schrödinger equation.

$$H_{el}(\vec{r},\vec{R})\,|\psi_K^A(\vec{r};\vec{R})\rangle = W_K^A(\vec{R})\,|\psi_K^A(\vec{r};\vec{R})\rangle \tag{2.51}$$

This equation describes the wave function of the electrons within a fixed set of nuclear coordinates, yielding the electronic energy (Potential Energy Surface or PES) as a function of the nuclear coordinates. For the other term in the Hamiltonian in (2.50), we need to let the nuclear kinetic energy operator act on the BO wave function. For

ease of notation, the arguments of the wave functions will not be written explicitly.

$$\begin{aligned} T_N \left|\psi_K\right\rangle \left|\chi_{Kk}\right\rangle &= -\sum_J^N \frac{\hbar^2}{2M_J} \nabla_J^2 \left|\psi_K\right\rangle \left|\chi_{Kk}\right\rangle \\ &= -\sum_J^N \frac{\hbar^2}{2M_J} \left[\left|\psi_K\right\rangle \nabla_J^2 \left|\chi_{Kk}\right\rangle + 2\nabla_J \left|\psi_K\right\rangle \nabla_J \left|\chi_{Kk}\right\rangle + \left|\chi_{Kk}\right\rangle \nabla_J^2 \left|\psi_K\right\rangle\right] \end{aligned} \tag{2.52}$$

In the BO approximation, the operation of the nuclear kinetic energy operator on the electronic wave function will be ignored, removing the last two terms in the previous equation. This way (2.50) becomes:

$$\left|\psi_K^A(\vec{r};\vec{R})\right\rangle \left(W_K^A(\vec{R}) + T_N\right) \left|\chi_{Kk}^A(\vec{R})\right\rangle = E_{Kk}^A(\vec{r},\vec{R}) \left|\psi_K^A(\vec{r};\vec{R})\right\rangle \left|\chi_{Kk}^A(\vec{R})\right\rangle \tag{2.53}$$

Multiplying to the left with $\langle\psi_K^A(\vec{r};\vec{R})|$ and integrating yields:

$$\left(W_K^A(\vec{R}) + T_N\right) \left|\chi_{Kk}^A(\vec{R})\right\rangle = E_{Kk}^A \left|\chi_{Kk}^A(\vec{R})\right\rangle \tag{2.54}$$

The total Schrödinger equation (2.46) can thus be solved in the BO approximation by first solving the electronic Schrödinger equation (2.51). The electronic energy $W_K^A(\vec{R})$ can then be used as a potential energy term for solving the nuclear Schrödinger equation (2.54).

2.2.2.2 Vibrational Electric Dipole Transition Moment

The calculation of the vibrational electric dipole transition moment (EDTM) can be done by inserting the BO wave function (2.49) into the definition of the EDTM (2.30). The dipole moment operators used are given by (2.11). For a vibrational transition $\Psi_{Gg} \rightarrow \Psi_{Ge}$ where the molecule remains in the electronic ground state G this becomes:

$$\left\langle\chi_{Gg}\right| \left\langle\psi_G\right| \vec{\mu} \left|\psi_G\right\rangle \left|\chi_{Gg}\right\rangle = \left\langle\chi_{Gg}\right| \left\langle\psi_G\right| \vec{\mu}^e \left|\psi_G\right\rangle + \vec{\mu}^n \left|\chi_{Ge}\right\rangle \tag{2.55}$$

The nuclear electric dipole moment operator does not act on the electronic wave function $\psi_G(r;\vec{R})$ and can thus be brought outside the integral $\langle\psi_G(\vec{r};\vec{R})|\,\vec{\mu}^n\,|\psi_G(\vec{r};\vec{R})\rangle$. It is clear that this gives rise to a separate electronic and nuclear contribution to the EDTM, and these will be treated below.

Electronic contribution to the EDTM The β Cartesian component of the electronic part of the EDTM is given by:

$$\langle \chi_{Gg} | \langle \psi_G | (\vec{\mu}^e)_\beta | \psi_G \rangle | \chi_{Ge} \rangle \tag{2.56}$$

Because of the orthogonality of the vibrational wave functions, an explicit dependence of the integrand $\langle \psi_G | (\vec{\mu}^e)_\beta | \psi_G \rangle$ must be induced to obtain a non-zero integral over the nuclear coordinates. This can be done using a Taylor series expansion around the equilibrium position $\vec{R}^0$ of the nuclei.

$$\langle \psi_G | (\vec{\mu}^e)_\beta | \psi_G \rangle = (\langle \psi_G | (\vec{\mu}^e)_\beta | \psi_G \rangle)_0 + \sum_{J\alpha} \left(\frac{\partial \langle \psi_G | (\vec{\mu}^e)_\beta | \psi_G \rangle}{\partial R_{J\alpha}} \right)_0 (R_{J\alpha} - R^0_{J\alpha}) + ... \tag{2.57}$$

where the zero subscript denotes evaluation of the derivative at equilibrium geometry. With this, and making use of the orthonormality of the nuclear wave functions we obtain for the nuclear component of the EDTM:

$$\langle \Psi_{Gg} | (\vec{\mu}^e)_\beta | \Psi_{Ge} \rangle = \sum_{J\alpha} \left(\frac{\partial \langle \psi_G | (\vec{\mu}^e)_\beta | \psi_G \rangle}{\partial R_{J\alpha}} \right)_0 \langle \chi_{Gg} | (R_{J\alpha} - R^0_{J\alpha}) | \chi_{Ge} \rangle \tag{2.58}$$

At this point we define the atomic polar tensor (APT), which has both nuclear and electronic contributions per atom. The electronic part is given by:

$$E^J_{\alpha\beta} = \left(\frac{\partial \langle \psi_G | (\vec{\mu}^e)_\beta | \psi_G \rangle}{\partial R_{J\alpha}} \right)_0 \tag{2.59}$$

Inserting this into the previous expression gives for the electronic part of the EDTM:

$$\langle \Psi_{Gg} | (\vec{\mu}^e)_\beta | \Psi_{Ge} \rangle = \sum_{J\alpha} E^J_{\alpha\beta} \langle \chi_{Gg} | (R_{J\alpha} - R^0_{J\alpha}) | \chi_{Ge} \rangle \tag{2.60}$$

The derivative in the APT can be calculated using coupled perturbed Hartree-Fock techniques. The calculation of the integral of the nuclear wave functions is relatively straightforward in the harmonic approximation, and will be discussed in more detail later in this chapter.

Nuclear contribution to the EDTM For the nuclear contribution to the EDTM, a similar approach is used. It is defined by:

$$\langle \Psi_{Gg} | \, (\vec{\mu}^n)_\beta \, | \Psi_{Ge} \rangle = \langle \chi_{Gg} | \, \vec{\mu}^n \, | \chi_{Ge} \rangle \tag{2.61}$$

As before we write down a first order Taylor expansion around the equilibrium nuclear coordinates for $(\vec{\mu}^n)_\beta$.

$$(\vec{\mu}^n)_\beta = [(\vec{\mu}^n)_\beta]_0 + \sum_{J\alpha} \left(\frac{\partial (\vec{\mu}^n)_\beta}{\partial R_{J\alpha}} \right)_0 (R_{J\alpha} - R^0_{J\alpha}) + ... \tag{2.62}$$

Again, we insert this in the equation for nuclear contribution to the EDTM and make use of the orthonormality of the nuclear wave functions.

$$\langle \Psi_{Gg} | \, (\vec{\mu}^n)_\beta \, | \Psi_{Gg} \rangle = \sum_{J\alpha} \left(\frac{\partial (\vec{\mu}^n)_\beta}{\partial R_{J\alpha}} \right)_0 \langle \chi_{Gg} | \, (R_{J\alpha} - R^0_{J\alpha}) \, | \chi_{Gg} \rangle \tag{2.63}$$

The nuclear contribution to the atomic polar tensor is very easily calculated (cf. equation (2.11)) and is given by:

$$N^J_{\alpha\beta} = \left(\frac{\partial (\vec{\mu}^n)_\beta}{\partial R_{J\alpha}} \right)_0 = Z_J e \delta_{\alpha\beta} \tag{2.64}$$

where $\delta_{\alpha\beta}$ is the Kronecker delta and equals 1 only if $\alpha = \beta$. The nuclear contribution to the EDTM thus becomes:

$$\langle \Psi_{Gg} | \, (\vec{\mu}^n)_\beta \, | \Psi_{Gg} \rangle = \sum_{J\alpha} N^J_{\alpha\beta} \langle \chi_{Gg} | \, (R_{J\alpha} - R^0_{J\alpha}) \, | \chi_{Ge} \rangle \tag{2.65}$$

2.2.2.3 Vibrational Magnetic Dipole Transition Moment

Similar as for the EDTM (cf. equation (2.55)), the vibrational MDTM can be calculated by inserting the magnetic dipole moment operator into the dipole transition integral:

$$\langle \chi_{Gg} | \, \langle \psi_G | \, \vec{m} \, | \psi_G \rangle \, | \chi_{Ge} \rangle = \langle \chi_{Gg} | \, \langle \psi_G | \, \vec{m}^e \, | \psi_G \rangle + \vec{m}^n \, | \chi_{Ge} \rangle \tag{2.66}$$

The calculation of both contributions is more involved than for the EDTM. First of all, the magnetic dipole moment operator now contains a momentum operator

which requires some additional manipulations to evaluate this within the harmonic approximation. Moreover, it will be shown that the electronic contribution to the MDTM vanishes within the BO approximation. To resolve this, several approaches are valid which are in fact equal in spirit.[10,29,42–45] In this work, the approach developed by P.J. Stephens will be followed.[41,42]

Nuclear contribution to the MDTM Again, the nuclear part can be brought out of the electronic wave function integral. Inserting the nuclear magnetic dipole moment operator yields:

$$\langle \Psi_{Gg} | \, \vec{m}^n \, | \Psi_{Ge} \rangle = \langle \chi_{Gg} | \, \vec{m}^n \, | \chi_{Gg} \rangle = \sum_J \frac{Z_J e}{2M_J c} \langle \chi_{Gg} | \, \vec{R}_J \times \vec{P}_J \, | \chi_{Ge} \rangle \tag{2.67}$$

Since by definition $\vec{R}_J - \vec{R}_J^0$ is parallel to the momentum $\vec{P}_J$ of a nucleus (the change of position follows the velocity vector), one can write for the β-component of the MDTM:

$$\begin{aligned} \langle \chi_{Gg} | \, (\vec{\mu}^n)_\beta \, | \chi_{Ge} \rangle &= \sum_J \frac{Z_J e}{2M_J c} \langle \chi_{Gg} | \, (\vec{R}_J^0 \times \vec{P}_J)_\beta \, | \chi_{Ge} \rangle \\ &= \sum_{J\alpha\gamma} \frac{Z_J e}{2M_J c} \epsilon_{\alpha\beta\gamma} R^0_{J\gamma} \langle \chi_{Gg} | \, P_{J\alpha} \, | \chi_{Ge} \rangle \end{aligned} \tag{2.68}$$

Here we have written the vectorial product by means of the Levi-Civita third rank tensor.[46] In view of the Ehrenfest theorem[35] $\vec{P}_J = -i\hbar\vec{\nabla}_J$ and the commutator relationship $\left[\vec{R}_J, T_N\right] = \frac{\hbar^2}{M_J}\vec{\nabla}_J$ we can write:[41]

$$\vec{P}_J = -i\frac{M_J}{\hbar}\left[\vec{R}_J, T_N\right] \tag{2.69}$$

and with this the expression for the nuclear MDTM becomes:[47]

$$\begin{aligned} \langle \chi_{Gg} | \, \vec{P}_J \, | \chi_{Ge} \rangle &= -i\frac{M_J}{\hbar}\left(\langle \chi_{Gg} | \, \vec{R}_J T_N \, | \chi_{Ge} \rangle - \langle \chi_{Gg} | \, T_N \vec{R}_J \, | \chi_{Ge} \rangle \right) \\ &= -i\frac{M_J}{\hbar}\left(\langle \chi_{Gg} | \, \vec{R}_J (T_N + W_G^A) \, | \chi_{Ge} \rangle - \langle \chi_{Gg} | \, (T_N + W_G^A) \vec{R}_J \, | \chi_{Ge} \rangle \right) \\ &= -i\frac{M_J}{\hbar}\left(E_{Ge}^A - E_{Gg}^A \right) \langle \chi_{Gg} | \, \vec{R}_J \, | \chi_{Ge} \rangle \\ &= -i\frac{M_J}{\hbar}\left(E_{Ge}^A - E_{Gg}^A \right) \langle \chi_{Gg} | \, \vec{R}_J - \vec{R}_J^0 \, | \chi_{Ge} \rangle \end{aligned} \tag{2.70}$$

where we have used the nuclear Schrödinger equation (2.54) and the fact that, due to the orthogonality of the vibrational wave functions $\langle \chi_{Gg} | \vec{R}^0_J | \chi_{Ge} \rangle = 0$. Inserting this into (2.68) gives the expression for the nuclear contribution of the MDTM:

$$\langle \Psi_{Gg} | (\vec{m}^n)_\beta | \Psi_{Ge} \rangle = -i \left(E^A_{Ge} - E^A_{Ge} \right) \sum_{J\alpha\gamma} \frac{Z_J e}{2\hbar c} \epsilon_{\alpha\beta\gamma} R^0_{J\gamma} \langle \chi_{Gg} | R_{J\alpha} - R^0_{J\alpha} | \chi_{Ge} \rangle \tag{2.71}$$

Similarly as for the EDTM, we can write this expression more simply by defining the Atomic Axial Tensor (AAT). The nuclear contribution to the AAT becomes:

$$J^J_{\alpha\beta} = \frac{ieZ_J}{4\hbar c} \sum_\gamma \epsilon_{\alpha\beta\gamma} R^0_{J\alpha} \tag{2.72}$$

With this, the final expression for the nuclear contribution to the MDTM is:

$$\langle \Psi_{Gg} | (\vec{m}^n)_\beta | \Psi_{Ge} \rangle = -2 \left(E^A_{Ge} - E^A_{Gg} \right) \sum_{J\alpha} J^J_{\alpha\beta} \langle \chi_{Gg} | R_{J\alpha} - R^0_{J\alpha} | \chi_{Ge} \rangle \tag{2.73}$$

Electronic contribution to the MDTM Looking at (2.66) the electronic contribution to the MDTM is:

$$\langle \chi_{Gg} | \langle \psi_G | \vec{m}^e | \psi_G \rangle | \chi_{Ge} \rangle \tag{2.74}$$

The electronic wave functions, being eigenfunctions of an unperturbed Hamiltonian, can be chosen real.[37] Also, the electronic magnetic dipole moment operator is purely imaginary (cf. equation (2.11)) and, as for any operator associated with an observable quantity, needs to be Hermitian.[35] Therefore, the electronic part of the integral is:

$$\langle \psi_G | \vec{m}^e | \psi_G \rangle = \langle \psi_G | \vec{m}^e | \psi_G \rangle^* = - \langle \psi_G | \vec{m}^e | \psi_G \rangle = 0 \tag{2.75}$$

This means that within the BO approximation the electronic contribution to the MDTM becomes zero. A solution to this non-physical result was formulated by Stephens, who by perturbing the adiabatic BO wave function with a magnetic field added an imaginary part to the electronic wave function, thus nullifying equation (2.75).[10] This was also done in a more explicit manner by others, but since the equations obtained by Stephens were the first to be implemented, these will be presented here.

2.2.2.4 Beyond Born-Oppenheimer: electronic MDTM

As mentioned before we need to implement corrections to the BO wave function using first order perturbation theory. As perturbation Hamiltonian we use the terms of the nuclear kinetic energy operator T_N that were neglected in the BO-approximation, which are the second and third terms in equation (2.52) representing action of the T_N operator on the electronic wave function.

$$T_N^{(1)} = \vec{\nabla}_\lambda^e \vec{\nabla}_J^e + 2\vec{\nabla}_J^e \vec{\nabla}_J^N \tag{2.76}$$

where $\vec{\nabla}_J^e$ and $\vec{\nabla}_J^N$ denote the gradient operator operating on the electronic or nuclear wave function respectively. The corrected wave function is:

$$\Psi_{Kk}^{corr} = \Psi_{Kk} + \sum_{K'k' \neq Kk} \frac{\langle \Psi_{K'k'} | \, T_N^{(1)} \, | \Psi_{Kk} \rangle}{E_{Kk} - E_{K'k'}} \cdot \Psi_{K'k'} + ... \tag{2.77}$$

In this equation $T_N^{(1)}$ represents the two terms of T_N acting on the electronic wave function. Using this function to calculate the electronic part of the MDTM and retaining only first order terms (the zeroth order term disappears, cf. (2.75)) we can write:

$$\begin{aligned} \langle \Psi_{Gg}^{corr} | \, \vec{m}^e \, | \Psi_{Ge}^{corr} \rangle = & \sum_{Kk \neq Ge} \langle \Psi_{Gg} | \, \vec{m}^e \, | \Psi_{Kk} \rangle \, \frac{\langle \Psi_{Kk} | \, T_N^{(1)} \, | \Psi_{Ge} \rangle}{E_{Ge} - E_{Kk}} \\ & + \sum_{Kk \neq Gg} \langle \Psi_{Kk} | \, \vec{m}^e \, | \Psi_{Ge} \rangle \, \frac{\langle \Psi_{Gg} | \, T_N^{(1)} \, | \Psi_{Kk} \rangle}{E_{Gg} - E_{Kk}} \end{aligned} \tag{2.78}$$

For ease of notation, we now consider only the first term. All manipulations for the second term are similar. Writing the first term explicitly, we have:

$$\begin{aligned} & \sum_{Kk \neq Ge} \langle \Psi_{Gg} | \, \vec{m}^e \, | \Psi_{Kk} \rangle \, \frac{\langle \Psi_{Kk} | \, T_N^{(1)} \, | \Psi_{Ge} \rangle}{E_{Ge} - E_{Kk}} \\ & = \sum_{Kk \neq Ge} \frac{\langle \chi_{Gg} | \, \langle \psi_G | \, \vec{m}^e \, | \psi_K \rangle \, | \chi_{Kk} \rangle \, \langle \chi_{Kk} | \, \langle \psi_K | \, T_N^{(1)} \, | \psi_G \rangle \, | \chi_{Ge} \rangle}{E_{Ge} - E_{Kk}} \\ & = \sum_J \sum_{Kk \neq Ge} \frac{-\hbar^2}{2M_J} \frac{\langle \chi_{Gg} | \, \langle \psi_G | \, \vec{m}^e \, | \psi_K \rangle \, | \chi_{Kk} \rangle \, \langle \chi_{Kk} | \, \langle \psi_K | \, \vec{\nabla}_J^e \vec{\nabla}_J^e + 2\vec{\nabla}_J^e \vec{\nabla}_J^N \, | \psi_G \rangle \, | \chi_{Ge} \rangle}{E_{Ge} - E_{Kk}} \end{aligned}$$

Note that according to this expression, only mixing of excited electronic BO states ($K \neq G$) contribute to the MDTM. This expression can be simplified by making some approximations. First of all, the Franck-Condon principle states that for vibronic transitions, because the nuclear mass is much larger than that of an electron, electronic transitions occur within a stationary nuclear framework.[37] This translates into the fact that electronic matrix elements can be evaluated at the ground-state equilibrium geometry, evaluated at $\vec{R} = \vec{R}^0$ which is indicated by the 0-subscript.

$$\begin{aligned}
\langle\psi_G|\,\vec{m}^e\,|\psi_K\rangle &\approx \langle\psi_G|\,\vec{m}^e\,|\psi_K\rangle_0 \\
\langle\psi_G|\,\vec{\nabla}_J^2\,|\psi_K\rangle &\approx \langle\psi_G|\,\vec{\nabla}_J^2\,|\psi_K\rangle_0 \\
\langle\psi_G|\,\vec{\nabla}_J\,|\psi_K\rangle &\approx \langle\psi_G|\,\vec{\nabla}_J\,|\psi_K\rangle_0
\end{aligned}$$

As a second approximation the vibrational contribution to the energy difference between the two vibronic states can be neglected:

$$E_{Ge} - E_{Kk} \approx W_G^0 - W_K^0 \tag{2.79}$$

Because of this we can bring the sum of vibrational states in the numerator to closure ($\sum_k |\chi_{Kk}\rangle \langle\chi_{Kk}| = 1$), thus eliminating the sum over vibrational states in (2.78). With this, the first term of (2.78) becomes:

$$\begin{aligned}
&\sum_{K\neq G} \frac{-\hbar^2}{M_J} \frac{\langle\chi_{Gg}|\,\langle\psi_G|\,\vec{m}^e\,|\psi_K\rangle_0\,\langle\psi_K|\,\vec{\nabla}_J^e\,|\psi_G\rangle_0\,\vec{\nabla}_J^N\,|\chi_{Ge}\rangle}{W_G^0 - W_K^0} \\
&= \sum_{J\alpha}\sum_{K\neq G} \frac{-\hbar^2}{M_J} \frac{\langle\psi_G|\,\vec{m}^e\,|\psi_K\rangle_0\,\langle\psi_K|\,\frac{\partial}{\partial R_{J\alpha}}\,|\psi_G\rangle_0}{W_G^0 - W_K^0}\,\langle\chi_{Gg}|\,\frac{\partial}{\partial R_{J\alpha}}\,|\chi_{Ge}\rangle
\end{aligned} \tag{2.80}$$

where the Laplacian term on the electronic wave function is left out because of the orthogonality of vibrational wave functions within the same electronic state. A similar expression can be found for the second term of (2.78). Also, by integrating by parts it follows that $\langle\psi_K|\,\frac{\partial}{\partial R_{J\alpha}}\,|\psi_G\rangle_0 = \langle\psi_K|\,|\psi_G\rangle_0 - \langle\psi_G|\,\frac{\partial}{\partial R_{J\alpha}}\,|\psi_K\rangle_0 = -\langle\psi_G|\,\frac{\partial}{\partial R_{J\alpha}}\,|\psi_K\rangle_0$. With this, the total expression for the electronic part of the magnetic dipole transition moment is given by:

$$\langle\Psi_{Gg}^{corr}|\,\vec{m}^e\,|\Psi_{Ge}^{corr}\rangle = -2\sum_{J\alpha}\sum_{K\neq G} \frac{\langle\psi_G|\,\vec{m}^e\,|\psi_K\rangle_0\,\langle\psi_K|\,\frac{\partial}{\partial R_{J\alpha}}\,|\psi_G\rangle_0}{W_G^0 - W_K^0}\,\langle\chi_{Gg}|\,\frac{\partial}{\partial R_{J\alpha}}\,|\chi_{Ge}\rangle \tag{2.81}$$

As a final step, the overlap of the nuclear coordinate derivative of the vibrational wave functions can be written as demonstrated in equation (2.70). We finally find the expression for the electronic part of the MDTM:

$$\langle \Psi_{Gg}^{corr} | \, \vec{m}^e \, | \Psi_{Ge}^{corr} \rangle = \\ 2(E_{Ge} - E_{Gg}) \sum_{J\alpha} \sum_{K \neq G} \frac{-\hbar^2}{M_J} \frac{\langle \psi_G | \vec{m}^e | \psi_K \rangle_0 \langle \psi_K | \frac{\partial}{\partial R_{J\alpha}} | \psi_G \rangle_0}{W_G^0 - W_K^0} \langle \chi_{Gg} | \, R_{J\alpha} - R_{J\alpha}^0 \, | \chi_{Ge} \rangle \tag{2.82}$$

This expression corresponds to the vibronic coupling theory by Nafie and Friedman.[10,43] Through mixing with excited electronic BO wave functions, the electronic contribution to the MDTM becomes non-zero. Also note that through the $\vec{m}^e$ operator, imaginary character is added to the corrected wave function. However, evaluation of (2.82) is impracticable because of the presence of the sum over all excited electronic states. This could partially be resolved with the average excites-state energy approximation or the sum-over-states vibronic coupling theory, but with undetermined accuracy. The first exact method to circumvent the evaluation of all excited electronic states was given by the Magnetic Field Perturbation (MFP) Theory. Here, the sum of all the matrix elements $\langle \psi_G | \, \vec{m}^e \, | \psi_K \rangle_0$ is evaluated by perturbing the ground state electronic wave function with a stationary magnetic field.

2.2.2.5 Magnetic Field Perturbation Theory

Two perturbations are needed to evaluate the sums of electronic matrix elements. For the nuclear coordinate derivative matrix elements, a nuclear coordinate derivative perturbation of the electronic wave function is suggested to add explicit dependence on the nuclear geometry.

Nuclear Displacement Perturbation We start by expanding the ground state electronic wave as a Taylor series around the equilibrium geometry:

$$\psi_G(\vec{r}, \vec{R}) = \psi_G(\vec{r}, \vec{R}^0) + \sum_{J\alpha} \left(\frac{\partial \psi_G}{\partial R_{J\alpha}} \right)_0 (R_{J\alpha} - R_{J\alpha}^0) + ... \tag{2.83}$$

Similarly, the electronic Hamiltonian corresponding to the electronic wave function can be expanded around the equilibrium geometry:

$$H_{el} = H_{el}^0 + \sum_{J\alpha} \left(\frac{\partial H_{el}}{\partial R_{J\alpha}} \right)_0 (R_{J\alpha} - R_{J\alpha}^0) + ... \tag{2.84}$$

Using the first order term of (2.84) as the perturbation Hamiltonian, the corrected electronic wave function according to first-order perturbation theory is:

$$\psi_G(\vec{r}, \vec{R}) = \psi_G^0 + \sum_{J\alpha} \sum_{K \neq G} \frac{\langle \psi_K | \frac{\partial H_{el}}{\partial R_{J\alpha}} | \psi_G \rangle_0}{W_G^0 - W_K^0} \psi_K^0 (R_{J\alpha} - R_{J\alpha}^0) + ... \tag{2.85}$$

By comparison of (2.85) and (2.83), the nuclear coordinate derivative of the ground state electronic wave function can be written as:

$$\left(\frac{\partial \psi_G}{\partial R_{J\alpha}} \right)_0 = \sum_{K \neq G} \frac{\langle \psi_K | \frac{\partial H_{el}}{\partial R_{J\alpha}} | \psi_G \rangle_0}{W_G^0 - W_K^0} \psi_K^0 \tag{2.86}$$

Substituting this into (2.82) yields:

$$\begin{gathered} \langle \Psi_{Gg}^{corr} | \, \vec{m}^e \, | \Psi_{Ge}^{corr} \rangle = \\ -2(E_{Ge} - E_{Gg}) \sum_{J\alpha} \sum_{K \neq G} \frac{\langle \psi_G | \vec{m}^e | \psi_K \rangle_0 \langle \psi_K | \frac{\partial H_{el}}{\partial R_{J\alpha}} | \psi_G \rangle_0}{(W_G^0 - W_K^0)^2} \langle \chi_{Gg} | \, R_{J\alpha} - R_{J\alpha}^0 \, | \chi_{Ge} \rangle \end{gathered} \tag{2.87}$$

Magnetic Field Perturbation To evaluate the electronic magnetic dipole moment matrix elements, a magnetic field perturbation is at issue. As stated before (equation (2.10)) (the electronic part of) the perturbation Hamiltonian for a molecule in a magnetic field $\vec{B}$ along the β-direction is:

$$H^{(1)} = -(\vec{m}^e)_\beta B_\beta \tag{2.88}$$

As before, we write down the Taylor series to first order of the electronic wave function, but this time with respect to the external magnetic field.

$$\psi_G(\vec{r}, \vec{R}^0, B_\beta) = \psi_G^0 + \left(\frac{\partial \psi_G(\vec{r}, \vec{R}^0, \vec{B})}{\partial B_\beta} \right)_0 B_\beta + ... \tag{2.89}$$

where the derivative is evaluated at equilibrium geometry and zero magnetic field strength. Again, we find from perturbation theory, with the perturbation Hamiltonian stated above:

$$\psi_K(\vec{r},\vec{R}) = \psi_K^0 + \sum_{K'\neq K} \frac{\langle\psi_{K'}| - (\vec{m}^e)_\beta |\psi_K\rangle_0 B_\beta}{W_K^0 - W_{K'}^0}\psi_{K'}^0 + ... \tag{2.90}$$

Combining the previous two equations, the sum of the electronic magnetic dipole moment matrix elements in (2.82) can be written as follows:

$$-\sum_{K\neq G} \frac{\langle\psi_K| (\vec{m}^e)_\beta |\psi_G\rangle_0}{W_G^0 - W_K^0}\psi_K^0 = \left(\frac{\partial\psi_G(\vec{r},\vec{R}^0,\vec{B})}{\partial B_\beta}\right)_0 \tag{2.91}$$

As can readily be seen from equation (2.82), the product of magnetic dipole moment matrix elements and nuclear displacement derivative matrix elements can be reproduced by calculating the overlap between the derivatives obtained in (2.91) and (2.86).

$$\begin{aligned}\left\langle \left(\frac{\partial\psi_G}{\partial R_{J\alpha}}\right)_0 \middle| \left(\frac{\partial\psi_G}{\partial B_\beta}\right)_0 \right\rangle &= -\sum_{K,K'\neq G} \frac{\langle\psi_{K'}| \frac{\partial H_{el}}{\partial R_{J\alpha}} |\psi_G\rangle_0^*}{W_G^0 - W_{K'}^0} \frac{\langle\psi_K| (\vec{m}^e)_\beta |\psi_G\rangle_0}{W_G^0 - W_K^0}\delta_{KK'} \\ &= \sum_{K\neq G} \frac{\langle\psi_G| (\vec{m}^e)_\beta |\psi_K\rangle_0 \langle\psi_K| \frac{\partial H_{el}}{\partial R_{J\alpha}} |\psi_G\rangle_0}{(W_G^0 - W_K^0)^2}\end{aligned} \tag{2.92}$$

which corresponds exactly to the sum over excited electronic states in (2.87). This means that the MDTM can be written as follows:

$$\langle\Psi_{Gg}^{corr}| \vec{m}^e |\Psi_{Ge}^{corr}\rangle = -2(E_{Ge}-E_{Gg}) \sum_{J\alpha} \left\langle \left(\frac{\partial\psi_G}{\partial R_{J\alpha}}\right)_0 \middle| \left(\frac{\partial\psi_G}{\partial B_\beta}\right)_0 \right\rangle \langle\chi_{Gg}| R_{J\alpha} - R_{J\alpha}^0 |\chi_{Ge}\rangle \tag{2.93}$$

Similarly as for equation (2.71), we now can define the electronic contribution to the atomic axial tensor.

$$I_{\alpha\beta}^J = \left\langle \left(\frac{\partial\psi_G}{\partial R_{J\alpha}}\right)_0 \middle| \left(\frac{\partial\psi_G}{\partial B_\beta}\right)_0 \right\rangle \tag{2.94}$$

which gives for the electronic contribution to the MDTM:

$$\langle\Psi_{Gg}^{corr}| \vec{m}^e |\Psi_{Ge}^{corr}\rangle = -2(E_{Ge} - E_{Gg}) \sum_{J\alpha} I_{\alpha\beta}^J \langle\chi_{Gg}| R_{J\alpha} - R_{J\alpha}^0 |\chi_{Ge}\rangle \tag{2.95}$$

2.2.3 The Harmonic Approximation

Although expressions for the atomic polar and axial tensors have been derived, we need to discuss how to evaluate the integral over the nuclear wave functions in the expressions for the EDTM and MDTM.

2.2.3.1 Normal Modes

As explained before, the nuclear wave functions are obtained by solving the nuclear Schrödinger equation (2.54):

$$(W_K^A + T_N)\,|\chi_{Kk}^A(\vec{R})\rangle = E_{Kk}^A\,|\chi_{Kk}^A(\vec{R})\rangle \tag{2.96}$$

The potential energy W_K is obtained as the eigenvalue of the electronic Schrödinger equation (2.51). However, if the oscillations around the equilibrium geometry $\vec{R}^0$ are small, this potential energy can be written as a Taylor series around $\vec{R}^0$.[48]

$$W_K^A(\vec{R}) = W_K^A(\vec{R}^0) + \sum_i \left(\frac{\partial W_K^A}{\partial \vec{R}_i}\right)_0 (\vec{R}_i - \vec{R}_i^0) + \frac{1}{2}\sum_{i,j}\left(\frac{\partial^2 W_K^A}{\partial \vec{R}_i \partial \vec{R}_j}\right)_0 (\vec{R}_i - \vec{R}_i^0)(\vec{R}_j - \vec{R}_j^0) + \ldots \tag{2.97}$$

The i and j indices are labels of the nuclei, the 0 subscript denotes that the derivatives are evaluated the equilibrium geometry. Because of this, the first derivative equals zero, and thus the second term in (2.97) vanishes. The first term merely adds a constant to the potential energy and can be chosen zero. For sufficiently small oscillations, higher order terms can be neglected (harmonic approximation),[31] leaving us with:

$$W_K^A(\vec{R}) = \frac{1}{2}\sum_{i,j}\left(\frac{\partial^2 W_K^A}{\partial \vec{R}_i \partial \vec{R}_j}\right)_0 (\vec{R}_i - \vec{R}_i^0)(\vec{R}_j - \vec{R}_j^0) \tag{2.98}$$

The second order derivatives of the energy are the force constants of the oscillations, and are gathered in the so-called Hessian matrix $\mathbf{F}$ of dimension $(3N \times 3N)$, with N the number of atoms in the molecule. If $\mathbf{R}$ is defined as a $3N \times 1$ column vector containing all nuclear displacements for each Cartesian coordinate, the above equation can be written as:

$$W_K^A(\vec{R}) = \frac{1}{2}\mathbf{R}^T\mathbf{F}\mathbf{R} \tag{2.99}$$

Inserting this into the nuclear Schrödinger equation gives:

$$(-\sum_i \frac{\hbar^2}{2M_i}\nabla_i^2 + \frac{1}{2}\mathbf{R}^T\mathbf{F}\mathbf{R})\,|\chi_{Kk}(\vec{R})\rangle = E_{Kk}\,|\chi^A_{Kk}(\vec{R})\rangle \tag{2.100}$$

The Hessian matrix $\mathbf{F}$ has, unlike the kinetic energy term, off-diagonal elements with mixed derivatives of the potential energy. This makes the nuclear Schrödinger equation non-separable. This can be resolved by transforming the coordinate system in such a way that the Hessian matrix becomes diagonal while maintaining the independence of nuclear contributions the the kinetic energy. First, both $\mathbf{R}$ and are mass-weighted.

$$\begin{aligned} F^{MW}_{ij} &= \frac{F_{ij}}{\sqrt{M_i M_j}} \\ q_k &= \frac{R_k}{\sqrt{m_i}} \qquad k = 3i-2, 3i-1, 3i \end{aligned} \tag{2.101}$$

The symmetric square matrix $\mathbf{F}^{MW}$ can be diagonalized by a unitary transformation matrix $\mathbf{U}$ which has the eigenvectors of the Hessian matrix as its columns, yielding a diagonal matrix $\mathbf{\Lambda}$ with the eigenvalues as the elements.

$$\mathbf{U}^T\mathbf{F}^{MW}\mathbf{U} = \mathbf{\Lambda} \tag{2.102}$$

From the eigenvalues λ_i, the vibrational frequencies can be calculated:

$$\tilde{\nu}_i = \sqrt{\frac{\lambda_i}{4\pi c^2}} \tag{2.103}$$

The first 6 eigenvalues equal zero for non-linear polyatomic molecules, and correspond to translation and rotation of the molecule as a whole.[48] If we now substitute the coordinates in the Hamiltonian of (2.100) for the so-called normal coordinates ($\mathbf{q} = \mathbf{QU}$), we get:

$$\begin{aligned} (-\sum_i \frac{\hbar^2}{2M_i}\nabla_i^2 + \frac{1}{2}\mathbf{R}^T\mathbf{F}\mathbf{R}) &= -\frac{\hbar^2}{2}\sum_i \frac{\partial^2}{\partial Q_i^2} + \frac{1}{2}\mathbf{Q}^T\mathbf{U}^T\mathbf{F}^{MW}\mathbf{U}\mathbf{Q}) \\ &= -\frac{\hbar^2}{2}\sum_i \frac{\partial^2}{\partial Q_i^2} + \frac{1}{2}\mathbf{Q}^T\mathbf{\Lambda}\mathbf{Q}) \\ &= -\frac{\hbar^2}{2}\sum_i \frac{\partial^2}{\partial Q_i^2} + \frac{1}{2}\lambda_i Q_i^2) \end{aligned} \tag{2.104}$$

With this, (2.100) becomes:

$$(-\frac{\hbar^2}{2}\sum_i \frac{\partial^2}{\partial Q_i^2} + \frac{1}{2}\lambda_i Q_i^2)) \left|\chi_{Kk}(\vec{R})\right\rangle = E_{Kk} \left|\chi_{Kk}(\vec{R})\right\rangle \tag{2.105}$$

Since the Hamiltonian is a sum of terms in one variable only, this wave equation is now separable into 3N-6 differential equations in one variable, one for each normal coordinate. We have thus reached the intended goal of the coordinate transformation.

$$-\frac{\hbar^2}{2}\frac{\partial^2\phi_{ki}(Q_i)}{\partial Q_i^2} + \frac{1}{2}\lambda_i Q_i^2 \phi_{k_i}(Q_i) = E_{k_i}\phi_{k_i}(Q_i) \tag{2.106}$$

The total nuclear wave function of vibrational state k can then be written as a product of the resulting wavefunction for each mode.[48]

$$\chi_{Kk}(\vec{R}) = \phi_{k_1}(\vec{Q_1})\phi_{k_2}(\vec{Q_2})\cdots = \prod_i \phi_{k_i}(\vec{Q_i}) \tag{2.107}$$

Equations of the form of (2.106) are a standard problem in quantum mechanics. The solutions are called Hermite polynomials and the corresponding energies are given by:[37]

$$E_{k_i} = (\nu_i + \frac{1}{2})\hbar\omega_i \qquad \omega_i = \sqrt{\lambda_i} \qquad \nu_i = 0, 1, 2, \ldots \tag{2.108}$$

The coordinate transformation between the Cartesian displacement $\vec{R}_J - \vec{R}_J^0$ and the normal coordinates Q_i is given by:

$$\Delta\mathbf{R}_J = \sum_i \left(\frac{\partial \mathbf{R}_J}{\partial Q_i}\right)_{Q=0} Q_i = \mathbf{S}_J\mathbf{Q} \tag{2.109}$$

$\mathbf{S}$ can be interpreted as contribution of each nuclear displacement for a given normal mode (and thus vibrational transition), and is closely related to the unitary transformation $\mathbf{U}$.[10]

2.2.3.2 Dipole Transition Moments in the Harmonic Approximation

Having described the framework of the harmonic approximation, we can now use this to evaluate the integral $\langle\chi_{Gg}| R_{J\alpha} - R^0_{J_\alpha} |\chi_{Ge}\rangle$ in the equation for both the electric

and magnetic dipole transition moment. From the previous, we have:[48]

$$\langle \chi_{Gg} | \, R_{J\alpha} - R^0_{J\alpha} \, | \chi_{Ge} \rangle = \sum_i S^\alpha_{J,i} \, \langle \chi_{Gg} | \, Q_i \, | \chi_{Ge} \rangle \tag{2.110}$$

By inserting (2.107) and making use of the properties of Hermite polynomials, this reduces to:[37,48]

$$\langle \chi_{Gg} | \, R_{J\alpha} - R^0_{J\alpha} \, | \chi_{Ge} \rangle = \left(\frac{\hbar}{2\omega_i} \right)^{1/2} S^\alpha_{J,i} \tag{2.111}$$

2.2.4 Vibrational Dipole Transition Moments: Summary

With this, we can now write the final expression for the β-component of the EDTM and the MDTM associated with the i^{th} normal mode of a vibrational transition $0 \to 1$:

$$\begin{aligned}
&EDTM: \\
&\langle 0 | \, (\vec{\mu})_\beta \, | 1 \rangle_i = \left(\frac{\hbar}{2\omega_i} \right)^{1/2} S^\alpha_{J,i} \sum_{J\alpha} \left(P^J_{\alpha\beta} \right) \\
&\langle 0 | \, (\vec{\mu}^e)_\beta + (\vec{\mu}^n)_\beta \, | 1 \rangle_i = \left(\frac{\hbar}{2\omega_i} \right)^{1/2} S^\alpha_{J,i} \sum_{J\alpha} \left(E^J_{\alpha\beta} + N^J_{\alpha\beta} \right) \\
&\qquad = \left(\frac{\hbar}{2\omega_i} \right)^{1/2} S^\alpha_{J,i} \sum_{J\alpha} \left(\left(\frac{\partial \, \langle \psi_G | \, (\vec{\mu}^e)_\beta \, | \psi_G \rangle}{\partial R_{J\alpha}} \right)_0 + Z_J e \delta_{\alpha\beta} \right) \\
&MDTM: \\
&\langle 0 | \, (\vec{m})_\beta \, | 1 \rangle_i = \left(2\hbar^3 \omega_i \right)^{1/2} S^\alpha_{J,i} \sum_{J\alpha} \left(A^J_{\alpha\beta} \right) \\
&\langle 0 | \, (\vec{m}^e)_\beta + (\vec{m}^n)_\beta \, | 1 \rangle_i = \left(2\hbar^3 \omega_i \right)^{1/2} S^\alpha_{J,i} \sum_{J\alpha} \left(I^J_{\alpha\beta} + J^J_{\alpha\beta} \right) \\
&\qquad = \left(2\hbar^3 \omega_i \right)^{1/2} S^\alpha_{J,i} \sum_{J\alpha} \left(\left\langle \left(\frac{\partial \psi_G}{\partial R_{J\alpha}} \right)_0 \middle| \left(\frac{\partial \psi_G}{\partial B_\beta} \right)_0 \right\rangle + \frac{ieZ_J}{4\hbar c} \sum_\gamma \epsilon_{\alpha\beta\gamma} R^0_{J\alpha} \right)
\end{aligned}$$

These equations express the EDTM and MDTM, needed for the calculation of the dipole and rotational strength (and thus the IR and VCD intensities) in a way that can be evaluated using molecular orbitals (MO) that are given as a linear combination of atomic orbitals (LCAO). The derivatives with respect to the nuclear coordinates and an external magnetic field translate to derivatives of the molecular orbital coefficients (and

of the basis functions in case of nuclear displacements),[49] which can be calculated using Coupled Perturbed Hartree-Fock (CPHF) or Coupled Perturbed Kohn-Sham (CPKS) theory.[50,51] This will not be discussed in this short introduction.

2.3 Optical Rotatory Dispersion

As a second chiroptical technique that was used frequently throughout this thesis, optical rotation (OR), or its wavelength dependent form optical rotatory dispersion (ORD) is discussed. Although optical rotation dispersion is very closely related to circular dichroism and can even directly be obtained from it,[10] its first theoretical derivation by Rosenfeld[52] will be illustrated briefly in this section.[37]

2.3.1 The Origin of Optical Rotation

Optical rotation, which is the rotation of the plane of polarization of electromagnetic radiation passing through an optically active medium, stems from the difference between the indices of refraction of left and right circularly polarized light. This is reflected in the propagation vector $\vec{k}$ of the electric (or magnetic) field vector of the radiation (equation (2.1)).

$$\vec{k}_{\pm} = \frac{2\pi\nu n_{\pm}}{c}\vec{e}_k \tag{2.112}$$

with ν the light frequency and where the $+$ and - subscripts denote right and left CPL. As linearly polarized light is a superposition of left and right CPL of equal amplitude, it is quite easily calculated that the radiation after passing through the medium of length l, is still linearly polarized and that the plane of polarization has rotated by:[29]

$$\Delta\theta = \frac{\omega l(n_- - n_+)}{2c} \tag{2.113}$$

2.3.2 Polarizabilty Tensor

To find an expression for this difference in refractive indices, we consider a medium for which the polarization of the molecules is proportional to the electric field and the rate of change of the magnetic field ($P = N\alpha\vec{E} - N\beta\dot{\vec{B}}$, with N the number density of the molecules).[29] Using this polarization in solving the Maxwell equations yields for the refractive index:

$$n_{\pm} \approx 1 + \frac{\alpha N}{2\epsilon_0} \pm \frac{\omega\beta N}{2c\epsilon_0} \tag{2.114}$$

and for the rotation angle of the plane of polarization:

$$\Delta\theta = 1/2Nl\mu_0\omega^2\beta \tag{2.115}$$

α is the polarizability tensor and describes the linear change of dipole moment with the electric field $\vec{E}$, and β is its magnetic counterpart. Also, since the energy change of the system occurs through coupling of the dipole moment with the electric field of the radiation (cf. equation (2.10)) we can write:[50]

$$\alpha = -\left(\frac{\partial^2 E}{\partial \vec{E}^2}\right)_0 = \left(\frac{\partial \langle \vec{\mu} \rangle}{\partial \vec{E}}\right)_0 \tag{2.116}$$

$$\beta = -\left(\frac{\partial^2 E}{\partial \vec{E} \partial \dot{\vec{B}}}\right)_0 = \left(\frac{\partial \langle \vec{\mu} \rangle}{\partial \dot{\vec{B}}}\right)_0 \tag{2.117}$$

where the derivatives of the energy E are evaluated at electric/magnetic field strength $\vec{E} = \vec{B} = 0$. Note that β is not to be confused with the hyperpolarizability. To find β, and thus the optical rotation angle, we need to find an expression for $\langle \vec{\mu} \rangle$ which is linear in $\vec{E}$ and $\dot{\vec{B}}$. Just as for circular dichroism, this can be done using time-dependent perturbation theory, using the same perturbation Hamiltonian ((2.10) and (2.13)). This means that we can use the same coefficients $a_k(t)$ as in (2.18):

$$a_k(t) = \frac{1}{i\hbar} \int_0^t H_{kn}^{(1)}(t) e^{i\omega_{kn} t} dt \tag{2.118}$$

With this, the expectation value of the dipole moment with the perturbed wave functions becomes (where + denotes right and - left CPL):

$$\begin{aligned} \langle \vec{\mu}_\pm \rangle &= \vec{\mu}_0 + \sum_{k \neq 0} \left(\langle 0 | \vec{\mu} | k \rangle a_{k,\pm} e^{-i\omega_{k0} t} + \langle k | \vec{\mu} | 0 \rangle a_{k,\pm}^* e^{i\omega_{k0} t} \right) \\ &= \frac{2}{\hbar} Re \left[\sum_{k \neq 0} \left(\frac{\omega_{k0}}{\omega_{k0}^2 - \omega^2} \right) \langle 0 | \vec{\mu} | k \rangle \langle k | \vec{\mu} | 0 \rangle \overbrace{E_0 \left(\cos(\omega t) \vec{e}_x \pm \sin(\omega t) \vec{e}_y \right)}^{\vec{E}_\pm} \right] \\ &- \frac{2}{\hbar} Im \left[\sum_{k \neq 0} \left(\frac{\omega}{\omega_{k0}^2 - \omega^2} \right) \langle 0 | \vec{\mu} | k \rangle \langle k | \vec{m} | 0 \rangle \underbrace{B_0 \left(\pm \cos(\omega t) \vec{e}_x + \sin(\omega t) \vec{e}_y \right)}_{\dot{\vec{B}}_\pm} \right] \end{aligned} \tag{2.119}$$

Indeed, an expression is found for the electric dipole moment as a linear function of $\vec{E}_\pm$ and $\dot{\vec{B}}_\pm$. After averaging over all orientations we find for β:

$$\beta = \frac{2}{3\hbar} \sum_{k \neq 0} \frac{Im \left[\langle 0 | \vec{\mu} | k \rangle \langle k | \vec{m} | 0 \rangle \right]}{\omega_{k0}^2 - \omega^2} \tag{2.120}$$

This quantity relates closely to the so-called electric dipole-magnetic dipole polarizability tensor ($\beta = -\omega^{-1}(G'_{xx} + G'_{yy} + G'_{zz})/3$).[53] In the static limit for which $\omega \ll \omega_{k0}$ (2.120) simplifies to:[54–56]

$$\beta = \frac{2\hbar}{3} \sum_{k \neq 0} \frac{Im\left[\langle 0|\,\vec{\mu}\,|k\rangle\,\langle k|\,\vec{m}\,|0\rangle\right]}{\left(E_k^0 - E_0^0\right)^2} \tag{2.121}$$

In a similar fashion as in 2.2.2.5, the sum over states can be overcome as follows in this static approximation using first-order perturbation theory:

$$\begin{aligned} \frac{\partial \psi_0}{\partial B_\beta} &= \sum_{k \neq 0} \frac{\langle k|\,(\vec{m})_\beta\,|0\rangle}{E_k^0 - E_0^0} \psi_k^0 \\ \frac{\partial \psi_0}{\partial E_\alpha} &= \sum_{k \neq 0} \frac{\langle k|\,(\vec{\mu})_\alpha\,|0\rangle}{E_k^0 - E_0^0} \psi_k^0 \end{aligned} \tag{2.122}$$

and with this:[57]

$$\beta_{\alpha\beta} = \frac{2\hbar}{3} Im\left[\left\langle \frac{\partial \psi_0}{\partial E_\alpha} \middle| \frac{\partial \psi_0}{\partial B_\beta} \right\rangle\right] \tag{2.123}$$

This again shows the close relation between ORD and CD (compare with equation (2.94)). It is even possible to directly obtain an ORD curve from an CD spectrum through the Kramers-Kronig transform between the real (ORD) and the imaginary (CD) parts of the index of refraction.[10]

2.4 Raman Optical Activity

The last chiroptical technique that will be briefly discussed is Raman optical activity (ROA). As the name suggests, this is the circular polarized counterpart of Raman spectroscopy, as is VCD for IR. Raman scattering is a process in which an incident photon is inelastically scattered by a molecule, thereby gaining or losing energy. This can be understood as a response of the polarizability, which we encountered in equation (2.116), to the incident radiation, moderated by the change of the charge distribution (and thus the dipole moment) during a vibrational transition.[58] Therefore, the Raman intensity is given by:

$$I_{\zeta'\beta} \propto \left| \langle 0| \alpha_{\zeta'\beta} |1\rangle (\vec{E})_\beta \right|^2 = \left| \left\langle 0 \middle| \frac{\partial(\vec{\mu})_{\zeta'}}{\partial(\vec{E})_\beta} \middle| 1 \right\rangle (\vec{E})_\beta \right|^2 \tag{2.124}$$

where ζ' is the scattered photon polarization and $\alpha_{\zeta'\beta}$ is the same quantity as encountered in the first term of (2.119). As for other chiroptical techniques, to include optical activity we need to extend our description of the dipole moment to incorporate also the dependence of the magnetic field, and in the case of ROA the electric field gradient:[29]

$$(\vec{\mu})_\alpha = \alpha_{\alpha\beta}(\vec{E})_\beta + \alpha'_{\alpha\beta}\omega^{-1}(\dot{\vec{E}})_\beta + G'_{\alpha\beta}\omega^{-1}(\dot{\vec{B}})_\beta + \frac{1}{3}A_{\alpha\beta\gamma}(\vec{\nabla})_\beta(\vec{E})_\gamma + \dots \tag{2.125}$$

Here, the electric dipole-magnetic dipole polarizability tensor $G'_{\alpha\beta}$ (cf. 2.3.2) and the electric dipole-quadrupole polarizability tensor $A_{\alpha\beta\gamma}$ are defined. $\alpha'_{\alpha\beta}$ corresponds to the imaginary part of the electric dipole-dipole polarizability. These quantities are given by:[29]

$$\begin{aligned}
\alpha_{\alpha\beta} &= \frac{2}{\hbar}\sum_{k\neq 0}\left(\frac{\omega_{k0}}{\omega_{k0}^2-\omega^2}\right) Re\left[\langle 0|(\vec{\mu})_\alpha|k\rangle\langle k|(\vec{\mu})_\beta|0\rangle\right] \\
\alpha'_{\alpha\beta} &= -\frac{2}{\hbar}\sum_{k\neq 0}\left(\frac{\omega}{\omega_{k0}^2-\omega^2}\right) Im\left[\langle 0|(\vec{\mu})_\alpha|k\rangle\langle k|(\vec{\mu})_\beta|0\rangle\right] \\
G'_{\alpha\beta} &= -\frac{2}{\hbar}\sum_{k\neq 0}\left(\frac{\omega}{\omega_{k0}^2-\omega^2}\right) Im\left[\langle 0|(\vec{\mu})_\alpha|k\rangle\langle k|(\vec{m})_\beta|0\rangle\right] \\
A_{\alpha\beta\gamma} &= \frac{2}{\hbar}\sum_{k\neq 0}\left(\frac{\omega_{k0}}{\omega_{k0}^2-\omega^2}\right) Re\left[\langle 0|(\vec{\mu})_\alpha|k\rangle\langle k|(\mathbf{\Theta})_\beta|0\rangle\right]
\end{aligned} \tag{2.126}$$

All these quantities contain a sum over (electronic) states of the dipole or multipole operators. Note that the vibrational contributions to $G'_{\alpha\beta}$ correspond to the VCD rotational strength, again showing the close relationship between ROA and VCD. The electric dipole operator $\vec{\mu}$ and the magnetic dipole operator $\vec{m}$ were defined before (equation (2.11)). The electric quadrupole operator is defined as:[10]

$$\mathbf{\Theta}_{\alpha\beta} = -\frac{e}{2}\sum_i \left(3(\vec{r}_i)_\alpha(\vec{r}_i)_\beta - (\vec{r}_i)_\alpha(\vec{r}_i)_\alpha\right) \tag{2.127}$$

where the summation goes over all electrons i for ROA applications. The vibrational transition moment of these polarizability tensors, needed for the evaluation of the intensity (2.124), can then be calculated similarly as for VCD, as illustrated for the electric dipole-dipole polarizability below:[59]

$$\begin{aligned}\langle\chi_{Gg}|\,\alpha_{\alpha\beta}\,|\chi_{Ge}\rangle_i &= \left\langle \chi_{Gg}\left|\frac{2}{\hbar}\sum_{k\neq 0}\left(\frac{\omega_{k0}}{\omega_{k0}^2-\omega^2}\right) Re\left[\langle 0|\,(\vec{\mu})_\alpha\,|k\rangle\,\langle k|\,(\vec{\mu})_\beta\,|0\rangle\right]\right|\chi_{Ge}\right\rangle_i \\ &= \frac{2}{\hbar}\sum_{k\neq 0}\left(\frac{\omega_{k0}}{\omega_{k0}^2-\omega^2}\right) Re\left[\frac{\partial\left(\langle 0|\,(\vec{\mu})_\alpha\,|k\rangle\,\langle k|\,(\vec{\mu})_\beta\,|0\rangle\right)_0}{\partial\vec{Q}_i}\right]\langle\chi_{Gg}|\,Q_i\,|\chi_{Ge}\rangle\end{aligned} \tag{2.128}$$

where the same normal modes Q_i as for VCD are used, having exactly the same vibrational frequencies and movements (cf. equation (2.109)). The calculated intensities can then be linked to experimental observables. Several experimental set-ups lead to different observables, depending on the scattering angle and the polarization states of the incident and scattered light.[44]

$$\begin{aligned}\left[I_R^U(180°) - I_L^U(180°)\right]^i_{Gg,Ge} &= \frac{8K}{c}\left[12\,\langle\chi_{Gg}|\,\beta(G')^2 + 4\beta(A)^2\,|\chi_{Ge}\rangle_i\right] \\ \left[I_Z^R(90°) - I_Z^L(90°)\right]^i_{Gg,Ge} &= \frac{4K}{c}\left[6\,\langle\chi_{Gg}|\,\beta(G')^2 - 2\beta(A)^2\,|\chi_{Ge}\rangle_i\right] \\ \left[I_U^R(0°) - I_U^L(0°)\right]^i_{Gg,Ge} &= \frac{8K}{c}\left[\langle\chi_{Gg}|\,90\alpha G' + 2\beta(G')^2 - 2\beta(A)^2\,|\chi_{Ge}\rangle_i\right]\end{aligned} \tag{2.129}$$

where the angle is the scattering geometry, the superscripts of the intensity denote the polarization state of the incident light and the intensity subscripts the polarization state of the scattered light. It can readily be seen that the ROA intensity is largest in the backscattering (180 °) measurement, which is therefore by far the most common experimental set-up.[10] In this thesis, results are related to a so-called Scattered Circular

Polarization (SCP)-ROA instrument, which uses unpolarized incident radiation and measures the difference in intensity of the right and left circularly polarized scattered radiation.[10] For unpolarized Raman spectra in the SCP set-up, the intensity is:

$$\left[I_R^U(180°) + I_L^U(180°)\right]_{Gg,Ge}^i = 4K\left[45\left\langle\chi_{Gg}\right|\alpha^2\left|\chi_{Ge}\right\rangle_i + 7\left\langle\chi_{Gg}\right|\beta(\alpha)^2\left|\chi_{Ge}\right\rangle_i\right] \tag{2.130}$$

where all tensor components have been averaged over all orientations, producing quantities invariant to rotation of the coordinate system. These Raman (2) and ROA (3) invariants are given by:

$$\alpha^2 = \frac{1}{9}\alpha_{\alpha\alpha}\alpha_{\beta\beta} \tag{2.131}$$

$$\beta\left(\alpha\right)^2 = \frac{1}{2}\left(3\alpha_{\alpha\beta}\alpha_{\alpha\beta} - \alpha_{\alpha\alpha}\alpha_{\beta\beta}\right) \tag{2.132}$$

$$\alpha G' = \frac{1}{9}\alpha_{\alpha\alpha}G'_{\beta\beta} \tag{2.133}$$

$$\beta\left(G'\right)^2 = \frac{1}{2}\left(3\alpha_{\alpha\beta}G'_{\alpha\beta} - \alpha_{\alpha\alpha}G'_{\beta\beta}\right) \tag{2.134}$$

$$\beta\left(A\right)^2 = \frac{1}{2}\omega\alpha_{\alpha\beta}\epsilon_{\alpha\gamma\delta}A_{\gamma\delta\beta} \tag{2.135}$$

where the greek subscripts assume an Einstein summation over all Cartesian coordinates, and ϵ is the Levi-Civita tensor.

2.5 Nuclear Magnetic Resonance

Nuclear magnetic resonance (NMR) is a well established technique in the structure determination of organic molecules. Although it is most often used as an experimental technique using rules of thumb for the interpretation of the spectra, in this thesis calculated chemical shifts are frequently used. We take a brief look at the physics behind the phenomenon of NMR, and mainly at how the resonance frequency of the nuclei changes with the chemical (molecular) environment of the nucleus (for example $^{13}\mathrm{C}$ or $^{1}\mathrm{H}$) in question. This chemical shift (δ) is defined by the magnetic shielding tensor σ.

2.5.1 Basic Principles of Nuclear Magnetic Resonance

Each nucleus has intrinsic or spin angular momentum $\vec{I}$ of magnitude $\hbar\sqrt{I(I+1)}$ and associated with this a nuclear magnetic dipole moment:[31]

$$\vec{m}_N = g_N \frac{e}{2m_p c}\vec{I} = \gamma_N \vec{I} \tag{2.136}$$

with g_N the nuclear g-factor, m_p the proton mass and γ_N is the nuclear magnetogyric ratio. In the presence of an external magnetic field the interaction energy between the nuclear magnetic moment and the magnetic induction is:

$$H^{(B)} = -\vec{m}_N \cdot \vec{B} = -\gamma_N \vec{I} \cdot \vec{B} \tag{2.137}$$

The energy of the system thus depends on the external magnetic field strength and the nuclear-spin quantum number I, and the application of the magnetic field has generated an energy separation between the different states. If this system is now exposed to electromagnetic radiation, we again arrive in the situation described in section 2.1.2. The perturbation due to the electromagnetic radiation is similar to (2.137) and the probability of making the transition $n \to k$ is (cf. equation (2.18)):[31]

$$P_{kn}(t) = \frac{1}{\hbar^2}\left| \int_0^t \langle\psi_k| - \gamma_N \vec{I} \cdot \vec{B}(t) \, |\psi_n\rangle \, e^{i\omega_{kn}t} dt \right|^2 \tag{2.138}$$

where the magnetic field is now periodically changing as in (2.4). When the radiation frequency ω approaches the energy difference between the states $\omega_{kn} = \gamma_N B$, resonance occurs and there is absorption of the electromagnetic radiation. The resonance

frequency thus varies linearly with the magnetic field strength. Usually, this resonance frequency falls into the radio-frequency (rf) range of the electromagnetic spectrum for common magnetic field strengths of 1-20 T. However, for molecules this field is not exactly the same as the applied external field. The local magnetic field experienced by each nucleus also depends on the magnetic field arising from the movement of the electrons, induced by the external magnetic field (magnetic shielding tensor giving rise to the chemical shift), and on the (indirect) interaction with the spin angular momentum of the other nuclei in the molecule (spin-spin coupling giving rise to fine structure of NMR spectra). In the following, only the former will be discussed as it plays an important role in the results of this thesis.

2.5.2 Magnetic Shielding Constant

In this section we describe the response of the electronic energy to both the external magnetic field and the magnetic field caused by the nuclei. An electron current density is induced counteracting the applied external field $\vec{B}$, which lies at the basis of the chemical shift.[37] The local magnetic field at each nucleus is given by:

$$\vec{B}_i = (1 - \sigma_i)\vec{B} \tag{2.139}$$

σ_i is a second-rank tensor called the shielding constant, describing the reduction of the field experienced by nucleus i. The energy of the molecule can be written as a function of the external and nuclear magnetic field:

$$E(\vec{B}_{ext}, \vec{m}_N) = E_0 + \frac{1}{2}\left(\frac{\partial^2 E}{(\partial \vec{B})^2}\right)_0 \cdot \vec{B}^2 + \frac{1}{2}\left(\frac{\partial^2 E}{(\partial \vec{m}_N)^2}\right)_0 \cdot \vec{m}_N^2 + \left(\frac{\partial^2 E}{\partial \vec{B} \partial \vec{m}_N}\right)_0 \cdot \vec{B} \cdot \vec{m} \tag{2.140}$$

where the 0 subscripts signifies that the derivatives are being evaluated at $\vec{B} = 0$ and $\vec{m}_N = 0$. The first order terms are not written since they vanish for closed-shell systems. By inserting the local magnetic induction at nucleus i (2.139) in the expression for the interaction of the nuclear magnetic moment with the external field (2.137) and identifying the linear dependence in $\vec{m}_N$ and $\vec{B}_{ext}$, the expression for the shielding constant becomes:[60,61]

$$\sigma_i = \left(\frac{\partial^2 E}{\partial \vec{B} \partial \vec{m}_N}\right)_0 \tag{2.141}$$

The quadratic terms in (2.140) correspond to the molecular magnetizability and the spin-spin coupling in NMR respectively, and will not be discussed in the context of this thesis. From time-independent perturbation theory, we can write the second order correction to the energy as:[50,62]

$$\frac{\partial^2 E}{\partial \vec{B} \partial \vec{m}_N} = \left\langle 0 \middle| \frac{\partial^2 H}{\partial \vec{B} \partial \vec{m}_N} \middle| 0 \right\rangle - 2 \sum_{n \neq 0} \frac{\langle 0| \frac{\partial H}{\partial \vec{B}} |n\rangle \langle n| \frac{\partial H}{\partial \vec{m}_N} |0\rangle}{E_n - E_0} \tag{2.142}$$

To evaluate this we need to find the correct Hamiltonian to describe the molecule, and more specifically the electronic movement, in the magnetic field. Using the canonical momentum ($\vec{p} \rightarrow \vec{p} + e\vec{A}$) we can write the Hamiltonian for the molecule in the presence of a magnetic field $\vec{B}$:[37]

$$H = H^0 + \underbrace{\frac{e}{m_e} \vec{A} \cdot \vec{p}}_{H^{(1)}} + \underbrace{\frac{e^2}{2m_e} A^2}_{H^{(2)}} \tag{2.143}$$

where $\vec{A}$ is the vector potential associated with the magnetic field. We consider two sources of the magnetic field and thus the vector potential: a uniform external magnetic field and the field generated by the magnetic dipole moments of the nuclei:[63]

$$\begin{aligned} \vec{A}_{ext} &= 1/2 \vec{B} \times \vec{r} \\ \vec{A}_{nuc} &= \left(\frac{\gamma_N \mu_0}{4\pi r^3} \right) \vec{I} \times \vec{r} \end{aligned} \tag{2.144}$$

Here, $\vec{r}$ is the distance of an electron to the nucleus. Note that electron spin is not considered for NMR shielding constants. Looking at equations (2.143) and (2.144) it follows that several terms will appear in the perturbation Hamiltonian and thus the energy expression. The $H^{(1)}$-term describes interaction between the external and nuclear magnetic fields with the electronic orbital momentum and is linear in the magnetic field. The second order $H^{(2)}$-term has three contributions: two quadratic contributions in the external magnetic field and the nuclear magnetic moment, and a mixed bilinear term coupling the nuclear magnetic moment with the external magnetic field.[50,62] Looking at (2.140) and (2.142), we can see that linear terms in $\vec{B}$ and/or $\vec{m}_N$ are of interest for the shielding constant: the $H^{(1)}$-term and the bilinear term of

$H^{(2)}$.

$$\begin{aligned} H^{(1)} &: \left(\vec{A}_{ext} + \vec{A}_{nuc}\right) \cdot \vec{p} \\ &= \frac{1}{2}\vec{B} \cdot \vec{l} + \frac{\gamma_N \mu_0}{4\pi r^3}\vec{I} \cdot \vec{l} \end{aligned} \tag{2.145}$$

where $\vec{l} = \vec{r} \times \vec{p}$ is the orbital angular momentum. The first term is the *orbital-Zeeman* term and the second is the *Paramagnetic Spin-Orbit* operator. The derivatives with respect to $\vec{B}$ and $\vec{m}_N$ are easily calculated from this. The bilinear term in both sources of the magnetic field is the *diamagnetic shielding* operator and is given by:

$$H^{(2)}_{\vec{B},\vec{I}} = \frac{e^2 \gamma_N \mu_0}{16 m_e \pi r^3} \left(\vec{B} \times \vec{r}\right) \cdot \left(\vec{I} \times \vec{r}\right) \tag{2.146}$$

For a freely rotating molecule, the expectation value of this expression can be written as the *Lamb* formula:[37]

$$\left\langle 0 \middle| H^{(2)}_{\vec{B},\vec{I}} \middle| 0 \right\rangle = \left(\frac{e^2 \mu_0}{12 m_e \pi}\right) \left\langle 0 \middle| \frac{1}{r} \middle| 0 \right\rangle \tag{2.147}$$

Inserting the above expressions for the Hamiltonian derivatives finally gives for the isotropic shielding constant ($\sigma = Tr[\sigma]$) of nucleus i in a freely rotating molecule:

$$\sigma_{\mathbf{i}} = \left(\frac{e^2 \mu_0}{12 m_e \pi}\right) \left\langle 0 \middle| \frac{1}{r} \middle| 0 \right\rangle - \left(\frac{e^2 \mu_0}{12 m_e^2 \pi}\right) \sum_{n \neq 0} \frac{\langle 0| \vec{l} |n\rangle \langle n| \frac{\vec{l}}{r^3} |0\rangle}{E_n - E_0} \tag{2.148}$$

Evaluation of the second-order energy derivative involves derivatives of the electronic wave function to the magnetic field which is obtained using CPHF or CPKS methods, similar as for VCD (cf. equation (2.91)).[62] Therefore, calculation of magnetic shielding constants requires little extra effort when VCD calculations are performed.[34,64]

2.5.3 Relating Magnetic Shielding to Experimental Chemical Shifts

Usually, chemical shifts relative to that of an internal standard, mostly tetramethylsilane (TMS), are measured. Thus, one needs to calculate also the magnetic shielding tensor for TMS, and then obtain the chemical shift using the definition:

$$\delta_i = \sigma_{TMS} - \sigma_i \tag{2.149}$$

For most organic molecules, this value is positive for protons and carbon atoms since the electron current density, and thus the paramagnetic shielding, is relatively high for the TMS protons and carbon atoms. A more elegant way of obtaining the chemical shift relative to TMS, is by performing a linear regression of the calculated shielding constants for each nucleus under consideration with the measured chemical shift. Not only is the calculation of the magnetic shielding of TMS avoided this way, the slope obtained by the linear regression also serves as a scaling factor to eliminate systematic error in the computed magnetic shielding.[65] The regression expression is:

$$\begin{aligned} \sigma_i &= \alpha\delta_i + \beta \\ \delta_i &= \frac{\sigma_i - \beta}{\alpha} \end{aligned} \tag{2.150}$$

The β-intercept is an estimate for the TMS magnetic shielding (2.149), whereas the slope α serves to fit the calculated values for the chemical shielding to the experimental ones, thus removing systematic error.[66,67] In the case of a tight fit with the experimental data, a slope close to -1 is found.

Unlike the chiroptical methods discussed in this chapter, NMR gives no information about the chirality of the sample under study. Studies of the chemical shifts do have an added value for comparison of species with multiple stereogenic centres (diastereoisomers) for which no mirror relationship exists for both the molecular structures and their chiroptical spectra. Two statistical methods are used, both developed by Smith and Goodman,[68,69] which are used in slightly different circumstances.

In case that the NMR chemical shieldings of two diastereomeric samples are measured, we need to determine which of the experimental NMR spectra corresponds best to which set of calculated chemical shifts, so determining the relative configuration of the samples. This can be done by comparing the differences of the calculated chemical shifts for all relevant nuclei, with the differences of the measured chemical shifts of the same nuclei. If the difference of the calculated chemical shift of nucleus i of molecule A and B is given as $\Delta_{i,calc} = \delta_i^A - \delta_i^B$ and of the experimental shifts of sample I and II by $\Delta_{i,exp} = \delta_i^I - \delta_i^{II}$, the CP3-value is defined as:

$$CP3 = \frac{\sum_i f_3(\Delta_{i,exp}, \Delta_{i,calc})}{\sum \Delta_{i,exp}^2} \tag{2.151}$$

where

$$f_3(\Delta_{i,exp}, \Delta_{i,calc}) = \begin{cases} \Delta^3_{i,exp}/\Delta_{i,calc} \; if \; \Delta_{i,calc}/\Delta_{i,exp} > 1 \\ \Delta_{i,exp}/\Delta_{i,calc} \; otherwise \end{cases} \tag{2.152}$$

It can readily be seen that the value for CP3 increases whenever both Δ-values have the same sign, and gives a rather high penalty when the calculated difference is opposite in sign to the measured one. Also, if the differences have the same sign, but $\Delta_{i,calc} > \Delta_{i,exp}$, which also corresponds to poor agreement, the value of CP3 is increased less. The denominator in (2.151) is used for normalization, yielding a value of $+1$ for perfect agreement of A with I and B with II, and a value of -1 if A corresponds to II and B to I. Moreover, it is possible to assign a level of confidence to the information obtained with the CP3 calculation. Using Bayes' theorem, the probability that the proposed configuration is correct given the calculated CP3 value is:[68]

$$P(AC_1|value) = \frac{P(value|AC_1) \times P(AC_1)}{P(value)} \tag{2.153}$$

This algorithm proves very useful in assigning the relative configuration of diastereomers when two experimental samples are available. However, in some cases, only one diastereomer, and thus one set of experimental data, is available. Smith and Goodman have developed an algorithm that calculates the deviation of both calculated chemical shifts with the experiment.[69]

$$e = \delta_{i,calc} - \delta_{i,exp} \tag{2.154}$$

This error function is assumed to obey a t-distribution with mean μ and standard deviation σ. The probability that candidate structure A, with calculated shifts $\delta^A_{i,calc}$ corresponds to the experiment is then given by:

$$P(A|\delta_1, \delta_2 \ldots \delta_n) = \frac{\prod_{i=1}^{n} \left[1 - T^{\nu}\left(\frac{|(\delta^A_{i,calc} - \delta_{i,exp}) - \mu|}{\sigma}\right)\right]}{\sum_{J=1}^{M} \prod_{i=1}^{n} \left[1 - T^{\nu}\left(\frac{|(\delta^J_{i,calc} - \delta_{i,exp}) - \mu|}{\sigma}\right)\right]} \tag{2.155}$$

where n is the number of nuclei considered, M is the number of candidate structures and T^{ν} is the cumulative t-distribution function for ν degrees of freedom. With (2.155) a probability can be assigned to each candidate structure, allowing for a straightforward

evaluation of which calculation corresponds best to the experimental data.

2.6 Interpretation of Molecular Property Tensors

2.6.1 Dipole Transition Moments

The electric and magnetic dipole transition moments have to be interpreted as the response of the electric and magnetic dipole moment to the change in vibrational state, and thus the change of the charge distribution (electric) or charge velocity distribution (magnetic) with change of the nuclear configuration. This is calculated by expanding the electronic wave function to first order in the normal coordinates or normal coordinate velocities.[10]

$$\langle \Psi_{G0} | \vec{\mu} | \Psi_{G1} \rangle_i = \left(\frac{\partial \langle \psi_G | \vec{\mu} | \psi_G \rangle}{\partial Q_i} \right)_0 \langle \chi_{G0} | Q_i | \chi_{G1} \rangle \tag{2.156}$$

$$\langle \Psi_{G0} | \vec{m} | \Psi_{G1} \rangle_i = \left(\frac{\partial \langle \psi_G | \vec{m} | \psi_G \rangle}{\partial \dot{Q}_i} \right)_0 \langle \chi_{G0} | \dot{Q}_i | \chi_{G1} \rangle \tag{2.157}$$

The first equation describes a linear movement of charge (through the definition of $\vec{\mu}$) with nuclear oscillations (EDTM). The second equation quantifies the change of circular motion (since $\vec{m} \propto \vec{r} \times \vec{p}$) of charge with the vibrational transition (MDTM). Taking the square of the EDTM gives rise to a linear oscillation of charge, which is the dipole strength. Taking the scalar product of the EDTM with the MDTM, combines linear motion of charge with circular motion into helical motion of charge. This helical motion is chiral in its helical rotation sense, and gives rise to the rotational strength.

$$D_i = \left| \left(\frac{\partial \langle \vec{\mu} \rangle}{\partial Q_i} \right)_0 \langle \chi_{G0} | Q_i | \chi_{G1} \rangle \right|^2 \tag{2.158}$$

$$R_i = Im \left[\left(\frac{\partial \langle \vec{\mu} \rangle}{\partial Q_i} \right)_0 \left(\frac{\partial \langle \vec{m} \rangle}{\partial \dot{Q}_i} \right)_0 \langle \chi_{G0} | Q_i | \chi_{G1} \rangle \langle \chi_{G0} | \dot{Q}_i | \chi_{G1} \rangle \right] \tag{2.159}$$

2.6.2 Molecular Property Tensors as Energy Derivatives

The derivatives used for determining the dipole and rotational strength, being the APT and AAT, can be used to make a first order expansion of the dipole moments with

respect to nuclear coordinates.[58]

$$\vec{\mu} = \vec{\mu}_0 + \sum_i \left(\frac{\partial \vec{\mu}}{\partial \vec{R}_i} \right)_0 d\vec{R}_i + \dots \tag{2.160}$$

$$\vec{m} = \vec{m}_0 + \sum_i \left(\frac{\partial \vec{m}}{\partial \dot{\vec{R}}_i} \right)_0 d\dot{\vec{R}}_i + \dots \tag{2.161}$$

Note that the nuclear velocities have to be used to correctly describe the magnetic moment with oscillation of nuclei. Because the dipole moments are also the derivatives of the energy with respect to an electric or magnetic field:[50]

$$\vec{\mu} = \left(\frac{\partial E}{\partial \vec{E}} \right)_0 \qquad \vec{m} = \left(\frac{\partial E}{\partial \vec{B}} \right)_0 \tag{2.162}$$

we can write down the APT and AAT as energy derivatives:

$$APT \propto \frac{\partial^2 E}{\partial \vec{E} \partial \vec{R}} \tag{2.163}$$

$$AAT \propto \frac{\partial^2 E}{\partial \vec{B} \partial \dot{\vec{R}}} \tag{2.164}$$

Similarly, we have found for the electric dipole-magnetic dipole polarizability (cf. (2.116)) used for ORD and ROA:

$$G' \propto \frac{\partial^2 E}{\partial \vec{E} \partial \dot{\vec{B}}} \tag{2.165}$$

and for the magnetic shielding tensor:

$$\sigma_i \propto \frac{\partial^2 E}{\partial \vec{B} \partial \vec{m}_N} \tag{2.166}$$

This shows that all molecular properties encountered can be related to the energy dependence of the molecule to the perturbation causing the molecular response.

Chapter 3

Measurement of Vibrational Circular Dichroism

In the previous chapter we have seen how rotational strengths can be calculated ab initio. Calculated IR and VCD spectra can be obtained by superimposing the (Lorentzian broadened) dipole or rotational strengths of all the 3N-6 normal modes at the corresponding harmonic frequencies. By comparing this with the experimental spectrum, one can conclude whether the sample corresponds to the configuration of the calculated species, or to that of its mirror image (i.e. its enantiomer). In this chapter, we briefly discuss how such an experimental spectrum can be obtained, and which methods can be used to improve the quality of the relatively weak CD signal.

3.1 Fourier Transform IR Spectroscopy

At the basis of modern VCD spectroscopy lies a Fourier transform infrared (FT-IR) spectrometer. The beam from the light source is divided into two separate beams that are reflected on a fixed and a moveable mirror (figure 3.1). On recombining at the beam splitter, interference is induced depending on the wavelength and the optical path length difference or retardation δ caused by the movable mirror. For $\delta = n\lambda$, with λ the wavelength of the radiation and n an integer, constructive interference is observed. For $\delta = (n + 1/2)\lambda$ destructive interference occurs. The intensity for

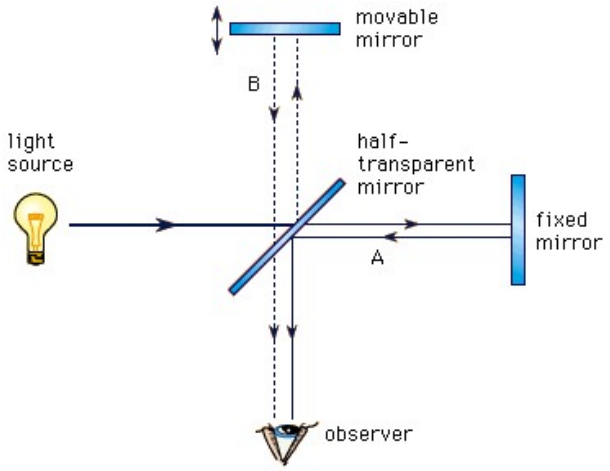

Figure 3.1: Working principle of an interferometer. The movable mirror changes the path length δ of beam B , causing interference with beam A when combined at the half transparent mirror.[70]

wavenumber $\bar{\nu}$ at a retardation δ is given by:[71]

$$I(\delta) = 0.5 I(\bar{\nu}) \cos(2\pi\bar{\nu}\delta) \tag{3.1}$$

Considering the fact that the IR light source is polychromatic, the actual intensity interferogram results from a superposition of the intensity for each wavelength:

$$I(\delta) = 0.5 \int_0^\infty I(\bar{\nu}) \cos(2\pi\nu\delta + \theta(\bar{\nu}))d\bar{\nu} \tag{3.2}$$

The phase shift θ arises from the different speeds at which signals at different frequencies pass through the electronics of the spectrometer. This phase shift can be determined using a birefringent stress plate and corrected for using built-in electronic phase correction functionality.[10] An example of an interferogram is given in figure 3.2. The retardation can be written as a function of the moving mirror velocity V_M as $\delta = 2V_M t$ where V_M is given in $cm.s^{-1}$. Inserting this expression for the retardation in equation (3.1) gives the intensity as a function of time, given by a superposition (the integral) of the intensities at each wavelength (the integrand). Using a Fourier transformation one can convert this time-dependent intensity expression into an intensity expression as a function of frequency (or wavenumber), which corresponds to the desired spectrum.

$$I(\bar{\nu}) = 0.5 \int_{-\infty}^{\infty} I(\delta) \cos(2\pi\bar{\nu}\delta) d\delta \tag{3.3}$$

Values for V_M are of the order of 1 $cm.s^{-1}$, yielding a Fourier frequency $f_F = 2V_M\bar{\nu}$ of about 1 to 2 kHz for the spectral range of 1000-2000 cm^{-1}.

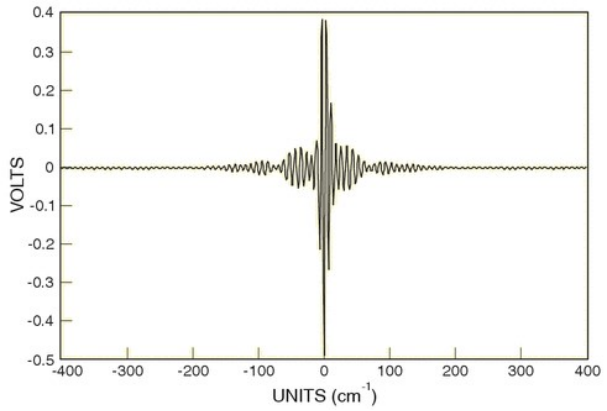

Figure 3.2: Example of an interferogram, giving the signal strength as a function of the retardation. When the distance to both mirrors is equal (zero path difference or ZPD), a maximum in the intensity is observed.

3.2 Vibrational Circular Dichroism Spectroscopy

VCD is defined as the difference in absorption of left minus right circularly polarized light. Due to the relative weakness of VCD signals (about 10^{-4} to 10^{-5} compared to the corresponding IR)[58] one cannot simply obtain VCD spectra by subtracting the absorbance spectra for left and right CPL. To resolve this, dual polarization modulation is used: not only is the polychromatic IR light modulated by the interferometer at the Fourier frequency, a second modulation is applied by the photoelastic modulator (PEM), converting linearly polarized light coming from the linear polarizer P to alternating (at modulation frequency ω_M) left and right circularly polarized light (cf. figure 3.3).[72]

After going through the sample and the detector D, the electronic processing of the detected doubly modulated signal begins (dashed lines in Figure 3.3). This signal is demodulated by a lock-in amplifier (LIA), tuned at the PEM frequency (usually

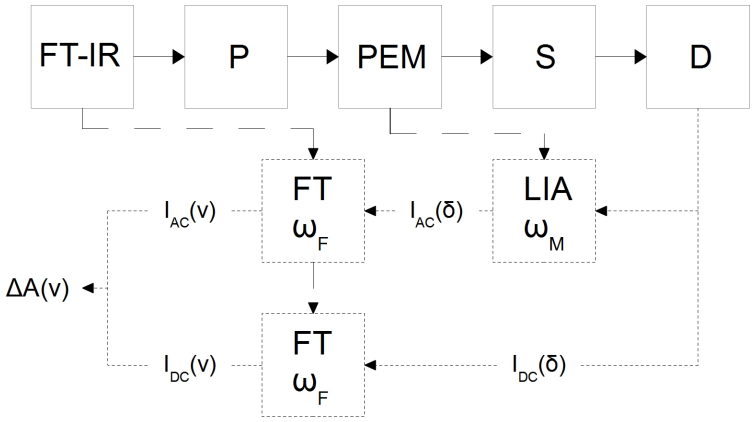

Figure 3.3: Optical (solid) and electronic (dashed) block diagram of a single PEM FT-VCD spectrometer. The polychromatic IR light consecutively passes a linear polarizer, PEM, the sample and the detector. Using a LIA tuned to the PEM frequency a AC signal is extracted and Fourier transformed. The low-frequency DC signal is Fourier transformed and gives rise to the IR. The VCD is obtained by dividing the AC spectrum by the DC spectrum.

about 50 kHz), giving rise to an AC interferogram $I_{AC}(\delta)$. The LIA acts as a filter, as only the amplitude of the signal that varies at the selected frequency is let through. Subsequently, this can be Fourier transformed (equation (3.3)) to give a wavenumber dependent signal $I_{AC}(\bar{\nu})$. The low frequency part of the detector signal, which is modulated only at the Fourier frequency and was isolated using a low-pass filter, gives rise to the normal IR spectrum after Fourier transformation.[73]

3.2.1 Photoelastic Modulator

The PEM is an optical device that transforms linearly polarized light to alternating left and right circularly polarized light. Its operation is based on the photo-elastic effect: a mechanically stressed optical material exhibits birefringence proportional to the applied strain. This strain is exerted by so-called piezo-electric transducers, that convert electrical signals from an external circuit to mechanical longitudinal vibrations.[74] The optical element is usually made of ZnSe for measurements in the mid-IR region (figure 3.4).

The linear polarizer P is placed at an angle of 45° from the fast and slow axis of the PEM. The electrical field associated with the radiation then has two components,

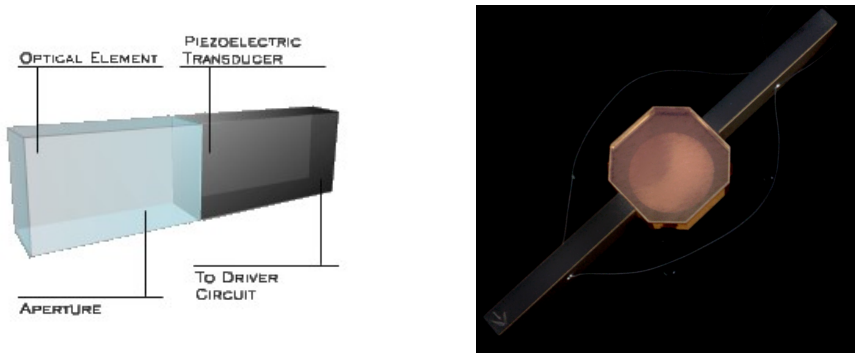

Figure 3.4: Visualization of a PEM[75] and a picture of one of the PEMs in the BioTools ChiralIR-2X.

one parallel to the slow axis (E_x) and one parallel to the fast axis (E_y) (Figure 3.5). Upon compression of the optical element in the x-direction, the x-component

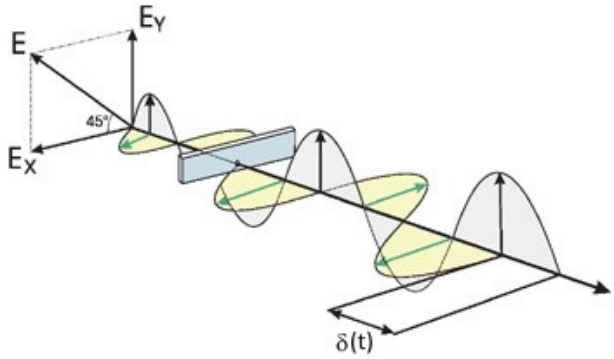

Figure 3.5: Shift of the x-component of the radiation relative to the y-component after passing through the PEM.[75]

travels slightly faster ($n_x < n_y$), and the opposite is true when the optical element is stretched. Note that the exact same reasoning holds for the magnetic field associated with the radiation. The retardation $\delta_M(t)$ of one component compared to the other thus depends on the refractive index on both axes, and the thickness z of the optical element.

$$\delta_M(t) = z[n_x(t) - n_y(t)] \tag{3.4}$$

If the amount of strain is chosen such that the two components are shifted by a quar-

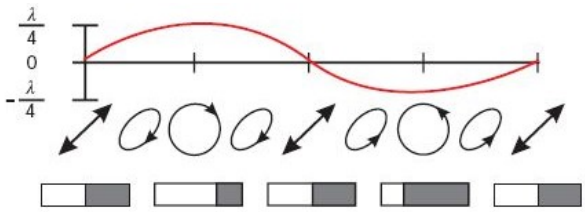

Figure 3.6: Linearly polarized light is converted to right and left circularly polarized states as the PEM cycles between stretching and compression. In between the CPL states elliptically polarized light is produced.[75]

ter of a wavelength, the resulting electric field vector traces out a helix and circularly polarized light is created. More specifically, compressing the optical element yields left CPL (LCPL) and stretching gives rise to right CPL (RCPL) (figure 3.6). The vibration of the piezoelectric transducer induces a sinusoidal behaviour of the retardation between the two components:[10]

$$\alpha_M(\bar{\nu}) = \alpha_M^0(\bar{\nu}) sin(\omega_M t) \tag{3.5}$$

where ω_M is the oscillation frequency of the PEM and α_M^0 is the maximum retardation phase angle for a given wavelength of incident light and is proportional to the voltage applied on the piezoelectric transducer. This is wavelength dependent because a given retardation value incurs a smaller phase shift for increasing wavelengths.

3.2.2 Optical Path Analysis for VCD Measurements

In this section the Stokes-Mueller formalism[10] is used to describe the effect of the sequence of optical elements (cf. figure 3.3) on the final signal reaching the detector. In this formalism, the polarization state of the radiation is described by a Stokes vector, and the action of an optical element is contained in a Mueller matrix, which upon multiplication with the Stokes vector of the incident light produces the Stokes vector of the resulting radiation. The Stokes vector is defined as:[10]

$$\mathbf{S} = \begin{pmatrix} I_{tot} \\ I_0 - I_{90} \\ I_{45} - I_{135} \\ I_R - I_L \end{pmatrix} \tag{3.6}$$

The subscripts of the intensities expresses how the polarization of the radiation is divided into two orthogonal polarization differences (second and third row) and in difference in circular polarization (last row). Only the total intensity, given in the first row, can be detected by the detector. For vertically polarized light (0°) the Stokes vector becomes:[73]

$$\mathbf{S}_P = \frac{I_0(\bar{\nu})}{2} \begin{pmatrix} 1 \\ 1 \\ 0 \\ 0 \end{pmatrix} \tag{3.7}$$

The effect of an optical element is described by multiplying the Stokes vector from the left with a (4×4) Mueller matrix. The elements of the resulting Stokes vector are given by the corresponding row of the Mueller matrix. For example M_{42} describes the circular polarization resulting from the action of the optical element on the vertically (0°) and horizontally (90°) polarized components of the incident radiation. The effect of the PEM on the radiation coming from the vertically positioned linear polarizer can be written as:

$$\begin{aligned} \mathbf{S}_{PEM} = \mathbf{M}_{PEM}\mathbf{S}_P &= \frac{I_0(\bar{\nu})}{2} \begin{pmatrix} 1 & 0 & 0 & 0 \\ 0 & \cos[\alpha_M(\bar{\nu})] & 0 & -\sin[\alpha_M(\bar{\nu})] \\ 0 & 0 & 1 & 0 \\ 0 & \sin[\alpha_M(\bar{\nu})] & 0 & \cos[\alpha_M(\bar{\nu})] \end{pmatrix} \begin{pmatrix} 1 \\ 1 \\ 0 \\ 0 \end{pmatrix} \\ &= \frac{I_0(\bar{\nu})}{2} \begin{pmatrix} 1 \\ \cos[\alpha_M(\bar{\nu})] \\ 0 \\ \sin[\alpha_M(\bar{\nu})] \end{pmatrix} \end{aligned} \tag{3.8}$$

where $\alpha_M(\bar{\nu})$ is given in (3.5). We learn from this expression that the total intensity remains unaltered after passing through the PEM (ignoring reflection and absorption losses), and that some of the linearly polarized light is converted to CPL, depending on the value of $\alpha_M(\bar{\nu})$. Next, the radiation passes through the sample, the Mueller matrix of which can be expressed in terms of linear and circular birefringence (LB and CB) and linear and circular dichroism (LD and CD). The absorption by the sample is

governed by the absorbance factor in front of the Mueller matrix.

$$\mathbf{M}_S = 10^{-A(\bar{\nu})} \begin{pmatrix} 1 & -LD & -LD' & CD \\ -LD & 1 & CB & -LB \\ -LD' & -CB & 1 & LB' \\ CD & LB & -LB' & 1 \end{pmatrix} \tag{3.9}$$

For a solution with random movement of molecules, the LD and LB terms can be assumed zero. The LB elements can be used to account for linear birefringence caused by strain on for example the sample cell windows, but this will be ignored for the following. By definition:

$$CD = \frac{ln(10)}{2}(A_L - A_R) = 1.1513\Delta A(\bar{\nu}) \tag{3.10}$$

With this, the Stokes vector of the light reaching the detector can be calculated.

$$\mathbf{S}_S = \frac{I_0(\bar{\nu})10^{-A(\bar{\nu})}}{2} \begin{pmatrix} 1 + 1.1513\Delta A(\bar{\nu})\sin[\alpha_M(\bar{\nu})] \\ \cos[\alpha_M(\bar{\nu})] \\ 0 \\ 1.1513\Delta A(\bar{\nu}) + \sin[\alpha_M(\bar{\nu})] \end{pmatrix} \tag{3.11}$$

Assuming no polarization sensitivity of the detector, only the total intensity is measured. This finally gives for the spectrum at the detector:

$$I_D(\bar{\nu}) = I_{DC}(\bar{\nu}) + I_{AC}(\bar{\nu}) = \frac{I_0(\bar{\nu})10^{-A(\bar{\nu})}}{2}\left(1 + 1.1513\Delta A(\bar{\nu})\sin[\alpha_M(\bar{\nu})]\right) \tag{3.12}$$

The detected signal thus has a low-frequency part $I_{DC}(\bar{\nu})$ modulated at the Fourier frequency and a high-frequency signal $I_{AC}(\bar{\nu})$ which is also modulated at the PEM frequency (cf. equation (3.5)). From (3.12) the DC absorption spectrum can easily be calculated:

$$A(\bar{\nu}) = -\log_{10}\left(\frac{2I_{DC}(\bar{\nu})}{I_0(\bar{\nu})}\right) \tag{3.13}$$

where $I_0(\bar{\nu})$ is the measured reference spectrum without the sample in place (or only a solvent sample). To evaluate the doubly modulated term $I_{AC}(\bar{\nu})$, we write down

the double sinusoidal dependence as a sum of odd-order Bessel functions.[46]

$$\sin[\alpha_M(\bar{\nu})] = \sin[\alpha_M^0(\bar{\nu})sin(\omega_M t)] = 2\sum_{n=1}^{\infty} J_{2n-1}[\alpha_M^0(\bar{\nu})]sin[(2n-1)\omega_M t] \quad (3.14)$$

Using a lock-in amplifier, only the amplitude of the first harmonic at the PEM frequency ω_M $(n = 1)$ is retained. The doubly modulated AC signal then becomes:[10]

$$I_{AC}(\bar{\nu}) = \frac{I_0(\bar{\nu})10^{-A(\bar{\nu})}}{2} 1.1513\Delta A(\bar{\nu}) 2J_1[\alpha_M^0(\bar{\nu})] \quad (3.15)$$

and the differential absorption spectrum of left minus right CPL can then be measured as the ratio of the AC-signal and the DC signal.

$$\Delta A(\bar{\nu}) = \frac{1}{2J_1[\alpha_M^0(\bar{\nu})]1.1513} \left(\frac{I_{AC}(\bar{\nu})}{I_{DC}(\bar{\nu})}\right) \quad (3.16)$$

The differential absorption can thus be obtained by demodulating both the $I_{AC}(\bar{\nu})$ and the $I_{DC}(\bar{\nu})$ signals, and dividing the first by the second. The proportionality factor $\frac{1}{2J_1[\alpha_M^0(\bar{\nu})]1.1513}$ can be obtained by a calibration measurement, which is discussed in the following section.

3.2.3 Intensity Calibration

The calibration curve can be measured by replacing the sample by a linear birefringent plate (BP) with its fast and slow axes parallel to the fast and slow axes of the PEM. The linear birefringence induces a phase shift $\alpha_B(\bar{\nu}) \propto \bar{\nu}$ between the two polarization components, which is now constant in time as opposed to the phase shift induced by the PEM. Because of this, linear and circular polarization state intensities (cf. (3.9)) are interchanged. The CB, CD and LB terms in (3.9) can be considered zero for a birefringent plate. After the BP, a second polarizer, called the analyzer, is placed parallel (0°) or orthogonal (90°) to the first one. The Mueller matrix of the combination of the BP at $45°$ and the analyzer at $0°$ (+ sign) or $90°$ (- sign) is given by:

$$\mathbf{M}_{cal} = \frac{1}{2}\begin{pmatrix} 1 & \pm\cos[\alpha_B(\bar{\nu})] & 0 & \pm\sin[\alpha_B(\bar{\nu})] \\ \pm 1 & \cos[\alpha_B(\bar{\nu})] & 0 & \sin[\alpha_B(\bar{\nu})] \\ 0 & 0 & 0 & 0 \\ 0 & 0 & 0 & 0 \end{pmatrix} \quad (3.17)$$

Multiplying this from the right with $\mathbf{S}_{PEM}$ from equation(3.8), the intensity observed at the detector is given by the first element of the resulting Stokes vector:

$$I_D(\bar{\nu}) = \frac{I_0(\bar{\nu})}{4}\left[\underbrace{1 \pm J_0[\alpha_M^0(\bar{\nu})]\cos[\alpha_B(\bar{\nu})]}_{I_{DC}}\underbrace{\pm 2J_1(\alpha_M^0\bar{\nu})\sin(\omega_M t)\sin[\alpha_B(\bar{\nu})]}_{I_{AC}}\right] \tag{3.18}$$

Here we can identify a DC part, modulated only at the Fourier frequency and an AC part, also modulated at the PEM frequency. As for the normal VCD measurement, these two signals can be divided, and for a calibration measurement this yields:

$$\left(\frac{I_{AC}(\bar{\nu})}{I_{DC}(\bar{\nu})}\right)_{cal} = \frac{\pm 2J_1(\alpha_M^0\bar{\nu})\sin(\omega_M t)\sin[\alpha_B(\bar{\nu})]}{1 \pm J_0[\alpha_M^0(\bar{\nu})]\cos[\alpha_B(\bar{\nu})]} \tag{3.19}$$

After passing the lock-in amplifier, only the intensity of the PEM-modulated term is retained ($2J_1(\alpha_M^0\bar{\nu})\sin(\omega_M t)\sin[\alpha_B(\bar{\nu})] \rightarrow 2J_1(\alpha_M^0\bar{\nu})\sin[\alpha_B(\bar{\nu})]$). This gives rise to two curves, which can be measured separately by changing the orientation of the analyzer from parallel to the polarizer (+ sign) to orthogonal to the polarizer (- sign). The birefringent plate is constructed such that $\alpha_B(\bar{\nu}) = \pi/100\bar{\nu}$. Because of this, the denominator of (3.19) becomes 1 at $\bar{\nu} = (2n+1)50cm^{-1}$. Depending on the position of the analyzer, the ratio of the AC signal and the DC signal at these wavenumbers becomes:

$$\left(\frac{I_{AC}(\bar{\nu} = (2n+1)50)}{I_{DC}(\bar{\nu} = (2n+1)50)}\right)_{cal} = \pm 2J_1(\alpha_M^0\bar{\nu}) \tag{3.20}$$

If the absolute value of both calibration spectra in (3.19) is considered, the sign dependence in (3.20) is removed, which means that $2J_1(\alpha_M^0\bar{\nu})$ now corresponds to the crossing points of the two calibration spectra for the selected wavenumbers. Drawing a smooth curve through these crossing points, we finally obtain an intensity calibration curve which can be used in (3.16) to obtain a calibrated VCD spectrum (Figure 3.7).

3.3 Practical Aspects of VCD Experiments

The measurement of VCD has undergone a big evolution since the first measurements in the 1970's.[76,77] The relatively weak VCD signal can be extracted with an acceptable signal-to-noise ratio (S/N) using double modulation with a PEM, which was the subject of the previous sections. To further improve spectrum quality, Nafie has proposed a dual source operation.[10] In this set-up, two IR sources are combined with opposite

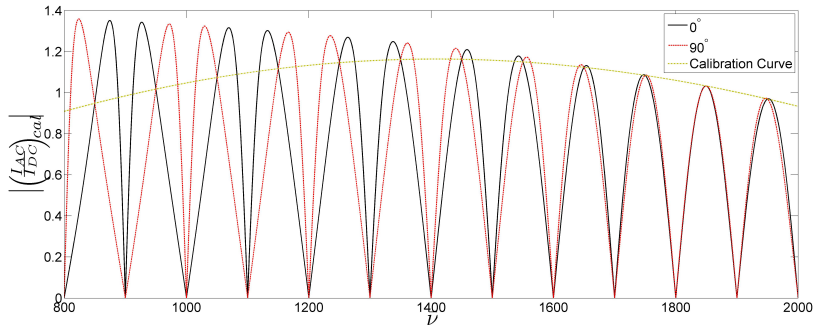

Figure 3.7: Calibration curve (yellow) obtained by connecting the crossing points of the calibration measurement for vertical (black) and horizontal (red) placement of the analyzer.

Fourier phases and orthogonal polarization, which leads to less detector saturation for a larger VCD signal. This is a standard feature for the BioTools ChiralIR-2X VCD-spectrometer, which was used for all VCD measurements in this thesis.

In the optical path analysis of the VCD measurement, all unexpected sources of linear and circular birefringence, arising for example from mechanical stress on sample cell windows, mirrors, imperfect alignment, ... were ignored. In an actual measurement, these can be significant and give rise to a non-zero baseline. Nafie therefore introduced a dual-PEM spectrometer, placing a second PEM at a slightly different modulation frequency and retardation value. Using a similar Stokes-Mueller analysis as before, it can be shown[73] that all intensity at the detector originating from linear birefringence in the optical pathway can be eliminated. Only linear birefringence from between the two PEMs (originating from the sample cell) is retained, which can also be removed by continuously rotating the sample cell during measurement. All measurements in this thesis were performed with a dual PEM configuration. The PEMs are operated with a maximum retardation value α_M^0 that gives an optimal amount of circular polarization for the spectral region of interest in this thesis, which is 1000-1800 cm^{-1}. Therefore, the maximal phase shift is set at about 105° or 1.83 radians of a 1400 cm^{-1} wave, giving maximal circular polarization throughout the spectrum.

Even with this, a perfectly flat baseline is very hard to obtain. In the ideal case in which a racemate of the sample is available, a measurement of this racemate is subtracted from the chiral sample measurement. The idea is that all artefacts arising from imperfections in the optical pathway or due to the solvent and its interaction with

the sample are equally present in both measurements, which allows for elimination of these artefacts through baseline subtraction. In case no racemate is available, a solvent-only baseline is subtracted. Although artefacts from the optics are eliminated this way, absorbance artefacts are not exactly equal and this method thus only gives an approximate baseline. In practice, however, the solvent subtraction procedure yielded a good baseline for almost all experiments performed.

Chapter 4

A Confidence Level Algorithm for the Determination of Absolute Configuration Using Vibrational Circular Dichroism or Raman Optical Activity

4.1 Introduction

The active pharmaceutical ingredient (API) of many drugs and drug candidates is chiral. Although until recently drugs with chiral API's were largely commercialized as racemates, more recently single-enantiomer APIs are taking a commanding priority in the market. This extraordinary interest in chiral, single enantiomer molecules as API's calls for very reliable methods for the assignment of their absolute configuration (AC). As the absolute configuration of a molecule may have very significant consequences for the activity of the molecule as a drug, international regulatory agencies have become increasingly strict and require both enantiomers of a chiral drug candidate to be tested separately for their therapeutic and adverse effects before the actual drug

can be launched.[78] Over the past decades vibrational circular dichroism (VCD) and Raman optical activity (ROA), jointly called vibrational optical activity (VOA) methods, in combination with ab initio calculations, have become reliable methods for the assignment of the AC of chiral molecules in the solution phase.[79,80]

Unfortunately, it is not possible to directly deduce structural information from an experimental VCD spectrum. Therefore, theoretical spectra for a postulated absolute configuration, computed by using reliable quantum chemical algorithms developed over the past decades,[42,43] are used to establish the link between the experimental spectrum and the AC. Based on the agreement between both spectra, meaning the location, sign and intensity of the bands, the AC can be determined. However, measured spectra are inherently different from results of a quantum mechanical calculation. Difficulties in assigning the AC can arise for more complex molecules exhibiting high conformational flexibility or tendency towards self aggregation,[81,82] form complexes with solvents[83–85] or show other effects that are normally not or insufficiently well described by the theoretical methods. On a more technical level, the many approximations taken in the computational approach, such as the use of a finite basis set and, at the density functional theory (DFT) level, the functional, also have an impact. A trained eye is often used to assess the degree of agreement between computed and experimental spectra while taking into account the possible complications described above."Human eye" comparison, however, may be very subjective and can be biased by personal interpretation especially when the agreement is only of intermediate quality. In order to avoid such bias and further improve the reliability of VCD, additional numerical comparisons should be performed. The classical but very time consuming method is to individually link IR fundamentals in the theoretical and experimental spectrum. Then one derives rotational strengths from the experimental VCD bands and determines the correlation between measured and calculated rotational strengths with emphasis on the agreement in sign. A review of such successful assignments can be found in the publication of Stephens.[24]

Up until now very few studies have been published that discuss criteria to assess whether a reliable assignment of the AC has been made. In an interview,[86] Minick explains the quality assessment used at GlaxoSmithKline: the key to confident predictions at GSK is the value of the [..] coefficients of correlation between the intensities of 10 to 15 corresponding bands in the calculated and measured spectra. Our assignments are considered reliable if r^2 is at least 90%. Such an approach is rather tedious because individual bands need to be crosslinked between theory and experiment and because

choosing a reduced number of bands in establishing the absolute configuration may introduce some arbitrariness. In search of a more direct and immediate quantification of the agreement, a neighbourhood similarity (NS) measure has previously been introduced for VCD.[87–90] This similarity measure, based on the overlap between measured and calculated spectra, takes into account the neighbourhood in direct proximity of the bands. Despite earlier fruitful applications of such NS measures,[87–90] no test of such measures has been performed over a wider set of molecules for which the AC is known from other approaches such as explicitly correlating VCD bands between theory and experiment or other experimental techniques such as X-ray diffraction. Moreover, no confidence level has yet been established for VCD assignments. This paper addresses both issues. First we apply the NS and related measures, described below, to a larger set of molecules, and secondly we establish a confidence level for the assignment of the AC of a new molecule. Although herein only VCD will be discussed, the proposed algorithm is also considered valuable for the comparison of ROA spectra.

4.2 Theoretical Background

4.2.1 Neighbourhood Similarity (NS)

The similarity measure used in this study for the quantification of the agreement between the calculated, $f(\nu)$, and measured, $g(\nu)$, IR or VCD spectra, where ν is the frequency, is a fairly straightforward adaptation of a cosine-based similarity measure as will be demonstrated in detail below. The present algorithm is an updated version of the one used previously by Kuppens et al.,[87–90] following up on work by De Gelder et al.[91] for comparing powder diffraction spectra. Instead of such a generalized cosine in a multidimensional vector space, one can also use the arithmetic mean as normalizing term or, in fact, any other similarity measure, including the Tanimoto one as recently used by Shen et al.[92] As the similarity measure used in the present paper differs somewhat from previous expressions[87–91] based on the generalized cosine, we opt for a re-derivation and a detailed description of the algorithm. We first establish what parameters a program for VCD spectrum similarity should contain to allow meaningful similarity measures:

1. It is well-known that computed absorption frequencies are overestimated. The common approach to correct for this effect is to introduce a global scale factor. We therefore introduce a scaling factor σ that acts on the theoretical spectrum

$f(\nu)$. The scale factor depends on the chosen theoretical method and lies for most cases between roughly 0.96 and 1.02 when hybrid density functionals are used.[93] The algorithm described herein allows for optimization of this parameter in the way detailed below.

2. Although advances in spectrometers have reduced the uncertainty in the position of the baseline substantially, some degree of uncertainty may remain. We therefore allow a uniform shift of the baseline. The highest absolute VCD intensity in the experimental spectrum is sought and the shift is varied between $-x$ and $+x$ where x equals a user-chosen percentage of this absolute value. Experience has shown that 10 % is often a good choice. The baseline shift is then optimized in the way described below and applied over all frequencies in the experimental spectrum. The need for shifting the baseline is dependent on the quality of the experimental spectra and for most modern spectrometers is likely to be less important.

3. Even when a scale factor is introduced, one cannot account for all possible local shifts. Different techniques have been implemented to take such effects into account. First of all, the theoretical spectrum for every conformation of a molecule is a line spectrum and in order to make the global molecular theoretical spectrum mimic more closely the experimental spectrum, the collection of the theoretical conformational spectra is combined using Boltzmann weighting and each line in the resulting molecular line spectrum is broadened using a Lorentzian band shape. In the next step, the global scale factor is applied. To account for small local shifts required to bring the theoretical and experimental spectrum closer to each other, instead of using a uniform scale factor, one could use different factors for different types of vibrations, and thus perform a different scaling for each type of vibration in the spectrum.[94] This obviously requires having different scaling factors for different vibrations which again requires individual assignment of bands to correlate them to a specific type of vibration and to establish some sort of database of scale factors. This is a rather tedious procedure. Therefore, herein small local shifts are taken into account in a different way. Instead of using a point by point comparison between the theoretical and experimental spectrum, we arrange that the experimental spectrum at every point bears to some degree information on the surrounding frequencies and their accompanying VCD intensities. This is done by replacing the original experimental spectrum

at every frequency ν_0 by one where the intensity of the surrounding points is included. These points are weighted in such a way that their contribution becomes smaller as they are farther from ν_0:

$$g(\nu_0) \leftarrow \int g(\nu) w(\nu - \nu_0) d\nu \tag{4.1}$$

The weighting function $w(\nu - \nu_0)$ determines the extent to which the neighbourhood of ν_0 is taken into account. In this study a triangular weighting function was chosen. This allows one to take into account the neighbourhood with a width of $-l$ and $+l$ around each point in the spectrum:

$$\begin{aligned} w(\nu - \nu_0) &= 1 - \frac{|\nu - \nu_0|}{l} && |\nu - \nu_0| \leq l \\ w(\nu - \nu_0) &= 0 && |\nu - \nu_0| > l \end{aligned} \tag{4.2}$$

The shape of the weighting function is chosen based on the fact that corresponding bands in the experimental and theoretical spectrum can be shifted locally from each other. The value of l has to be chosen carefully in order to avoid linking too distant bands. The default has been set to 20 cm $^{-1}$ but can optionally be changed. Although the entire algorithm has been set up to minimize user bias, the need to choose some user-determined parameters does rely on an experienced user to make all choices within physically appropriate limits.

Taking into account that we henceforth consider the theoretical spectrum to be the original computed spectrum with Lorentzian broadening and scaling and the experimental spectrum to be the original spectrum modified through Equation (4.1) and with a shifted baseline, the generalized cosine similarity expression is given by:

$$S_{fg} = \frac{\int_a^b f(\nu) g(\nu) d\nu}{\sqrt{\int_a^b f^2(\nu) d\nu \int_a^b g^2(\nu) d\nu}} \tag{4.3}$$

Obviously, this degree of similarity depends on the values for the parameters described above, which can optionally also be optimized as is described below. As is clear from Equation (4.3), the similarity can be computed for any range of frequencies through choosing the lower and upper frequency (resp. a and b in Equation (4.3)). If within this range a peak can be established to be an artefact, it should be replaced by zero intensity over the range of the artefact in both the theoretical and experimental

spectrum so as not to bias the similarity in any undesirable way. The interesting aspect of Equation (4.3) is that the similarity measure always lies within 0 and 1, provided that the intensity over all frequencies has the same sign. This is a consequence of the properties of vector spaces with an inner product as present in the numerator of Equation (4.3). Equation (4.3) is readily applicable to IR spectra, henceforth denoted S_{fg}^{IR}, but needs to be adapted to be useful for VCD spectroscopy.

4.2.2 VCD Neighbourhood Similarity and Enantiomeric Similarity Index

Equation (4.3) is a normalized quantity with values within the interval [0,1] (or [0,100] as percent scale). Here 1 (or 100) corresponds to the comparison of identical spectra. Having an index that is for all molecules confined to the same range of values is very useful as it allows comparing results for different molecules. This would not be the case with for instance a Euclidean distance where no upper limit can be given. For VCD spectra, computing the similarity between spectra is slightly more involved. By the very nature of a differential spectroscopy, the intensity at a given frequency can have both signs, positive or negative. One could opt to simply use Equation (4.3) to compute the similarity and not take the sign into account in any special way. This has the drawback that the overlap between spectra in regions of equal sign between the theoretical and experimental spectra and regions of opposite sign can compensate in the integral in the numerator of Equation (4.3), possibly leading to undesirable effects. In order to avoid this, we simply split the scaled theoretical and the experimental spectrum into a positive and a negative spectrum. Following Equation (4.3), a similarity measure is computed for the positive spectra only ($S_{fg}^{++,VCD}$) and one for the negative spectra only ($S_{fg}^{--,VCD}$). In order to have one single similarity measure, Σ_{fg}, a weighted mean of both similarities is computed as:

$$\Sigma_{fg} = \frac{\Phi^{++} S_{fg}^{++,VCD} + \Phi^{--} S_{fg}^{--,VCD}}{\Phi^{++} + \Phi^{--}} \tag{4.4}$$

The weight Φ^{++} simply reflects the amount of VCD signal of specific sign in the theoretical and experimental spectrum, that is, it is the sum of the surface of the positive theoretical and experimental spectra:

$$\Phi^{++} = \int_{f(\nu)>0} f(\nu)d\nu + \int_{g(\nu)>0} g(\nu)d\nu \tag{4.5}$$

Φ^{--} is analogous but for the negative parts of the spectra. As $S_{fg}^{\pm\pm,VCD}$ lies always within the limits [0,1] and $\Phi^{\pm\pm}$ is always a positive number, Σ_{fg} also lies in the range [0,1] so that it can still be considered a similarity measure. In the same way as described above, one can also compute the similarity measure $\Sigma_{\bar{f}g}$ for the theoretical spectrum $\bar{f}(\nu)$ of the other enantiomer with respect to the experimental spectrum.

Kuppens et al.[87–90] suggested the difference between the neighbourhood similarities of the measured VCD spectra versus each of the corresponding calculated spectra of both enantiomers as a criterion to assess the degree of success of a VCD assignment of the AC. This differential neighbourhood similarity measure, that is, the enantiomeric similarity index, ESI, gives information about the discriminating power between the two enantiomers. In this work the absolute value of the ESI, henceforth denoted Δ is used throughout:

$$\Delta = \left|\Sigma_{fg} - \Sigma_{\bar{f}g}\right| = |ESI| \tag{4.6}$$

If the measurement and simulation of the spectra are reliable, the calculated VCD spectrum for one enantiomer should show good agreement with the measured VCD, while the spectrum of the opposite enantiomer should hardly show any agreement. This is the basis of the discrimination potential of VCD. Δ is limited to the interval [0,1]. High Δ values indicate that one of the computed enantiomeric spectra has a significantly better agreement with the observed spectrum $g(\nu)$ compared to the other. Low values indicate that $f(\nu)$ and $\bar{f}(\nu)$ have similar values of Σ and thus, that assignment of the AC via VCD cannot be performed with high reliability. Note that the scale factor is obtained as the value that gives the highest similarity for the IR spectrum and the shift in the baseline is determined as the value that gives the largest Σ for the most similar enantiomer by developing the parameter in a simple grid.

Only the regions where the sign in the theoretical and experimental spectra agrees contribute to the similarity in $S_{fg}^{++,VCD}$ and $S_{fg}^{--,VCD}$ and thus in Σ_{fg} as introduced in Equation (4.4). This means that regions in the spectra where the sign of the rotational strength in the theoretical and experimental spectrum differs do not play a role. However, the introduction of Δ in fact introduces these regions in the following way. Starting from Equation (4.6), we have:

$$\Delta = \left| \frac{\Phi_{fg}^{++} S_{fg}^{++,VCD} + \Phi_{fg}^{--} S_{fg}^{--,VCD}}{\Phi_{fg}^{++} + \Phi_{fg}^{--}} - \frac{\Phi_{fg}^{-+} S_{fg}^{-+,VCD} + \Phi_{fg}^{+-} S_{fg}^{+-,VCD}}{\Phi_{fg}^{-+} + \Phi_{fg}^{+-}} \right| \tag{4.7}$$

where we used the mirror image relationship between the VCD spectra of two enan-

tiomers. Δ thus introduces the effect of having regions in the computed and experimental spectra that do not agree in sign. Although numerical measures similar to the one introduced in this paper had been tested in several cases,[87–90] their use must be validated in order to allow them to be used more universally. Herein, this is done by testing them on a much larger set of molecules for which the AC has been determined correctly. Therefore, Σ and Δ values have been computed for such a database. If these results reveal that they can be used reliably, a confidence level measure can be introduced (see below) by projecting the values of the similarity for the best fitting enantiomer, Σ^{max}, and the accompanying Δ of a new VCD experiment in the set of known values from the database. If the new assignment would fall outside the range of pairs of Σ and Δ for previous successful AC determinations, the new assignment may be unreliable.

4.3 Results

4.3.1 Test Database for VCD Similarity Analysis

The AC of 83, mostly pharmaceutical compounds was previously assigned after thorough analysis of the agreement between measured and calculated IR and VCD spectra using the elaborate peak-by-peak comparison and regression between dipole and rotational strengths extracted from theory and experiment. Moreover, for several molecules, the assignment of the AC was confirmed by other techniques such as X-ray diffraction. The database contains both relatively small and rigid molecules but also larger and flexible molecules so that the database represents qualitatively the diverse nature of molecules submitted to VCD analysis. The database also contains molecules with more than one chiral centre. The theoretically calculated spectra all come from DFT-based calculations using hybrid functional and at least double zeta quality basis sets and were conformationally averaged using Boltzmann weights. The lowest level used for the calculations corresponds to the B3LYP/6-31G*[95–97] level which is a relatively routine level that nevertheless often gives VCD spectra of satisfactory quality.[88] All calculations were performed using the Gaussian-03 package.[98]

For each of the assignments the similarity measures introduced above were computed as well as the value for Δ from Equation (4.6). The window size, l, of the triangular weighting function in Equation (4.1) was set to 20 cm^{-1} for all calculations. In general, this value has proven to give overall larger enantiomeric discrimination

power. The factor used to scale the frequencies of the calculated spectra is varied numerically between 0.96 and 1.02 until the maximum similarity in the IR spectrum has been found. In general, only the range between 1000 cm^{-1} and 1500 cm^{-1} has been considered to compute similarity measures because carbonyl-stretching vibrations, which occur in the range of 1600 to 1750 cm^{-1}, are often heavily influenced by the solvent and this functional group occurs ubiquitously in molecules submitted to VCD analysis. In order to include sufficient bands in the analysis, it is important that at least a 400 cm^{-1} span of frequencies is compared. Using such a window, experience shows that sufficient information is introduced in the similarity algorithm. As described above, the similarity measures may also be influenced by the position of the baseline of the observed VCD spectrum. In order to take into account a possible small offset from zero, the measured VCD spectrum was shifted up and down within a range of 10 % of the maximal intensity, until a maximum Σ^{max} value was obtained.

For the database of 83 compounds the Δ value was optimized for every molecule and Σ was computed for both enantiomers. The highest value of Σ, Σ^{max}, among both enantiomers is plotted as a function of the corresponding Δ value as shown in Figure 4.1. The blue markers represent instances of agreement between the enantiomer corresponding to Σ^{max} and the AC assignment based on thorough analysis of the measured and calculated VCD spectrum using elaborate band-by-band correspondence and comparison of the rotational strengths or an AC based on X-ray diffraction. By contrast, the red dots correspond to cases where the enantiomer corresponding to Σ^{max} does not agree with the result of the more thorough determination of the AC. By plotting a new molecule whose VCD spectrum has been measured and for which Σ^{max} and Δ have been computed, one can readily assess whether the assignment of the AC can be expected to be reliable or not. It is important to stress that the use of the present algorithm is not directed towards replacing the manual assignment of the AC by a numerical technique. The similarity analysis is aimed at providing the chemist an indication of whether the assignment made is at par in the level of confidence with the bulk of previous successful assignments. It also flags cases where the chemist might possibly want to reconsider the assignment made by, for example, checking the result for a different stereo-isomer, but also in that case a convincing manual assignment remains strictly required.

Based on the plot in Figure (4.1), confidence levels can be set up for future new AC assignments. We numerically express the degree to which VCD can still be considered to have reliably assisted in the assignment of the absolute configuration by computing

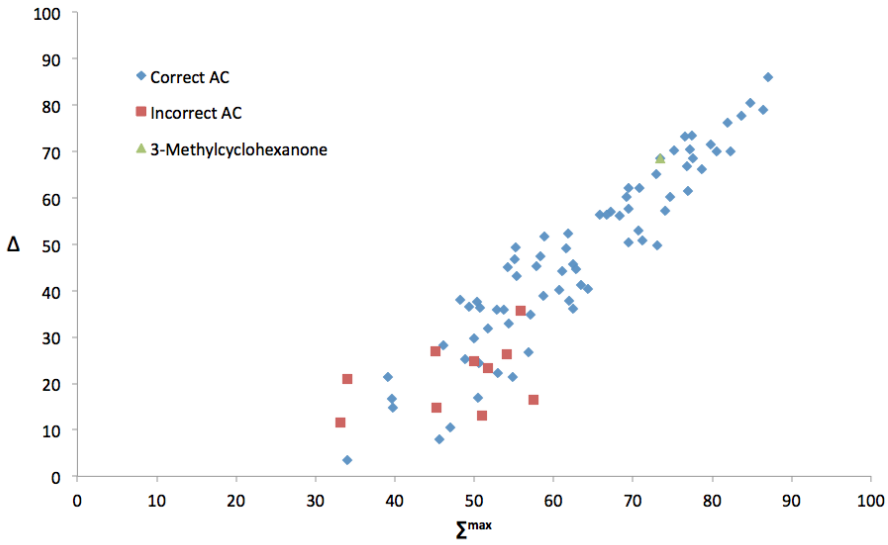

Figure 4.1: Plot of previous assignments in terms of Σ^{max} and Δ (both in %). The colour codes reflect the extent to which application of the current procedure led to the correct conclusion (blue) or the wrong conclusion (red) on the AC with respect to more elaborate VCD assignments. The green marker indicates the position of a new AC assignment with respect to the database (see text).

the ratio of the number of correct assignments with respect to the total number of attempted assignments around the position of the newly assigned AC of molecule a. Specifically, we choose the following scheme for a confidence level (CL) (Eq. (4.8)):

$$CL(a) = \frac{\sum_i^N e^{-\alpha d_{ia}^2} \delta_i(correct)}{\sum_i^N e^{-\alpha d_{ia}^2}} \tag{4.8}$$

In this equation, d_{ia} is the Euclidean distance between a molecule i from the database and new molecule a in Figure 4.1, N is the number of molecules in the database and $\delta_i(correct)$ is a logical construction that assigns a weight equal to one to a database compound i if the presently described algorithm was correct at giving a higher similarity for the enantiomer that corresponds to the one that was actually used in the VCD experiment. The exponent α has been chosen as 0.015, based on the fact that tests revealed this gives a smooth transition from the area with mostly molecules where the algorithm indeed points out the same AC as the assigned one to the area with more wrong ACs. Wrong in this case is defined as a case where the algorithm did not successfully give the correct isomer the largest similarity. Inspection of Figure 4.1 shows that for several molecules the highest similarity was found for the wrong AC. Many of those lie in an area where Δ is also low, meaning that there the difference in similarity of the computed spectrum with respect to experiment for the two enantiomers is low. This suggests that any user-made assignment of a molecule in that region, based on correlation of bands, must be considered with extra care. There is one molecule with a relatively high Δ and Σ^{max} value but for which the algorithm led to the wrong conclusion although for the majority of points in that region of Figure 4.1 the algorithm led to the correct enantiomer having the highest similarity. Molecules, for which the similarity algorithm reveals the highest similarity for the wrong enantiomer, are important as they delineate the area above which no wrong results occur and play an important role in the confidence level.

The confidence level is a simple numerical value that basically expresses how far to the upper right a new assignment lies in Figure 4.1 and supplements the conclusion that can be drawn based on the location of a new assignment in Figure 4.1. The algorithm thus assists the chemist in answering the question to what extent a given assignment appears to be reliable, or in simpler terms: when a chemist has answered the question on the AC, the algorithm tells how much confidence can be put to this answer. If the degree of confidence is small, this may suggest trying a different assignment, which obviously also must be first checked by visual verification and analysis of the bands or

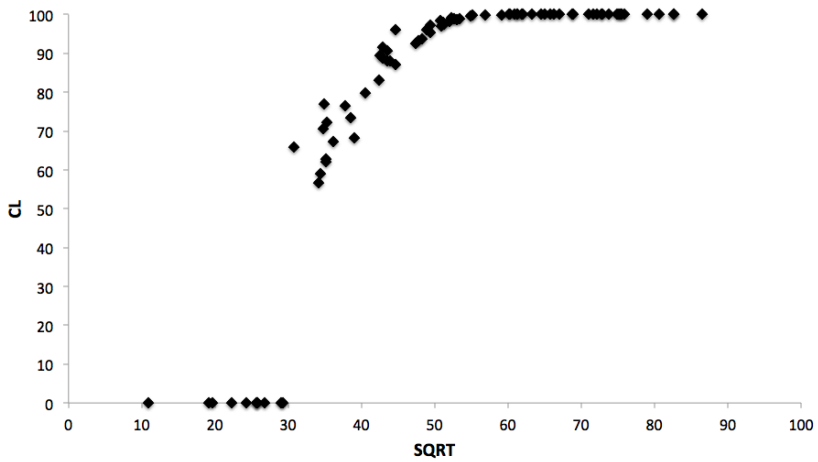

Figure 4.2: Variation of CL (in %) as a function of the generalized coordinate SQRT (see text, in %).

may point out other difficulties like problems with basis set, incomplete representation of the conformational distribution etc. Figure 4.2 shows how CL with exponent 0.01 behaves when going from the lower left corner of the plot in Figure 4.1 to the upper right corner. To show this in a simple 2D graph, a generalized coordinate of both coordinates in Figure 4.1 has been made. This coordinate is denoted SQRT and is the geometric average of the two coordinates of every molecule in Figure 4.1. The choice for the geometric average means that both levels of confidence must be sufficiently high. The CL performs in the desired way by attaching the highest confidence only to the points where the generalized coordinate is high, that is, it reflects how far to the upper right an assignment lies in Figure 4.1.

Note that in Figure 4.2 several molecules appear to have a confidence level equal to zero. This is coded into the algorithm based on the experience that from the moment the Δ and Σ^{max} values grow too small, any use of the algorithm is discouraged and the manual assignment is also best checked thoroughly.

A key element is naturally the database. In this context it is worth noting that all theoretically calculated spectra were performed in a state of art way to eliminate the risk that a poor conformational analysis combined with the wrong enantiomer could eventually appear to result in a high level of confidence. Several perturbations were undertaken in the database to establish whether, for example, the use of a wrong spec-

trum (as in: taken from calculations or experimental data from the wrong molecule) could easily lead to a high level of confidence. From our experiments this did not seem to be the case. However, it needs to be stressed that the calculations must always be performed after proper conformational analysis and must use well established density functionals and sufficiently large basis sets. In one case in the database, the wrong diastereomer would have had a relatively high level of confidence provided a physically unacceptable scale factor was used. Hence, it is important to take into account all the information provided by the algorithm.

4.3.2 Similarity Measures and Confidence Levels for (+)-3R-Methylcyclohexanone and (+)-R-Limonene

As an example of the use of the data in Figure 4.1 and the confidence level, CL, similarity measures and confidence levels were computed for the VCD-based assignment of the AC of (+)-3*R*methylcyclohexanone. A thorough analysis of the measured and calculated IR and VCD spectra of the molecule has already been discussed extensively in literature.[99–101] The aforementioned similarity measures of the compound were obtained after running CompareVOA,[102] the program in which the here described algorithms have been implemented. In Figure 4.3, the measured IR and VCD spectra and the scaled computed spectra (B3LYP/cc-pVTZ, scale factor 0.986 based on CompareVOA) are shown. The intensities have been scaled to emphasize the agreement between both sets of spectra. The measured spectrum very clearly corresponds to the R configuration as is easily confirmed by visual inspection of the spectra and agrees with the mentioned previous assignments.

The magnitude of the optimal scale factor (0.986) that maximizes the similarity between the theoretical and experimental IR spectrum lies within the range of scale factors used for harmonic spectra obtained with hybrid density functionals.[93] For $f(\nu)$ corresponding to the R configuration the IR spectra lead to $S_{fg}^{IR} = 77.30\%$. For VCD $\Sigma_{fg} = 73.41\%$ and $\Sigma_{\bar{f}g} = 4.84\%$ resulting in $\Delta = 68.57\%$. Based on the value of Σ_{fg} and Δ, it is concluded that the AC of the compound is R with confidence level equal to 99.9%. One of the more appealing aspects of computing the different measures for an AC assignment is that one can also plot the newly assigned molecule together with all molecules of the database as in Figure 4.1. It shows that the molecule, indicated by the green marker, indeed lies among all previously correctly assigned AC's.

The computation of all required integrals to establish the confidence level can be

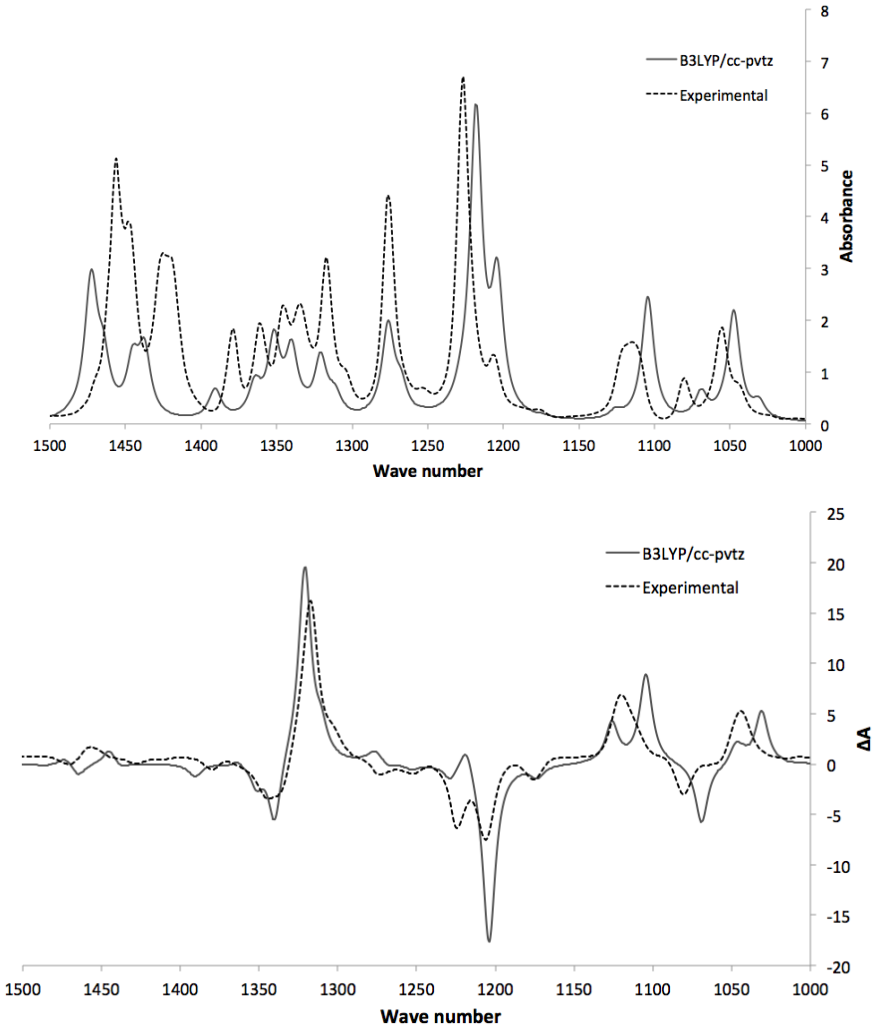

Figure 4.3: Calculated (B3LYP/cc-pVTZ) and observed IR (a) and VCD (b) spectra for (+)-3*R*-methylcyclohexanone. The absorbance and ΔA values are shown in scaled units (see text) versus wave numbers in cm^{-1}.

performed in just a few seconds. Obviously, an automated approach to establishing the AC using the algorithm described here should not replace chemical correlation and expertise. The reliability of the new method clearly depends on the quality of the observed and calculated spectra and needs to be established by an experienced VCD user. In cases where experimental effects like intermolecular association occur but are not taken into account in the computations, one should not use this measure because theory and experiment are too far apart. However, in such cases the introduced measures tend to immediately classify the assignment as having a low confidence level and at the same time positions the molecule in the lower left corner of Figure 4.1. We therefore suggest to always make sure that the following requirements are fulfilled: First, experimental measurements should be performed according to best VCD practice. Second, a good level of theoretical calculation must be used. Then the numerical measures, as presented here, should be computed and can serve as a guide to possibly improve, for example, the calculation of the quantum chemical spectra or as an indication to look for other effects that may lower the degree of confidence. VCD expertise does remain a third requirement as some of the capabilities of CompareVOA must be used carefully, for example, the possibility to exclude some bands from the similarity analysis. In all cases, a first assignment by an experienced VCD user is required after which CompareVOA can express the reliability of the assignment or possibly may suggest the user to consider a different stereochemistry or suggest that some aspects of the VCD analysis should be improved.

In a second thorough test of the algorithm we took (+)-*R*-limonene and examined whether the level of calculation has a significant influence on the level of confidence of the VCD assignment. Pleasingly, this proved not the case as for all possible combinations of eight density functionals and seven basis sets, the level of confidence had a spread of below 1 % compared to the confidence level of nearly 100 % for most combinations. Naturally, it remains important that the database and the results of the algorithm only be used in combination with sufficiently high level VCD calculations. Although for manual assignments, the B3LYP/6-31G* level was found to be the most modest acceptable level,[88] experience with the current algorithm points out that the aug-cc-pVDZ basis set leads to significantly higher similarity values. As an example, the value for Δ is about 20 % higher using the aug-cc-pVDZ basis set versus the 6-31G* basis set, in both cases using the B3LYP functional. Advances in computer architecture and algorithms make this admittedly larger basis set routinely applicable.

Comparing our similarity measures with the method developed by Shen et al.,[92]

some similarities but also some differences are observed. The algorithm of Shen et al. computes the spectrum similarities via a Tanimoto coefficient. The local shift of the bands is not taken into account through the use of triangular weighting functions, as was done here. In their approach, the scaled spectrum is divided into a number of bands and the frequency of each band is again shifted in search for the nearby maximal IR similarity. Finally the scaled and shifted bands are pieced together. A few bands, however, may need additional shifting, which is handled by a user-controlled shifting adjustment. This makes the method more laborious and possibly more open to bias. Secondly, the obtained VCD similarity value ranges from -1 (opposite enantiomer) to 1 (correct enantiomer) and it is suggested that in order to establish high confidence AC determination the associated absolute value of the similarity measure should be greater than 0.2. In our CompareVOA program, however, the study of a data set of 83 compounds enabled us to specify the level of confidence for each AC assignment and to get a more direct feeling for the quality of the assignment based on the position of the newly assigned molecule in previous successful assignments. This is a major advantage over the program suggested by Shen et al.

4.4 Conclusions

Herein, a very fast and transparent method is suggested to quantify the confidence level of an assignment of absolute configuration. The method developed is based on neighbourhood similarity measures for a quantum chemically computed and an experimental infrared spectrum with minimum intervention of the user. This similarity measure is extended to VCD by considering separately the similarity for the positive and the negative part of computed and experimental VCD spectra. This is done for both enantiomers and the absolute difference in VCD similarity with respect to experiment, is calculated. A successful assignment is characterized by high similarity between theory and experiment for one enantiomer and a low value for the other enantiomer.

In the next step, the procedure described above was applied for a large set of molecules. It was found that for a large majority of molecules, the similarity measures immediately result in the correct enantiomer to have the highest similarity to experiment. Based on the results for the entire database, a numerical confidence level is computed that reflects the percentage of assignments made using the procedure that resulted in correct assignments.

In all cases, the algorithm presented should be used to answer the question of how reliable an assignment made is. It cannot replace expert assignment but simply attaches a degree of confidence of the assignment and can possibly suggest routes for improvement of the experiment, calculation or assignment.

Chapter 5

Vibrational Circular Dichroism versus Optical Rotation Dispersion and Electronic Circular Dichroism for Diastereomers: the Stereochemistry of 3-(1'-hydroxyethyl)-1-(3'-phenylpropanoyl)-azetidin-2-one

The absolute configuration of a relatively large and conformationally flexible chiral compound, 3-(1'-hydroxyethyl)-1-(3'-phenylpropanoyl)-azetidin-2-one, is determined using Vibrational Circular Dichroism (VCD) spectroscopy, Optical Rotation Dispersion (ORD) and Electronic Circular Dichroism (ECD). To that end a state of the art experimental VCD spectrum is compared to a theoretical spectrum and the absolute configuration is assigned. ORD and ECD are also used in the assignment to investi-

gate the complementarity of the three techniques. VCD spectroscopy is found to have important advantages over ORD and ECD for diastereomers. The concept of robust modes is applied to this conformationally flexible molecule, showing that its use is limited for such large and flexible molecules.

5.1 Introduction

Chirality is of utmost importance since it lies at the very basis of life on Earth. Many of the essential building blocks of biologically important compounds are chiral. Although different enantiomers of a molecule appear to have the same characteristics for many properties, they can also have drastically different properties in the presence of other chiral compounds. Especially in fields like drugs and catalysis, a different so-called absolute configuration (AC) can lead to different properties such as rendering one stereo-isomer to have medicinal activity and another to be possibly lethal.[103] As a consequence, there is a lot of interest in ways to establish the absolute configuration of a molecule. Many techniques exist although often differing in their range of applicability, routine availability, etc.[27] Well-known techniques are X-ray diffraction, Electronic Circular Dichroism (ECD), specialised NMR techniques, retrosynthesis, Optical Rotation Dispersion (ORD)... During the past decades the range of applicable methods has been extended with Vibrational Circular Dichroism (VCD), a technique that relies on the different behaviour of enantiomers towards circularly polarized light.[10,29,44,104] Among the advantages of VCD one can count the fact that a relatively simple set of experimental manipulations can be performed on liquids avoiding among others time consuming and sometimes even impossible crystallisation.[20,21] However, techniques like ECD, ORD and VCD, although apparently very promising, also have their drawbacks. All three techniques lead to experimental data that cannot directly be linked to an absolute configuration (AC). This is obviously a very important drawback as for ORD, for example, one often needs to rely on analogies to other molecules to establish the AC. Such a procedure is error prone. This drawback has, however, been seriously reduced with the advent of powerful quantum chemical algorithms that allow us to compute spectra *ab initio* for a given AC, after which through confrontation between an experimental and a theoretical spectrum, one can assign to what AC the experimental sample corresponds. In case of VCD, the Stephens formulation of VCD[42] can rightfully be considered a breakthrough and algorithms[105] are now implemented in

several commonly available software packages such as Gaussian,[64] ADF,[106] Dalton[107] and Jaguar.[108] The calculation of ORD has become available more recently.[57]

Currently, most applications of circular dichroism and ORD are restricted to pairs of enantiomers. For VCD some examples have been published where the technique has been used for the determination of the AC for diastereomers[3,89,109–117] although this number is vastly smaller than the number of applications for enantiomers. Moreover, in many cases the relative stereochemistry of the asymmetric carbons is already known.

Historically, VCD spectroscopy has mainly been used for relatively small molecules with consequently limited flexibility. Besides the challenge of diastereomers, VCD is not yet a routine practice for large flexible molecules or for cases where solvent-solute interactions play an important role, leading in some cases even to induced VCD bands in achiral solvent molecules.[84,85] The aim of the present paper is to examine and compare the performance of ORD, ECD and VCD as techniques for assigning the AC of a relatively large and flexible molecule and to determine to what extent ORD, ECD or VCD can distinguish the AC of a molecule with several chiral centres without other experimental information. Furthermore we examine, to the best of our knowledge for the first time, the robustness of the VCD modes as introduced by Nicu et al.[47,118] and its alternative formulation by Gobi et al.[119] to establish whether there exist one or more modes that are sufficiently robust over all conformations of a fairly large and flexible molecule.

As a test molecule, we opted for 3-(1'-hydroxyethyl)-1-(3'-phenylpropanoyl)-azetidin-2-one[120] (see figure 5.1), a molecule that contains two chiral centres along with several functional groups that not seldom are considered problematic for VCD in solution. Typical functional groups of that kind are carbonyl groups whose VCD signature is often hard to reproduce using theoretical calculations and hydroxyl groups that may be involved in significant solvent-solute interactions. Inspection of the molecule in figure 5.1 also immediately suggests substantial conformational flexibility with each possible diastereomer leading to possibly dozens of conformations.

5.2 Experimental and Computational Details

5.2.1 Experimental Details

The title molecule **1** is a key-intermediate in the synthesis of a small library of Fatty Acid Amide Hydrolase (FAAH) inhibitors.[120] It was obtained in two steps from 3(S)-[1'(R)-

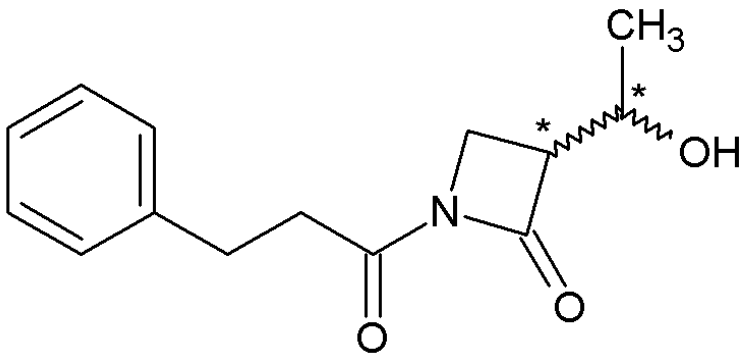

Figure 5.1: Structure of 3-(1'-hydroxyethyl)-1-(3'-phenylpropanoyl)-azetidin-2-one (**1**). Chiral centres are indicated by *. The ring asymmetric carbon atom will from now on be referred to as 3, the hydroxyethyl asymmetric carbon as 1'.

(*t*-butyldimethylsilyloxy)-ethyl]-azetin-2-one. Briefly, the starting material (1 equivalent) dissolved in dichloromethane (10 mL / mmol) was treated with 3-phenylpropanoyl chloride (2 equivalents) and pyridine (2 equivalents) (24 h, reflux), then worked-up with 10% Na_2CO_3. Column chromatography on silica gel gave 3(*S*)-[1'(*R*)-(*t*-butyldimethylsilyloxy)-ethyl]-1-(3'-phenylpropanoyl)-azetidin-2-one in 90% yield: R_F = 0.53 (cyclohexane / EtOAc 5:3); ^{1}H NMR (300 MHz, $CDCl_3$) δ = 0.06 (s, 3 H), 0.09 (s, 3 H), 0.85 (s, 9 H), 1.20 (d, 3 H, J = 6.3 Hz), 2.95-3.06 (m, 4 H), 3.23 (m, 1 H), 3.56 (dd, 1 H, J = 6.7 Hz and 7.2 Hz), 3.70 (dd, 1 H, J = 3.6 Hz and 7.2 Hz), 4.31 (m, 1 H), 7.11-7.40 (m, 5 H); HRMS: calculated for $C_{20}H_{31}NO_3SiNa$ = 384.1971; found = 384.1974. One equivalent of the previous compound in acetonitrile (30 mL / mmol) was treated at -5 °C with 12 N HCl (5 equivalents) and 17 N AcOH (7 equivalents) for 30 minutes and then for 3 hours at 0 °C. Concentration, dilution in EtOAc, washing with 10% $NaHCO_3$ and brine, and column chromatography on silica gel yielded **1** in 78% yield as a white powder: R_F = 0.09 (cyclohexane / EtOAc 5:3); Mp = 64.5-65.5 °C; ^{1}H NMR (300 MHz, $CDCl_3$) δ = 1.28 (d, 3 H, J = 6.4 Hz), 1.91 (br s, 1 H), 2.88-3.12 (m, 4 H), 3.25 (m, 1 H), 3.60 (m, 2 H), 4.22 (m, 1 H), 7.12-7.38 (m, 5 H);^{13}C NMR (75 MHz, $CDCl_3$) δ = 21.7, 30.2, 38.4, 39.2, 55.9, 64.9, 126.4, 128.6, 128.7, 140.4, 166.1, 170.4; HRMS: calculated for $C_{14}H_{17}NO_3Na$ = 270.1106; found = 270.1109.

For the spectroscopic measurements, **1** was dissolved in $CDCl_3$(99.8%, Aldrich) and in CCl_4 (99.9%, Aldrich) with a concentration between 0.04M and 0.05M. The IR- and VCD-spectrum were recorded on a ChiralIR-2X dual PEM[73] VCD-spectrometer

(BioTools, Inc). The solution and the solvent were recorded separately, using a demountable liquid cell with BaF_2 windows and 100 μm spacers, and a resolution of 4 cm^{-1}. The solution spectra were recorded twice for 6.5h, accumulating 40 000 scans, whereas for the solvent a total of 25 000 scans were recorded. For both IR and VCD, the solution spectra were solvent subtracted. The ORD was recorded at 5 different wavelengths (589, 578, 546, 436 and 365 nm) using a Perkin-Elmer 241MC polarimeter. The solvent of choice was $CHCl_3$, using a concentration of 0.765g/100mL. Finally, ECD measurements were performed using a Chirascan-Plus ECD spectrometer (Applied Photophysics). Concentrations of 0.04 M, 0.004 M and 0.00135 M in trifluoroethanol (TFE) were used in combination with a 500 μm path length. UV absorbance and ECD were recorded simultaneously.

5.2.2 Computational Details

Since VCD, ORD and ECD data are heavily dependent on the molecular conformation, a thorough conformational analysis is of prime importance. In this work a stochastic search was carried out using the MMFF,[121] MMFF94S[122] and SYBYL[123] molecular mechanics force fields, as implemented in the Spartan '08 (Monte Carlo)[124] and the Conflex ('reservoir filling')[125–127] software packages.

1 gives rise to 4 diastereomers among which two pairs have an enantiomeric relationship. Given the simple mirror image symmetry of the VCD and ECD spectra and sign inversion in ORD for enantiomers for each enantiomeric pair, it suffices to compute only one enantiomer. Specifically in this case, the two structures for which theoretical spectra have been computed correspond to 3(*S*)-(1'(*R*)-hydroxyethyl)-1-(3'-phenylpropanoyl)-azetidin-2-one (henceforth denoted as 3*S*1'*R*-**1**) and 3(*S*)-(1'(*S*)-hydroxyethyl)-1-(3'-phenylpropanoyl)-azetidin-2-one (henceforth denoted as 3*S*1'*S*-**1**). Since many redundant conformers were found by the different approaches, redundant conformers were removed before proceeding to ab initio geometry optimisations. This was done through comparison of the eigenvalues of the internuclear distance matrix. DFT calculations of VCD, ECD and ORD were carried out using the B3LYP functional[96,105,128] and the aug-cc-pvdz[129] basis set, as implemented in Gaussian 09.[64] Where needed or beneficial for the further discussion, spectra for the other enantiomers have been obtained from those calculated. For IR the spectra of two enantiomers are the same, whereas for VCD the mirror image was used. Solvent effects were included using the self-consistent reaction field model (PCM),[130,131] using a dielectric constant

for chloroform of $\epsilon = 4.71$. For the construction of the final spectra, dipole and rotational strengths for each normal mode were converted to molar extinction coefficients (L mol^{-1}cm^{-1}).[32] For VCD, a Lorentzian broadening was applied to mimic the physical line broadening in the experimental spectra. A full width at half maximum of 15 cm^{-1} was used for both IR and VCD. For the ECD-spectra, a Gaussian broadening was applied using a half bandwidth at $1/e$ peak height of 20 nm.[132] The broadening was done for every conformer. The resulting spectra over all conformations were combined in a Boltzmann weighted manner based on the enthalpy, at 289.15 K and using standard conditions.

For the VCD-analysis, a robust mode analysis was carried out to evaluate the reliability of the sign and magnitude of the rotational strength for each calculated normal mode and to examine whether the property of robustness of a certain mode is transferable from one conformation to another. A band is considered robust[133] if the angle between the electric (EDTM) and magnetic dipole transition moment (MDTM) vectors is such that small changes in the calculations, such as the functional or basis set, are unlikely to lead to a significant change in the rotational strength. This angle determines the sign of the calculated normal mode for each conformer, and is given by:[47,118]

$$cos\alpha = \frac{\left\langle \Psi_i \middle| \vec{\mu}_{elec} \middle| \Psi_f \right\rangle \cdot Im\left[\left\langle \Psi_i \middle| \vec{\mu}_{mag} \middle| \Psi_f \right\rangle\right]}{\left\| \left\langle \Psi_i \middle| \vec{\mu}_{elec} \middle| \Psi_f \right\rangle \cdot Im\left[\left\langle \Psi_i \middle| \vec{\mu}_{mag} \middle| \Psi_f \right\rangle\right] \right\|} \tag{5.1}$$

where the denumerator contains the norm of the EDTM and MDTM vectors. As the sign of all VCD bands is the primary criterion used in a VCD assignment, one needs to focus on bands for which sign reversal is unlikely, even if changing some computational parameters could cause significant changes in α. Angles with a deviation in absolute value of more than 30° from 90° are considered robust by Nicu et al.[47,118,134] meaning they are not likely to show a sign change under a (modest) change in computational strategy. Recently, Gobi et al.[119] claimed that a gauge independent measure for the robustness of a normal mode *k* is given by:

$$\zeta_k = \frac{\|\vec{\mu}_{mag,k}\| \cos\alpha}{\|\vec{\mu}_{elec,k}\|} = \frac{R_k}{D_k} \tag{5.2}$$

It is stated that this solves issues related to origin dependence of the robust mode criterion of Nicu et al. In fact, this measure has been used for long time in VCD and

corresponds to the anisotropy ratio g_a of a transition k:

$$g_a = \frac{\Delta\epsilon_a}{\epsilon_a} = \frac{4R_k}{D_k} \tag{5.3}$$

As the presently examined molecule is quite large, origin dependence is rather discomforting so the measure by Gobi et al. is used in the results. According to Gobi et al. the sign of a VCD band becomes unreliable if g_a is under 10 ppm, thus if the anisotropy is smaller than 40 ppm. However, the rotational strength for a band can have both signs or equivalently the cosine can have both signs and so for every band with negative rotational strength, the index is automatically below 40 ppm. We therefore used the absolute value of the rotational strength:

$$g'_a = \frac{4\,|R_k|}{D_k} \tag{5.4}$$

5.3 Results and Discussion

5.3.1 Conformational analysis

The molecular mechanics conformational analysis carried out as described above yielded 89 and 260 conformers for the 3*S*1'*R*-**1** and 3*S*1'*S*-**1** diastereomers, respectively. The geometries of all these conformers was further optimised using the B3LYP functional and the 6-31G* basis set as an intermediate step, followed by further optimization at the B3LYP/aug-cc-pVDZ level. From the resulting unique minima, only those with a Boltzmann population above 1% were retained for further study. For 3*S*1'*R*-**1** this led to 20 unique conformers and for 3*S*1'*S*-**1** to 15. For these conformers, geometry optimisations, VCD spectra, ECD spectra and ORD were calculated at the B3LYP/aug-cc-pVDZ level of theory including a PCM self-consistent reaction field (ϵ = 4.71).[85,135] Results of these final calculations are used throughout what follows.

The 20 conformers of 3*S*1'*R*-**1** studied are listed in table 5.1, together with their representative dihedral angles, relative enthalpies and Boltzmann weights. The numbering of the atoms is given in figure 5.2. Concerning the planar imide part, all conformations are in the *s-trans* configuration (i.e. *trans* configuration over a single bond). A planar propanoyl chain lying in the imide plane gives the most stable conformers, followed by those where the propanoyl plane is perpendicular to the imide plane.

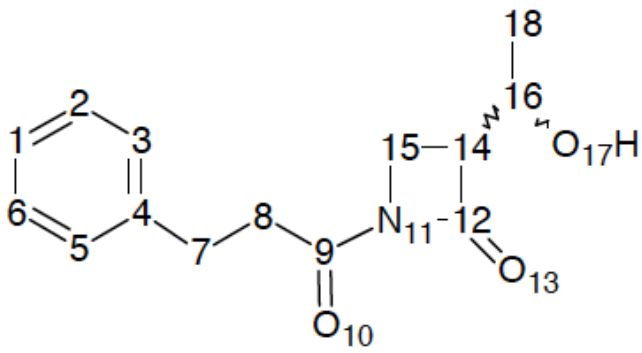

Figure 5.2: Atom labels used in tables 1 and 2. Atom numbering without chemical symbol denotes a carbon atom.

Changing levels of theory (change of basis set or inclusion of solvent effects with the PCM method), was found to have only a minor effect on the geometry of each conformation. However, significant changes in the Boltzmann weights did appear (see supplementary material for results at the B3LYP/6-31G* level). Given the influence of the conformation on VCD spectra, this is an important and possibly highly influential finding. Yet, as will be shown below, in the case of **1**, conformations can be gathered in classes for which the spectrum is remarkably similar over all members of each class while the sum of the Boltzmann weights over an entire class varies much less upon changing the level of theory than the individual conformational weights. For 3*S*1'*R*-**1**, the potential energy surface (PES) appears to have many low-lying minima without a dominant minimum at any level of theory.

Based on inspection of table 5.1, there is a clear preference for only two out of the 3 possible staggered arrangements for the dihedral angle C_{12}-C_{14}-C_{16}-O_{17}. This allows us to define two classes in the conformer distribution: a class with a dihedral angle close to -167° (class a), and a group with a dihedral angle close -51° (class b) for the C_{12}-C_{14}-C_{16}-O_{17} dihedral angle.

A similar analysis for 3*S*1'*S*-**1** (table 5.2 also shows two classes, namely one where the 1'-hydroxyethyl dihedral angle (C_{12}-C_{14}-C_{16}-O_{17}) is close to +50° (class a) and another where it is close -66° (class b).

The fact that in both cases the conformations can be gathered in two classes is important for the study of the VCD characteristics. Density Functional Theory has a

Conf.	**W(%)**	Δ**H**$^\circ$	$\mathbf{O_{10}}$-$\mathbf{C_9}$-$\mathbf{C_8}$-$\mathbf{C_7}$	$\mathbf{C_9}$-$\mathbf{C_8}$-$\mathbf{C_7}$-$\mathbf{C_4}$	$\mathbf{C_{12}}$-$\mathbf{C_{14}}$-$\mathbf{C_{16}}$-$\mathbf{O_{17}}$
1 (b)	12.03	0	3.0	-178.9	-52.1
2 (a)	11.28	0.04	-1.0	179.4	-167.5
3 (b)	10.57	0.08	3.1	-178.9	-50.5
4 (a)	8.71	0.19	-1.2	179.3	-163.1
5 (b)	4.87	0.54	-92	178	-52.2
6 (b)	4.87	0.54	93.1	-176.4	-52.3
7 (a)	4.56	0.57	-93.2	177.4	-166.9
8 (a)	4.28	0.61	92.9	-176.1	-167.6
9 (b)	4.01	0.65	93.9	-176.5	-50.5
10 (b)	4.01	0.65	-91.2	177.7	-50.5
11 (b)	4.01	0.65	27.6	72	-52.5
12 (a)	3.52	0.73	25.1	72.8	-167.5
13 (a)	3.52	0.73	-93.4	177.5	-162.7
14 (a)	3.3	0.77	-29.7	-72.8	-167.4
15 (a)	3.1	0.8	92.8	-176.2	-163.5
16 (b)	3.1	0.8	28.7	71.7	-51.5
17 (b)	2.9	0.84	-18.7	-74.6	-52.2
18 (a)	2.72	0.88	25.3	72.7	-163.4
19 (b)	2.39	0.96	-35.9	-71.7	-51.6
20 (a)	2.24	1	-30.3	-72.7	-163.4

Table 5.1: Dihedral angles (in degrees), Boltzmann weights (W, 298.15K, in %) and relative enthalpies (ΔH$^\circ$, in kcal/mole) for the most abundant conformers at the B3LYP/aug-cc-pVDZ/PCM level of theory for 3*S*1'*R*-**1**. The numbering of the atoms is given in figure 5.2. For each conformer, the class to which it belongs is included by either (a) or (b) (see text).

significant uncertainty in Boltzmann weights over conformational populations, in the sense of dependence on the functional and basis set. Given that different conformations of the same molecule may lead to significantly different VCD spectra, this may sometimes prove problematic for assigning the AC, especially when no distinctively more stable global minimum structure is found.

As mentioned above, B3LYP/6-31G* calculations indeed reveal significant differences in Boltzmann weight for the individual conformations compared to the data in table 5.1. On the other hand, the sum of the weights over a separate class does not change so dramatically. This is illustrated by the data in table 5.3, where the results shows that for some selected individual conformations, the changes in Boltzmann weight can be very large whereas if we sum over all conformations of a class, the resulting sum is much more stable.

Conf.	W	ΔH°	O_{10}-C_9-C_8-C_7	C_9-C_8-C_7-C_4	C_{12}-C_{14}-C_{16}-O_{17}
1 (b)	29.44	0.00	0.3	-179.7	-66.4
2 (b)	11.17	0.58	92.4	-177.7	-66.2
3 (b)	10.47	0.61	-93.9	176.5	-66.2
4 (a)	9.81	0.65	-0.3	-179.8	49.3
5 (b)	9.20	0.69	26.9	71.8	-66.5
6 (b)	9.20	0.69	-27.5	-73.5	-66.3
7 (a)	3.72	1.23	92.3	-177.5	49.5
8 (a)	3.49	1.26	-92.9	176.0	50.1
9 (a)	2.87	1.38	-93.2	175.9	49.4
10 (a)	2.69	1.42	-25.5	-73.8	49.8
11 (a)	2.22	1.53	-26.5	-73.6	49.7
12 (a)	1.95	1.61	25.0	73.7	49.7
13 (b)	1.95	1.61	-105.6	61.6	-66.4
14 (a)	1.83	1.65	29.3	72.8	50.9

Table 5.2: Dihedral angles (in degrees), Boltzmann weights (W, 298.15K, in %) and relative enthalpies (ΔH°, in kcal/mole) for the most abundant conformers on the B3LYP/aug-cc-pVDZ/PCM level of theory for 3S1'S-**1**. The numbering of the atoms is given in figure 2. For each conformer the conformer class to which it belongs is included by either (a) or (b) (see text).

If it would be so that the VCD spectra for different conformations within a class are sufficiently similar or if clear marker VCD bands can be identified for each class, then VCD would still be reliable for such a large and flexible molecule. This is indeed the case, as will be shown below.

5.3.2 IR and VCD Spectra

To facilitate the discussion of the spectra, the main features of the IR and VCD-spectra are referred to using the common numbering as shown in figures 5.3 and 5.4.

Figure 5.3 shows the experimental IR-spectrum together with the calculated spectra for both diastereomers. Both show a good agreement with the experiment, although the spectral features between 1225 $cm^{-1}$and 1275 cm^{-1}(6 and 7) are more correctly reproduced for the 3*S*1'*R*-**1** spectrum. For both calculated spectra, a global scale factor of 0.982 was found to be adequate to compensate for the harmonic overestimation of the frequency.[136] This optimal scale factor was found using the CompareVOA algorithm, by maximizing the IR-similarity.[1]

3S1'R-1		**aug-cc-pVDZ/PCM**	**aug-cc-pVDZ**	**6-31G***
Individual conformer	1	12.0	4.4	2.5
	19	2.4	4.4	27.8
Class	a	47.2	53.7	33.1
	b	52.8	46.3	66.9
3S1'S-1				
Individual conformer	4	9.8	3.1	1.9
	14	1.8	1.7	17.1
Class	a	71.4	82.5	64.6
	b	28.6	17.5	35.4

Table 5.3: Boltzmann weights (298.15K, in %) for several basis sets. For both diastereomers, the change in Boltzmann weight for selected individual conformers can be almost an order of magnitude larger than the change in Boltzmann weight of a class.

The calculated VCD-spectra for the 3*S*1'*S*-**1** and 3*S*1'*R*-**1** diastereomers are shown together with the experimental VCD spectra in figure 5.4. At first glance, both the 3*S*1'*S*-**1** and the 3*S*1'*R*-**1** spectra seem to reproduce the main features of the experimental spectrum. It is often the case that two diastereomers have similar spectra (IR and VCD), both resembling the experiment. Therefore, a thorough analysis of both the IR and VCD spectra must be made for both diastereomers. In this analysis, we make use of the fact that although a frequency shift is possible between experimental and calculated spectra, this shift must be consistent for the IR and VCD-spectrum.

For the 3*S*1'*R*-**1** spectrum, a very good agreement is found in which all VCD-bands are predicted correctly (cf. numbers shown in figure 5.4), and VCD frequency shifts with respect to the experimental spectrum are consistent with the shifts found in the IR-spectrum, except for peak 8. For this signal, the experimental VCD and IR have a maximum at exactly the same wavenumber showing that the bands can be attributed to the same normal mode of vibration. In the calculated spectra the maximum of the IR-band is located at 1316 cm^{-1}, whereas the maximum of the positive VCD-band is located at 1305 cm^{-1}.

Nonetheless, it is clear that the broad positive VCD-band 8 comprises a collection of normal modes of vibration with large dipole strengths and strong positive rotational strengths. This is correctly reproduced by the calculations, regardless of the fact that the maximal dipole strength among the modes in the band does not correspond to

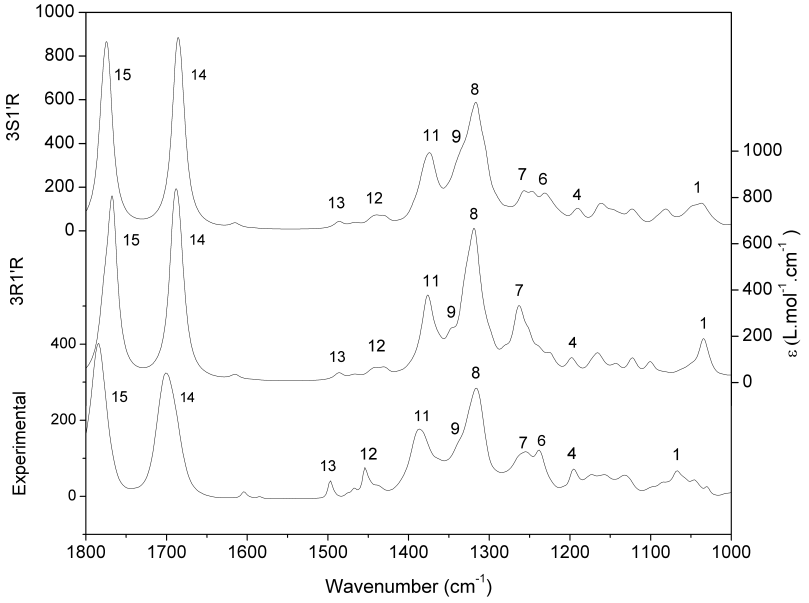

Figure 5.3: Experimental IR-spectrum (lower), together with the Boltzmann averaged calculated spectra, for both 3*S*1'*R*-**1** (upper) and 3*S*1'*S*-**1** (middle). To allow proper numerical comparison, both experimental absorption and calculated dipole strengths were converted to extinction coefficients.

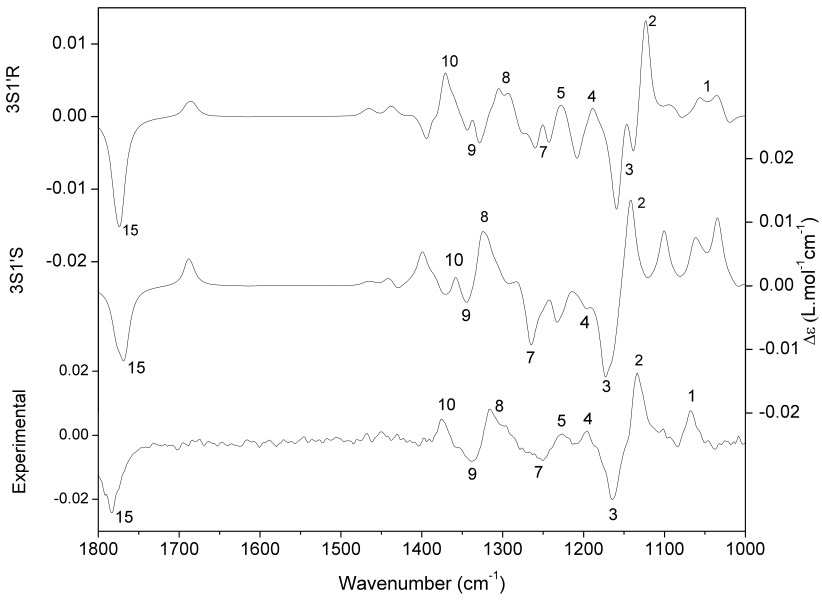

Figure 5.4: Experimental VCD-spectrum (lower), together with the Boltzmann averaged calculated spectra, for both 3*S*1'*R*-**1** (upper) and 3*S*1'*S*-**1** (middle). Both experimental differential absorption and calculated rotational strengths were converted to differential extinction coefficients to allow proper numerical comparison. The numbering of the transitions is identical to that in Figure 5.3.

the maximal rotational strength among the modes. The small negative VCD-signal between peak 4 and 5 is heavily overestimated in the calculated spectrum, but has the correct sign. The VCD-signal of the ring-bound carbonyl stretch (15) is predicted correctly, but the predicted small positive carbonyl stretch peak at 1700 cm^{-1} is not found in the experimental VCD, as is the negative signal at 1400 cm^{-1}. In the context of VCD spectra for large molecules, this is a very satisfactory agreement.

The 3S1'S-**1** VCD-spectrum also shows some similarity with the experiment, but when closely analysed in combination with the IR-spectrum, it becomes clear that it does not match well:

- There is an important positive VCD-pattern between 1400 and 1450 cm^{-1} for the calculated spectrum which is absent in the experimental VCD-spectrum.
- The intense series of peaks between 1010 cm^{-1} and 1120 cm^{-1} in the calculated

VCD-spectrum can in no way be matched with the experimental spectrum.

- Peak 4 is negative while it should be positive. Between peak 4 and 6 (IR), there should also be a positive peak in the VCD. For 3*S*1'*S*-**1**, a negative signal is predicted.

- In the IR, peaks 4, 6 and 7, correctly predicted for 3*S*1'*R*-**1**, are very poorly reproduced in the IR-spectrum of 3*S*1'*S*-**1**.

These important differences, together with the fact that 3*S*1'*R*-**1** spectrum shows almost perfect agreement with the experiment, leads to the conclusion that the β-lactam ring stereocentre has the *S*-configuration, and the 1'-hydroxyethyl chain has the *R*-configuration. The above results show that, although diastereomers often have similar VCD-spectra, the combination of VCD with IR is a powerful tool in assigning the absolute configuration of a molecule with two chiral centres, since the combination is able to distinguish between diastereomers.

A strong solvent solute interaction can heavily influence the VCD spectrum.[84,85] A way to rule out that solvation, not taken properly into account in the calculations, is to record the spectrum in an apolar medium. Despite low solubility, a VCD spectrum could be recorded in CCl_4. This spectrum, however, showed no significant differences with the $CDCl_3$ spectrum, showing that for the species under study no important intermolecular solvent-solute interactions occur (see supplementary material).

To further assess the reliability of the above assignment of the AC, a numerical analysis, free from human bias, was performed using the CompareVOA algorithm.[1] It can be seen in table 5.4 that the spectrum for 3*S*1'*R*-**1** better matches the experiment than 3*S*1'*S*-**1**. In table 5.4, Σ^{max} is the similarity between the experimental spectrum and the relevant theoretical spectrum (3*S*1'*R*-**1** or 3*S*1'*S*-**1**). Δ is the difference in similarity between the experimental spectrum and the relevant theoretical spectrum or its enantiomer. So for 3*S*1'*R*-**1**, the similarity between theory and experiment is 78.4%. The similarity for 3*R*1'*S*-**1**, would be 68.7% lower. So there is clearly higher similarity for 3*S*1'*R*-**1**. 3*S*1'*S*-**1**, and its enantiomer both clearly have a lower similarity so the overall conclusion is again that 3*S*1'*R*-**1** fits best. Table 5.4 also shows that IR does not distinguish between both diastereomers as the IR similarity (TNS) is virtually the same.

Because of the many more or less equally stable conformers contributing to the spectrum, it is very hard to label bands to individual normal modes. For each of

	TNS (IR)	Σ^{max}	Δ
3S1'R-1	97.3	78.4	68.7
3S1'S-1	95.2	62.3	36.5

Table 5.4: Numerical comparison of both calculated diastereomers to the experiment using the CompareVOA algorhitm. TNS (IR) gives the similarity index for the IR. The clear preferences to the 3*S*1'*R*-**1** diastereomer is in accordance with the visual interpretation.

these conformers, normal modes have different frequencies, signs and strengths. A Boltzmann weighted spectrum of a flexible molecule is thus a complex combination of different normal modes of several conformers. Therefore, it is not feasible to relate every experimental band to a computed rotational strength, as is often done for small molecules.[88,89,137–140]

In large and flexible molecules like **1**, one must take into account the uncertainty in Boltzmann weights from DFT calculations. This is highly relevant here as there is no single conformation with a distinctively higher Boltzmann weight. However, as mentioned above, the conformers of both diastereomers can be gathered in two classes, depending on the dihedral angle of the hydroxyethyl chain. This hydroxyethyl chain, in close proximity to both stereocentres, may have a large influence on the VCD-spectrum of a conformer. Therefore, conformers belonging to the same class might have very similar VCD-spectra for bands closely related to this particular conformational property. Visual comparison of spectra revealed that indeed, conformations of one single class give rise to a common signature in the spectra, whereas those of the other class have a common but distinctly different signature from the first class. In order to avoid subjective human eye comparison, a numerical similarity measure Σ_{fg} was computed between the VCD-spectra of 2 conformers using the algorithm described in Debie et al.[1] This algorithm expresses how similar two spectra are on a scale of 0-100. It is found that conformers belonging to the same class tend to have a large value for Σ_{fg}. This distinction between both classes is even clearer when the Σ_{fg} calculation is limited to the region of 1000 - 1250 cm^{-1} (table 5.5). In this region, normal modes closely involving the hydroxyethyl group (i.e. normal modes for which the hydroxyethyl atoms have an important contribution in the Cartesian displacement vector of the normal mode) form the major features of the spectrum.

The average off-diagonal similarity between conformers within the (a) class is around 90% and within class (b) around 84%. The average similarity between a

	1 (b)	**2 (a)**	**3 (b)**	**5 (b)**	**7 (a)**	**8 (a)**
1 (b)	100	6	78	94	0	1
2 (a)	6	100	3	6	88	91
3 (b)	78	3	100	80	3	2
5 (b)	94	6	80	100	4	8
7 (a)	0	88	3	4	100	95
8 (a)	1	91	2	8	95	100

Table 5.5: Similarity measure Σ_{fg} of the VCD-spectra of 6 conformers of 3*S*1'*R*-**1**, in %, for the region 1000 cm^{-1} to 1250 cm^{-1}. Conformers of the same class have a large similarity index, whereas conformers of different classes show almost no similarity. This proves that the spectral features in this region are mainly dependent on the hydroxyethyl dihedral angle.

conformer from one class with that of another is only 4%. This classifies the region between 1000 cm^{-1} and 1250 cm^{-1} as a clear marker and shows that some VCD-signals are very closely related to the conformational properties in the proximity of the chiral centres. Also, as was shown before, the Boltzmann weight of each class fluctuates less with change of calculation parameters than the Boltzmann distribution of the individual conformers. This is the reason that the main features of VCD-spectra may be retained across different levels of theory or even when using only a subset of the conformational ensemble. It thus seems that, at least in this case, the conformational complexity is partially compensated by the fact that a change in conformational distribution has a relatively smaller effect on the final spectrum. A similar, although less distinct, result was also obtained for 3*S*1'*S*-**1**. The resulting data can be found in the supplementary information.

Although two classes of conformers with similar VCD-features can be found, only a few peaks can be assigned unambiguously to a normal mode of a certain class. Conformers of class (a) are responsible for peak 2 (normal mode 52) and the strong negative peak at 1160 cm^{-1} which is part of peak 3 (normal mode 55-56). The negative signal at 1140 cm^{-1}, also part of peak 3 in the Boltzmann weighted spectrum, can be assigned to normal mode 53 of the (b)-conformers. The rest of the Boltzmann weighted calculated spectrum originates from a complex combination of signals, and cannot be easily assigned to normal modes.

5.3.3 Robustness

The VCD absorption intensity for a specific peak depends on the magnitudes of the ETDM and MTDM and on the angle subtended between those (see equation (5.1)). The concept of robustness of peaks in computed VCD spectra was introduced by Nicu et al.[47,118] and is based on their observation that the angle between both transition dipole moments is found to depend quite significantly on the specific choice of computational parameters, including the DFT functional, basis set, or treatment of solvation.[47,118,133] Changing some of these parameters is found to sometimes lead to shifts in the angle of several tens of degrees. Given that the very first criterion for correlating bands between theory and experiment is the sign of the absorption peaks, it is easily understood that peaks with angles around 90° could easily change sign and thus alter the assignment of the AC upon a change in one of the computational parameters. Similarly, Gobi et al.[119] suggest that VCD-bands with a value for g_a less than 40 ppm are not to be trusted (see equation 5.2). However, we use the absolute value of this measure (see equation 5.3) and consider a band non-robust if, again, g'_a is less than 40 ppm.

Up to now the concept of robust modes has been applied only to cases where the number of conformations was fairly low. Gobi et al.[119] did test this for a small peptide, revealing that with their measure the frequency of non-robust modes is much lower than when using the cut-off in angle as used by Nicu et al.[141] In this work we test the added value of this concept for conformationally more flexible molecules. When dealing with such molecules, a number of new issues must be dealt with concerning vibrational modes.[115] First, what to think of a situation where two energetically (almost) degenerate minima have two almost coincident VCD absorption peaks, one characterised by an angle far from 90° (corresponding to $g'_a < 40$ ppm)? Is that region in the spectrum to be used or not? This is a very important question as in the present case we find that if one would hold a position that "if any lower lying minimum has a value for $g'_a < 40$ ppm for an absorption in the spectral zone of interest, this zone should not be considered trustworthy", we would quickly have to decide for the present molecule that almost no robust zones remain in the VCD spectra, impeding, for the present molecule and likely all other flexible molecules, the use of VCD based assignment of absolute configuration through combining theory and experiment. Indeed, g'_a is heavily dependent on molecular conformation, meaning that even for very similar vibrations the value can change substantially between conformations. In table

Normal Mode	ν(cm-1)	Conformer 1	2	3	4	5	6	7	8	9	10	11	12	13	14	15	16	17	18	19	20
44	1006	351	-20	69	-93	-484	39	22	409	123	-68	428	-7	-69	63	-153	-297	-48	15	65	87
45	1012	81	23	186	13	-214	4	10	-96	133	-323	352	13	-3	26	263	99	20	47	70	-267
46	1043	190	-503	-99	34	-111	-503	16	80	70	-81	-73	1	15	38	-50	-14	-1	-8	29	-495
47	1050	-647	-18	-517	114	292	-26	71	107	15	-6	268	75	21	116	3	80	52	-13	26	-10
48	1069	14	12	109	-87	-58	48	-107	35	33	149	-62	-59	90	53	34	-195	-145	107	50	-1
49	1084	-5	157	-59	107	93	322	154	-52	270	-52	47	-41	27	-25	-31	-21	131	144	192	120
50	1099	24	201	-170	-54	-106	195	-2	-425	-82	0	-61	29	-16	14	96	68	18	28	59	-61
51	1109	-1	-214	-3	14	-41	-292	-166	49	196	114	-73	-54	155	332	-276	30	-129	193	181	-79
52	1141	223	259	261	-113	339	217	324	-149	-22	-11	340	-103	-7	-118	356	-103	345	-13	-5	262
53	1158	597	-190	18	-459	-48	238	-85	-488	92	86	-64	-465	-77	-472	-102	-446	-138	159	77	-245
54	1166	-158	-407	-107	-236	482	231	615	-426	-787	75	-118	250	87	168	-459	187	-266	79	52	157
55	1172	-160	-713	-340	-214	-160	-457	-374	120	-211	-226	-73	193	175	136	-271	182	-493	-169	-143	-236
56	1183	-321	-101	338	176	-312	-98	-76	324	285	-358	-222	50	-232	46	176	-325	-61	103	87	-344
57	1191	32	174	62	18	-63	328	124	62	42	-17	22	310	-13	107	-53	39	142	272	152	-54
58	1212	389	501	479	-90	46	443	17	-304	-202	-91	-11	-75	-150	-77	-42	61	94	-148	-147	431
59	1219	-56	485	175	43	-94	-484	-536	-19	161	-149	-32	799	13	-655	-15	-81	495	761	-559	89
60	1240	-376	-387	-469	84	153	-519	183	-1290	-1665	1576	-4	267	-36	333	-117	1591	-175	-220	-103	-1056
61	1263	-11	-306	-350	-129	-48	217	90	256	-112	-26	124	-481	-33	19	-66	132	117	-512	372	-188
62	1285	-308	-81	-15	1821	245	75	71	-176	-7	-46	-79	-215	1373	43	203	-91	-57	-82	45	0
63	1308	108	201	1	-30	-41	-97	-525	113	-6	24	-382	11	128	-49	-99	56	-39	75	163	11
64	1333	-2	3	7	-1387	95	-14	74	-53	3	15	94	-64	-35	-100	66	-27	83	58	-24	-2
65	1343	672	-99	265	15	-78	90	103	68	38	-60	651	26	-1	54	45	-52	-80	-3	26	-84
66	1347	0	-266	-693	-86	-333	257	676	-375	-330	729	-29	-127	-187	176	-766	661	-286	-105	115	248
67	1352	3090	-104	-184	6373	-397	108	-490	-186	-191	216	4368	86	5680	-89	-335	378	-630	5	-68	206
68	1360	-280	25	-161	250	176	-50	-206	208	-64	-400	-206	-1678	-892	-397	-477	350	-464	61	-100	-355
69	1383	137	52	25	-148	-197	-5	-59	-193	127	29	-575	80	56	2	-101	-115	-6	71	51	94
70	1396	37	-106	68	47	-84	-85	94	123	51	70	-24	-100	49	-105	20	19	101	20	37	7
71	1410	-5	563	33	208	161	397	8	-177	17	-85	263	-363	-53	-445	264	-250	76	-52	-77	-39
72	1435	7	23	-93	-212	137	-24	-42	-57	-87	131	-3	26	3	-13	-95	170	-8	25	-14	107
73	1462	-126	-149	-275	155	-30	-147	33	-476	-436	342	-17	169	-122	137	-8	-24	29	-75	53	280
74	1467	380	240	-145	49	367	293	-104	211	-345	54	-159	189	46	-93	-437	367	201	47	-76	-112
75	1470	-133	222	403	-88	-450	-33	-138	513	32	64	-67	-154	47	133	35	-481	-133	184	-95	299
76	1473	117	-236	445	-81	-284	223	240	-167	458	-512	117	-311	-49	96	451	-124	-265	-333	191	-441
77	1494	64	75	80	44	46	48	57	72	44	0	76	42	30	32	119	7	90	27	18	34
78	1514	-2	-3	24	-1	-19	0	0	29	29	-26	-1	-2	-1	1	30	-24	-2	-2	1	-23
79	1622	2	-49	56	15	-61	54	59	30	34	-24	2	-56	15	47	32	-30	-50	-58	46	-29
80	1644	-4	2	-26	-2	27	-7	-8	-20	-20	16	-3	1	-2	-7	-21	20	1	1	-7	29
81	1716	1	9	-43	2	54	-5	-4	-55	-56	53	2	9	1	-4	-62	53	9	9	-5	54
82	1807	-20	-4	8	-13	-56	-29	-39	15	16	-38	-29	1	-11	-24	1	-40	-13	2	-23	-45

Table 5.6: Absolute value of the anisotropy ratio for all normal modes of all conformers of 3*S*1'*R*-**1**. Normal modes considered robust are marked in green, non-robust modes in red. As can be seen, most normal modes have a decent amount of robust conformers, which constitute the main contribution to the spectrum.

5.6 the values of g'_a for all vibrations between 1000 and 1800 cm^{-1} obtained for the 20 lowest energy conformations of 3*S*1'*R*-**1** are given. For ease of interpretation a colour code is used where red denotes non-robustness and green robustness. The ordering of the vibrational modes is simply based on increasing absorption wavenumber with a further label to identify the types of vibration. Inspection of the data in table 5.6 shows that apart from some exceptions, the different conformations give rise to a mix of robust and non-robust values for each normal mode studied. The exceptions are related to the normal modes 54, 55, 56, 74 and 76 for which all conformations give robust quantities, and to the normal modes 78, 79, 80, 81 and 82 for which almost all conformations yield a non-robust value. The pronounced non-robust character derived for the carbonyl stretching modes, mode 81 and 82, is in line with previous observation suggesting that reliable VCD intensities for these modes are difficult to predict.[133]

To assess the influence of the normal modes for which similar fractions of robust and non-robust parameters are derived, a reduced VCD spectrum was generated by considering only the robust modes. The resulting spectrum, obtained by ignoring the 231 non-robust modes out of 780 normal modes is shown in the supplementary information. Inspection of the full and of the reduced VCD spectra, shows that such a neglect of non-robust modes has little influence on the final spectrum. We thus conclude that only modes for which almost all conformations yield a non-robust character, including for example the carbonyl stretching modes 81 and 82, the sign and intensity of the resulting signals in the Boltzmann weighted VCD spectrum should be considered less trustworthy. This shows that for flexible molecules, the concept of robustness is useful mainly to eliminate those normal modes for which the vast majority of conformations indicate non-robustness. All other normal modes that are either mostly robust in the different conformations or show mixed robust/non-robust character over the set of conformations may be used in the assignment. This agrees in this molecule with the commonly known fact that the VCD characteristics of carbonyl stretches are hard to reproduce in DFT calculations with respect to experiment.

5.3.4 Optical Rotation Dispersion

Optical rotation (OR) and optical rotatory dispersion (ORD) have proven useful in the AC determination of chiral compounds with a single stereocentre.[137] Therefore, ORD was also applied for the present molecule to see if it is an alternative to VCD-spectroscopy in determining the AC of diastereomers having similar VCD-spectra. OR

was calculated both in the static field approximation, and in a frequency dependent calculation of the ORD at a set of 5 different wavelengths, namely 589, 578, 546, 436 and 365 nm.[54,55,57,142] Using only one frequency may cause significant influence of a possibly important nearby Cotton effect that could bias the results. Results of the ORD are shown in figure 5.5 for 3S1'R-**1** and 3*S*1'*S*-**1.** Both calculated ORD curves match more or less with the experimental curve and the uncertainty is too high to unambiguously determine the AC of **1**. ORD alone thus is not capable to determine the AC of the molecule under study.

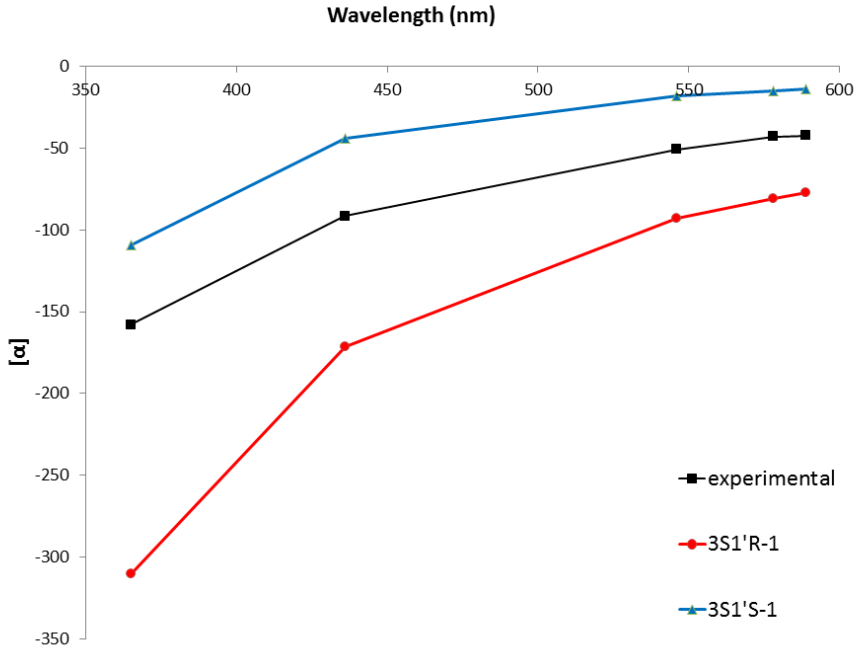

Figure 5.5: Calculated ORD of the two diastereomers of **1** compared to the experimental ORD curve.

In table 5.7, optical rotations at 589.3 nm for the ten most stable conformers of 3*S*1'*R*-**1** are shown. In contrast to the VCD data, there hardly is any correlation between the ORD and the 1-hydroxyethyl configuration. This is in line with the results of Kondru et al. stating that ORD heavily depends on conformational properties located further away from the chiral centres.[143] In fact, the dependence of optical rotation on conformation was already established 60 years ago by Kirkwood and co-

workers.[144]

Conf.	C_{12}-C_{14}-C_{16}-O_{17}	OR	OR (589.3 nm)	OR'	OR''
1 (b)	-52.1	-99	-145	-133	-155
2 (a)	-167.5	-19	-43	-54	-60
3 (b)	-50.5	-67	-106	-103	-123
4 (a)	-163.1	-46	-72	-67	-78
5 (b)	-52.2	-129	-198	-210	-207
6 (b)	-52.3	-53	-45	43	-22
7 (a)	-166.9	-47	-111	-167	-136
8 (a)	-167.6	5	34	79	40
9 (b)	-50.5	-14	-8	32	-14
10 (b)	-50.5	-93	-161	-200	-185

Table 5.7: OR angles for different levels of theory for the ten most stable conformers of 3*S*1'*R*-**1**. Also included is the dihedral angle C_{12}-C_{14}-C_{16}-O_{17}. OR and OR (589.3 nm) are respectively the B3LYP/aug-cc-pdvz/PCM static and frequency dependent OR angles. OR' and OR'' denote static OR angles at the B3LYP/6-31G* and B3LYP/aug-cc-pvdz levels of theory respectively.

Also, ORD seems to vary more between computational methods than VCD. All this implies that a change in conformational distribution, be it through a change in level of theory or change in the number of conformations considered, will have a more severe impact on ORD than on VCD. Previous research has shown that ORD calculated using the frequency dependent method gives similar results to the static approximation.[55] Therefore, it is suggested that the static approximation may suffice for the calculation of conformationally flexible molecules, since the error due to conformational variation is far more important.

Although ORD is not powerful enough to determine the AC of molecules like **1**, ORD may be a useful complementary technique to VCD when the ORD values have different signs for diastereomers with similar VCD spectra. This is not the case for the present molecules as ORD curves and static OR values for both diastereomers lie relatively close to the experimental values. The opposite was found by Polavarapu et al.,[145] where ORD for diastereomers having similar VCD-spectra did have different signs. ORD and VCD are thus inherently different probes of molecular structure, and their complementarity depends on the molecule being investigated.

5.3.5 Electronic Circular Dichroism

Finally, electronic circular dichroism (ECD) was applied in order to assign the AC. ECD is a popular method, mainly in bio-related molecules, for structure elucidation. However, it could also be of great use in the present case and knowledge of the compatibility and complementarity of different circular dichroism techniques is of general interest. In ECD far fewer absorption bands are available with often less expressed resolution.[44] In recent work, Cherblanc et al.[3] have shown that for answering questions such as whether a reaction occurs with retention or inversion of stereoconfiguration, combining different circular dichroism techniques is a clear advantage. For the present molecule, ECD data are shown in figure 5.6. For both 3*S*1'*R*-**1** and 3*S*1'*S*-**1** an agreement with the experiment is found between 175 and 205 nm. The region above 205 nm shows poor agreement for both diastereomers. For 3*S*1'*S*-**1**, a shift to longer wavelengths of 10 nm would greatly improve agreement, although important features remain absent. All this indicates that the amount of information is insufficient to rule out one of the two resulting diastereomers. The fact that VCD is able to distinguish here between diastereomers is in line with the fact that it has been appreciated that extending natural optical activity into the vibrational spectrum provides more detailed and reliable stereochemical information because a vibrational spectrum contains many more bands sensitive to the details of the molecular structure (3N-6 fundamentals, where N is the number of atoms).[44]

Naturally, the present finding for the molecule under study should not be considered a general conclusion and for other molecules, the complementarity of techniques may actually be much larger. This again indicates that combining different techniques may be an important extra asset.

5.4 Conclusion

In this study, we were able to determine the AC for a molecule of intermediate size, with two chiral centres and a large conformational flexibility, using IR and VCD spectroscopy. Although IR and VCD-spectra of diastereomers can be similar, a thorough analysis of both enables one to distinguish between diastereomers. We also found that ORD is not always a compatible technique to VCD for investigating diastereomers, since diastereomers having similar VCD-spectra not always have a different OR sign. The same was found for ECD. Thus, the added value of other chiroptical techniques than

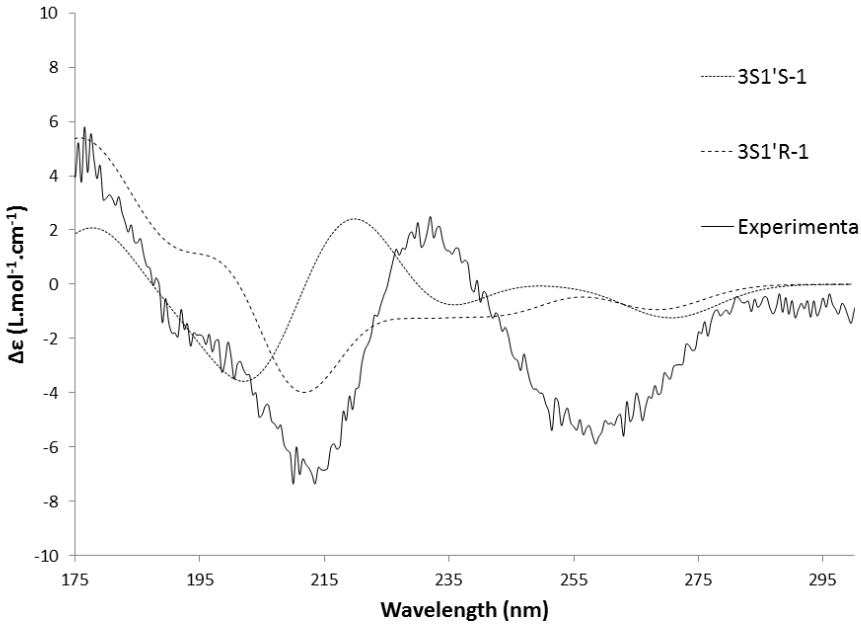

Figure 5.6: Experimental ECD-spectrum (0.00135M) of **1** compared to the calculated ECD-spectra of 3*S*1'*R*-**1** and 3*S*1'*S*-**1**. Both spectra show better agreement than the mirror image, but the agreement for both diastereomers is insufficient to assign the AC of the molecule under study. Increasing the concentration gives better S/N but limits the spectral range. The spectra at higher concentrations are given in the SI.

VCD appears to be limited in the determination of the AC of molecules with multiple stereocentres. Moreover, ORD calculations are not accurate enough and too dependent on the conformer distribution to be used as a single chiroptical technique in the AC determination of molecules with two chiral centres and significant conformational flexibility. VCD-spectroscopy however, proves to be relatively inert to conformational changes far from the chiral centres, and to changes in method of calculation. Finally, the concept of robust modes was assessed in the context of flexible molecules. Little coherence was found in the robustness of a normal mode between different conformers. Only modes where almost all conformers yield non-robust parameters should be considered non-robust. Most modes, however, have sufficient conformers contributing robust modes to be considered trustworthy in the AC determination.

5.5 Supporting Information

Conformer	W (cc-pVDZ)	W (6-31G*)
1	4.062	1.848
2	10.042	3.527
3	10.042	6.733
4	4.932	2.724
5	2.756	1.427
6	2.584	1.254
7	5.987	2.244
8	5.987	2.244
9	5.261	3.527
10	4.932	3.527
11	2.271	1.848
12	5.613	3.763
13	3.137	1.732
14	5.613	1.522
15	2.94	1.732
16	5.613	6.733
17	1.643	1.522
18	3.137	3.1
19	4.062	20.205
20	2.756	1.427

Table SI 5.1: Boltzmann weights (%) for B3LYP/6-31G* and B3LYP/cc-pVDZ for 3S1'R-**1**.

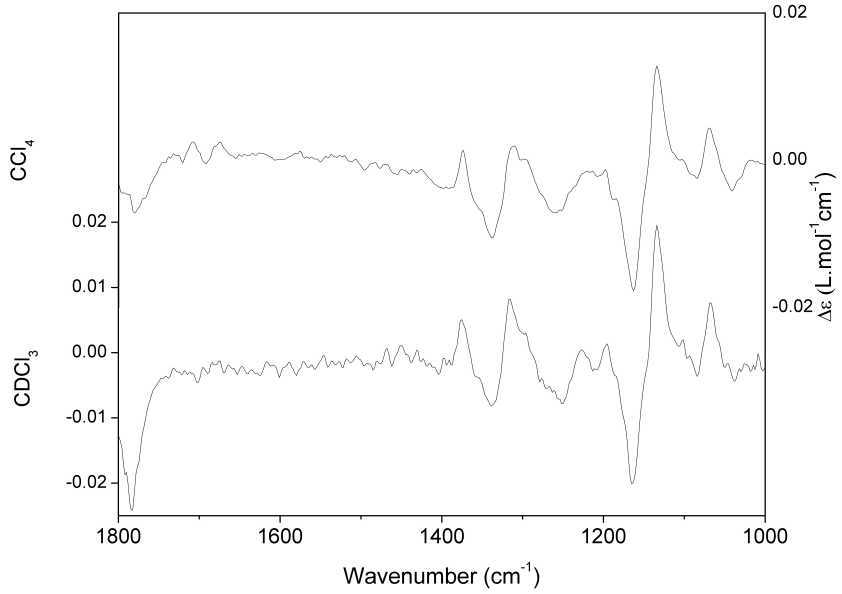

Figure SI 5.1: Experimental spectra for **1** in $CDCl_3$ and CCl_4. Apart from some details and baseline position no differences can be seen, showing that solvent effects are of minor importance for the molecule under study.

	1 (b)	**2 (b)**	**3 (b)**	**4 (a)**	**7 (a)**	**8 (a)**
1 (b)	100	72	76	40	47	47
2 (b)	72	100	54	21	43	23
3 (b)	76	54	100	33	32	56
4 (a)	40	21	33	100	77	73
7 (a)	47	43	32	77	100	74
8 (a)	47	23	56	73	74	100

Table SI 5.2: Similarity measure Σ_{fg} of the VCD-spectra of 6 conformers of 3S1'S-**1**, in %, for the region 1000 cm^{-1} to 1500 cm^{-1}. Conformers of the same class have a fairly large similarity index, whereas conformers of different classes show less similarity. This proves that the spectral features in this region are also dependent on the hydroxyethyl dihedral angle, although to a lesser extent than for 3S1'R-**1**.

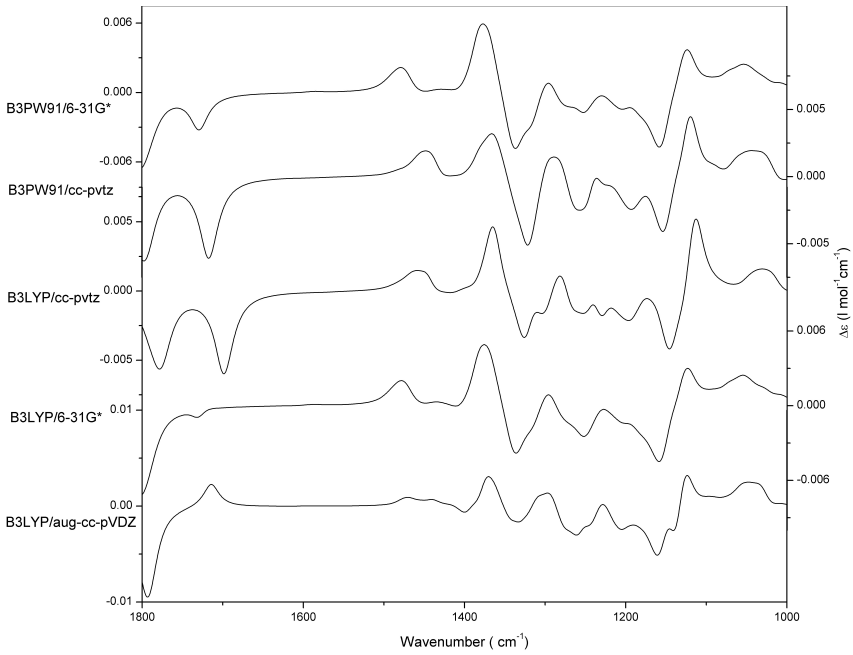

Figure SI 5.2: Boltzmann weighted, Lorentzian broadened VCD spectra for 3S1'R-**1** on 5 different levels of theory. Visual inspection as well as numerical data (Table SI 5.3) suggest that little to no sign changes occur when going from one level of theory to another.

Functional	**Basis set**	Σ_{max}
B3LYP	**6-31G***	85.1
	cc-pVTZ	73.2
	aug-cc-pVDZ	90.6
B3PW91	**6-31G***	79.8
	cc-pVTZ	76.4

Table SI 5.3: Similarity of the calculated VCD-spectra on different levels of theory compared to the B3LYP/aug-cc-pVDZ/PCM level of theory used in the article. The data show a very high similarity between levels of theory.

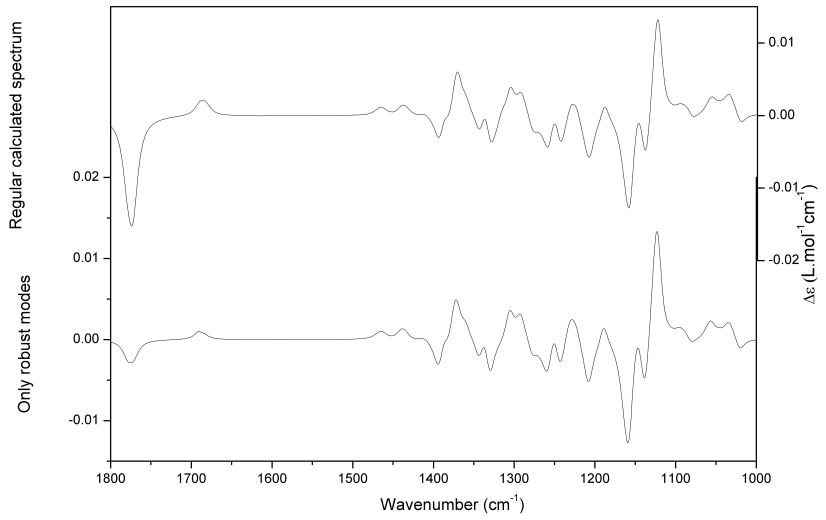

Figure SI 5.3: VCD spectra for 3S1'R-**1** generated as usual (upper) and with non-robust modes left out (lower).

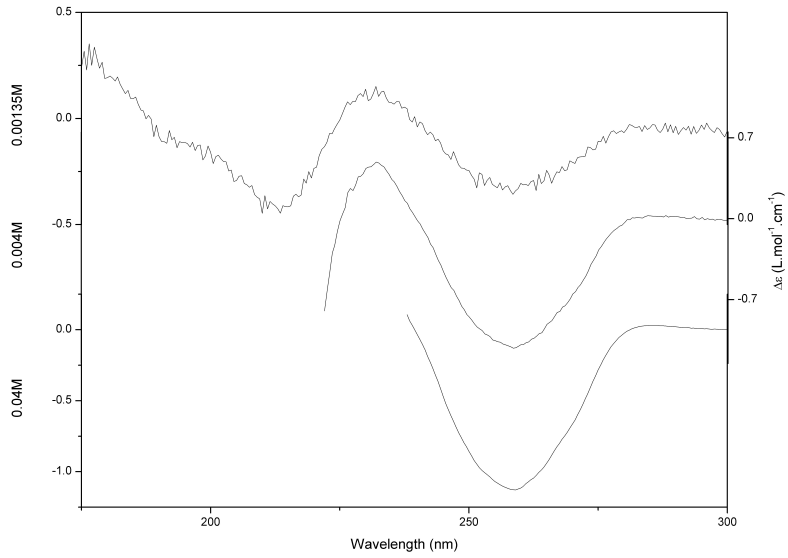

Figure SI 5.4: ECD-spectra measured for low (top), medium (middle) and high (bottom) concentration. Increasing the concentration vastly improves S/N but yields spectra in a limited spectral range.

Chapter 6

Synthesis and Chiral Characterisation of the Natural Product Building Block 5-(3-bromophenyl)-4-hydroxy-5-methylhexan-2-one using Chiroptical Spectroscopy

6.1 Introduction

Knowledge of the absolute configuration (AC) of organic molecules is of prime importance. Some well-known methods for AC elucidation are X-ray diffraction (XRD), (2D-)NMR studies or stereoselective total synthesis. XRD requires good quality single crystals, which are not always available. NMR and synthesis require the addition of chiral shift reagents and/or derivatization of the compound under study. For the determination of the AC in solution, without the need of any derivatization, several techniques have gained importance in recent years.[146–148] These techniques are based on the fact

that chiral molecules interact differently with left and right circularly polarized light (CPL). The most important of these techniques with respect to absolute configuration determination are electronic circular dichroism (ECD), vibrational circular dichroism (VCD) and optical rotatory dispersion (ORD).[42,44] The first two CD techniques are based on differential absorption of left and right CPL, whereas ORD measures the difference in the real part of the refractive index under left and right CPL.[10] All three techniques have proven useful in the determination of the AC of chiral molecules. However, VCD shows clear advantages over the other two techniques. First of all, since ORD and ECD are phenomena related to electronic transitions in the molecule, relatively few transitions are available to determine the AC, which makes it hard to assess the reliability of the determination. VCD, on the other hand, relies on vibrational transitions of which there are significantly more. This gives us much more detail and thus provides us with more information for the AC determination. Moreover, in many cases the amount of information in a VCD spectrum is sufficient to even distinguish between several diastereomers, which is most often harder with ECD and ORD.[26,145] Therefore VCD, among other chiroptical techniques, is becoming the method of choice in the AC determination of natural products and analogues.[3,85,109–111,115–117,149–155]

Since a measured VCD or ECD spectrum cannot readily be related to a certain AC, it is necessary to simulate the spectrum of a chosen configuration using quantum chemical calculations, and compare the experimental signs and intensities to the calculated ones. The method of choice for these simulations is almost always density functional theory (DFT), since DFT calculations are known to give reliable results at an acceptable computational cost. The advent of several user-friendly commercial software packages[64,106–108] has therefore induced an ever increasing interest in chiroptical techniques for AC determination.

In this work, 3 chiroptical techniques are combined to determine the AC of 5-(3-bromophenyl)-4-hydroxy-5-methylhexan-2-one (**1**), and their performance will be evaluated. It is well known that the combination of these methods provides a more confident assignment of the AC of a molecule.[26,137,145] Compound **1** was synthesized from 3-bromophenylacetonitrile, whereby the key asymmetric step is a proline-catalyzed directed aldol reaction. This reaction type is often used as a stereoselective step in the synthesis of natural products and their precursors.[156–167] As it is often difficult to determine the AC without further laborious derivatization after the aldol reaction, these techniques can prove to be very useful. Hence, compound **1** was found to be an excellent test case for the comparison of different methods to establish the absolute

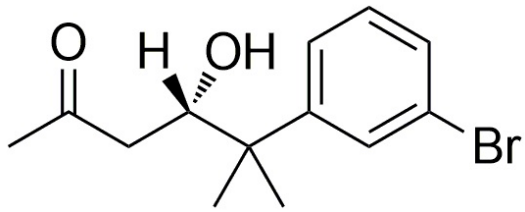

Figure 6.1: (S)-5-(3-bromophenyl)-4-hydroxy-5-methylhexan-2-one (**1**)

configuration.

6.2 Experimental Section

6.2.1 Synthesis

Synthesis of 2-(3-Bromophenyl)-2-methylpropanenitrile (**3**).[168] To a stirring solution of 3'-bromophenylacetonitrile (**2**) (22.15 g, 113 mmol) in dry THF (330 ml) at -40 °C was added KOt-Bu (27.90 g, 249 mmol) and the mixture was stirred for 8 min. After dropwise addition of MeI (17.6 ml, 283 mmol) the cooling bath was removed and the reaction was stirred at room temperature. TLC analysis (after micro-extraction with 1 M HCl/Et2O; eluent: pentane/diethyl ether 9/1) indicated completion of the reaction after 2.5 h. A 1 M HCl solution (50 ml) was added to the pink suspension and the yellow mixture was poured into H_2O (150 ml), followed by extraction (3 x 200 ml EtOAc). The combined organic fractions were washed with saturated $NaHCO_3$/brine 2/1 (300 ml), dried over anhydrous $MgSO_4$ and concentrated in vacuo. The resulting brown oil was filtered over a silica plug (pentane/diethyl ether 8/2). After evaporation in vacuo, the filtration procedure was repeated to give 3 as a clear, yellow oil (24.80 g, 98%): ^{1}H NMR (300 MHz, acetone-d6) $\delta = 7.71$ (s, 1H), 7.58-7.52 (m (app. t), 2H), 7.41-7.36 (m, 1H), 1.74 (s, 6H); ^{13}C NMR (75 MHz, acetone-d6) $\delta =$ 145.5, 131.8, 131.7, 129.1, 125.2, 124.7, 123.3, 37.9, 29.0; IR (HATR) 3066 (w), 2982, 2937, 2875 (w), 2237, 1594, 1566, 1476, 1418, 1392, 1369, 1274 (w), 1239, 1198, 1176 (w), 1114, 1091, 1074, 997, 934, 879, 847, 784 (s), 722, 692 (s), 657 cm^{-1}; MS (EI) 226 (5), 225 (M+., 47), 224 (6), 223 (M+., 46), 211 (12), 210 (100), 209 (12), 208 (98), 183 (7), 181 (9), 144 (9), 130 (9), 129 (78), 128 (18), 115 (10), 103 (7), 102 (21), 101 (12), 77 (11), 76 (11), 75 (12), 74 (5), 51 (9), 50 (7).

2-(3-Bromophenyl)-2-methylpropanal (**4**).[169] To a stirring solution of **3** (24.50 g,

109 mmol) in THF (175 ml) at 50°C was added DIBAL-H (1.5 M in toluene, 87.5 ml, 137 mmol) dropwise over 1 h. After the addition was completed, the mixture was stirred for 2 h at the same temperature. A solution of HCl (6 M, 330 ml) was added, the cooling bath was removed and the reaction mixture was stirred for 1 h. The mixture was poured into H_2O (165 ml) and the phases were separated. The water phase was extracted (5 x 330 ml CH_2Cl_2) and the combined organic fractions were washed with saturated $NaHCO_3$/brine 1/1 (300 ml), dried over anhydrous $MgSO_4$ and concentrated in vacuo. Flash chromatography (pentane/diethyl ether 85/15) provided **4** as a clear, colorless oil (23.68 g, 95%): ^{1}H NMR (300 MHz, acetone-d6) $\delta = 9.54$ (s, 1H), 7.50-7.47 (m, 2H), 7.39-7.32 (m, 2H), 1.46 (s, 6H); ^{13}C NMR (75 MHz, acetone-d6) $\delta = 202.3$, 145.5, 131.5, 131.01, 130.6, 126.8, 123.4, 51.0, 22.8; IR (HATR) 3440 (w), 3065 (w), 2973, 2932, 2874 (w), 2807, 2705, 1723 (s), 1592, 1564, 1477, 1409, 1394, 1365, 1305 (w), 1240, 1175 (w), 1113 (w), 1092, 1074, 996, 947 (w), 911, 879, 845, 783, 760, 694 (s), 670 cm^{-1}; MS (EI) 229 (1), 228 (M+., 8), 227 (1), 226 (M+., 8), 200 (13), 199 (100), 198 (12), 197 (90), 171 (33), 169 (33), 119 (5), 118 (31), 117 (19), 115 (10), 103 (7), 102 (8), 91 (7), 77 (8),41 (6).

4(*S*)-5-(3-Bromophenyl)-4-hydroxy-5-methyl-2-hexanone (**1**). To a suspension of **4** (20.44 g, 90 mmol) and D-proline (2.07 g, 18 mmol) in DMSO (18 ml, purissima, dried over molecular sieves) was added acetone (162 ml, HPLC grade) and the mixture was stirred at ambient temperature for 12 days. The mixture was filtered over a silica plug (eluent: diethyl ether). After in vacuo evaporation, flash chromatography (CH_2Cl_2/acetone 97/3) provided 1 as a clear oil (24.60 g, 96%, 97% ee): $[\alpha]_D$ -22.1 (c 1.47, $CHCl_3$); $[\alpha]_{365}$ -54.4 (c 1.47, $CHCl_3$); ^{1}H NMR (300 MHz, benzene-d6) $\delta =$ 7.60 (app. t, J = 1.9 Hz, 1H), 7.22 (d, J = 7.9 Hz, 1H), 7.08 (d, J = 7.9 Hz, 1H), 6.80 (app. t, J = 7.9 Hz, 1H), 3.99-3.95 (m, 1H), 3.09-3.01 (m, 1H), 1.96-1.78 (m, 2H), 1.37 (s, 3H), 1.12 (s, 3H), 1.11 (s, 3H); ^{13}C NMR (75 MHz, benzene-d6) $\delta =$ 208.7, 150.0, 130.3, 130.0, 129.5, 125.8, 123.0, 74.5, 45.0, 41.9, 30.1, 26.0, 22.7; IR (HATR) 3471 (broad), 3061 (w), 2969, 2359, 2333 (w), 1708 (s), 1592, 1564, 1473, 1412, 1361, 1289, 1238, 198, 1167, 1110, 1095, 1067, 994, 967, 792 cm^{-1}; MS (EI) 228 (12), 226 (12), 200 (12), 199 (100), 198 (12), 197 (94), 171 (32), 169 (31), 118 (26), 117 (17), 115 (9), 103 (6), 102 (8), 91 (7), 77 (8), 41 (9); HRMS (ESI) m/z [M + H]$^+$ for $C_{13}H_{17}{}^{79}BrO_2$ calcd 285.0485, found 285.0492.

For the determination of the enantiomeric excess, **1** was converted to the (*R*)-Mosher ester. LC-MS analysis of the latter on a Luna C18(**2**) column with a gradient of 40 to 100% acetonitrile in water in 1 h showed 2 diastereomers with a retention

time of 42.7 min (disfavored product, 1.3 %) and 43.2 min (favored product, 98.7 %).

6.2.2 Computational Details

Conformational analysis was performed on the molecular mechanics level with the MMFF, MMFF94S[121,122,170,171] and MM3[172] force fields. Spartan '08[124] and Conflex[125–127] software packages were used to perform a stochastic and reservoir filling search respectively. A total of 34 different conformers were found and these were further optimized using Density Functional Theory (DFT) calculations, combining the B3LYP functional with the 6-311G* basis set as implemented in the Gaussian 09[64] package. This yielded 19 unique conformers. Their relative Boltzmann weights were calculated using the Gibbs free energies, at 298.15 K. In each step, redundant conformers were detected using the eigenvalues of the internuclear distance matrix of the conformers.

For the VCD- and IR-spectrum, the harmonic frequencies of these optimized structures were calculated and the dipole and rotational strengths determined. The scale factor to compensate for the overestimation of the harmonic frequencies[136] was determined using the CompareVOA[1] program. All calculated spectra are shown with a Lorentzian broadening FWHM of 10 cm^{-1}, unless mentioned otherwise. For the ten most stable conformers, an optimization and VCD-calculation was performed using the 6-311+G*, cc-pVDZ and aug-cc-pVDZ basis sets using the same functional. Also, for each basis set a calculation using a polarizable continuum model (PCM) with a dielectric constant for chloroform of ϵ=4.71 was carried out. In all calculations the Gaussian 09 default integral equation formalism variant of PCM (IEFPCM) was used.[131] Optical rotatory dispersion was calculated at 5 wavelengths (589, 578, 546, 436 and 365 nm) using the same functional and the 6-311G* basis set, with a PCM solvent approach.[54,173] Finally, ECD calculations were carried out using TDDFT calculations (taking into account 20 excited states) with the CAM-B3LYP functional and the 6-311+G* basis, on the previously optimized geometries.[174] The CAM-B3LYP functional has been shown to give better results than B3LYP for properties for which the long-range exchange interaction is of importance, such as excitations in TDDFT.[135,175] Here, we also repeated the calculation using a PCM approach for the 2,2,2-trifluoroethanol (TFE) solvent (ϵ=26.726), since this is shown to have an important influence on the ECD calculation.[135]

For the IR and VCD spectra the line spectra of these conformers were Lorentzian

broadened using a full width at half maximum (FWHM) of 10 cm^{-1}, based on the visual resemblance with the experiment. The Boltzmann population weight was determined by Gibbs free energy. The final calculated spectrum is the Boltzmann population weighted sum of these 19 individual spectra. For the ECD spectrum, a Gaussian broadening was applied with a half bandwidth at 1/e peak height of 20 nm.[132]

6.2.3 Experimental Details

For the VCD measurements, 10.9 mg of **1** was dissolved in $CDCl_3$ (99.98%, Aldrich) for a total of 500 μL solution. The spectrum for solvent and sample were recorded separately for 5h in a detachable cell with BaF_2 windows and a 100 μm path in a BioTools ChiralIR2X VCD spectrometer. The PEMs were optimized at 1400 cm^{-1} and the resolution was 4 cm^{-1}. The VCD spectra shown have the pure solvent spectrum subtracted from the sample spectrum, since only one enantiomer was available and hence no spectrum from a racemic mixture could be used. The ORD was recorded at 5 different wavelengths (589, 578, 546, 436 and 365 nm) using a Perkin-Elmer 241MC polarimeter, at 25°C. The solvent of choice was $CHCl_3$. Finally, ECD measurements were performed using a Chirascan-Plus ECD spectrometer (Applied Photophysics). A series of concentrations in TFE, in combination with a 500 μm path length, was used, ranging from 0.19M (which has the highest S/N but lowest range) to 0.00003M (which has the lowest S/N but largest range). UV absorbance and ECD were recorded simultaneously.

6.3 Results and Discussion

6.3.1 Synthesis

(*S*)-5-(3-Bromophenyl)-4-hydroxy-5-methylhexan-2-one (**1**) is obtained from 3-bromophenylacetonitrile (**2**) according to the following scheme:

6.3.2 Conformational Analysis

Conformational analysis using the three different force fields yielded a total of 34 different conformers. These conformers were then further optimized at the B3LYP/6-311G* level of theory, giving a total of 19 conformers. Of these 19 conformers, a total of 9 conformers were in the range of 3 kcal/mole of the most stable one. The rest

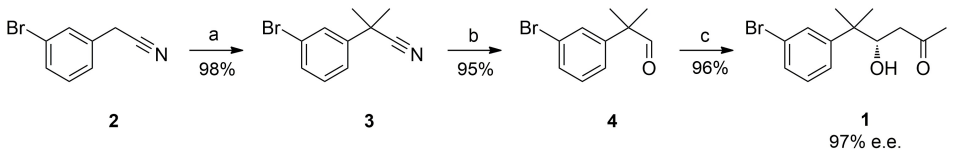

Scheme 6.1: Synthesis of **1**. For more information on the synthesis we refer to the experimental section. a) i) KOt-Bu, THF, -40C, 8 min; ii) MeI, -40C rt, 2.5 h ; b) i) DIBAL-H, toluene, -50C, 3 h; ii) 6M HCl, -50C rt, 1 h; c) D-Proline, acetone / DMSO, rt, 12 days

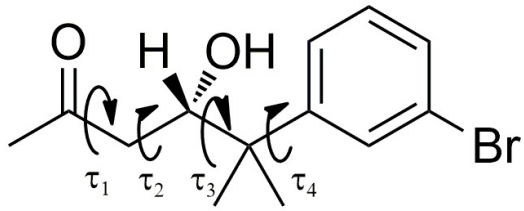

Figure 6.2: Descriptive dihedral angles in the conformational analysis of **1**.

of the conformers, contributing less than 0.2% in the Boltzmann distribution, will be ignored in the rest of this work. The four most important conformational variables are shown in figure 6.2.

For the most stable conformers, the carbonyl functional group is nearly coplanar with the α and β carbon atoms. This allows for a rather strong intramolecular hydrogen bond (bond lengths 1.99 - 2.03 Å), explaining the stability of these conformers (**1**a–**1**g) over others (**1**h–**1**i) (table 6.1). Also, repulsion between the alcohol oxygen lone pairs and the π-cloud of the aromatic ring makes conformers **1d–1g** significantly less stable than **1a–1c**. Boltzmann weights of all conformers are given in table 6.2. Since it is well established that the conformational distribution has a significant influence on the calculated IR and VCD-spectrum,[176–179] the Boltzmann weights were also calculated using three additional basis sets. Although differences in energetic ordering of the conformers occur, for each basis set the main contributors are conformers **1a–c**.

6.3.3 IR and VCD Spectra

IR and VCD spectra were obtained as explained in the experimental section. As it was found that the B3LYP/6-311G* calculations most accurately reproduce all features in

	τ_1	τ_2	τ_3	τ_4
1a	-13.1	62.2	-176.8	-119.8
1b	-15.3	61.3	71	118.4
1c	-14.7	61.3	71.5	-60.1
1d	-12.5	60.9	-64.4	-98.1
1e	-12.5	61.8	-62.6	-72.4
1f	-11.8	62.6	-62.6	110.9
1g	-11.2	61	-64.3	81.1
1h	67.1	66.6	-59.2	111.5
1i	69.8	65.6	-58.8	-69.4

Table 6.1: Values for the dihedral angles (B3LYP/6-311G*) shown in figure 6.2 for the conformers shown in figure 6.3.

	Boltzmann weight(%)			
	6-311+G*	**6-311G***	**aug-cc-pVDZ**	**cc-pVDZ**
1a	47.3	50.2	55.5	25.6
1b	21.8	29.9	19.7	25.6
1c	16.8	13.8	15.2	33.2
1d	2.8	2.3	5.4	3.2
1e	2.8	N/A	N/A	1.9
1f	2.8	1.0	N/A	7.0
1g	2.1	1.3	4.2	1.9
1h	2.1	0.8	0.0	1.2
1i	1.6	0.6	0.0	0.3

N/A means that no minimum energy structure could be located for that conformation or that the conformation converged to another structure for the basis set mentioned.

Table 6.2: Boltzmann weights (%) for the conformers using different basis sets. Although there are important differences in the calculated Boltzmann weights, conformers **1a**, **1b** and **1c** are by far the most abundant for all methods.

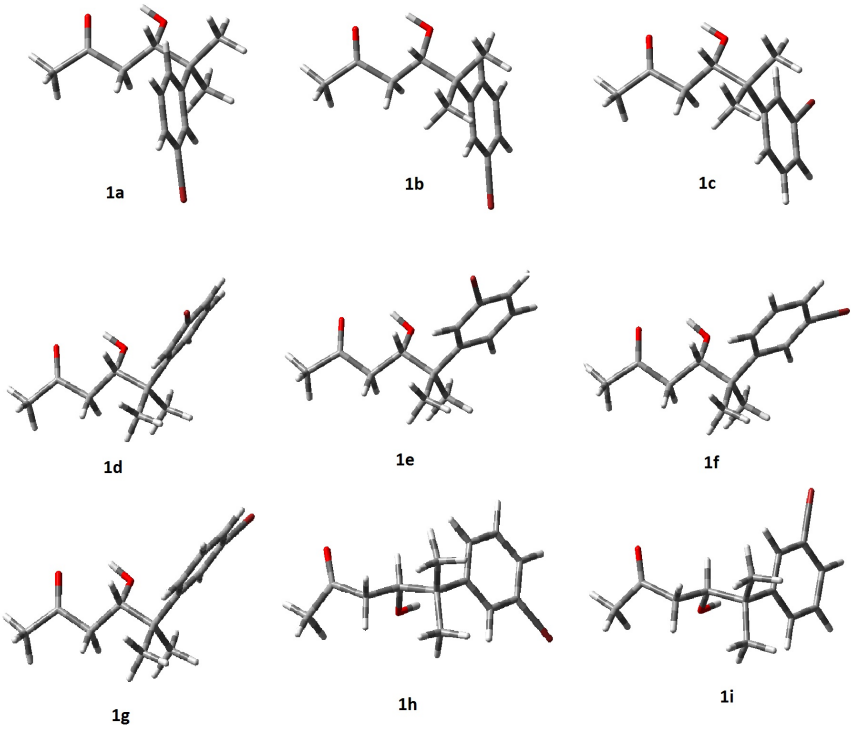

Figure 6.3: The nine most stable conformers of **1**. Conformers **1a**-**1g** are stabilized by an internal H-bond, which is reflected in the corresponding Boltzmann weights. Conformers with the aromatic ring pointing away from the alcoholic oxygen are the most stable.

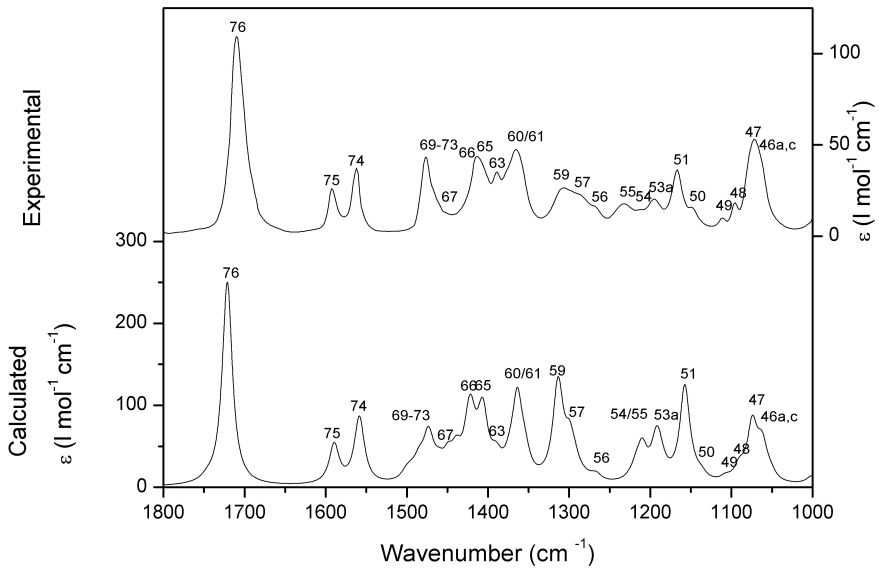

Figure 6.4: Experimental (upper) and calculated (lower, B3LYP/6-311G*) IR-spectrum for **1**. Normal mode numbering is arbitrary.

the experimental spectra (vide infra), only those results are discussed in detail here and the reader is referred to the supplementary information for other spectra. The IR and VCD calculations using the PCM solvent model[131] give almost identical spectra as the gas-phase calculations for all levels of theory, so only B3LYP/6-311G*/PCM will be shown. For the calculated spectra, a global scaling factor of 0.971 was used to compensate for the overestimation of vibrational frequencies in the harmonic approximation. This scaling factor was obtained through maximizing the IR similarity using the CompareVOA[1] algorithm, and is in agreement with values found in literature.[180] A visual band to band correlation was performed by assigning, where possible, a normal mode to each band. As can be seen in figures 6.4 and 6.5, agreement is very good and allows for a reliable AC determination.

For the IR, the only shortcomings are the overestimation of the intensity of normal modes 53-55 and 57-59. Other than that, all peaks are reproduced fairly well and allow for a precise band to band correlation between the IR and VCD spectra.

For the VCD spectra, we again have good agreement, although some important

features are not correctly reproduced. First, we see a sign flip for the carbonyl stretch, normal mode 76. As it is often the case that peaks involving a carbonyl group are unreliable, little consequence is given to this, especially since this normal mode has a low anisotropy value for the three most stable conformers (41, 8 and 26 ppm respectively). This causes the sign of the rotational strength of this normal mode to be unreliable or 'non-robust'.[2,119,133] Next, a couple of normal modes have a heavily underestimated intensity, although the sign is calculated correctly (68a/69c, 63b,c , 60a/61). Finally, the important pattern between 1100 cm^{-1} and 1160 cm^{-1} is not adequately reproduced. Moreover, this feature is not adequately reproduced in any of the other levels of theory. As can be seen in figure 6.7, none of these calculations were able to reproduce the signal. Also, the pattern does not show up in any of the important conformers, ruling out the possibility of the bands being averaged out due to conformational flexibility and the use of approximate Boltzmann weights (figure 6.6). However, the solid agreement between the other regions of the spectrum allows for an unambiguous determination of the AC as (*S*)-(-)-5-(3-bromophenyl)-4-hydroxy-5-methylhexan-2-one.

The spectra of the three most abundant conformers allow us to assess the conformational distribution. The pattern at 1200 cm^{-1} (normal modes 54/55) clearly suggests that conformer **1**a is the most stable conformer, whereas the distinct negative signal at 1300 cm^{-1} (normal mode 57) indicates that also conformers **1b** and/or **1c** are of importance, albeit to a lesser extent than **1a**.

As mentioned above, it was found that the B3LYP/6-311G* combination gives the spectra most similar to the experimental ones. Figure 6.7 shows the spectra obtained at the different levels of theory versus the experimental spectrum. All methods show a very satisfactory similarity to experiment, although not all basis sets are able to correctly reproduce the signal at 1200 cm^{-1}. A CompareVOA[1] analysis was performed for a subset of levels of theory. Here, the default triangular weighting function of broadness l=20 cm^{-1} was applied to the experimental spectrum, and the theoretical spectrum was obtained using a standard Lorentzian broadening of 10 cm^{-1} FWHM. The range 1000-1500 cm^{-1} was considered, since in this case this region is the most information-rich and has the highest signal-to-noise (S/N) ratio. The results are shown in table 6.3. While the visual resemblance between theory and experiment is excellent, the results below are rather disappointing, although they clearly confirm the manual assignment.

Close inspection of the spectra in figures 6.4 and 6.5 reveals that the alignment of the scaled simulated spectrum and its experimental counterpart is nearly perfect. This

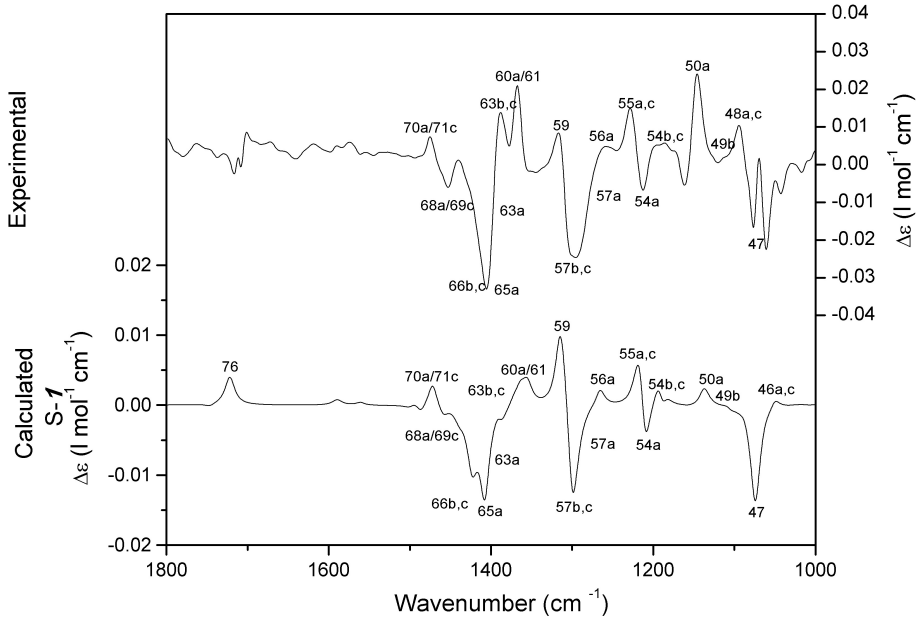

Figure 6.5: Experimental (upper) and calculated (lower, B3LYP/6-311G*) VCD-spectrum for **1**. Normal mode numbering is arbitrary. Only the carbonyl stretch mode has opposite sign. The intensities of modes 68a/69c, 63b,c and 60a/61 are severely underestimated, and the pattern near 1150 cm^{-1} is not reproduced accurately.

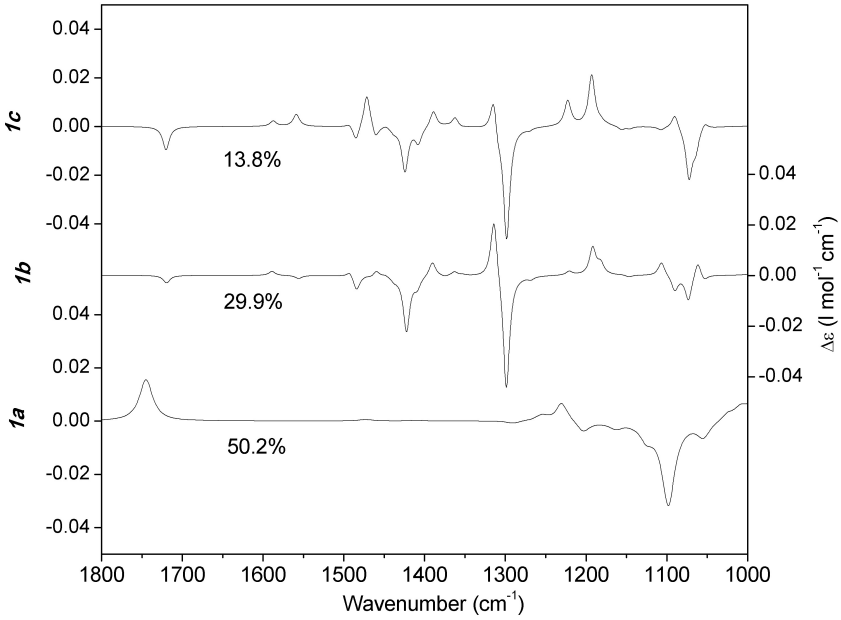

Figure 6.6: Calculated VCD-spectra for the three most abundant conformers at the B3LYP/6-311G* level.

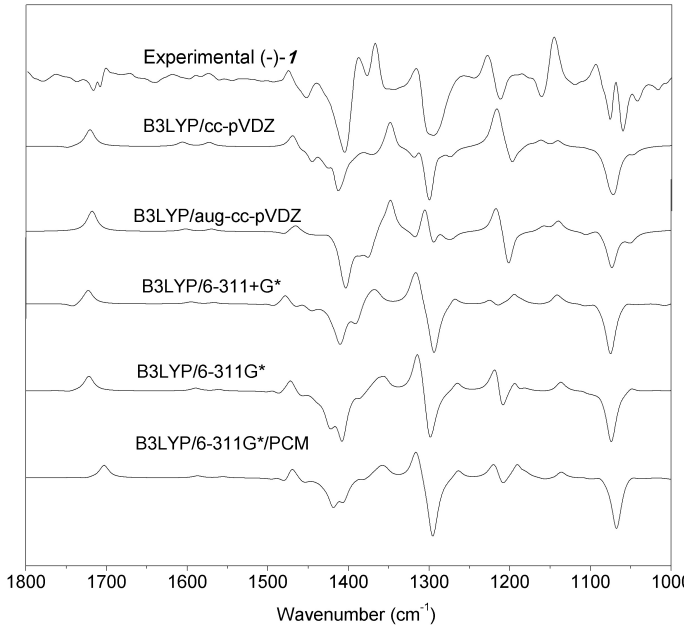

Figure 6.7: Calculated VCD spectra for a subset of the methods of calculation. A Lorentzian broadening with a FWHM of 15cm^{-1} is used.

Basis set	Optimized scale factor (%)	IR similarity (%)	Σ(%)	Δ (%)	Confidence Level (%)
aug-cc-pVDZ	0.983	90.0	63.8	44.5	83
6-311+G*	0.975	91.1	69.3	57.2	96
6-311G*	0.971	88.4	68.8	57.8	96
cc-pVDZ	0.98	85.5	67.2	53.4	91
6-311G*/PCM	0.973	88.7	68.4	61.7	98

Table 6.3: CompareVOA results using the default value for weighting function broadness of l=20 cm^{-1} and Lorentzian broadening FWHM of 10 cm^{-1}. The results clearly confirm the assignment of *S*-**1**, but not as convincingly as one would expect from the visual resemblance.

means that application of the triangular weighting function in CompareVOA, designed to allow for local shifts between theory and experiment, is less relevant. In this case, it may increase the Σ value of the incorrect enantiomer (generating overlap where there is none), yielding lower Δ values. This can be seen in figure 6.8, where we show a contour plot of the Δ value versus the Lorentzian broadening FWHM (abscissa) and the broadness l of the triangular weighting function w (ordinate).

Here, we see that the largest Δ value, thus the largest discriminative power, is achieved using a lower triangular weighing width, and a larger FWHM value. The effect of the triangular weighting width l exists because there is a very good frequency alignment in this case. For the correct enantiomer, this smaller weighting function reduces the Σ value to a lesser extent than it will for the incorrect enantiomer, resulting in a larger discriminative power (Δ). We also see that the largest Δ values are obtained using a high FWHM of over 20 cm^{-1}. In cases like this, where similarity between both spectra is good, this large FWHM value has the same effect as weighing the theoretical spectrum with a triangular weighting function, in addition to the usual Lorentzian broadening. Weighing only one of two nearly identical spectra will induce a smaller similarity between both. The problem arising from weighing only one of the spectra is currently being addressed in a modified CompareVOA algorithm. We therefore propose that, in case a nearly perfect alignment with respect to normal mode frequencies is observed between experimental and calculated spectrum, a smaller triangular weighting function is chosen when using the CompareVOA program. In this case we found l=10 cm^{-1} to be more appropriate than the default value of l=20 cm^{-1}. The corresponding CompareVOA results are shown below in table 6.4.

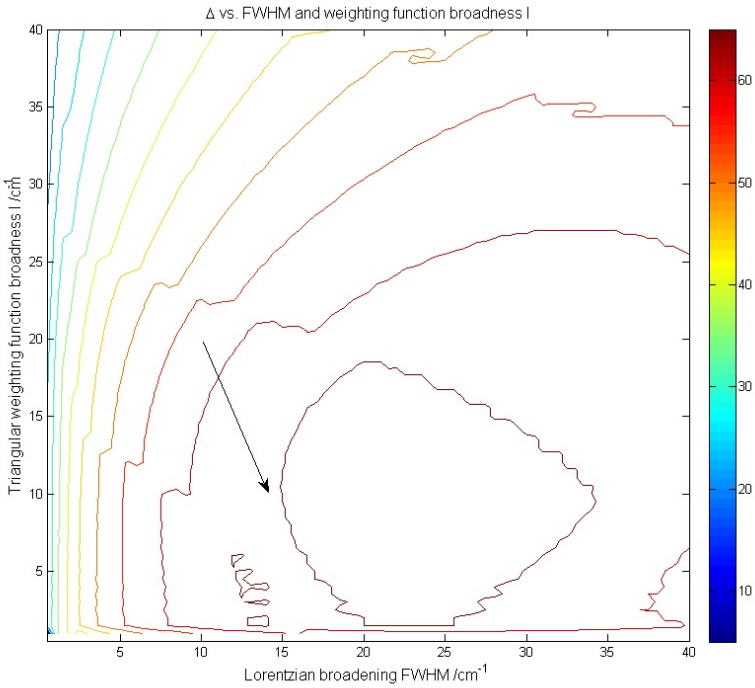

Figure 6.8: Contour plot of Δ values (cf. eq. 4.6) with respect to Lorentzian broadening FWHM on the horizontal axis and triangular weighting function broadness l (cf. Chapter 4) on the vertical axis. The highest discriminative power is found for very large FWHM values (over 20 cm^{-1}) and l values lower than the default value of 20 cm^{-1}. The arrow shows the change from default parameters to the situation in table 6.4.

We see a very significant increase in Δ value of about 10% for all basis sets when using these new parameters, and thus a much more reliable assignment. The aug-cc-pVDZ basis sets performs significantly worse than the other basis sets. This is due to the poor reproduction of bands 57-59 in the VCD by the former basis set. Here too, almost no difference between gas-phase and PCM calculations was found.

6.3.4 ORD Analysis

Since ORD is a readily available experimental technique in most laboratories, ORD calculations using TDDFT as mentioned in the methods section were performed to test its potency in assigning the AC. Results of the experiment and calculations are

Basis set	Optimized scale factor (%)	IR similarity (%)	Σ (%)	Δ (%)	Confidence Level (%)
aug-cc-pVDZ	0.984	90.7	68.2	53.4	92
6-311+G*	0.975	94.8	75.7	66.7	99
6-311G*	0.972	88.5	76.7	69.8	99
cc-pVDZ	0.981	85.4	75.2	63.3	99
6-311G*/PCM	0.973	92.1	75.8	72.5	99

Table 6.4: CompareVOA values using l=10 cm^{-1} and FWHM=15 cm^{-1} instead of the default value of 20 cm^{-1} and FWHM=10 cm^{-1}(table 6.3).

shown in figure 6.9. Although the calculations overestimate the increase in rotation with lowering wavelength, the results indeed confirm the conclusion that the AC is (S)-(-)-5-(3-bromophenyl)-4-hydroxy-5-methylhexan-2-one.

6.3.5 ECD

Results of ECD are shown in figure 6.10. Theoretical calculations were performed as described in the experimental section, both with and without PCM modelling of the solvent (2,2,2-trifluoroethanol, ϵ=26.726). To obtain optimal agreement between experiment and theory, the calculated ECD spectra were blue shifted with 20 nm. Only one distinct band is present, and is correctly reproduced by the calculations. The calculations also suggest a small negative signal at about 220 nm, but this cannot be seen in the experiment. However, the dominant feature is correctly predicted, thus ECD analysis again confirms the results obtained with the other techniques. We also note a limited difference between the gas-phase and PCM calculations.

6.4 Conclusion

In this work, we have characterized the stereochemistry of 5-(3-bromophenyl)-4-hydroxy-5-methylhexan-2-one (**1**), a building block obtained via a proline-catalyzed asymmetric aldol reaction, the latter being a widespread used key reaction in the stereoselective synthesis of natural product precursors. To do this, we have investigated the conformational distribution and confirmed this using the VCD results. A total of three chiroptical techniques were combined to provide an unambiguous determination of the AC as *S*-(-)-**1**. This conclusion was reached independently by all 3 methods, giving us

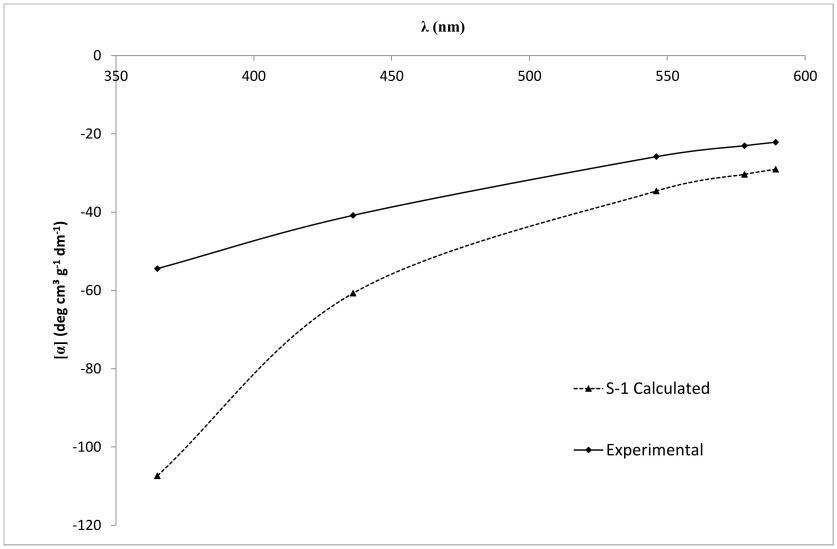

Figure 6.9: ORD calculations (B3LYP/6-311G*/PCM) show reasonable agreement with the experiment, confirming the results of the VCD analysis that (-)-**1** corresponds to S-**1**.

a very high confidence in the assignment. Furthermore, we investigated the influence of the broadness of the triangular weighting function and the Lorentzian broadening of the calculated spectrum on the CompareVOA analysis. In cases where the frequency alignment between theory and experiment is nearly perfect, we suggest that a smaller weighting function is used of 10 cm^{-1}, since this significantly improves the discriminative power between the two enantiomers.

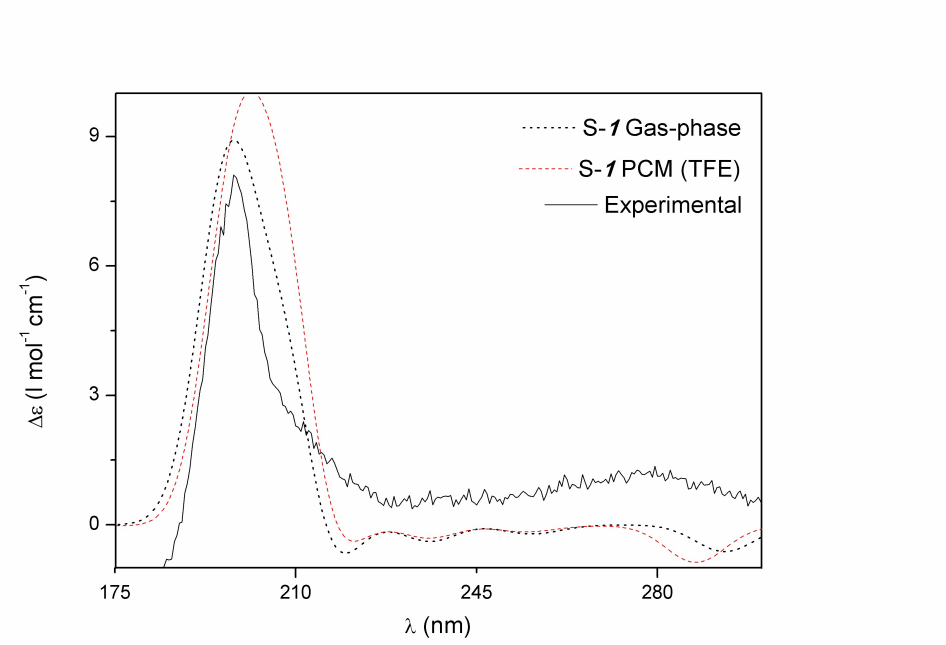

Figure 6.10: ECD spectra for **1**. The gas-phase calculated(CAM-B3LYP/6-311+G*) spectrum (dotted,black) and the PCM (TFE) spectrum (dashed,red) are nearly identical, and give good agreement with the experiment (solid). This again confirms the previous conclusion. The observed spectrum shown was measured as the lowest (0.00003M) of a concentration series in order to obtain the largest possible wavelength range.

Chapter 7

The Stereochemistry of the Tadalafil Diastereoisomers: a Critical Assessment of Vibrational Circular Dichroism (VCD), Electronic Circular Dichroism (ECD) and Optical Rotatory Dispersion (ORD)

7.1 Introduction

Many top-selling drugs contain chiral molecules as active pharmaceutical ingredients.[181] Regulatory agencies such as the American Food and Drug Administration (FDA) have issued a general policy, stating among others that specifications for a final product should include identity, strength, quality and purity from a stereochem-

ical viewpoint,[19] and for new pharmaceutical compounds, stereoisomers should be separately assessed for their therapeutic and side effects. Not only is the need for understanding chiral structure and function driven by legislative bodies but also by the fundamental need for understanding the role chirality plays in chemical processes and biological systems. To meet both needs, a reliable and streamlined approach for absolute configuration (AC) determinations of chiral molecules is of prime importance. Although X-ray diffraction (XRD),[20,182] NMR methods[183,184] and chemical correlation via synthesis[185] have been developed over past years to address this problem, these methods often require a rather significant amount of effort and resource.

Suitable spectroscopic methods for establishing the stereochemistry of compounds, preferably directly in solution, are clearly needed. Chiroptical spectroscopy[23] is the collection of spectroscopic techniques that allow distinguishing stereoisomers by their different response to electromagnetic radiation of different handedness. Unfortunately, these spectroscopic methods lead to experimental spectra that are not easily interpretable. Thanks to the development of algorithms for theoretical calculation of the spectra,[56,186–190] chiroptical spectroscopy has grown tremendously and nowadays, parallel to the experimental measurement of spectra, theoretical predictions are made for the spectrum of each configuration such that by comparing the set of theoretical spectra and the experimental ones, one can assign the AC. Another prime contributor to the growth of the field is the advances made in state of the art instrumentation.[72,73,191,192] Chiroptical spectroscopy for determining AC's mainly includes vibrational circular dichroism (VCD),[193] Raman optical activity (ROA),[29] electronic circular dichroism (ECD)[194] and optical rotatory dispersion (ORD).[54] VCD and ROA are collectively known as vibrational optical activity (VOA)[10] relying on vibrational transitions, while ECD and ORD rely on electronic transitions.

Generally, in case of molecules with multiple stereogenic elements (diastereoisomers), knowledge of the relative stereochemistry typically comes from NMR spectra or XRC data. IR spectroscopy itself can in some cases also be used to determine the relative stereochemistry,[195] and the combination of VCD with IR appears promising in assigning the stereochemistry if the spectra are analyzed in detail. The number of applications of VCD for the determination of the AC of diastereoisomers increases every year but in most cases the relative stereochemistry is already known. In the present study, the AC of all stereoisomers of tadalafil is established from VCD.

Tadalafil is a cGMP specific phosphodiesterase type 5 (PDE5) inhibitor similar to sildenafil and vardenafil,[196] and has enhanced PDE5/PDE1 and PDE5/PDE6 se-

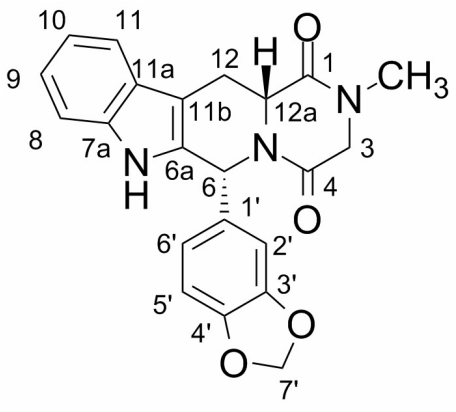

Figure 7.1: Structure of tadalafil and atom numbering. Tadalafil has two chiral centers: C6 and C12a, and thus 4 diastereoisomers, i.e. (6*R*, 12a*R*) (shown in figure), (6*S*, 12a*S*), (6*S*, 12a*R*) and (6*R*, 12a*S*).

lectivity compared to sildenafil.[197] The FDA approved tadalafil for the treatment of erectile dysfunction, pulmonary arterial hypertension and benign prostatic hyperplasia.[198] Tadalafil contains two chiral centers at C6 and C12a, thus giving rise to four stereoisomers in total ((6*R*, 12a*R*), (6*S*, 12a*S*), (6*S*, 12a*R*) and (6*R*, 12a*S*), see the structure in figure 7.1). The purpose of the present paper is to investigate if VCD itself allows for the determination of the AC of tadalafil without prior knowledge on their relative stereochemistry. Using all four diastereoisomers, experimental and theoretical spectra were obtained. Although the absolute configuration was known for each diastereoisomer, the study proceeds as if the AC was unknown for the different samples. The knowledge of the AC is only used afterwards to establish whether or not VCD does suffice for a complete AC assignment of all 4 samples. Besides VCD, IR and NMR spectra are also used to determine the relative stereochemistry. ECD and ORD spectroscopy, as possible alternative chiral spectroscopies to VCD, are also used to investigate the complementarity of the three chiroptical techniques.

7.2 Experimental Section

7.2.1 Experimental Details

The four diastereoisomers of tadalafil were received from RK TECH, Hungary with purity 99.8 % and were used without further purification. (6*R*, 12a*R*)-tadalafil is

the active ingredient of Cialis® and Adcirca®. The crystal structure of (6*R*, 12a*R*)-tadalafil has been reported,[197] and was deposited (refcode: IQUMAI) in the Cambridge Structural Database (CSD). The structures of (6*R*, 12a*R*)-tadalafil cocrystallized with methylparaben, propylparaben and hydrocinnamic acid have been deposited with the refcodes as LASZUC, LATBAL and LATBEP, respectively, in the CSD.

NMR Spectroscopy ^{1}H, ^{13}C, COSY, NOESY and HMQC were recorded at 400 MHz (^{1}H) and 100 MHz (^{13}C) using $CDCl_3$ as solvent and tetramethylsilane (TMS) as internal standard.

(6*R*, 12a*R*)-I (and (6*S*, 12a*S*)-II, using sample-AC correspondence based on X-ray data and VCD assignment). ^{1}H NMR ($CDCl_3$) δ 7.81 (s, 1H), 7.60 (dd, 1H, J=6.8, 1.6 Hz), 7.28-7.12 (m, 3H), 6.85 (dd, 1H, J=8.4, 2.0 Hz), 6.73 (d, 1H, J=1.6 Hz), 6.69 (d, 1H, J=8.0 Hz), 6.15 (s, 1H, C6-H), 5.88 (d, 1H, J=1.6 Hz, C7'-H), 5.85 (d, 1H, J=1.6 Hz, C7'-H), 4.31 (dd, 1H, J=11.6, 4.4 Hz, C12a-H), 4.10 (dd, 1H, J=17.6, 1.6Hz, C3-H), 3.94 (d, 1H, J=17.6 Hz, C3-H), 3.78 (dd, 1H, J=16.0, 4.4 Hz, C12-H), 3.21 (ddd, 1H, J=16.0, 11.6, 1.2Hz, C12-H), 3.04 (s, 3H); ^{13}C NMR ($CDCl_3$) δ 166.8, 166.4, 147.9, 147.1, 136.6, 135.4, 132.8, 126.2, 122.5, 120.7, 120.1, 118.6, 111.2, 108.2, 107.5, 106.6, 101.2, 56.7, 56.2, 52.1, 33.6, 23.9.

(6*S*, 12a*R*)-III (and (6*R*, 12a*S*)-IV, using sample-AC correspondence based on X-ray data and VCD assignment). ^{1}H NMR ($CDCl_3$) δ 7.94 (s, 1H), 7.53 (d, 1H, J=8 Hz), 7.31 (d, 1H, J=8 Hz), 7.26-7.13 (m, 2H), 6.97 (d, 1H, J=0.8 Hz, C6-H), 6.81 (s, 1H), 6.71 (d, 2H, J=1.2 Hz), 5.93 (s, 2H, C7'-H), 4.35 (dd, 1H, J=12.0, 4.4 Hz, C12a-H), 4.13 (dd, 1H, J=17.6, 1.2Hz, C3-H), 3.99 (d, 1H, J=17.6 Hz, C3-H), 3.55 (dd, 1H, J=15.6, 4.4 Hz, C12-H), 2.99 (s, 3H), 2.95 (ddd, 1H, J=16.0, 12.0, 1.2Hz, C12-H); ^{13}C NMR ($CDCl_3$) δ 165.5, 161.6, 148.2, 148.1, 136.4, 132.1, 129.8, 126.3, 122.8, 122.5, 120.1, 118.5, 111.2, 109.2, 109.1, 108.3, 101.4, 52.5, 51.9, 51.5, 33.4, 27.6.

IR and VCD spectroscopy IR and VCD were recorded on a BioTools dual-PEM ChiralIR-2X spectrometer at room temperature. The PEMs were optimized for 1400 cm^{-1} and a resolution of 4 cm^{-1} was used throughout. For all experiments, solutions of 2.0 mg in 0.1 mL of $CDCl_3$ were investigated, using a 100 μm path-length cell equipped with BaF_2 windows. The solution spectra were recorded twice for 20 000 scans. As both enantiomers are available for each enantiomeric pair, baseline corrections were introduced using the spectrum of a virtual racemate.

ECD spectroscopy The experimental spectra were recorded on a Jasco J-710 spectrometer at room temperature. The wavelength studied ranges from 184 to 320 nm. The step size was set to 0.5 nm. A scanning speed of 100 nm/minute was used throughout. During all experiments, solutions in 2,2,2-trifluoroethanol with a concentration of 1.0 mg mL^{-1} were used in combination with a 1 mm optical path liquid cell.

ORD spectroscopy ORD spectra were recorded on a Jasco P-2000 spectrometer equipped with different optical filters optimized for 365, 405, 436, 546, 578, 589 and 633 nm at room temperature. For all experiments, 2, 2, 2-trifluoroethanol was used as a solvent, in combination with a 50 mm pathlength cell at room temperature. The concentrations used were 6.0 mg /mL for I and II, and 1.0 mg / mL for III and IV.

7.2.2 Computational Details

As most properties are shared between enantiomers and given the simple mirror image relationship between the geometries and chiroptical spectra of enantiomers, it suffices to compute only one representative of each enantiomeric pair. The geometry of the other enantiomer and its chiroptical properties are then easily obtained as the mirror images. In this work, geometry optimizations and spectral properties were calculated for the (6*R*, 12a*R*) and (6*S*, 12a*R*) stereoisomers. In order to obtain good starting points for ab initio geometry optimizations for the minima on the potential energy surface, extensive conformational searching was first performed at the molecular mechanics level using the MMFF94,[121] Sybyl[123] and MMFF94S[122] molecular mechanics force fields, as implemented in the Spartan 08[124] and the Conflex[125–127] software packages using respectively the Monte Carlo and 'reservoir filling' algorithms. The reason for choosing different force fields lies in the fact that different force fields are known to sometimes give significantly different potential energy surfaces and hence may reveal new stationary points on these surfaces.

After this first step, the minima were further optimized at the Density functional theory level using Gaussian 09[64] with functionals and basis sets depending on the type of calculation. For each stationary point, the Hessian was diagonalized to establish that it corresponds to a minimum. Boltzmann populations, required to calculate Boltzmann weighted spectra, were derived from the relative enthalpies of the conformations studied using a temperature of 298 K.

IR and VCD spectra were computed at the B3LYP/6-31G(d), SCRF-B3LYP/6-31G(d), and SCRF-ωB97X-D/6-31G(d) levels of theory, with SCRF[131] referring to the integral equation formalism model used to account for solute-solvent interactions, using a dielectric constant for chloroform of ϵ=4.71. The 6-31G(d) basis set is the minimum recommended basis set for VCD calculations.[10] The B3LYP functional is a commonly used functional for VCD calculations,[193] while the ωB97X-D functional is long-range corrected with dispersion corrections.[199] To allow comparison with experimental data, Lorentzian broadening was applied using a full width at half maximum of 10 cm^{-1}.

NMR shielding constants were computed using two different approaches. The first is based on the use of linear regression data as suggested by Lodewyk et al.[65] This entails geometry optimizations of all conformations of all diastereoisomers at the B3LYP/6-31+G(d,p) level in the gas phase. As all diastereoisomers have several stable conformations, Boltzmann weights were computed albeit using relative enthalpies instead of the relative free energies because entropies are often unreliable. The NMR shielding constants were then computed by the gauge including atomic orbital (GIAO) method at the SCRF-mPW1PW91/6-311+G(2d,p) level using the implicit solvent model (chloroform, ϵ=4.71) and the B3LYP/6-31+G(d,p) geometries (SCRF-mPW1PW91/6-311+G(2d,p)//B3LYP/6-31+G(d,p)). Shielding constants related to the hydrogen atoms in the methyl group were averaged. NMR chemical shifts relative to TMS were obtained applying linear regression parameters, notably for ^{1}H data, the slope and intercept used were set to -1.0936 and 31.8018, respectively, while for the ^{13}C data values of -1.0533 and 186.5242 were used in the formulae given by Lodewyk et al. and the Cheshire database of these authors.[200]

The interest in this approach stems from the fact that the regression also takes into account experimental data. One could, alternatively, also compute these fully ab initio. We thereto optimized all structures at the SCRF-mPW1PW91/6-311+G(2d,p) level (chloroform, ϵ=4.71) for all conformations. NMR shielding constants were then computed using the GIAO method. Shielding constants related to the methyl group were averaged again based on enthalpies. NMR chemical shifts relative to TMS were obtained applying linear regression between computed isotropic shielding constants of both (6*R*, 12a*R*) and (6*S*, 12a*R*) and experimental chemical shifts of both experimental samples I and III. For ^{1}H data, the slope and intercept used were -1.1039 and 32.2560, respectively, while for the ^{13}C data values of -1.0358 and 187.9864 were used. A tight correlation is indicated by the high R^2 values of 0.9970 and 0.9991 for ^{1}H and ^{13}C data, respectively.

ECD and ORD spectra were computed at the SCRF-CAM-B3LYP/cc-pVDZ level using a dielectric constant for 2,2,2-trifluoroethanol of ϵ=26.7 and for geometries optimized at that same level. CAM-B3LYP combines the hybrid qualities of B3LYP and the long-range correction, performing better in describing charge transfer excitations.[175,201] ECD calculations were performed for the first 50 excited electronic states. Rotatory strength values, calculated within the velocity representation, have been used for the ECD spectral simulations. The ECD spectra were obtained using Gaussian broadening[132] with a half-width of $\Delta = 0.3$ eV at 1/e of peak height. Frequency-dependent optical rotations were calculated at 7 wavelengths, i.e. 365, 405, 436, 546, 578, 589 and 633 nm.

7.3 Results and Discussion

First the results of the conformational analysis are presented followed by the results of the use of IR and VCD to assign the absolute configuration, and then NMR is used to confirm the relative stereochemistry. Finally ECD and ORD are used to confirm the absolute configuration.

7.3.1 Conformational Analysis

The molecular mechanics search yielded 8 and 11 conformers for the (6*R*, 12a*R*) and (6*S*, 12a*R*) diastereoisomers, respectively. These geometries were further optimized at the different levels of theory described above for the IR, VCD, NMR, ECD and ORD calculations, respectively. The most abundant conformers are shown in Figure 7.2 and the Boltzmann weights based on relative enthalpies are listed in Table 7.1. The key structural difference among these conformers lies in the rotation of the 1, 3-benzodioxolyl group and puckering of the 3', 4'-OCH_2O ring. It is also worth noting that the Boltzmann weights may change significantly upon changing the level of theory including the (dis)appearance of minima depending on the level of theory. In order to exclude this as artifacts of the conformational searching and to double check the data in Table 7.1, geometries absent for a specific method but present for another, were taken from the latter and used as starting point for optimizations at the former level.

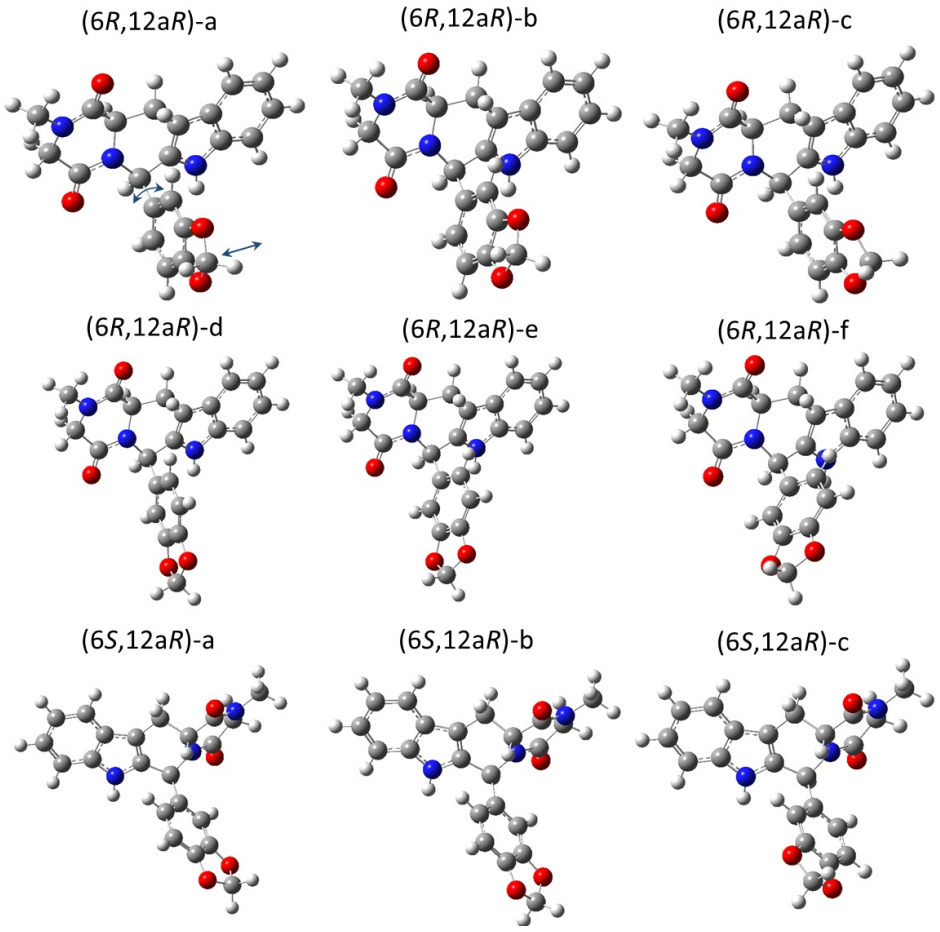

Figure 7.2: Optimized conformers of (6*R*, 12a*R*) and (6*S*, 12a*R*)–tadalafil at the SCRF-ωB97XD/631G(d) level of theory. The arrows indicate that the main stereostructural differences lies in the rotation of the 1,3–benzodioxolyl group and puckering of the 3', 4'–OCH_2O ring.

	B3LYP/6-31G(d)	SCRF-B3LYP/6-31G(d)	SCRF-ωB97X-D/6-31G(d)	SCRF-mPW1PW91/6-311+G(2d,p)	B3LYP/6-31+G(d,p)	SCRF-CAM-B3LYP/cc-pVDZ
(6R, 12aR)-a			21.9	32.0		28.1
b	37.9	32.2	21.8		38.6	
c	36.1	31.2	20.7	31.3	35.8	28.1
d			13.8	20.6		16.3
e		19.1	11.8	16.0	25.6	14.2
f	26.0	17.5	10.0			13.3
(6S, 12aR)-a	37.0	38.3	40.2	37.5	38.3	36.9
b	36.5	37.7	37.4	35.7	34.0	38.4
c	26.4	24.0	22.4	26.7	27.7	24.7

Table 7.1: Boltzmann weights (%) for the most abundant conformers for both diastereoisomers of tadalafil computed for geometries optimized at the level of theory indicated.

7.3.2 Assigning the Relative Stereochemistry: IR Spectra

The experimental IR spectra of the four samples were compared to the calculated ones of (6*R*, 12a*R*) and (6*S*, 12a*R*) at the SCRF-ωB97X-D/6-31G(d) level of theory (Figure 7.3). As IR spectra for enantiomers are the same, assignments are made down to the level of enatiomeric pairs.

Two frequency regions are crucial for distinguishing the two diastereoisomers. First of all, between 1480 cm^{-1} and 1400 cm^{-1}, the separated peaks 3, 4, 5 and 6 of sample I (and II) match better with the calculated spectrum of (6*R*, 12a*R*). The peak 6 of sample I (and II) stands out from the rest, and its vibrational mode is mainly localized CH_3 asymmetric deformation. Furthermore, the peaks 3, 4 and 5 of sample III (and IV) and (6*S*, 12a*R*) resemble each other more closely. Transitions in the region represent mainly CH_3 asymmetric and symmetric deformation, conjugated ring deformations, CH_2 scissoring, C-N stretching, and bending involving the C-H group at the two chiral centers. Secondly, between 1280 cm^{-1} and 1200 cm^{-1}, the two separated peaks 12 and 13 of sample III (and IV) are better reproduced in the IR spectrum of (6*S*, 12a*R*). Transitions in the region mainly involve C-H bending at the two chiral centers, rocking of H atoms on the benzyl rings, conjugated rings deformations and C3-H_2 wagging. These important features lead to a provisional assignment of samples I and II as (6*R*, 12a*R*) and its enantiomer, and of samples III and IV as (6*S*, 12a*R*) and its enantiomer.

To ensure the visual interpretation was not subject to human bias, the Com-

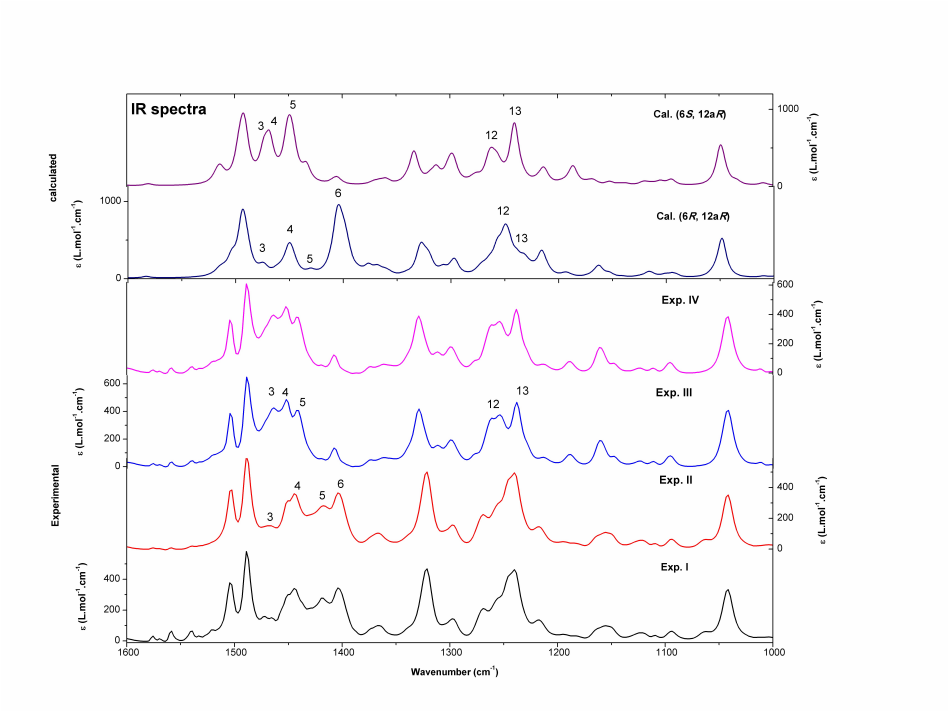

Figure 7.3: Calculated SCRF–ωB97XD/631G(d) IR spectra of (6R, 12aR) and (6S, 12aR) (upper) and experimental IR spectra of the four samples (I, II, III and IV, lower). Important similarity features are numbered. Calculated (6R, 12aR) is plotted in navy line, (6S,12aR) in purple line, experimental I in black line, II in red line, III in blue line and IV in magenta line.

		Cal.(6R, 12aR)		Cal.(6S, 12aR)	
Sample	**Calculated level**	**Scaling factor (%)**	**IR similarity (%)**	**Scaling factor (%)**	**IR similarity (%)**
(I,II)	B3LYP/6-31G (d)	0.969	83.4	0.968	85.6
	SCRF-B3LYP/6-31G (d)	0.972	88.8	0.971	88.2
	SCRF-ωB97XD/6-31G(d)	0.956	90.4	0.954	86.8
(III, IV)	B3LYP/6-31G (d)	0.967	77.9	0.971	85.5
	SCRF-B3LYP/6-31G (d)	0.972	81.4	0.974	90.5
	SCRF-ωB97XD/6-31G(d)	0.956	77.9	0.956	94.6

Table 7.2: Numerical comparison describing the similarity in the range of 1200-1550 cm^{-1} between the calculated IR spectra for diastereoisomers at three calculated levels and the experimental IR spectra for the sample pairs (I,II) and (III, IV).

pareVOA algorithm[1] based on neighbourhood similarity[87–91] was used to evaluate the IR similarity (Table 7.2). The calculated IR spectra were scaled to compensate for the overestimation of the vibrational frequencies in the harmonic approximation. This scale factor is chosen in such a manner that the calculated IR spectrum gives the largest similarity to the experimental one. The four experimental IR spectra can be clearly separated into two pairs, as enantiomers have identical IR spectra. The pair (III, IV) has a clearly higher similarity with (6*S*, 12a*R*) than (6*R*, 12a*R*), which agrees with the manual assignment. However, the IR similarity for the pair (I, II) is high for both comparisons, indicating that it may not be sufficient to distinguish between diastereoisomers based solely on IR spectroscopy in this case.

7.3.3 Assigning the Absolute Configuration: VCD Spectra

The experimental VCD spectra of the four samples compared to the calculated ones of (6*R*, 12a*R*) and (6*S*, 12a*R*) at the SCRF-ωB97X-D/6-31G(d) level of theory are shown in Figure 7.4.

Comparing the spectra of sample I and (6*R*, 12a*R*), and of sample III and (6*S*, 12a*R*), good agreement is found in which all intense VCD peaks are correctly predicted in the region of 1600-1000 cm^{-1}. Two features are used to distinguish between the two diastereoisomers. First in the region of 1350-1250 cm^{-1}, the peaks 9, 10, 11 in I show an intense triplet which is reproduced only by the spectrum of (6*R*, 12a*R*), while in III only a negative peak 9 and a broad positive peak 10 are found. These transitions represent mainly C-H bending at the two chiral centers, C3-H and C12-H bending and conjugated rings deformation. The other feature lies in the region of 1550-1400 cm^{-1}, the characteristic peaks 1, 2, 3, 4, and 5 in I only appear similarly in the spectrum of (6*R*, 12a*R*), while the peaks 1, 2, 3, 4 and 5 in III show a different pattern which is well

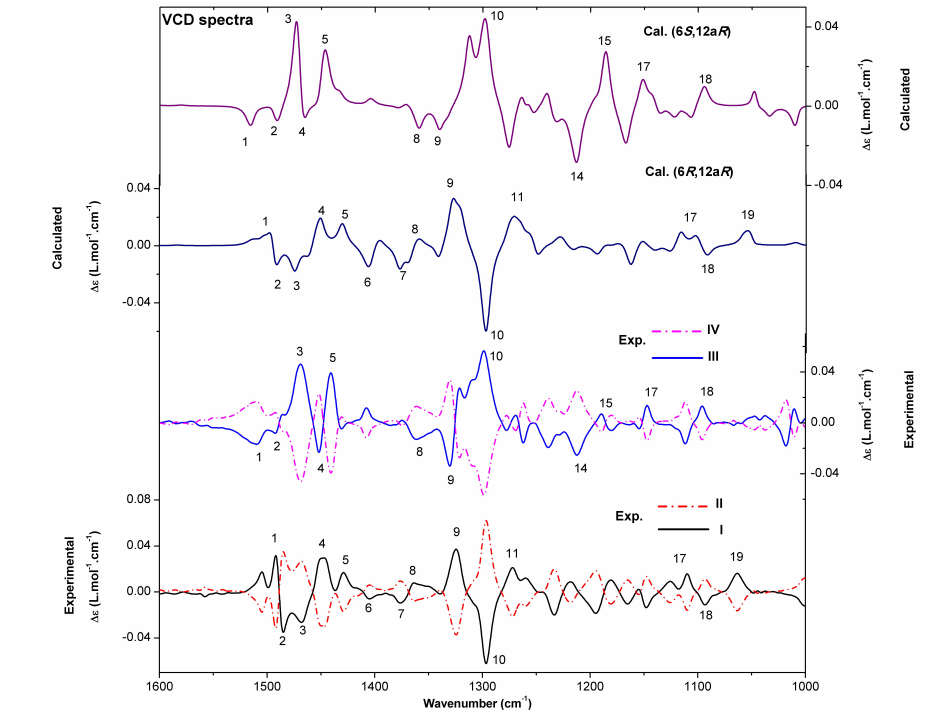

Figure 7.4: The experimental VCD spectra of the samples compared to the calculated ones of (6*R*, 12a*R*) and (6*S*, 12a*R*) at the SCRFωB97XD/631G(d) level of theory. Important similarity features are numbered. Calculated (6*R*, 12a*R*) is plotted in navy, (6*S*,12a*R*) in purple, experimental I in black solid line, II in red dash dot line, III in blue solid line and IV in magenta dash dot line.

reproduced by the spectrum of (6*S*, 12a*R*). Such transitions are mostly related to CH_3 asymmetric deformation, C7'-H_2 and C3-H_2 scissoring, C6-H bending and conjugated rings deformation. These important differences, together with the IR assignment, lead to the conclusion that I has the absolute stereochemistry (6*R*, 12a*R*), II (6*S*, 12a*S*), III (6*S*, 12a*R*) and IV corresponds to (6*R*, 12a*S*). It should be mentioned that the diastereoisomers in the regions of 1350-1250 cm^{-1} and 1550-1480 cm^{-1}, have similar IR spectra. VCD in such a case is also much richer in information for assigning relative stereochemistry compared to IR spectra.

To further assess the reliability of the absolute stereochemistry assignment, the CompareVOA algorithm[1] was used to evaluate the VCD similarity. The calculated VCD spectra were scaled using the same scale factors that were used for IR spectra. Single VCD similarity Σ has a value between 0 and 100 %, and gives the similarity between the calculated and experimental VCD spectra. The enantiomeric similarity index Δ gives the difference between the values of Σ for both enantiomers of a given diastereoisomer. Σ and Δ are then compared to a database of previous validated assignments to get a confidence level. For the pair (I, II), the results shown in Table 7.3 indicate good agreement between (6*R*, 12a*R*) and I with large values of Σ and Δ ($\Sigma > 60$ % and $\Delta > 40$ %), whereas no good agreement is found for (6*S*, 12a*R*) or its mirror image (6*R*, 12a*S*). All levels of theory give consistent results. Inclusion of the implicit solvent improves the VCD similarity between (6*R*, 12a*R*) and I significantly, and the ωB97X-D functional improves it further. This agrees with the manual assignment of VCD spectra. Numerical comparisons together with the manual assignment thus unambiguously assign the absolute configuration of I as (6*R*, 12a*R*) and II as (6*S*, 12a*S*) solely based on VCD spectra without prior knowledge on their relative stereochemistry. For sample III in the other pair, the results in Table 7.3 indicate good similarity for both (6*S*, 12a*R*) and (6*S*, 12a*S*). However, based on IR similarity (Figure 7.3 and Table 7.2), the configuration is most likely (6*S*, 12a*R*). All three calculation levels also give consistent results. Unlike in the case of (I, II), including the solvent model only slightly improves the agreement with the B3LYP functional. Moreover, as the (6*S*, 12a*S*) assignment shall be attributed to II, the only possible absolute configuration of III is (6*S*, 12a*R*).

As a supplemental aid in determining the absolute configuration,[202] in Figure 7.5 the observed IR and VCD difference spectra for I minus III are compared to the calculated difference spectra for (6*R*, 12a*R*) minus (6*S*, 12a*R*). The intense features 3, 6, 9 in the IR difference spectrum and 3, 10 in the VCD difference spectrum are well

		(6R, 12aR)			(6S, 12aS)			(6S, 12aR)			(6R, 12aS)		
Sample	Calculated level	Σ (%)	Δ (%)	Confidence Level (%)	Σ (%)	Δ (%)	Confidence Level (%)	Σ (%)	Δ (%)	Confidence Level (%)	Σ (%)	Δ (%)	Confidence Level (%)
I	B3LYP/6-31G (d)	59.6	34.1	88	-	-	-	-	-	-	51.1	9.8	57
	SCRF-B3LYP/6-31G(d)	62.1	42.2	97	-	-	-	-	-	-	56.6	21.7	62
	SCRF-ωB97XD/6-31G(d)	82.6	72.2	99	-	-	-	-	-	-	62.1	36.1	93
II	B3LYP/6-31G (d)	-	-	-	59.6	34.1	88	51.1	9.8	57	-	-	-
	SCRF-B3LYP/6-31G (d)	-	-	-	62.1	42.2	97	56.6	21.7	62	-	-	-
	SCRF-ωB97XD/6-31G (d)	-	-	-	82.6	72.2	99	62.1	36.1	93	-	-	-
III	B3LYP/6-31G (d)	-	-	-	66.0	51.6	99	71.5	56.4	99	-	-	-
	SCRF-B3LYP/6-31G (d)	-	-	-	72.0	61.7	99	76.8	64.8	99	-	-	-
	SCRF-ωB97XD/6-31G (d)	-	-	-	59.4	37.4	92	80.9	71.6	99	-	-	-
IV	B3LYP/6-31G (d)	66.0	51.6	99	-	-	-	-	-	-	71.5	56.4	99
	SCRF-B3LYP/6-31G (d)	72.0	61.7	99	-	-	-	-	-	-	76.8	64.8	99
	SCRF-ωB97XD/6-31G (d)	59.4	37.4	92	-	-	-	-	-	-	80.9	71.6	99

Table 7.3: Numerical comparison describing the similarity in the range of 1200-1550 cm^{-1} between the calculated VCD spectra for stereoisomers at three calculated levels and the experimental VCD spectra for samples I, II, III and IV.

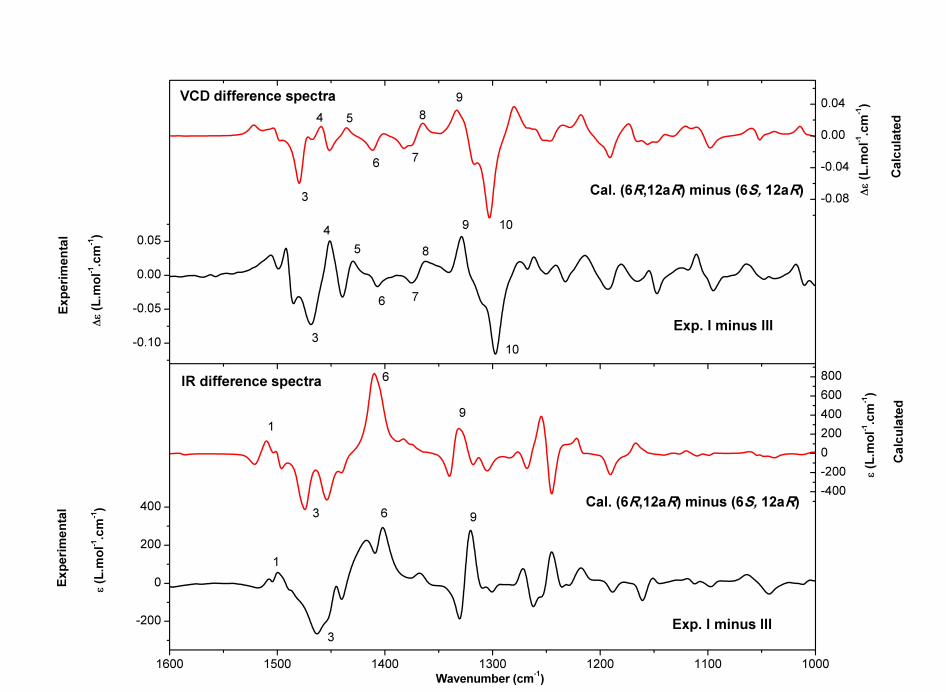

Figure 7.5: The observed IR and VCD difference spectra of I minus III compared to the calculated difference spectra of (6*R*, 12a*R*) minus (6*S*, 12a*R*) at the SCRFωB97XD/631G(d) level of theory. Important similarity features are numbered. Calculated difference spectra are plotted in red line and experimental ones in black line.

reproduced by the calculated ones. The results further validate the stereochemistry assignment of I as (6*R*, 12a*R*), and III as (6*S*, 12a*R*).

7.3.4 Confirming the Relative Stereochemistry: NMR spectra

In order to confirm the relative stereochemistry of tadalafil by IR and VCD, we turned to NMR. The experimental ^{1}H chemical shifts were assigned based on ^{1}H, ^{13}C, COSY, NOESY and HMQC NMR data, and agree well with the previous report. There are two clear differences in the ^{1}H experimental chemical shifts between sample pairs (I, II) and (III, IV) (see Figure 7.6). First in sample I, one of the H atoms attached to the C12 atom lies in the lower field (3.21 ppm) compared to the CH_3 group (3.04 ppm), while in sample III it is in the higher field (2.95 ppm) compared to the CH_3 group (2.99

ppm). Second, the H atom attached to atom C6 in sample III has a large shift to the lower field (6.97 ppm) compared to the value of 6.15 ppm in sample I. Despite these remarkable differences, however, it is hard to link these features directly to the relative stereochemistry. We therefore compare them to the calculated data at the two levels of SCRF-mPW1PW91/6-311+G(2d,p)//B3LYP/6-31+G(d,p) suggested by Lodewyk et al.[65] and SCRF-mPW1PW91/6-311+G(2d,p)//idem fully ab initio computed. Idem stands for the level of theory for the geometry optimization when geometry optimization and calculations of expectation values were performed at the same level of theory. The scaled NMR chemical shifts from linear regression with isotropic shielding constants calculated at the SCRF-mPW1PW91/6-311+G(2d,p)//idem level are also shown in Figure 7.6. The scaled NMR chemical shifts calculated at the SCRF-mPW1PW91/6-311+G(2d,p)//B3LYP/6-31+G(d,p) level are shown in Figure SI 7.1 in the supporting information. To quantify the agreement between theory and experiment, we first use the corrected mean absolute error (CMAE)[203] for both ^{1}H and ^{13}C NMR chemical shifts. CMAE is computed as $(1/n)\sum_{i}^{n}|\delta_{cal}-\delta_{exp}|$,where δ_{cal} refers to the scaled calculated chemical shifts, δ_{exp} denotes experimental data, and n denotes the number of data. Table 7.4 shows a summary of CMAEs and the largest deviation ($\Delta\delta$) comparing the computed data to experimental ones at the two calculation levels. Inspection of the values of CMAE and $\Delta\delta$ shows good agreement between sample I and calculated (6*R*, 12a*R*), and sample III and calculated (6*S*, 12a*R*) at both two levels of theory. CMAEs are 0.98 and 0.065 ppm for ^{13}C and ^{1}H, respectively, and $\Delta\delta$ are 2.5 ppm and 0.26 ppm for ^{13}C and ^{1}H, respectively, between sample I and calculated (6*R*, 12a*R*) at the SCRF-mPW1PW91/6-311+G(2d,p)//idem level. (6*R*, 12a*R*) shows better agreement with sample I than III based on the CMAEs and $\Delta\delta$ for ^{13}C and ^{1}H data. Similarly, (6*S*, 12a*R*) displays better agreement with sample III. Furthermore, it is clear that the scaled NMR chemical shifts from linear regression with fully ab initio calculation results at the SCRF-mPW1PW91/6-311+G(2d,p)//idem level fit experimental data better than those do at the level of SCRF-mPW1PW91/6-311+G(2d,p)//B3LYP/6-31+G(d,p) based on the values CMAE and $\Delta\delta$.

To gain greater confidence in our tentative conclusion, the CP3[68] analyses developed by Smith and Goodman were used. CP3 statistical analyses are applied to assign relative configurations of diastereoisomers when both experimental data sets are available. Table 7.5 lists a summary of CP3 showing how the calculated data at the two levels compare to the experimental data. The values of CP3 for the right (I=(6*R*, 12a*R*) and III=(6*S*, 12a*R*)) assignment are 0.76, 0.85 and 0.81 for ^{13}C, ^{1}H and both

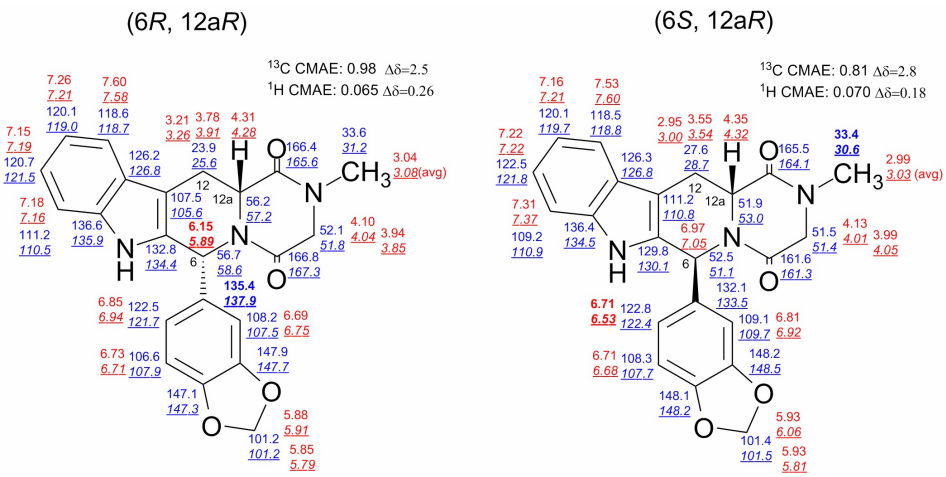

Figure 7.6: Computed H (red) and C (blue) chemical shifts (ppm, relative to TMS) at the SCRF mPW1PW91/6311+G(2d,p)//idem level compared to the experimental ones for (6*R*,12a*R*) and (6*S*,12a*R*)tadalafil. Experimental shifts are in normal text and computed shifts are in underlined italics. CMAE=corrected mean absolute error, computed as $(1/n)\sum_i^n |\delta_{cal} - \delta_{exp}|$,where δ_{cal} refers to the scaled calculated chemical shifts. $\Delta\delta$ =largest deviations, and are highlighted in bold text for each set of data.

			SCRF-mPW1PW91/ 6-311+G(2d,p)// B3LYP/6-31+G(d,p)		SCRF-mPW1PW91/ 6-311+G(2d,p)// idem	
Sample			(6*R*,12a*R*)	(6*S*,12a*R*)	(6*R*,12a*R*)	(6*S*,12a*R*)
I	^{13}C chemical shift	CMAE(ppm)	1.1	2.1	0.98	1.9
		$\Delta\delta$(ppm)	3.5	6.1	2.5	5.6
	^{1}H chemical shift	CMAE(ppm)	0.16	0.22	0.065	0.17
		$\Delta\delta$ (ppm)	0.29	0.71	0.26	0.90
III	^{13}C chemical shift	CMAE(ppm)	2.2	1.4	2.1	0.81
		$\Delta\delta$(ppm)	5.6	3.5	6.1	2.8
	^{1}H chemical shift	CMAE(ppm)	0.23	0.14	0.18	0.070
		$\Delta\delta$(ppm)	0.99	0.24	1.1	0.18

Table 7.4: CMAEs and largest deviations for comparison of calculated NMR chemical shifts at the two levels of SCRF-mPW1PW91/6-311+G(2d,p)//B3LYP/6-31+G(d,p) and SCRF-mPW1PW91/6-311+G(2d,p)//idem for each diastereoisomer with relative configuration to the experimental data for samples I and III.

		SCRF-mPW1PW91/ 6-311+G(2d,p)// B3LYP/6-31+G(d,p)		SCRF-mPW1PW91/ 6-311+G(2d,p)// idem	
		I=(6*R*,12a*R*) & III=(6*S*,12a*R*)	I=(6*S*,12a*R*) & III=(6*R*,12a*R*)	I=(6*R*,12a*R*) & III=(6*S*,12a*R*)	I=(6*S*,12a*R*) & III=(6*R*,12a*R*)
CP3	^{13}C data	0.74	-0.95	0.76	-1.12
	^{1}H data	0.82	-0.98	0.85	-1.13
	Both ^{13}C and ^{1}H data	0.78	-0.96	0.81	-1.13
Probability (%)	^{13}C data	100.0	0.0	100.0	0.0
	^{1}H data	99.9	0.1	100.0	0.0
	Both ^{13}C and ^{1}H data	100.0	0.0	100.0	0.0

Table 7.5: CP3 for comparison of calculated NMR chemical shifts at the two levels of SCRF-mPW1PW91/6-311+G(2d,p)//B3LYP/6-31+G(d,p) and SCRF-mPW1PW91/6-311+G(2d,p)//idem for each diastereoisomer with relative configuration to the experimental data for samples I and III.

data, respectively, and for the wrong (I=(6*S*, 12a*R*) and III=(6*R*, 12a*R*)) assignment are -1.12, -1.13 and -1.13 for ^{13}C, ^{1}H and both data respectively, and lead to a 100.0 % probability for the right assignment in all the cases at the SCRF-mPW1PW91/6-311+G(2d,p)//idem level. The values of CP3 for the calculation results at the level of SCRF-mPW1PW91/6-311+G(2d,p)//B3LYP/6-31+G(d,p) lead to the same conclusion, but are a little lower for the right assignment and for the ^{1}H data only, remaining 0.1 % probability leads to the wrong assignment.

The CP3 is consistent with the CMAEs and the deviations in Table 7.4 and gives quantifiable confidence. All the results indicate that it is reliable for the assignment of the sample pair (I, II) as (6*R*, 12a*R*) and its enantiomer, and (III, IV) as (6*S*, 12a*R*) and its enantiomer. The NMR chemical shifts scaled from linear regression procedures with isotropic shielding constants at the SCRF-mPW1PW91/6-311+G(2d,p)//idem level fit experimental data better than those at the level of SCRF-mPW1PW91/6-311+G(2d,p)//B3LYP/6-31+G(d,p), and also perform better in distinguishing between diastereoisomers.

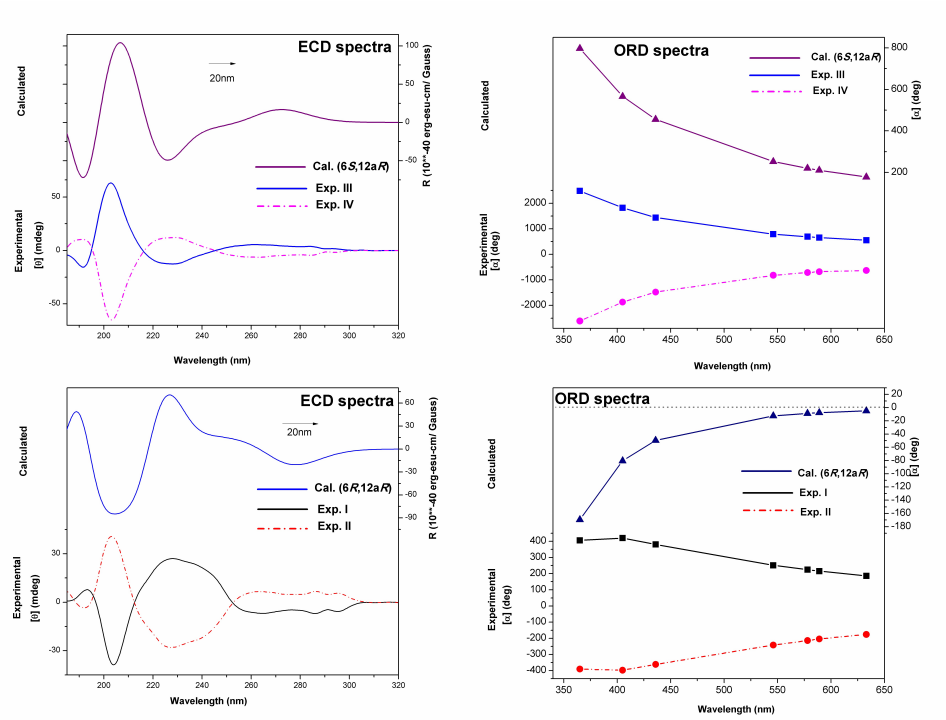

Figure 7.7: The experimental ECD (left) and ORD (right) spectra (above: III and IV, below: samples I and II) compared to the calculated ones of (6*R*, 12a*R*) and (6*S*, 12a*R*) at the SCRFCAMB3LYP/ccpVDZ level of theory.

7.3.5 Assigning the Absolute Configuration: ECD and ORD Spectra

To investigate the complementarity of chiroptical methods, ECD and ORD spectroscopy were applied for the present samples. The experimental ECD and ORD spectra of the four samples compared to the calculated ones of (6*R*, 12a*R*) and (6*S*, 12a*R*) at the SCRF-CAM-B3LYP/cc-pVDZ level of theory are shown in Figure 7.7. Calculated ECD bands are red-shifted by 20 nm to match the experimental data.[3]

From both the ECD and ORD spectra for samples (III, IV), it can be concluded that III agrees with (6*S*, 12a*R*) and IV corresponds to (6*R*, 12a*S*). The experimental ECD curve of III shows one sharp positive (203 nm), one broad negative (228 nm) and three small positive (262, 285 and 294 nm) Cotton effects (upper left in Figure 7.7). The specific rotation values of the pair (III, IV) (upper right in Figure 7.7) are

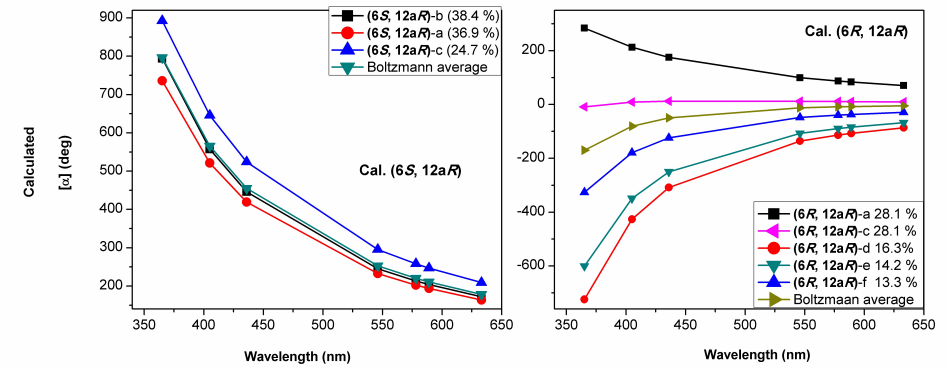

Figure 7.8: Contribution of the stable conformers to the Boltzmann averaged ORD spectra of (6*R*,12a*R*)(left) and (6*R*,12a*R*)(right) at the SCRF-CAM-B3LYP/cc-pVDZ level of theory.

much larger than those of the pair (I, II), and the three lowest-energy conformers of (6*S*, 12a*R*) have similar ORD values (left in Figure 7.8).

For the samples (I, II), the experimental ECD curve of I exhibits one sharp negative (204 nm), one broad positive (228 nm), one shallow negative (264 nm) and two small negative (286 and 295 nm) Cotton effects (lower left in Figure 7.7). There is reasonable agreement between (6*R*, 12a*R*) and I. However, no good agreement is found for ORD spectra (lower right in Figure 7.7). The absolute value of the experimental optical rotation of sample I (and II) in the explored region is much smaller than that of sample III (and IV). The calculated ORD response of (6*R*, 12a*R*) is negative for all wavelengths considered, and its absolute value on the vertical axis decreases faster than the increase of the wavelength on the horizontal axis. Examining the contribution from the predominant conformers of (6*R*, 12a*R*) (see right in Figure 7.8, and (6*R*, 12a*R*)-a, -c, -d, -e and -f in Figure 7.2), it is found that the calculated optical rotation of (6*R*, 12a*R*)-a is similar to that of sample I while three other conformers (6*R*, 12a*R*)-d, -e, -f have ORD values opposite in sign, and the optical rotation of (6*R*, 12a*R*)-c is very small around zero. The structural difference between these most stable conformers lies in the rotation of the 1, 3-benzodioxolyl group. In such a case, the calculated ORD values are thought to be sensitive to the Boltzmann ratio and also too small to be reliable.

The four stereoisomers can be clearly separated into two groups based on ECD or simply the ORD values, and III is assigned as (6*S*, 12a*R*) and IV as (6*R*, 12a*S*).

However, the absolute configuration of the other pair (I, II) is uncertain solely based on ECD and ORD spectroscopy.

7.4 Conclusion

Vibrational circular dichroism (VCD), electronic circular dichroism (ECD) and optical rotatory dispersion (ORD) were used to assign the stereochemistry of all four stereoisomers of tadalafil. The absolute configuration of the enantiomeric pair (6*R*, 12a*R*)/ (6*S*, 12a*S*) can be confidently assigned by VCD without prior knowledge of their relative stereochemistry, that is, VCD thus allows identifying diastereoisomers. For the other enantiomeric pair (6*S*, 12a*R*)/ (6*R*, 12a*S*), the stereochemistry is assigned after excluding the configuration already assigned to the enantiomeric pair (6*R*, 12a*R*)/(6*S*, 12a*S*). The IR and VCD difference spectra further confirm the assignment of all four stereoisomers. The relative stereochemistry is confirmed by NMR chemical shift calculations and CP3. The scaled NMR chemical shifts from linear regression procedures with isotropic shielding constants at the SCRF-mPW1PW91/6-311+G(2d,p)//idem level have a better distinguishing power between diastereoisomers than those at the level of SCRF-mPW1PW91/6-311+G(2d,p)//B3LYP/6-31+G(d,p) recommended by Lodewyk et al.[204] ECD and ORD methods can identify the enantiomeric pair (6*S*, 12a*R*)/(6*R*, 12a*S*), but for the other pair (6*R*, 12a*R*)/(6*S*, 12a*S*), the absolute configuration is uncertain as the lowest-energy conformers have ORD values opposite in sign and the specific rotation is small as well. As a result, VCD is clearly the most discriminatory method for diastereoisomers, and the combination of VCD and NMR is optimal.

7.5 Supporting Information

Geometries were optimized at the B3LYP/6-31+G(d,p) level in the gas phase and Boltzmann weights were based on relative enthalpies (instead, the relative free energies were used in the review by Tantillo et al.[205]). The NMR shielding constants were then computed by the GIAO method with the SCRF-mPW1PW91/6-311+G(2d,p) level (chloroform, ϵ=4.71). Shielding constants related to the methyl group were averaged before calculating the Boltzmann weighed shielding constants. The scaled NMR chemical shifts relative to TMS were obtained applying the linear regression

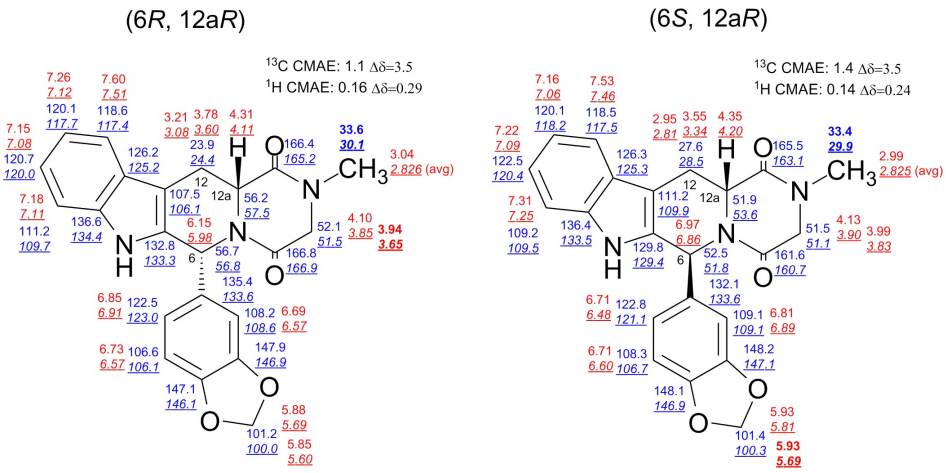

Figure SI 7.1: Computed H (red) and C (blue) chemical shifts (ppm, relative to TMS) at the SCRF-mPW1PW91/6-311+G(2d,p)//B3LYP/6-31+G(d,p) level compared to the experimental ones for (6*R*, 12a*R*)- and (6*S*, 12a*R*)-tadalafil. Experimental shifts are in normal text and computed shifts are in underlined italics. CMAE=corrected mean absolute error, computed as $(1/n)\sum_i^n |\delta_{cal} - \delta_{exp}|$,where δ_{cal} refers to the scaled calculated chemical shifts. $\Delta\delta$ =largest deviations, and for each set of data are highlighted in bold text.

parameters: for ^{1}H data, the slope and intercept used were set to -1.0936 and 31.8018, respectively, while for the ^{13}C data values of -1.0533 and 186.5242 were used. The experimental and scaled calculated chemical shifts are shown in Figure SI 7.1.

Chapter 8

Strength by Joining Methods: Combining Synthesis, NMR, IR and VCD for the Determination of the Relative Configuration in Hemicalide

8.1 Introduction

Many, if not most of natures most critical molecules in living organisms contain some element of chirality, be it through the chirality of nearly all amino acids, the chirality of a helix or combinations of different kinds of chirality. Chirality is also key to many of the chemical properties of a compound. This may range from somewhat innocent differences like difference in the smell of limonene (ranging from lemon to orange depending on the absolute configuration (AC)) to quite dramatic changes in properties as is the case in drugs. As a consequence, there is a large interest in methods to determine the AC of not only drug molecules but natural products in general. This is variably done using single crystal x-ray diffraction, Vibrational Circular Dichroism

(VCD), Raman Optical Activity (ROA), Electronic Circular Dichroism (ECD), specialized NMR methods or retrosynthesis. Many works use only one method although a combination of methods may prove more powerful. The added value of combining methods is clearly proven in the present case where the AC of a subunit of a 21 chiral center natural product is determined, which in turn leads to knowledge on the relative configuration in the large molecule.

The subject of the current work is a complex bioactive polyketide of marine origin, called hemicalide. Natural products of marine origin are of great interest for their pharmacological potential.[206] Unfortunately, the difficult isolation by extraction and thus low availability of these natural compounds from raw material may render complete structural elucidation including the complete stereochemistry very difficult. Recently, researchers of the CNRS–Pierre Fabre Laboratories, in collaboration with the Institut de Recherche pour le Développement (IRD), isolated for the first time, a complex bioactive polyketide from the marine sponge Hemimycale sp. collected in deep water around the Torres Islands (Vanuatu).[207] This new natural product, called hemicalide, is a highly potent mitotic blocker that, at subnanomolar concentrations and via a unique mechanism, exhibits antiproliferative activity against several human cancer cell lines.[207] Extensive NMR studies enabled the determination of the structure of hemicalide, featuring a 46 carbon atom backbone containing 21 stereocenters (Figure 8.1).[207] Unfortunately, due to the extremely limited supply of hemicalide (less than 1 mg), degradation and derivatization experiments could not be carried out and hence the configuration of the stereocenters could not be assigned. However, the promising biological activity of hemicalide stimulated further studies concerning the assignment of the relative configuration of the stereocenters in the key structural subunits; this as part of an ambitious program devoted to the total synthesis of this natural product and analogues thereof.

By careful comparison of the NMR data of hemicalide with those of appropriate diastereomeric model compounds, selected after careful NMR and/or computational conformational analyses, the relative configuration of the stereocenters in the C8-C13 segment[208] and in the C18-C24 α, β dihydroxy-δ lactone subunit[209] could be assigned. In the present work, we concentrate on the C36–C46 unit. The aim of the present study is to contribute to the assignment of the relative configuration of the C36–C46 subunit of hemicalide in general and, more specifically, to the assignment of the relative configuration of the asymmetric carbon C42. This is done using the VCD spectra of appropriate synthesized and NMR characterized model compounds of the

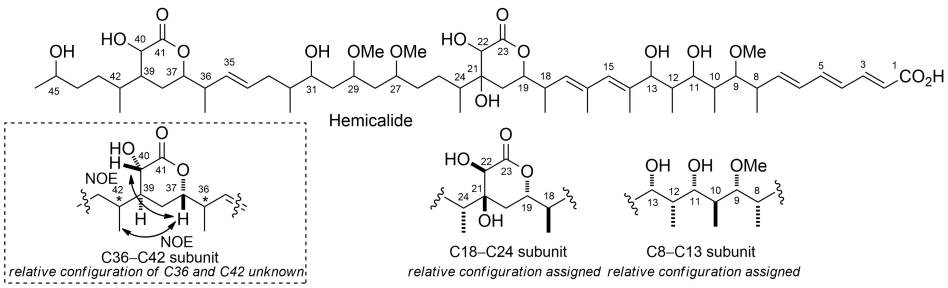

Figure 8.1: Structure of hemicalide and relative configuration of the C8-C13, C18-C24 and C37-C41 subunits. NOE=Nuclear Overhauser Effect

C36-C46 subunit of hemicalide. The need for VCD as final solver is due to the fact that, as described below, other techniques, including NMR, IR and synthesis, did not conclusively establish the absolute configuration of this center.

VCD relies on the different behavior of chiral molecules towards left and right circularly polarized light,[10,44,104] and has over the last decades become one of the prime methods for the determination of absolute configuration.[24,148,210] Its increasing appreciation is fueled by the advent of commercially available VCD spectrometers[73,211] and the availability of VCD algorithms in several quantum chemistry software packages.[64,106–108] Experiment and theory based simulation play an equally important role as experimental spectra can only be interpreted using knowledge from such simulations.[10,80,148] The number and complexity of structures analyzed more or less routinely also increases, making VCD a method of choice for AC determination of complex natural products.[109,115–117,137,149,151,152,212–216] This is possible due to the information richness of the VCD spectra that are vibrational in nature. Still, there are limiting factors in the applicability of VCD spectroscopy for AC determination. First, there is the number of chiral centers.[217] Although a mirror relationship exists between spectra of enantiomers, there is no such relation between spectra of diastereoisomers. Therefore, one needs experimental and calculated spectra of the highest quality to perform a band-by-band analysis, allowing for unambiguous AC determination. Over the last years, several uses of the method in the AC determination of diastereomeric compounds have been reported showing it to be a promising method also in such cases.[2,3,111,218–221] It is furthermore clear that the higher the number of chiral centers is, the more difficult it becomes to distinguish between epimers, since the two spectra may become less and less 'mirror images'. This is reflected also in the fact that con-

siderably fewer VCD assignments have been made on molecules with three or more chiral centers.[116,212–214,222,223] Another limiting factor is molecular size and especially the degree of flexibility of the molecule. Every conformer of a molecule of a given AC has a (possibly very) different VCD spectrum. Therefore, it is common practice to calculate VCD spectra for every conformer, and then take a Boltzmann average over all conformer spectra. Finding all abundant conformers obviously becomes harder as the molecule has more flexibility. Moreover, since all conformer spectra may be inherently different, a large number of conformers may lead to averaging out of important bands in the spectrum.

In view of the above, it is important to stress that for the C36-C46 subunit of hemicalide, the six chiral centers can give rise to $2^{(6-1)} = 32$ different relative configurations. Before discussing the results, we therefore first describe the general strategy used for the structure eludication of hemicalide. The key element in the strategy, described in detail by Fleury et al.,[208,209] is the consideration of hemicalide as a sequence of subunits for which the NMR data can be mimicked and, eventually, fully reproduced by synthesizing and characterizing a series of related model compounds that are structurally similar to the natural product and whose NMR data and synthesis allow to establish the configuration. So, effectively, synthesis and NMR are used to create a selection of known model compounds through which, by comparison of the NMR data, one can assign the configuration of the actual subunit as being that with the highest similarity in the NMR data with respect to hemicalide.

The choice of the model compounds to be studied is based on 2D NMR (NOESY) data obtained for the natural product, showing a *syn* relative orientation between the hydrogen atom at C37 with the side-chain at C39 and with the hydrogen atom at C40 in the ring of the C37–C41 α-hydroxy δ-lactone subunit. Taking into account these NMR data, and the fact that only the relative configuration of C36, C42 and C45 remains to be established, the set of model compounds can be largely reduced, leaving only 8 of the 32 possible relative configurations (Figure 8.1).

During the synthesis of the model compounds, it was found that epimers at C45 show quasi-identical NMR spectra, thereby making it impossible to establish the relative configuration at C45. It was therefore decided to focus on the structure elucidation of the C36–C42 subunit in the current study, using an arbitrarily chosen configuration at C45. This further reduced the subset to 4 model compounds. The diastereomeric δ-lactones **1a–1d**, closely related to the C36-C46 subunit of hemicalide, in which the three endocyclic stereocenters (C37, C39 and C40) possess the requisite relative con-

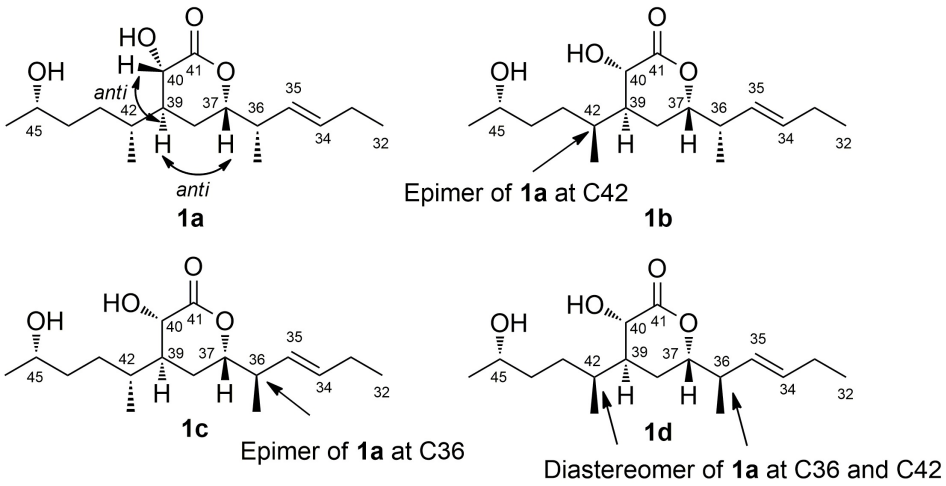

Figure 8.2: Model compounds **1d–1d** for the C36-C46 subunit of hemicalide.

figuration are shown in Figure 8.2. **1b** and **1c** are epimers of the δ-lactone **1a**, at C42 or C36, respectively. Compound **1d** is a diastereoisomer of **1a** at C36 and C42.

In our synthetic approach toward the epimeric model subunits **1a** and **1b**, δ-lactone **2** containing five of the six stereocenters (C36, C37, C39, C40 and C45) was prepared as a key intermediate (Scheme 8.1). Whereas the C45 and the C36 stereocenters in δ-lactone **2** both originated from the chiral pool, the absolute configurations of C37, C39 and C40 were controlled by diastereoselective reactions and unambiguously confirmed by NMR (NOESY) spectroscopy. To create the sixth stereocenter at C42, the hydrogenation of the trisubstituted alkene at C42-C43 in δ-lactone **2** was carried out in the presence of Crabtrees catalyst.[209] Although the diastereoselectivity was not high, this transformation conveniently afforded a 63:37 mixture of the epimers at C42, **3** and **3'**, which was useful for comparison. These two epimers could be separated by medium pressure liquid chromatography but attempts to obtain crystalline derivatives of 3 or 3' suitable for X-ray diffraction analysis were unsuccessful. This entails that the absolute configuration of C42 in compounds **3** and **3'** remains unknown. Compounds **3** (major diastereomer) and **3'** (minor diastereomer) were then individually converted into **1** and **1'**, respectively, after cleavage of the protecting groups and formation of the (E) alkene at C34–C35. Inspection of the NMR data of compound **1**, obtained from the major diastereomer **3**, revealed a perfect agreement with those of hemicalide whereas significant differences were observed for **1'**. Additionally, during the preparation of

model compounds related to **1c** or **1d**, it was observed that a different configuration at C36 led to major differences in the NMR spectra. Full details on the synthesis and characterization of the model compounds will be disclosed in a forthcoming paper.

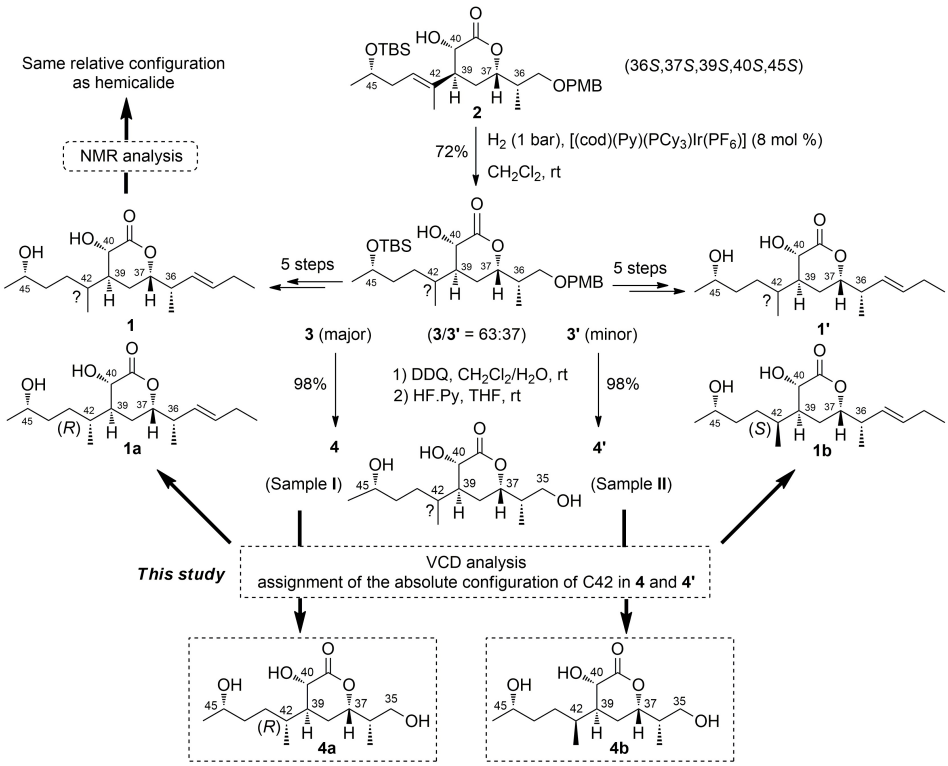

Scheme 8.1: Synthesis of the **1** and **1'** model subunits. From **3** and **3'**, epimeric compounds **4** (sample I) and **4'** (sample II), which are more suitable for VCD analysis, were also synthesized. Py = pyridine, cod = cycloocta-1,5-diene, PMB = 4 methoxybenzyl, TBS = tert-butyldimethylsilyl, DDQ = 2,3-dichloro-5,6-dicyano-1,4-benzoquinone.

Although the use of NMR drastically reduces the subset of model compounds, it does not allow assigning compounds **1** and **1'** to the model compounds **1a** and **1b**, or vice versa. Solving the missing link, i.e. assigning compound **1** to either **1a** or **1b**, is the purpose of the current VCD study. To avoid the conformationally challenging C32–C35 alkenyl group in **1a** and **1b**, and to avoid extra CPU requirements related to the incorporation of the TBS and PMB protecting groups, for the actual VCD study, compounds **3** and **3'**, which have the same configuration at all stereocenters as **1** and **1'**, were converted to the unprotected compounds **4** (sample I) and **4'** (sample II). In

the following, we report on the use of NMR to establish the relative configuration of the undetermined C42 stereocenter in the structurally complex epimers **4** and **4'**. No conclusive results could however be found and we then rely on VCD for the assignment of the relative configuration. The samples, containing six stereocenters, proved to be particularly challenging and constituted an excellent opportunity to demonstrate the utility and power of VCD for the stereochemical assignment of complex polyketide fragments. Combination of the VCD results obtained with those arising from stereoselective synthesis and manual NMR analysis allows assignment of the structure of compounds **4** and **4'** as **4a** and **4b**, respectively, and consequently the relative configuration of the C36–C42 subunit of hemicalide that corresponds to the model compound **1a**.

8.2 Experimental Section

8.2.1 Computational Details

For the calculation of the IR and VCD spectra of **4a** and **4b**, all significant conformers of the molecule are required such that Boltzmann averaged spectra can be computed. Due to the number of rotatable bonds, conformational analysis was performed using molecular mechanics force fields instead of direct ab initio potential energy hypersurface exploration. A combination of MMFF, MMFF94S[121,122,170] and SYBYL[123] force fields was used, using the search algorithms from the commercially available software packages Conflex[224] (reservoir filling), Spartan 08[124] (Monte Carlo) and ComputeVOA[225] (Monte Carlo). As is clear from scheme 8.1, five out of the six chiral centers have known stereochemistry, hence it is sufficient to calculate spectra for only two configurations, namely depending on the chosen C42 configuration. To accomplish this, 2 structures were drawn for which five chiral centers have the (*S*)-configuration, and the stereocenter at C42 is either (*R*) or (*S*). Each of these structures was then used as starting point for the conformational analysis described above. The many redundant conformers were removed through comparison of the eigenvalues of the internuclear distance matrix for each conformer. After this, conformers were optimized at the B3LYP/6-31G*[95,96] level of theory using Gaussian 09.[64] Again, redundant structures were removed and the retained conformers were finally optimized at the B3LYP/aug-cc-pVDZ[226] level, using a polarizable continuum model[131] for modelling the chloroform solvent (ϵ=4.7113). To investigate the influence of the solvent modelling, calculations

		Intercept	Slope	R	CMAE	$\Delta\delta$
			^{13}C			
4a	**Sample I**	188.34	-1.0111	0.9976	1.649	3.357
	Sample II	188.93	-1.0156	0.9953	2.142	7.522
4b	**Sample I**	188.43	-1.0104	0.9971	1.828	3.644
	Sample II	189.11	-1.0167	0.9982	1.509	3.14
			^{1}H			
4a	**Sample I**	31.915	-1.0806	0.976	0.51	0.754
	Sample II	31.838	-1.0175	0.9281	0.525	0.735
4b	**Sample I**	31.959	-1.1007	0.9825	0.126	0.387
	Sample II	31.884	-1.0378	0.937	0.185	0.898

Table 8.1: Linear regression data of calculated magnetic shielding constants with measured NMR chemical shifts for the two model compounds with both synthesized samples.

with and without PCM (Integral Equation Formalism) were performed. All calculations were done with 3 different basis sets, namely 6-31G*, 6-31+G* and aug-cc-pVDZ, combined with the B3LYP functional. To ensure only PES-minima are used, all conformers were checked for imaginary frequencies. For each conformer, dipole and rotational strengths were calculated and converted to molar extinction coefficients (L.mol^{-1}.cm^{-1}).[32] For both IR and VCD spectra, a Lorentzian broadening was applied with a rather large full width at half maximum (FWHM) of 18 cm^{-1}, as this gave the best visual comparison to experiment. A global scale factor, optimized for maximum IR similarity using CompareVOA,[1] was applied to compensate for the overestimation of the harmonic frequencies.[180] NMR chemical shifts were obtained by linear regression of the computed magnetic shielding constants, with experimental shifts obtained for sample I and sample II. For both calculated model compounds, this linear regression was performed twice: once for each sample. Both the slope and the intercept obtained from the linear regression was averaged and were found to be very similar between both sets of experimental data. Linear regression was done for ^{1}H and ^{13}C NMR separately. Chemical shifts were averaged using the Boltzmann weights of all conformers, and chemical shifts for equivalent methyl hydrogens were also averaged. These calculated shifts were then used in the online applet available from Smith and Goodman.[68] No prior assignment was used, i.e. the highest experimental shifts were compared to the highest calculated shifts, and so on. Regression data can be found in table 8.1.

8.2.2 Experimental Details

For measurement of the IR and VCD spectra, the samples corresponding to **4** (sample I) and **4'** (sample II) in scheme 8.1 were dissolved in $CDCl_3$ with concentrations of 0.16M and 0.11M respectively. These concentrations are too high for useful VCD measurements of the carbonyl stretch signal, but yielded the highest signal-to-noise ratio (S/N) for measurement of the fingerprint region (950 cm^{-1} - 1500 cm^{-1}). As the carbonyl function is susceptible to solvent interactions,[84,85,133] we choose to ignore this signal in the AC determination. The IR- and VCD-spectrum for the two diastereoisomers and the solvent were recorded on a ChiralIR-2X dual PEM VCD-spectrometer (BioTools, Inc) for a duration of 10 000 scans/sample. Since no enantiomers were available, baseline correction was performed using subtraction of the solvent VCD-spectrum. All samples were measured in a 100 μm path length cell with BaF_2 windows, and a resolution of 4 cm^{-1} was used throughout. NMR spectra were obtained at 400 MHz for ^1H and 100 MHz for ^{13}C using $CDCl_3$ as solvent and tetramethylsilane (TMS) as an internal standard. Sample I (corresponding to **4a** according to VCD analysis) ^1H NMR (400 MHz, $CDCl_3$) δ 4.47 (apparent dt, J = 11.3 Hz and J = 3.5 Hz, 1H, H37), 4.29 (d, J = 10.3 Hz, 1H, H40), 3.79 (m, 1H, H45), 3.64 (dd, J = 10.8 Hz and J = 7.7 Hz, 1H, H35), 3.65 (br s, 1H, OH), 3.60 (dd, J = 10.8 Hz and J = 5.3 Hz, 1H, H35'), 2.50 (br s, 1H, OH), 2.19 (br s, 1H, OH), 2.071.96 (m, 1H, H42), 1.961.81 (m, 3H, H39, H36 and H38), 1.721.61 (m, 1H, H38'), 1.581.48 (m, 1H, H44), 1.481.24 (m, 3H, H44' and H43), 1.19 (d, J = 6.1 Hz, 3H, H46), 0.98 (d, J = 7.0 Hz, 3H, C36 Me), 0.94 (d, J = 6.8 Hz, 3H, C42 Me); ^{13}C NMR (100 MHz, $CDCl_3$) δ 177.3 (s, C41), 76.1 (d, C37), 67.9 (d, C45 or C40), 67.0 (d, C45 or C40), 63.8 (t, C35), 40.7 (d, C39), 39.3 (d, C36), 36.6 (t, C44), 32.7 (d, C42), 30.5 (t, C43), 25.1 (t, C38), 23.6 (q, C46), 13.2 (q, C42 Me), 10.6 (q, C36 Me). Sample II (corresponding to **4b** according to VCD assignment): ^1H NMR (400 MHz, $CDCl_3$) δ 4.53 (apparent dt, J = 11.5 Hz and J = 3.5 Hz, ^1H, H37), 4.38 (d, J = 10.4 Hz, 1H, H40), 3.84 (br s, 1H, OH), 3.76 (m, 1H, H45), 3.63 (dd, J = 11.0 Hz and J = 8.0 Hz, 1H, H35), 3.57 (dd, J = 11.0 Hz and J = 5.1 Hz, 1H, H35'), 2.92 (br s, 2H, OH), 2.021.78 (m, 4H, H39, H36, H42 and H38), 1.77-1.67 (m, 1H, H43), 1.67-1.52 (m, 2H, H38' and H44), 1.19-1.28 (m, 1H, H43'), 1.20 (d, J = 6.2 Hz, 3H, H46), 1.08 (m, 1H, H44'), 0.99 (d, J = 6.8 Hz, 3H, C36 Me), 0.96 (d, J = 6.9 Hz, 3H, C42 Me); ^{13}C NMR (100 MHz, $CDCl_3$) δ 177.4 (s, C41), 75.6 (d, C37), 68.5 (d, C45), 66.8 (d, C40), 63.8 (t, C35), 41.9 (d, C39), 39.2 (d, C36), 37.2 (t, C44), 34.1 (d, C42), 26.9 (t, C43), 26.5

(t, C38), 23.7 (q, C46), 17.4 (s, C42 Me), 10.3 (q, C36 Me).

8.3 Results and Discussion

8.3.1 Conformational Analysis

From the structures of **4a** and **4b**, it is clear that the molecule has high conformational freedom stemming from unhindered rotations in the 5-hydroxyhexan-2-yl chain, the 1-hydroxypropan-2-yl chain and puckering of the lactone ring. This conformational flexibility yields a complex potential energy surface (PES) that can only be probed using stochastic search algorithms. Due to conformational averaging, in which conformers of the same absolute configuration may possibly yield VCD spectra that largely cancel in the Boltzmann weighted average spectrum, such flexible molecules can present rather weak VCD signals. Fortunately, this appears not to be the case for the molecules under study.

For the (*R*)-diastereoisomer (**4a**), conformational analysis led to 246 unique conformers, for the (*S*)-diastereoisomer (**4b**) 440 were found using B3LYP/6-31G* gas phase calculations. The 10 most stable conformers for **4a** and 35 in the case of the **4b** all have intramolecular hydrogen bonding (see Figure 8.3). This amounts to a cumulated Boltzmann weight of 91.8% and 92.6 % for the (*R*)- and (*S*)-diastereoisomer respectively. Since in solution unfolded molecules, not showing internal H-bonding, could be stabilized by solvent interaction and the Boltzmann weight of the folded structures appeared rather high for what would be expected in solution, PCM calculations were performed to allow stabilization of the unfolded structures. Indeed, we found diminished occurrence of the folded conformers when solvent modelling is included. This effect is much more outspoken for basis sets containing diffuse functions. Also, such basis sets have a much lower tendency of folding the conformers even in gas phase. A possible explanation for this is an intramolecular basis set superposition error (BSSE).[227] For small basis sets (e.g. 6-31G*) the number of basis functions on a hydroxyl hydrogen is limited. For the conformations showing intramolecular hydrogen bonding, this hydrogen can use basis functions of the nearby H-bond acceptor, which is one of the oxygen atoms in the molecule (Figure 8.3), artificially lowering the energy. Molecules without hydrogen bonding do not have this (artificial) stabilization, and thus will have higher energy. In order to avoid such an effect, we use larger basis sets.

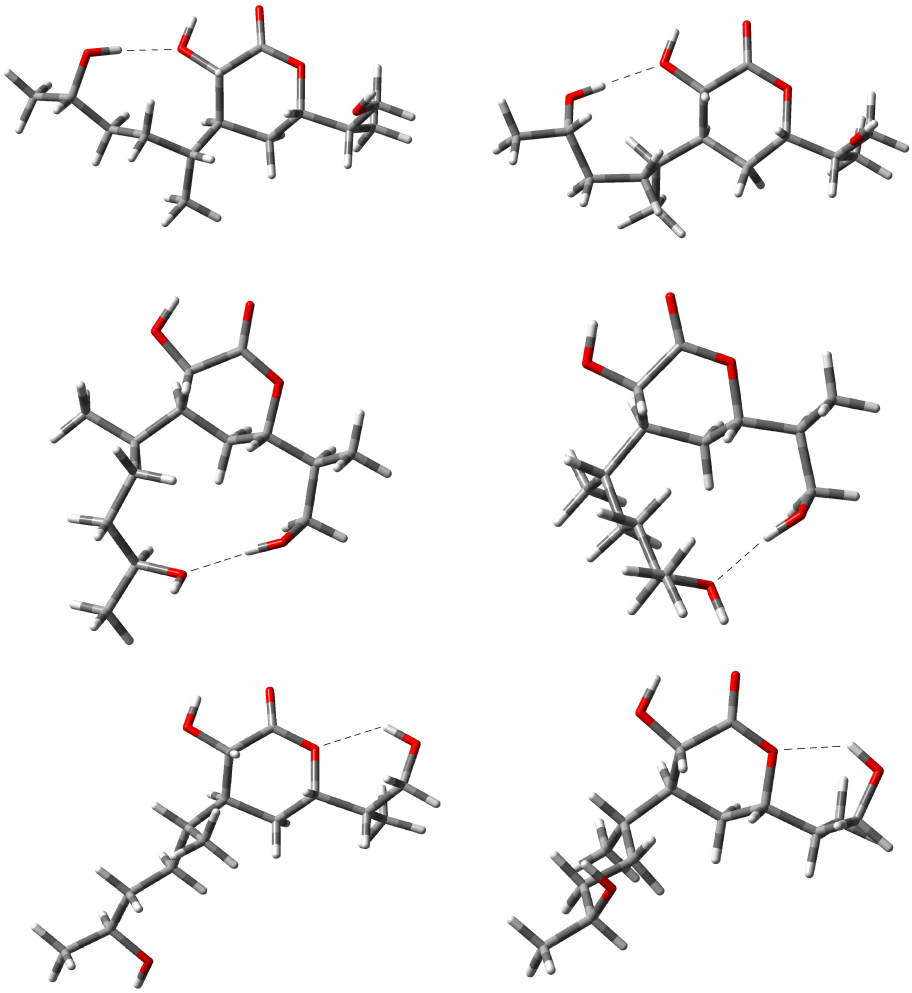

Figure 8.3: The three possibilities for intramolecular hydrogen bonding for the (*R*)-(**4a**) (left column) and (*S*)-**4b** (right column) diastereoisomers of **4**. The first type of hydrogen bond is with the hexan-2-yl alcohol group as donor and the hydroxy lactone as acceptor. In the second case the molecule folds to allow an interaction between the hydroxy groups on both side chains of the lactone ring. In the third type of hydrogen bonding the hydroxyl hydrogen the propan-2-yl side chain acts as a hydrogen bond donor to the lactone oxygen acceptor.

4a	6-31G*	6-31+G*	aug-cc-pVDZ
Gas phase	91.8	67.7	47.4
PCM	85.9	42.7	27.8
4b			
Gas phase	94.1	59.9	35.6
PCM	82.3	34.5	20.3

Table 8.2: Cumulative Boltzmann weight of conformers showing intramolecular hydrogen bonding. Addition of PCM solvent modelling slightly decreases the importance of intramolecular hydrogen bonding, but increasing the size of the basis set and adding diffuse functions has a much more dramatic effect.

As table 8.2 shows, when using a large enough basis set (aug-cc-pVDZ) in combination with a continuum solvent model (PCM), the tendency of intramolecular hydrogen bonding decreases significantly. We also attempted calculations using the aug-cc-pVTZ basis set but these turned out to be computationally too demanding.

In general spectroscopic data depend on the conformations of the molecule in the sense that different conformations may lead to significantly different spectra. VCD spectra are notoriously conformation dependent and in the present molecule, this may include a significant dependence on the population of hydrogen bonded conformations compared to non-hydrogen bonded ones. We therefore carefully examined the impact of different weights of both groups of conformations and refer to the detailed discussion on VCD spectra below for the results.

8.3.2 NMR Analysis

Since in this case we are only interested in the relative configuration of the model compounds under study, the use of NMR methods is an obvious choice if solution state methods are considered. Although 2D-NMR techniques (COSY, HMQC, NOESY) were useful in the determination of the stereogenic centres C37, C39 and C40, the relative configuration at C42 could not be established using these techniques. On the other hand, recent results using calculated NMR shielding constants in combination with statistical methods have proven very promising in determining the relative configuration of some natural products.[5,65,68,69] Therefore, it was investigated whether this methodology could aid in the determination of the relative configuration at C42 by comparison of experimental NMR chemical shifts on the two model compounds, and

	^{1}H	^{13}C	Total
Sample I	66.60%	97.00%	98.50%
Sample II	33.30%	3.00%	1.50%

Table 8.3: DP4 probability of both samples I & II compared to NMR data of the natural product

ab initio calculated NMR shielding constants for the two possible epimers. In the current work, two approaches were considered. First of all, we wanted to validate which of the model compounds considered corresponds to the same relative configuration as the natural product. Although this was already done manually, it would be nice to have a statistically validated evaluation of this assignment. Smith and Goodman have developed an algorithm (DP4) that assigns probabilities to the assignment based comparison of the calculated chemical shifts of both model compounds with the corresponding experimental shifts. However, we see no reason not to use this algorithm on the comparison of two experimental model compounds (sample I & II) with the natural product.[207] The analysis shows that there is a 98.5% chance that sample I has the same relative configuration as hemicalide, confirming the manual assignment (table 8.3).

To assign the relative configuration of the natural product, we thus need to assign the configuration of sample I (and sample II). Since conventional (2D-)NMR techniques were not adequate for the assignment, the use of the CP3 method by Smith and Goodman is considered. For this, differences in calculated chemical shifts (**4a–4b**) were compared to differences in measured chemical shifts for the samples (sample I–Sample II). To do this, chemical shifts were calculated from the magnetic shielding constants using a linear regression with the experimental shifts of the model compounds, as described in the experimental section. The sign of this CP3 parameter, together with its magnitude, is a measure for how good a calculated diastereomer corresponds to an experimental sample. The results are shown in table 8.4.

Although the overall probability of sample I corresponding to **4a** and sample II to **4b** is calculated as 97.1%, results of the ^{13}C and ^{1}H data contradict one another, making the assignment not trustworthy at all. This leads to the conclusion that a CP3 analysis on both ^{1}H and ^{13}C NMR spectra is always preferable: using only one of the two available NMR spectra would inevitably have led to a conclusion whereas the current analysis shows that no conclusions can be drawn from NMR. Also note that

CP3 values:	^{13}C data	^{1}H data	All data
(Sample I-Sample II) vs. (**4a**-**4b**)	0,69	-1,00	-0,16
(Sample I-Sample II) vs. (**4b**-**4a**)	-1,07	0,23	-0,42
Probabilities:			
(Sample I-Sample II) vs. (**4a**-**4b**)	100%	0,1%	97,1%
(Sample I-Sample II) vs. (**4b**-**4a**)	0,0%	99,9%	2,9%

Table 8.4: CP3 analysis of NMR spectra of sample I & II compared to calculated magnetic shieldings of **4a** and **4b**.

the calculated probabilities lead to a misperception of reliability. If all data are considered, we find negative CP3 values for both assignments, which means that important sign changes Δ_{exp} and Δ_{calc} (i.e. difference in chemical shift between corresponding nuclei of both configurations for experiment and calculation, respectively) are found and agreement between theory and experiment is not satisfying. This also confirms the manual NMR analysis, which showed that the relative configuration of the two diastereomers could not be assigned using NMR. To resolve this, we need rely on a more sensitive method when it comes to stereochemistry.

8.3.3 IR and VCD Analysis

Prior to the detailed discussion of the spectra, we address the issue raised above on possibly important changes in the calculated spectra with changes in the Boltzmann distribution, notably concerning differences in the populations of hydrogen bonded conformations versus those without. In the case of hemicalide, the shift in Boltzmann distribution between the levels of calculation seems to have a rather modest effect. To explain this, we have divided all conformers into two groups, one group containing all conformers showing intramolecular hydrogen bonding, and the other without hydrogen bonding. While the relative Boltzmann weights of the conformers within one group is kept constant, the total Boltzmann fraction of the H-bonded group was varied between 0 and 100%. Spectra of H-bonded and non H-bonded groups were then combined using these varying weights, and the VCD spectrum similarity with the experimental spectrum was calculated using the CompareVOA algorithm.[1] The results are shown in figure 8.4.

It is clear from the relatively small difference in similarity between the predicted spectrum without intramolecular hydrogen bonding conformations (0%) and that using

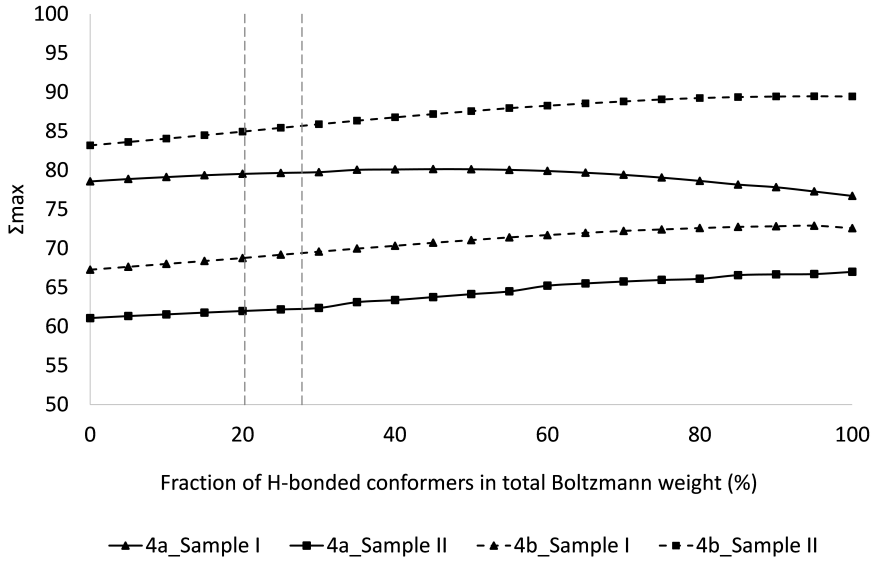

Figure 8.4: Similarity with varying weight of the group of intramolecular hydrogen bonded conformers. There is only a small change in spectrum similarity with varying fraction of H-bonded conformers, and in all cases the conclusion on the AC determination would be equal. The calculated (B3LYP/aug-cc-pVDZ/PCM) Boltzmann weight of H-bonded conformers is indicated by the vertical lines at 20.3% (**4b**) and 27.8% (**4a**).

only intramolecular hydrogen bonded structures (100%), the influence of the cumulative Boltzmann weight of H-bonded conformers is limited. It is also found that for any fraction of H-bonded conformers, the conclusion of the AC determination would be the same, since none of the lines in figure 8.4 cross. Although we do not claim any universal validity of this near invariance, it does help the assignment of the present molecule significantly.

The theoretically computed compounds 4a and 4b and experimental samples I and II comprise two sets of diastereoisomers, which means that there is no direct physical relationship between their spectra, unlike in the case of enantiomers that have the same IR spectra and mirror image VCD spectra. For this task of matching the experimental samples with the computed structures, in theory, IR could be sufficient for the AC determination of the two diastereoisomers, since the other five chiral centers have known stereochemistry. However, it may also occur that, since five out of six chiral centers are identical in the two structures under study, both structures have quite similar IR and/or VCD spectra. In figure 8.5 the calculated IR spectra of (S)-**4** and (R)-**4** are shown, together with both experimental spectra I and II.

Overall, we find good agreement between the observed and calculated IR-spectra. There is good alignment of the spectra, and all peaks are predicted correctly. Only the intensity of the peaks at 1035 cm^{-1}, 1210 cm^{-1}, 1390 cm^{-1} and 1460 cm^{-1} is underestimated. Both sets of spectra show high similarity, meaning that the two diastereomers have near identical IR spectra. The IR analysis can therefore not be used to determine the relative configuration. The IR spectra are still of use however, as they can be used to assign normal modes to the corresponding peaks in the VCD.

The calculated and observed VCD spectra are shown in figure 8.6. Unlike the IR, there are important differences between the VCD-spectra of the two diastereoisomers. This already shows that VCD is a much more sensitive probe for even the relative configuration of a molecule. The most important differences are located in the regions 1070-1170 cm^{-1} (bands 4-6) and 1350-1400cm^{-1} (bands 10-11).

Using this, and the fact that we have an overall excellent agreement allows us to conclude that the C42 atom has an (S) configuration for sample II (=**4b**) and the (R) configuration for sample I (=**4a**). To confirm our analysis, we make use of the CompareVOA[1] algorithm. We note that the CompareVOA algorithm is designed to distinguish between enantiomers, i.e. it only detects a preferential similarity to a spectrum or its mirror image. The algorithm yields two parameters: Σ is a measure for the similarity between the calculated and measured spectrum, and Δ tells us how much

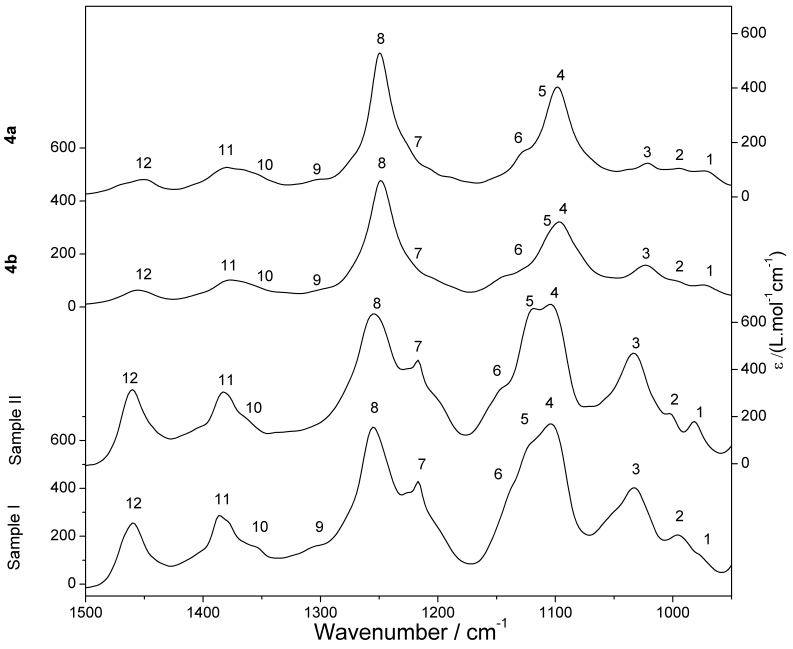

Figure 8.5: Calculated (upper) and observed (lower) IR-spectra of **4a**/**4b** and samples I/II. Both sets of spectra are almost equal. The quality of one-on-one agreement is for none of the possible matchings sufficient to aid in the determination of the AC.

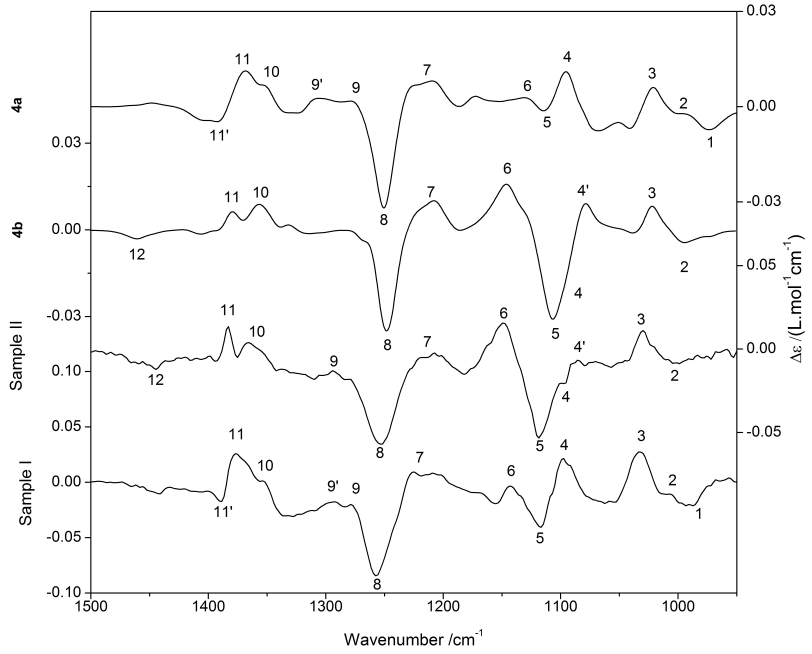

Figure 8.6: Calculated (upper) and observed (lower) VCD-spectra of **1**. As opposed to the IR spectra, we see clear differences between both sets of spectra. The most important of these are located at the regions of 1070-1170 cm^{-1} and 1350-1400 cm^{-1}. This enables us to use VCD to distinguish between the two diastereoisomers.

aug-cc-pVDZ/PCM	**Optimized scale factor (%)**	**IR similarity (%)**	**Σ (%)**	**Δ (%)**	**Confidence Level (%)**
II with **4a**	0.991	95.5	67.7	55.5	99
I with **4a**	0.990	95.0	79.7	68.2	100
II with **4b**	0.991	94.9	85.0	77.5	100
I with **4b**	0.991	94.0	61.9	38.2	94
II-I with **4b**-**4a**	0.991		78.2	63.6	100

Table 8.5: Neighborhood similarity analysis of both calculated spectra with both experiments. There is a superb similarity of the (*R*)-epimer (**4a**) calculated spectrum with the I experimental one, and of the (*S*)-epimer (**4b**) with the II experiment, confirming our visual interpretation. Although II with **4a** and I with **4b** also show reasonable similarity, this assignment can be unambiguously ruled out after comparing subtraction spectra.

the similarity is better for the calculated spectrum compared to its enantiomer. In this study, we are less interested in the information of the enantiomer of the calculated spectrum, since this involves a mirroring of all chiral centers, whereas five out of the six chiral centers are known to have the (*S*) configuration. Consequently, we are more interested in the similarity (Σ) of the two calculated spectra with the two experimental ones. This information is shown in table 8.5.

As expected from the visual interpretation of the spectra, we see very high and similar IR similarities for the two calculated spectra compared to the experimental ones. We see no higher preference for one calculation with one experiment, which means that IR is of little use in the determination of the AC. The VCD similarity Σ on the other hand, gives us more information. The (*R*) diastereomer (**4a**) gives the highest similarity with the I experiment (79.7 vs. 61.9) and the (*S*) diastereomer (**4b**) gives a preferred agreement with the II experiment (85.0 vs. 67.7). This confirms the visual interpretation. However, there are two issues with this conclusion. First of all, although the calculations have a preferential similarity with one of the experimental spectra, the agreement with the other experiment is also good, causing the differences in Σ values to be relatively small. Second, there is no measure of confidence that can be assigned to this difference in Σ value, since the CompareVOA database is based on

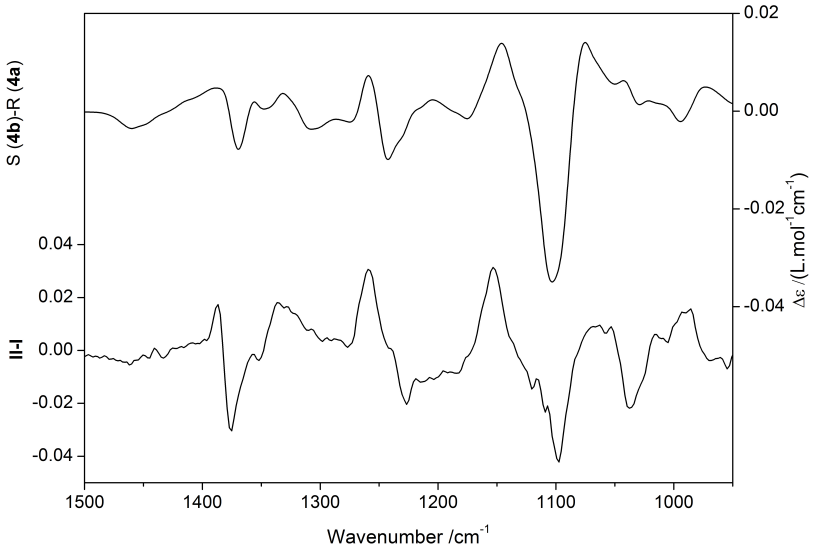

Figure 8.7: Subtraction spectra of the calculated epimer spectra (upper) and experimental epimer spectra (lower). (**4b**)-(**4a**) gives very good agreement with II-I, allowing the unambiguous assignment of II to **4b** and I to **4a**.

an analysis of a spectrum and its enantiomer. To resolve these issues, we performed a subtraction procedure. In this procedure, the spectra of the two diastereoisomers are subtracted for both the experiments and the calculations.[116] This way, one can imagine that the VCD signals due to the five equal stereocenters cancel, and roughly only the signals due to the C42 stereocenter remain. The result of this procedure is shown in figure 8.7.

We see a clear agreement between the **4b**-**4a** spectrum and the II-I spectrum. This again confirms the previous conclusion. Moreover, since the contribution of the five equal stereocenters is now roughly eliminated, we can consider this as spectra corresponding to a single chiral center molecule. This allows us to assess the quality of the AC determination using CompareVOA, as shown in table 8.3. Now there is a very high agreement for **4b**-**4a** with II-I, showing that that **4b** corresponds to II and **4a** to I. The high Δ value also shows that there is very little chance that II has the (R)-configuration at C42 and I the (S)-configuration. The latter conclusion could not be

obtained with the analysis on the original VCD spectra. Due to the excellent agreement between the NMR data of hemicalide and the closely related model compound **1** (corresponding to structure **1a**) in which the absolute configurations of all stereocenters are now known thanks to the assignment of C42 by VCD, our investigations enabled the assignment of the relative configuration of the five stereocenters in the C36-C42 subunit of the natural product.

8.4 Conclusion

In the present work, we have successfully assigned the relative configuration of the C36-C42 subunit of the marine natural product hemicalide by combining stereocontrolled synthesis with NMR, IR and VCD analysis. Diastereomeric model compounds corresponding to the C36-C46 subunit were synthesized for comparison of their ^{1}H and ^{13}C NMR data with those of the natural product. This yielded one compound **1** that shows excellent agreement with the natural product. The relative configuration at C42 could not be established with NMR or X-ray diffraction. First, an attempt was made to determine the relative configuration at C42 using a statistical analysis on calculated and measured NMR chemical shifts. However, different conclusions were reached based on the ^{13}C and ^{1}H spectra, despite of the seemingly high probabilities calculated by the algorithm. We recommend use of both ^{13}C and ^{1}H NMR for such an analysis, and sufficiently high (positive) CP3 values are a necessity if these results are to be used. To make an unambiguous assignment of the relative configuration, a VCD analysis was performed on **4** and **4'**. During these studies, the determination of the absolute configuration of one asymmetric carbon (C42) in these two key epimeric compounds was particularly challenging for VCD analysis due to the high number of conformations of both epimers, and the presence of six stereocenters (C36, C37, C39, C40, C42 and C45). It was shown that the commonly used 6-31G* basis set leads to overestimating the abundance of 'folded' conformers, i.e. conformers possessing intramolecular hydrogen bonding. Since BSSE may lie at the basis of this problem, we recommend the use of a large enough basis set that includes diffuse functions. Also, the use of a solvent model somewhat stabilizes the 'unfolded' conformers, contributing to a more realistic Boltzmann distribution. Finally, although the use of VCD (and IR) can be sufficient to assign the absolute configuration of epimers containing multiple stereocenters, subtracting the spectra of the epimers, for both the calculations and the

experiments, greatly enhances the power to distinguish between the epimers. Since this conceptually eliminates the influence of all but the mirrored stereocenters, the calculated subtraction spectrum is either identical or mirror image of the experimental subtracted spectra, greatly improving the quality of the analysis. The determination of the absolute configuration of C42 in the two key epimeric compounds (**4** and **4'**) allowed the assignment of the relative configuration of the C36-C42 subunit of the marine natural product hemicalide, thereby highlighting the ability and reliability of VCD analysis for structurally and stereochemically complex structures.

As a final note, it should be mentioned that the present VCD work does not allow to establish the absolute configuration of the entire fragment in hemicalide. The relative configuration is now known for the entire C36–C42 substructure but the completely enantiomeric form would fit the NMR data of hemicalide equally well. A noteworthy extra advantage of the current method entailing the study of fragments of the original molecule lies in the fact that one needs to model only small molecules and their relative configuration is the same in the large molecule. This means that e.g., problems related to (un)folding of the large molecule and the possible inadequacies of current DFT functionals to properly account for this are avoided.

Chapter 9

Combined Use of VCD, ROA and NMR in Natural Product Structure Elucidation: the Case of Galantamine

9.1 Introduction

(-)–Galantamine (**1**) (Figure 9.1) is an alkaloid found in the bulbs and flowers of several species from the Amaryllidaceae family, such as the Caucasian snowdrop (Galanthus woronowii), common snowdrop (Galanthus nivalis) and several species of daffodils (Narcissus spp.). It is approved by the European EMA (European Medicine Agency) and the US FDA (Food and Drug Administration) as a competitive inhibitor of acetylcholinesterase (AChE) and an allosteric modulator of the nicotinic acetylcholine receptor. It has been proven effective in the treatment of mild-to-moderate Alzheimers disease.[228,229] Due to the possibly significantly different biological activity of stereoisomers of medicinally active molecules, knowledge of the absolute configuration (AC) of a drug with the desired activity is of prime importance. It may also help in establishing how the drug works. Traditionally, X-ray diffraction[20] (XRD) has been the method of choice in absolute structure elucidation in this field. However, for XRD suitable crystals

are needed, which can be time consuming and sometimes even is impossible.[22,27]

In the past two decades, vibrational optical activity (VOA) methods,[10,44,80] such as vibrational circular dichroism (VCD)[24,42,146,148,230] and Raman optical activity (ROA)[29,231,232] have gained significant interest for stereochemical structure elucidation. This is mainly due to important improvements in instrumentation and simulation software, and the fact that these techniques can be used in the solution phases. This has led to numerous examples of successful determination of the AC of molecules, including many examples for alkaloids and other natural products using VCD[151,212–214,218,219,223,229,233] and/or ROA.[22,221,222,234–236]

In the current work, we investigate the structure elucidation of galantamine,[237] this time using only solution state techniques. This molecule has a complex stereochemistry, with 3 chiral centers, and thus 2^3=8 possible configurations. This allows a proper evaluation of the methods considered in view of their sensitivity towards multiple, nearby chiral centers. On the other hand, the rather rigid structure of galantamine avoids an important bias caused by a too complex potential energy surface with possibly incomplete conformational analysis. This way, the sensitivity to stereochemistry rather than to conformational flexibility of these solution state methods can be assessed. In what follows, we want to use two approaches to establish the AC where in each approach the first step deals with the relative configuration and the second concerns the AC. In the first approach nuclear magnetic resonance (NMR) is used to determine the relative configuration, followed by the second step where chiroptical methods are used to elucidate the absolute configuration. When using chiroptical methods such as VCD and ROA, the underlying unpolarized IR and Raman spectra respectively are routinely recorded as well. In the interest of time and resources, it would be interesting to establish whether the VCD or ROA spectra in themselves could already allow identifying the absolute configuration, thus without prior knowledge of the relative configuration from NMR.

In either approach, the focus lies on quantitative evaluation of experimental and calculated data to simplify interpretation, free of human bias. For the NMR analysis, the DP4 method of Smith and Goodman[69] is used to derive the relative configuration of galantamine from experiment and NMR magnetic shielding calculations.[65,67] For numerical comparison of computed and experimental (chir)optical spectra, we make use of the CompareVOA[1] algorithm and, for the first time on a natural product, the ACreliablity algorithm by Vandenbussche et al.[238] These methods make use of the overlap between experimental and calculated spectra for a certain absolute configu-

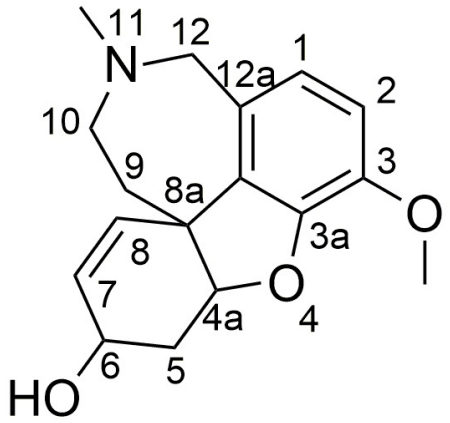

Figure 9.1: Structure and atom numbering of galantamine (**1**).

ration and its enantiomer. Whereas CompareVOA depends on the use of a database of former validated assignments, the ACreliability algorithm makes use of randomized spectra, eliminating bias inherent to the use of a database.

9.2 Experimental Section

9.2.1 Computational Details

Calculation of NMR, VCD and ROA spectra requires all conformers to be taken into account. Therefore, a stochastic conformational search with molecular mechanics force fields was performed on the 4 possible relative configurations shown in figure 9.2. For NMR, IR and Raman these four configurations have the same spectrum as their enantiomer. For VCD and ROA, the spectra of the enantiomers are the exact mirror images of the calculated spectra, justifying that only 4 configurations are calculated. For this, algorithms from the software packages Conflex[125] (reservoir filling) and Spartan 08[124] (Monte Carlo) were used, in combination with the MMFF94S end SYBYL force fields, respectively. These two parallel approaches yield some redundant conformers, which were removed prior to ab initio geometry optimization. All conformers were subsequently optimized at the B3LYP/6-31G* level of theory using Gaussian 09,[64] and all unique conformers within 5 kcal/mol of the most stable were optimized at the B3LYP/aug-cc-pVDZ level. Harmonic frequencies, dipole strengths and rotational strengths were then calculated at the same level of theory for each conformer. To

obtain the respective IR and VCD spectra, harmonic frequencies were scaled with a global scale factor σ optimized for maximum IR similarity using CompareVOA[1] and a Lorentzian broadening function[132] with a full width at half maximum (FWHM) of 10 cm^{-1} was applied for the dipole and rotational strengths. For Raman and ROA spectra the same level of theory was used, and Raman and ROA intensities were calculated with an incident light wavelength of 532 nm. Raman and ROA intensities were broadened with a Lorentzian function with FWHM of 20 cm^{-1}. Finally, magnetic shielding tensors were calculated using Gaussian 09 for comparison with experimental ^{1}H and ^{13}C data. All conformers were re-optimized and isotropic shielding constants were calculated at the mPW1PW91/6-311+G(2d,p) level of theory.[65,204] Isotropic shielding constants were converted to chemical shifts relative to tetramethylsilane (TMS) using linear regression with the experimental chemical shift data. Gauge independent atomic orbitals were used in all calculations, together with a self-consistent reaction field (SCRF) for solvent modelling, using a dielectric constant for chloroform of ϵ=4.71).

9.2.2 Experimental Details

Galantamine was obtained from State Key Laboratory of Applied Organic Chemistry, College of Chemistry and Chemical Engineering, Lanzhou University, Tianshui Nanlu, China.[239]

NMR spectroscopy ^{1}H, ^{13}C, COSY, NOESY and HMQC spectra were recorded in $CDCl_3$ at 400 MHz (^{1}H) and 100 MHz (^{13}C) with TMS as the internal standard. Galantamine (**1**): ^{1}H-NMR (400 Mhz, $CDCl_3$): δ 6.67 (1H, d, J=8.20Hz, CH3OCCHCH), 6.63 (1H, d, J=8.20Hz, CH3OCCHCH), 6.06 (1H, dd, J=10.4, 1.2Hz, CCH=CHCH(OH)), 6.01 (1H, ddd, J=10.4, 5.6, 1.2Hz, CCH=CHCH(OH)), 4.62 (1H, s, ArOCHCH2), 4.15 (1H, t, J=1.2Hz, CH=CHCH(OH)), 4.11 (1H, d, J=15.3Hz, NCH2Ar), 3.84 (3H, s, O-CH3), 3.72 (1H, d, J=15.3Hz, NCH2Ar), 3.30 (1H, dd, J=14.4, 12.8Hz, NCH2CH2), 3.07 (1H, d, J=14.4Hz, NCH2CH2), 2.70 (1H, ddd, J=14.8, 3.3,1.9Hz, OCHCH2CH(OH)), 2.42 (3H, s, NCH3), 2.10 (1H, td, J=12.8,2.8Hz, NCH2CH2), 2.01 (1H, ddd, J=16.0, 5.6, 2.4Hz, OCHCH2CH(OH)), 1.61 (1H, dd, J=10.0, 1.2Hz, NCH2CH2) ; ^{13}C-NMR (100 MHz, $CDCl_3$): δ 146.16 (C, COCH3), 144.54 (C, CH3OCCO), 133.27 (C, NCH2CCCO), 129.50 (C, NCH2CCCO), 128.00 (CH, CCH=CHCH(OH)), 126.93 (CH, CCH=CHCH(OH)), 122.44 (CH, CH3OCCHCH), 111.62 (CH, CH3OCCHCH), 88.96 (CH, CH(OH)CH2CHO), 62.29 (CH, CH=CHCH(OH)),

60.65 (CH2, NCH2Ar), 56.19 (CH3, ArOCH3), 53.96 (CH2, NCH2CH2), 48.41 (C, NCH2CH2CCH=CH), 42.01 (CH3,NCH3), 33.85 (CH2, CH(OH)CH2CHO), 30.19 (CH2, NCH2CH2C)

IR and VCD spectroscopy IR and VCD spectra for Galantamine were recorded on a BioTools ChiralIR-2X spectrometer. All measurements were done in $CDCl_2$ with a concentration of 0.168M. A cell with 100 μm path length and BaF_2 windows was used. Both the sample and the solvent spectrum were recorded with a resolution of 4 cm^{-1}, totaling 30 000 scans each with PEMs optimized at 1400 cm^{-1}. The final baseline corrected VCD spectrum was obtained through subtraction of the solvent spectrum.

Raman and ROA spectroscopy Raman and ROA spectra were recorded on a Chiral RAMAN (BioTools, Inc.) instrument, providing backscattering Raman and ROA (SCP180) data with a resolution of approximately 7 cm^{-1}. Galantamine was recorded in a 1M $CHCl_3$ solution for 420 minutes with a laser power at the source of 100 mW, using a 532 nm excitation wavelength.

9.3 Results and Discussion

In this section we completely determine the relative configuration of galantamine using NMR, and the absolute configuration using vibrational optical activity techniques. Although the use of NMR greatly simplifies the AC analysis using VCD and ROA, we also look into the potency of those techniques for determining the AC without prior knowledge of the relative configuration.

9.3.1 Conformational Analysis

The molecule under study, galantamine, possesses 3 asymmetric carbon atoms (4a, 6 and 8a), yielding $2^3 = 8$ possible absolute configurations. However, it is sufficient to consider only 4 configurations, since NMR is not sensitive to the absolute configuration (e.g. (4a*S*, 6*S*, 8a*S*) has the same NMR features as (4a*R*, 6*R*, 8a*R*)) and for the VOA techniques, we can obtain the spectrum of the enantiomer by simply mirroring the spectrum (i.e. spectrum of (4a*S*, 6*S*, 8a*S*) is the mirror image of the spectrum of (4aR, 6R, 8aR)). Since NMR, VCD and ROA are geometry (i.e. conformation) dependent properties, we have to perform a conformational analysis on all 4 configurations in

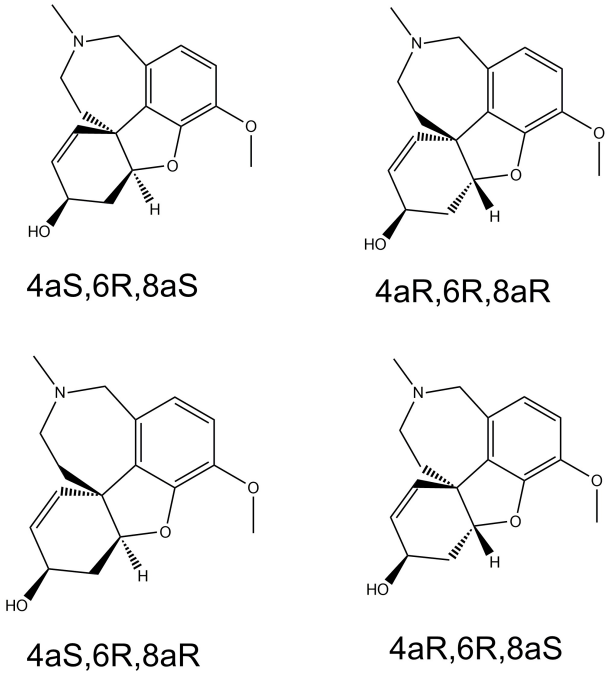

Figure 9.2: The four possible relative configurations of galantamine. NMR can be used to determine to which of these four configurations the natural product corresponds, but for determination of the AC, chiroptical techniques are required.

order to correctly calculate these properties. The 4 configurations considered are (4a*S*,6*R*,8a*S*), (4a*R*,6*R*,8a*R*) , (4a*S*,6*R*,8a*R*) and (4a*R*,6*R*,8a*S*) (see figure 9.2).

Conformational analysis was performed on these four compounds as described in the methods section. The number of minima in the potential energy surface (PES) on the B3LYP/6-31G* level of theory with $\Delta H^\circ < 5.0$ kcal/mole relative to the most stable conformer are shown in table 9.1

It can be seen that the (4a*S*,6*R*,8a*S*) configuration has considerably fewer conformers than the other three configurations. This is because it is the only configuration that allows for an intramolecular hydrogen bond between the alcohol hydrogen and the furan oxygen, largely reducing the flexibility of the 4a-8a six-membered ring. The other three configurations do not have such a restricting hydrogen bond, allowing additional flexibility in that ring.

Configuration	# of conformers
4a*R*,6*R*,8a*R*	40
4a*R*,6*R*,8a*S*	19
4a*S*,6*R*,8a*R*	17
4a*S*,6*R*,8a*S*	7

Table 9.1: Number of minima on the potential energy surface (B3LYP/6-31G*) for the four chosen relative configurations of galantamine.

9.3.2 Assignment of the Relative Configuration

9.3.2.1 NMR Analysis

Traditionally, (1D-)NMR, in combination with COSY, HMQC and NOESY experiments, is used for the determination of the relative configuration of natural products. Although successful, we opt for a different approach that is less labor intensive, can be partially automated and allows us to avoid bias by providing a level of confidence to the assignment of the relative configuration, which is not possible with a manual NMR assignment. This approach starts with the calculation of isotropic shielding constants[65] for all H and C atoms of each conformer of each configuration. We note that these shielding constants are readily available when a VCD calculation is performed. To obtain calculated chemical shifts that can be compared to the ^{1}H and ^{13}C experimental chemical shifts, we perform a linear regression of the shielding constant versus the experimental shifts. This linear regression is shown in figure 9.3 for the ^{1}H NMR experiment with the calculated shift of 4a*S*,6*R*,8a*S*-**1**. The linear regression data for the other diastereoisomers are completely analogous.

This linear fit has several advantages. First of all, the y-intercept gives an estimate for the isotropic shielding constant of the internal standard, most often TMS. This is used to convert the shielding constants to chemical shifts of an atom ($\delta_i = \sigma_{TMS} - \sigma_i$). Second, the slope of the linear fit can be used as a scale factor to correct for the systematic errors in the calculations, due to the many approximations made. Finally, the correlation coefficient r^2 gives a measure for the random error. A high r^2 denotes a tight fit to the experiment, meaning that the calculated shifts give an accurate estimate of the experiment. A lower r^2 is a sign that the experiment is not accurately reproduced, which can suggest that the calculation corresponds to another structure (relative configuration) than the experiment. The scaled calculated shifts can be

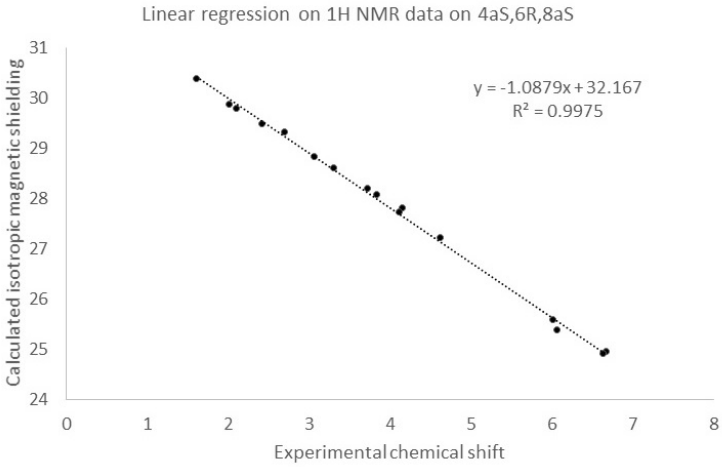

Figure 9.3: Linear regression of the calculated isotropic magnetic shieling for all H-atoms of 4a*S*,6*R*,8a*S*-**1** versus the chemical shifts from the ^{1}H-NMR experiment on galantamine.

obtained as:

$$\delta_i = \frac{intercept - \sigma_i}{-slope} \tag{9.1}$$

In order to evaluate the agreement between these calculated shifts and the experimental ones, two more parameters are computed. The first is the corrected mean absolute error (CMAE), computed as CMAE=$1/n \sum_1^n |\delta_{i,calc} - \delta_{i,exp}|$. The lower the CMAE value, the better the agreement with the experiment. To obtain a level of confidence for an NMR assignment, we also use the DP4 method proposed by Smith and Goodman.[69] In this method, we evaluate the probability that an observed error in chemical shift is obtained by chance for each possible configuration. Using Bayes' theorem, this is converted to the probability that each candidate structure is the correct one. For more information on DP4 probability, we refer to the paper by Smith and Goodman.[69] All ^{13}C and ^{1}H data have been processed this way, and the results are shown in table 9.2.

From table 9.2, it is very clear that for both ^{13}C and ^{1}H the 4a*S*,6*R*,8a*S*-**1** configuration gives the best fit to the experimental data. For this configuration, both ^{13}C and ^{1}H calculations give the lowest value for the CMAE and maximum error ϵ_{max}, and have the highest correlation coefficient r^2. These observations are indeed confirmed by the DP4 analysis, which gives a very high probability for the 4a*S*,6*R*,8a*S*-**1** configura-

Configuration	CMAE	max	r^2	slope	intercept	DP4 probability
^{1}H						
4a*S*,6*R*,8a*S*	0.067	0.183	0.998	-1.088	32.17	99.8%
4a*R*,6*R*,8a*R*	0.132	0.467	0.989	-1.082	32.16	0.2%
4a*S*,6*R*,8a*R*	0.249	0.856	0.963	-1.158	32.41	0.0%
4a*R*,6*R*,8a*S*	0.242	0.864	0.964	-1.175	32.48	0.0%
^{13}C						
4a*S*,6*R*,8a*S*	1.730	5.126	0.997	-1.032	187.50	99.4%
4a*R*,6*R*,8a*R*	2.101	6.208	0.996	-1.026	186.32	0.6%
4a*S*,6*R*,8a*R*	3.334	9.802	0.990	-1.053	188.18	0.0%
4a*R*,6*R*,8a*S*	3.866	12.646	0.985	-1.043	188.30	0.0%

Table 9.2: CMAE, maximum deviation, r^2, and DP4 probability for the comparison of calculated chemical shifts for all four configurations versus the experiments on the natural product. For both ^{1}H and ^{13}C NMR, 4a*S*,6*R*,8a*S*-**1** has the preferred relative configuration. The difference with 4a*R*,6*R*,8a*R*-**1** can however only be confidently established using Bayes' theorem as reflected in the DP4 probability.

tion. The three other configurations have a very small probability of being the correct structure. We also note that if ^{1}H and ^{13}C data are combined in the DP4 analysis, the probability that 4a*S*,6*R*,8a*S*-**1** is the correct structure rises to 100%. These results thus give a very high confidence that galantamine has the 4a*S*,6*R*,8a*S*-**1** or the 4a*R*,6*S*,8a*R*-**1** configuration, since NMR cannot distinguish between both enantiomers. We also note that in the current analysis, we have used the manual NMR assignment to link calculated magnetic shielding data to the correct experimental shift. It is possible to circumvent this manual assignment, by just assigning the lowest calculated shielding to the highest chemical shift and so on. This can save a lot of time on the manual assignment and, at least in this case, gave only very minor changes in linear regression data, and no changes at all in the DP4 analysis.

9.3.2.2 IR and Raman analysis

Although IR is not sensitive to the chirality of a molecule, it can be useful in two ways. First of all, it can aid in the band-to-band assignment of the calculated to the experimental VCD spectra, since vibrational modes in the VCD occur at the exact same wavelength as in the IR. Second, IR can be used to distinguish between diastereomeric configurations as there is no direct relationship between IR spectra of diastereomers.

Looking closely at the IR, we see that overall agreement is satisfying for all con-

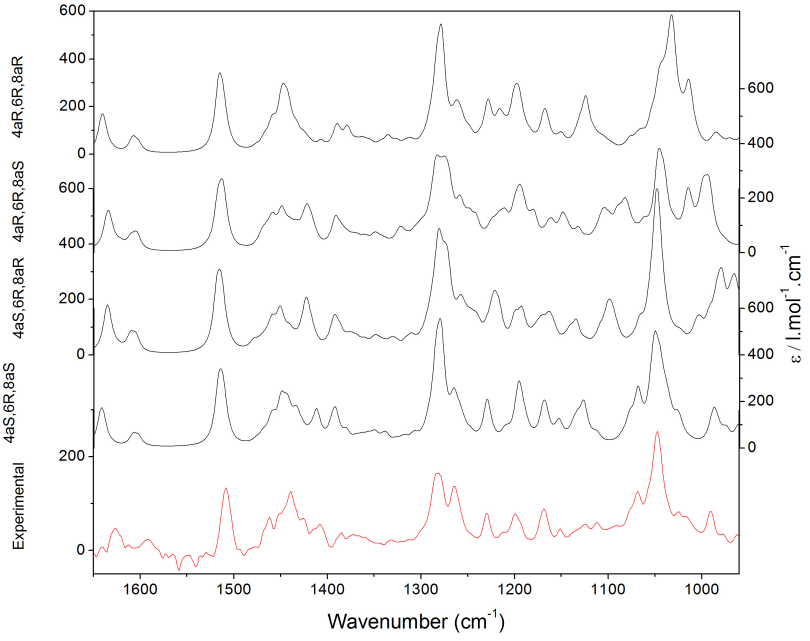

Figure 9.4: Boltzmann weighted calculated IR-spectra for all 4 calculated configurations of **1**, together with the experimental IR (bottom). All 4 configurations have for a large part similar spectra, which makes it hard to draw clear conclusions on the relative configuration of the sample.

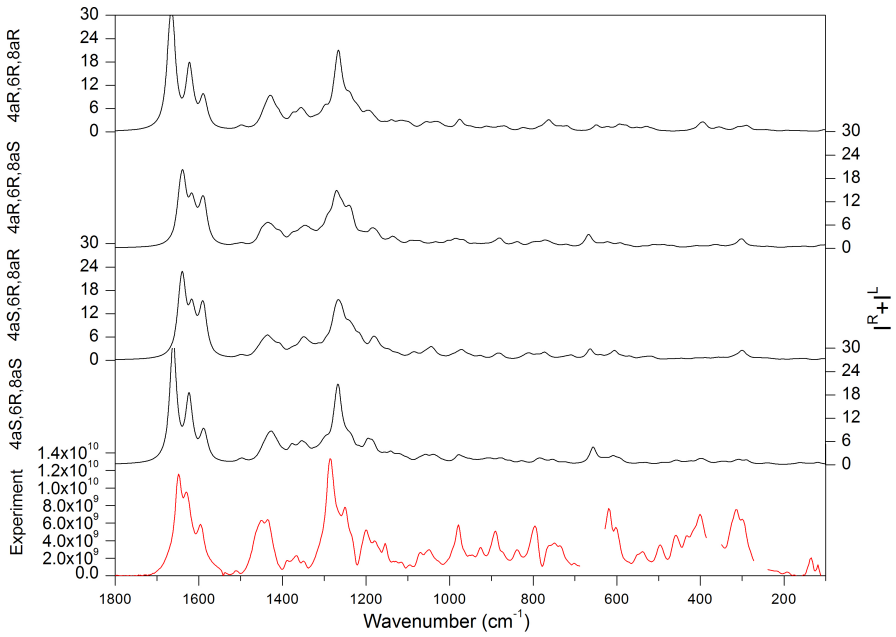

Figure 9.5: Boltzmann weighted theoretical Raman spectra for all 4 configurations considered, together with the experimental Raman (lower). The calculated spectra are very similar and configurational sensitivity is insufficient to draw conclusion regarding the relative configuration of galantamine. The regions deleted in the experimental Raman spectrum are due to strong solvent bands interfering with the spectrum.

figurations. However, the pattern between 970 and 1080 cm^{-1} is most adequately reproduced for the 4a*S*,6*R*,8a*S*-**1** configuration, as is the pattern between 1400 and 1475 cm^{-1}. This way, IR gives a first indication of the relative configuration of galantamine. However, the distinction between the 4 calculated spectra is far too limited to be able to draw any kind of conclusion on the relative configuration.

Looking at the Raman spectra in figure 9.5, we find a similar conclusion as was found for the IR. The main spectral features are similar for all four diastereomers, giving no additional information regarding the relative configuration. We thus find that the unpolarized IR and Raman spectra have insufficient configurational sensitivity to distinguish between multiple diastereomers and cannot directly aid in the determination of the relative configuration. These spectra are still useful however in the band-to-band assignment of their circularly polarized counterparts, VCD and ROA spectra.

To confirm the conclusion on the IR and Raman spectra, we also perform a numeri-

	IR		Raman	
Configuration	**Scale factor**	**Similarity**	**Scale factor**	**Similarity**
4a*R*,6*R*,8a*R*	0.99	88.7	0.997	72.6
4a*R*,6*R*,8a*S*	0.988	92.1	1.002	73
4a*S*,6*R*,8a*R*	0.989	89.4	0.993	80.1
4a*S*,6*R*,8a*S*	0.987	93.4	0.992	74.8

Table 9.3: Similarity of the IR and Raman spectra of all four calculated spectra with the experimental IR and Raman spectra.

cal analysis of the calculated IR and Raman compared with their respective experiments as shown in table 9.3. For the IR all configurations show a rather high similarity, with the value for 4a*S*,6*R*,8a*S*-**1** configuration being the highest. This is in accordance with the visual inspection, but again it is clear that differences between IR spectra are not sufficient for determination of the relative configuration. For the Raman spectra, overall lower similarities are found. This is due to the lack of large bands in the calculated spectra below 1100 cm^{-1}, whereas bands are found in the experiment for this region. Again, there is no configuration showing significantly larger similarity than the other, and hence no relative configuration can be assigned based on the Raman spectra.

In conclusion, linear regression of magnetic shielding constants with experimental chemical shifts is a powerful tool in the determination of the relative configuration of a molecule with multiple stereogenic centers. In addition, the DP4 method allows calculating the probability that a certain configuration corresponds to the experimental spectrum. There is a 100% probability that the 4a*S*,6*R*,8a*S*-**1** configuration has the same relative configuration as the natural product. We also find that the IR and Raman methods are insufficiently sensitive to stereochemical configurations to aid in the determination of the relative configuration of the natural product.

9.3.3 Assignment of the Absolute Configuration

9.3.3.1 VCD analysis

A VCD and ROA analysis of galantamine was performed with two approaches in mind. First, the NMR study gave a very confident assignment of the relative configuration, but is inherently unable to distinguish between enantiomers. This means that after the NMR study we still have two possible configurations for galantamine, namely 4a*S*,6*R*,8a*S*-**1** or its enantiomer, 4a*R*,6*S*,8a*R*-**1**. To distinguish between those two, we

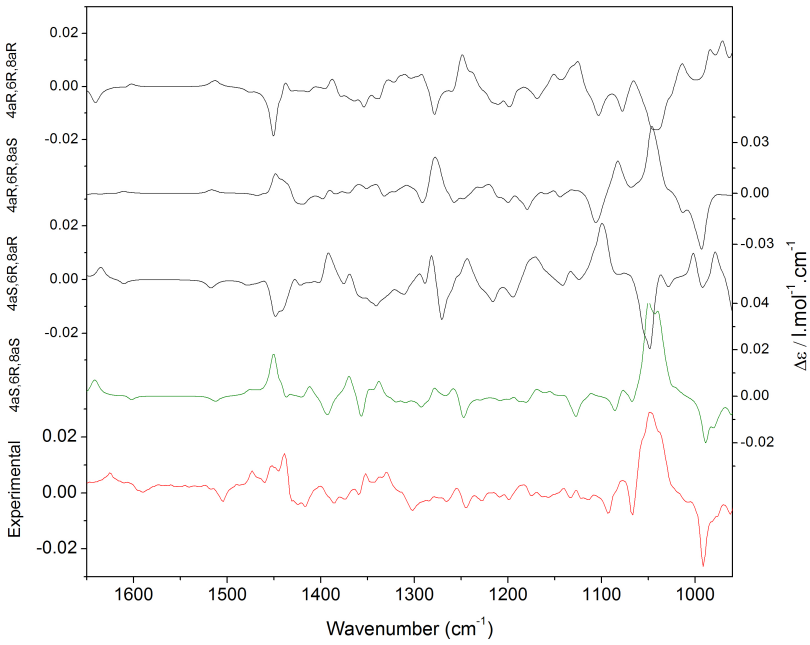

Figure 9.6: Boltzmann weighted calculated VCD-spectra for all 4 calculated configurations of **1**, together with the experimental VCD (bottom). VCD is clearly much more sensitive to changes in the stereochemistry of the molecules. The calculated VCD-spectrum corresponding to 4a*S*,6*R*,8a*S*-**1** has a very good agreement with experiment, whereas for the other configurations, important discrepancies are seen.

can use either VCD or ROA. Also, in this work we want to assess a second approach in which VCD and/or ROA are used for determining the AC without prior knowledge of the relative configuration. Therefore, all chiroptical calculations are performed not only on the 4a*S*,6*R*,8a*S*-**1** configuration, but on all 4 possible relative configurations. The experimental VCD spectrum of galantamine is shown in figure 9.6, together with the Lorentzian broadened and Boltzmann averaged calculated spectra of the four possible configurations.

When only the relative configuration from the NMR analysis is considered (green spectrum), it is clear that the spectrum shown for the 4a*S*,6*R*,8a*S* configuration shows much better agreement with the experiment than its enantiomer, 4a*R*,6*S*,8a*R*-**1**. Looking at all four diastereomers, VCD shows superior sensitivity to configurational changes as compared to IR since in this case important differences between the calculated spectra are present. The full spectrum, and in particular the patterns at 970-1100

cm^{-1}, 1410-1470 cm^{-1} and 1580-1630 cm^{-1} are reproduced adequately only for the 4a*S*,6*R*,8a*S*-**1** configuration. The spectrum for 4a*R*,6*R*,8a*S*-**1** (2nd spectrum from the top in figure 9.6) also gives a good agreement, but critically fails to reproduce the patterns at 1060-1100 cm^{-1}, 1250-1300 cm^{-1} and 1580-1630 cm^{-1}. This allows us to conclude unambiguously that the correct absolute configuration of galantamine is 4a*S*,6*R*,8a*S*. These results are confirmed numerically using the CompareVOA algorithm. For this analysis of the VCD data, we have compared the spectra of all configurations individually to the experimental spectrum. Results of this are shown below in table 9.4.

Configuration	**Scale factor**	Σ^{max}	**ESI**	**CL**
4a*R*,6*R*,8a*R*	0.99	70.5	-60.3	99
4a*R*,6*R*,8a*S*	0.988	74.8	66.8	100
4a*S*,6*R*,8a*R*	0.989	61.7	-51.0	99
4a*S*,6*R*,8a*S*	0.987	86.0	81.5	100

Table 9.4: Neighborhood similarity of the four calculated configurations with the experimental VCD as calculated with the CompareVOA algorithm. 4a*S*,6*R*,8a*S*-**1** has the highest similarity, confirming the visual inspection of the VCD-spectra. Note that the enantiomeric similarity index (ESI) and the confidence level (CL) only have meaning in the case 4a*S*,6*R*,8a*S* and its enantiomer are considered, since these values yield no information towards the preferential agreement of the diastereomers.

In this table, the results of the visual assignment are confirmed. The superior stereochemical sensitivity of VCD is also reproduced in the numerical analysis. We indeed find that 4a*S*,6*R*,8a*S*-**1** has by far the best agreement with the experiment, which is reflected in the high value for Σ^{max}. However, the agreement of the other three configurations is also satisfactory, albeit to a lesser extent than that of 4a*S*,6*R*,8a*S* (Σ^{max} = 86.0). We emphasize that the ESI value, and the corresponding confidence level, give a measure of how much better the agreement of a given configuration with the experiment is in comparison with its enantiomer (e.g. 4a*S*,6*R*,8a*S* vs. 4a*R*,6*S*,8a*R*), but gives no information on how much better the agreement of one configuration is compared to another configuration (diastereomer) (e.g. 4a*S*,6*R*,8a*S* vs. 4a*R*,6*R*,8a*S*). The only way of generating such information is by comparing subtraction spectra of two diasteromers,[116] which is only possible if experimental spectra for both diastereomers are available. We can conclude that the much higher Σ^{max} for 4a*S*,6*R*,8a*S*-**1** in comparison with the other configurations leads to the assignment the AC of galantamine as 4a*S*,6*R*,8a*S*-**1**.

Recently, a statistical validation method for chiroptical spectroscopy methods was developed by Vandenbussche et al.,[238] which allows to evaluate the probability that a random spectrum has better similarity with the experiment than the calculated one. This probability can be expressed in terms of a robustness P of the spectrum. This is particularly useful because this method generates a probability that a given calculated spectrum corresponds to an experimental one, without the need for a database with prior analyses, as is the case for CompareVOA.

The first result coming from this approach is a randomization plot showing the similarity of 25000 random spectra with the calculated one ($R_{x,calc}^{(VCD)}$) on the abscissa and with the experiment ($R_{x,exp}^{(VCD)}$) on the ordinate. In the case of perfect agreement between theory and experiment, this plot generates a straight line with slope 1 and intercept 0, and a correlation coefficient r of 1. Two of these plots, for 4a*S*,6*R*,8a*S*-**1** and for 4a*R*,6*R*,8a*S*-**1**, are shown below. These two configurations were selected because they have the highest similarity with the experiment according to the visual interpretation and both the numerical analyses.

For the case of 4a*S*,6*R*,8a*S*-**1**, the randomization plot is fairly linear, and the actual calculated spectrum has a much higher similarity than any of the randomized spectra. This is also reflected in the correlation coefficient r=0.898. For the 4a*S*,6*R*,8a*S* configuration a similar plot is found, albeit with a more circular distribution of the randomized spectra, yielding a lower correlation coefficient of r=0.732.

The similarity of the randomized spectra with the experiment($R_{x,exp}^{(VCD)}$) follows a normal distribution. From this distribution, one can calculate the corresponding robustness of the calculation, which is the chance that a random spectrum has a smaller similarity with the experiment than the actual calculation. This analysis was performed on all four configurations, and the most important results are summarized in table 9.5.

From table 9.5, it is clear that both the 4a*R*,6*R*,8a*S* and the 4a*S*,6*R*,8a*S* have a high similarity with the experiment and a high robustness. This confirms the conclusion of the CompareVOA analysis. The fact that the 4a*S*,6*R*,8a*S* configuration shows a higher similarity than the 4a*R*,6*R*,8a*S* configuration is a clear indication that the former corresponds to galantamine, but neither algorithm is able to quantify the certainty of this conclusion. Therefore, the manual assignment, in which sometimes subtle but important patterns are only correctly reproduced for the 4a*S*,6*R*,8a*S* configuration, is of key importance in the determination of the absolute configuration of galantamine.

We are able to determine the AC with VCD, without prior knowledge of the rel-

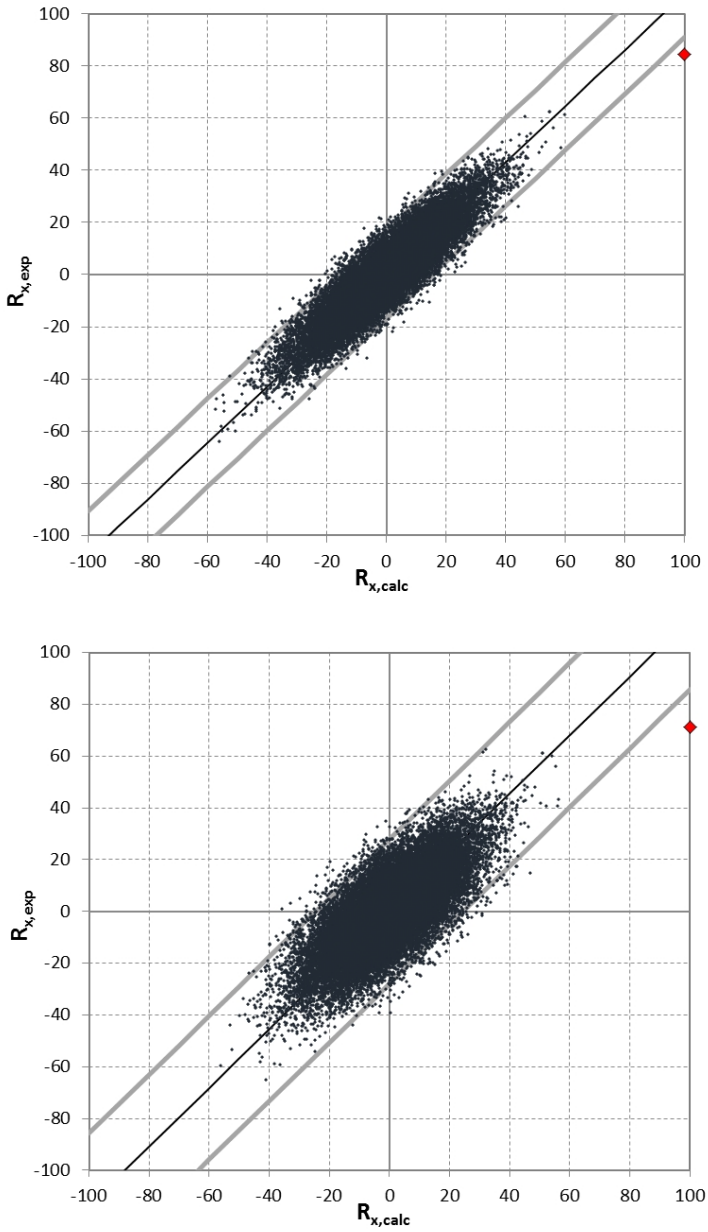

Figure 9.7: Randomization plots for the VCD spectra of 4a*S*,6*R*,8a*S*-**1**(top) and 4a*R*,6*R*,8a*S*-**1**(bottom). Although both configurations show a high similarity with the experiment, the randomization plot for 4a*S*,6*R*,8a*S*-**1** has a tighter distribution and the actual calculated spectrum has by far the highest similarity with the experiment, as indicated by the red dot.

	scalingfactor	IR-similarity	VCD-similarity	Robustness
AC	σ	**R_{fg} (IR) (%)**	**R_{fg} (VCD) (%)**	**P (%)**
4a*R*,6*R*,8a*R*	0.972	87.63	-59.36	99.9886
4a*R*,6*R*,8a*S*	0.972	90.10	71.36	99.9996
4a*S*,6*R*,8a*R*	0.972	89.19	-55.66	99.9690
4a*S*,6*R*,8a*S*	0.967	94.83	84.39	99.9999

Table 9.5: Similarity and robustness of VCD spectra according to Vandenbussche et al. As expected, 4a*S*,6*R*,8a*S*-**1** shows the best similarity, but the other configurations (especially 4a*R*,6*R*,8a*S*-**1**) also show good agreement with the experiment.

ative configuration from NMR. However, the combined use of NMR and VCD gives several advantages. First of all, use of NMR can remove any doubt on the assignment if one of the other diastereomers also has a reasonably high agreement (or Σ^{max}-value). In this case, any doubt arising from the relatively high Σ^{max} for 4a*R*,6*R*,8a*S*-**1** (74.8) is removed by the fact that the NMR agreement of 4a*R*,6*R*,8a*S* was very poor, resulting in a 0.0% DP4 probability that 4a*R*,6*R*,8a*S*-**1** has the correct relative configuration. Moreover, in case the NMR study gives a confident assignment of the relative configuration, the need to analyze VCD spectra of all possible diastereomers is removed. Since (1D-)NMR measurements are very commonly available and calculation of isotropic shielding constants come directly with VCD calculations, such an NMR analysis thus gives a very high confidence to the AC assignment of diasteromers for only a very limited additional cost. We also point out the fact that using linear regression and DP4 analysis removes the need for time consuming (interpretation of) NOESY experiments.

9.3.3.2 ROA Analysis

Parallel with the VCD analysis, we performed a similar ROA analysis on galantamine. ROA is an established tool in the structure determination of proteins and other biological molecules, but its use in the determination of the AC of natural products has been rather limited. The purpose of this study is to evaluate the capabilities of ROA in distinguishing between the 8 possible configurations. We also would want to know whether ROA can be used as a complementary tool to VCD. In other words, is there a clear preference in agreement with experiment for one of two diastereoisomers that have similar agreement in VCD (or NMR)? In the view of this work, this means

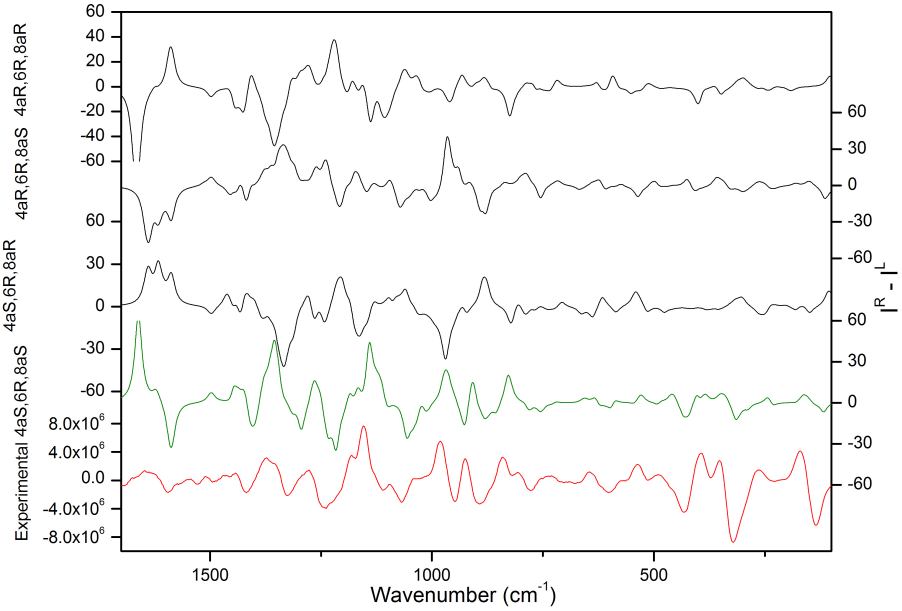

Figure 9.8: Boltzmann weighted theoretical ROA spectra for all 4 considered configurations considered, together with the experimental ROA (lower). The spectrum for 4a*S*,6*R*,8a*S*-**1** has by far the best agreement with the experiment. This again confirms the conclusion of the NMR and VCD analysis.

we want to see whether 4a*S*,6*R*,8a*S* and 4a*R*,6*R*,8a*S*, two configurations that showed rather good agreement with the experiment in the VCD, have significantly different similarity to the experiment for the ROA spectra. This might be the case, since VCD and ROA are two inherently different molecular properties. ROA spectra are shown in figure 9.8. As was the case for VCD, the ROA spectra are much more sensitive to stereochemical differences than their unpolarized Raman counterparts.

In the ROA spectra, as opposed to the Raman equivalents, there are very important differences between configurations. More specifically, only 4a*S*,6*R*,8a*S*-**1** has very good similarity with the experiment, and this for the complete range of the spectrum shown. The 4a*R*,6*R*,8a*S* configuration, which had good similarity in the VCD analysis with the experiment, shows much worse agreement with the ROA experiment. This proves that ROA and VCD are inherently different, and that these two techniques can complement each other in the structure elucidation of complex natural products with multiple chiral

Configuration	Scale factor	Σ_{max}	ESI
4a*R*,6*R*,8a*R*	0.997	46.5	-39.4
4a*R*,6*R*,8a*S*	1.002	37.4	25.7
4a*S*,6*R*,8a*R*	0.993	47.5	-36.5
4a*S*,6*R*,8a*S*	0.992	78.9	69.3

Table 9.6: Neighbourhood similarity of the four calculated configurations with the experimental ROA as calculated with the CompareVOA algorithm. 4a*S*,6*R*,8a*S*-**1** again has the highest similarity, confirming the results stated before. As opposed to the VCD data, the ROA analysis yields a much higher similarity for 4a*S*,6*R*,8a*S*-**1** than any other configuration, providing an unambiguous determination of the AC.

AC	σ	Rfg (Raman) (%)	Rfg (ROA) (%)	P (%)
4a*R*,6*R*,8a*R*	1.001	52.77	-33.94	99.6500
4a*R*,6*R*,8a*S*	1.001	53.69	22.74	93.3955
4a*S*,6*R*,8a*R*	0.997	51.53	-31.75	99.2602
4a*S*,6*R*,8a*S*	0.991	47.87	47.79	99.9949

Table 9.7: Similarity and robustness for ROA spectra according to Vandenbussche et al. Again, 4a*S*,6*R*,8a*S*-**1** shows the best similarity. As opposed to the situation on the VCD analysis, all other configurations perform significantly less.

centers. Additionally, ROA emerges as the superior stand alone method in this case, since only one configuration shows acceptable agreement thus allowing confident AC assignment using only ROA.

Again, these results are quantified using the same two algorithms used for the VCD analysis. The range of 100-1700 cm^{-1} was considered, but results in the range of 750-1700cm^{-1} are analogous. For the CompareVOA analysis (table 9.6), no confidence level was added since this is based on a database which contains only VCD analyses and is thus no measure for the quality of an ROA analysis.

We find that only 4a*S*,6*R*,8a*S*-**1** has a high similarity with the experiment which confirms our manual assignment. Looking at the data and the randomization plot of the method by Vandenbussche et al., we again see that only the 4a*S*,6*R*,8a*S* configuration has decently linear randomization plot (correlation coefficient r=0.650) and a high robustness (P=99.9949%). The 4a*R*,6*R*,8a*S* configuration on the other hand has a rather circular randomization plot, with a poor correlation coefficient of r=0.263 between the experimental and calculated spectrum. This is also reflected in a relatively low robustness P=93.3955.

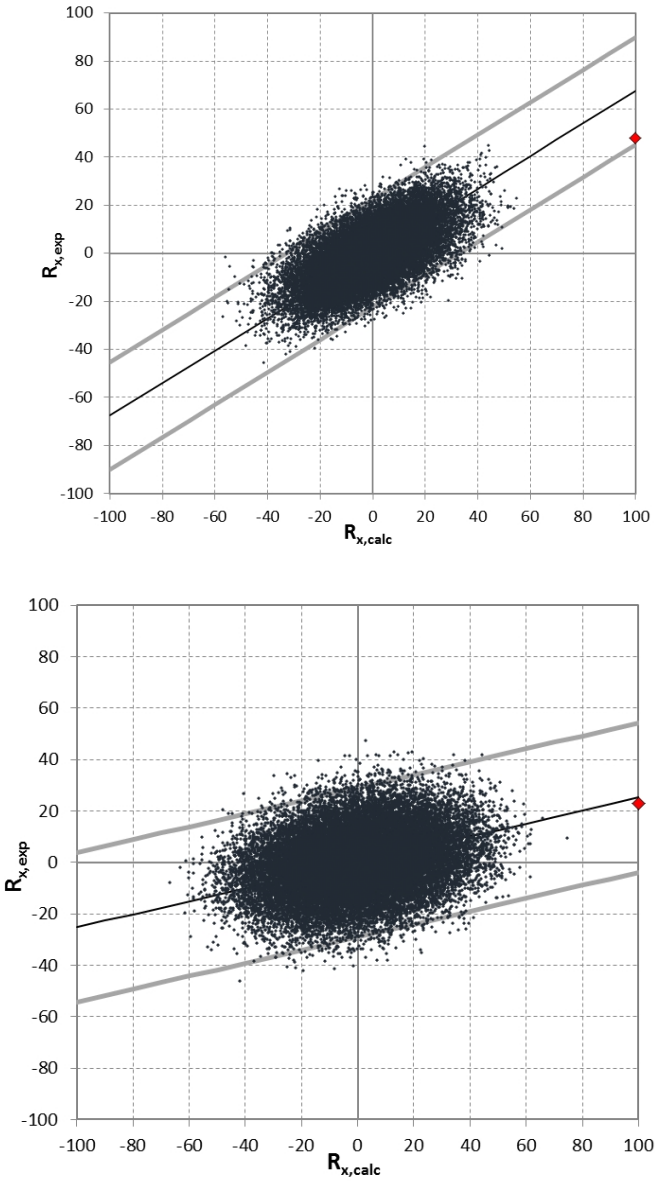

Figure 9.9: Randomization plots for the ROA spectra of 4a*S*,6*R*,8a*S*-**1**(top) and 4a*R*,6*R*,8a*S*-**1**(bottom). Both configurations had an acceptably linear distribution in the case of VCD, but for ROA the 4a*R*,6*R*,8a*S*-**1**(right) shows a rather circular distribution and low correlation, with a large portion of the random spectra showing higher similarity with the experiment than the actual calculation (red dot) as reflected in the low robustness value P.

The same conclusion is consistently found on the AC of galantamine, regardless of the method used for comparing calculated spectra with the corresponding experiment. Also, both VCD and ROA unambiguously lead to the same conclusion. What is really important however is that these methods clearly complement one another: configurations with similar spectra in one technique do not necessarily have similar spectra for the other technique. This was important for the 4a*R*,6*R*,8a*S* configuration, which had very good agreement with the natural product for VCD and the poorest agreement in the ROA. It is therefore stated that a combination of VCD with ROA can definitely have an added value in the AC determination of complex molecules with multiple stereocenters. Additionally, at least in the case of galantamine, the assignment of the AC is more conclusive for the ROA analysis. Whereas for VCD two configurations have rather high similarity with the experiment (cf. table 9.4 and 9.5), the ROA analysis leaves no doubt whatsoever on the AC of galantamine, and is thus preferable as a stand-alone technique (cf. table 9.6 and 9.7).

9.4 Conclusion

In this work, we have investigated the use of three solution state techniques, NMR, VCD and ROA, for the determination of the AC of natural products. Galantamine, which has a known configuration, was chosen for its stereochemical complexity, with 3 chiral centers, and a limited conformational flexibility. In this work, we have considered two pathways towards the determination of the absolute configuration.

In the first pathway, NMR measurements were first combined with quantum chemical calculations of the magnetic shielding constants to easily determine the relative configuration of galantamine without the need for NMR spectrum interpretation and 2D-NMR techniques. Moreover, using the DP4 method, a level of confidence can be attributed to this relative configuration. This way, the configuration was determined as 4a*S*,6*R*,8a*S*-galantamine or its enantiomer, 4a*R*,6*S*,8a*R*-galantamine with a very high level of confidence. In a second step the chiroptical techniques VCD and ROA are used to determine the absolute configuration of galantamine. The calculated VCD and ROA spectra for 4a*S*,6*R*,8a*S*-galantamine were found to have much better agreement with the natural product than its enantiomer 4a*R*,6*S*,8a*R*-galantamine, which enables us to determine the AC of galantamine as 4a*S*,6*R*,8a*S*. Moreover, a high level of confidence was found for the analysis using both CompareVOA and the ACreliability

method of Vandenbussche et al. Since the database used to assign this level of confidence in CompareVOA is comprised of VCD analyses, it is of no relevance in ROA. The robustness value of Vandenbussche et al. however is independent of a database, and thus gives a valid estimation of the level of confidence for both the VCD and ROA analysis.

In the second pathway, the VCD and ROA chiroptical techniques were considered to determine the AC without prior knowledge of the relative configuration of galantamine. In both techniques, we are able to identify 4a*S*,6*R*,8a*S*-galantamine as the correct absolute configuration. However, other diasteromers also show reasonable agreement with the experiment (4a*R*,6*R*,8a*S* in the case of VCD), and it is not possible to assign a level of confidence to the preferential agreement of 4a*S*,6*R*,8a*S*-galantamine compared to the other diastereomers. However, 4a*S*,6*R*,8a*S*-galantamine is the only absolute configuration that has very good agreement for both chiroptical techniques, and thus the combination of those two techniques enhances the discriminatory power of the analysis. From this, ROA appears to be the preferable stand-alone technique over VCD, at least in the case of galantamine. It should be stressed that the confidence level or robustness calculated by both numerical analyses considered gives no information on which diastereomer corresponds best to the molecule under study.

In conclusion, the preferred methodology to determine the AC of natural products with multiple chiral centers is to combine calculated VCD and/or ROA with NMR experiments and calculations, or alternatively, to use ROA experiment and calculations exclusively. Using NMR, we can determine the relative configuration with a given level of confidence, and using that, the absolute configuration can be assigned with a given level of confidence using VCD or ROA. Although ROA is very promising with respect to stereochemical sensitivity and discriminatory power, VCD has the advantage that it is calculated simultaneously with NMR. This combination of VCD and NMR provides an easy-to-use, low effort and reliable methodology for assigning the AC of this natural product. On the other hand, ROA, being inherently complementary to VCD, can be of added value in those cases where even the combination NMR and VCD is not sufficient in the determination of the AC of complex molecules.

Chapter 10

Summary and Conclusions

10.1 Chiral Structure Determination

In this thesis, the use of a collection of solution state methods to determine the stereochemistry, or more specifically the absolute configuration (AC) of an organic molecule, be it synthetic or a natural product, is investigated. The most important of these chiroptical methods for the current research are the so-called vibrational optical activity (VOA) methods, vibrational circular dichroism (VCD) and Raman optical activity (ROA). For VCD, the difference in absorption of left and right circularly polarized light (CPL) by the chiral sample is measured. ROA on the other hand makes use of the differential scattering of the two forms of CPL. These methods share the property that they probe the sensitivity of vibrational transitions of the molecule towards left and right circularly polarized light. This means that there are 3N-6 transitions or normal modes available to aid in the assignment of the AC, which is an important advantage over the other chiroptical methods, electronic circular dichroism (ECD) and optical rotatory dispersion (ORD). For these methods, electronic transitions lie at the basis of the chiral sensitivity, which yields a less information rich spectrum. For ORD, the rotation of the plane of polarization by the chiral sample is measured, whereas ECD is, analogous to VCD, caused by the different absorption of left and right CPL. A final method used frequently in this thesis is nuclear magnetic resonance (NMR) spectroscopy. Other than for the chiroptical methods, NMR is equal for a molecule and its mirror image. Although it has great merit in structure determination, NMR can

thus not be used to assign the AC of a molecule. However, NMR experiments can be compared to calculated NMR chemical shifts to aid in the determination of the relative configuration of molecules with multiple chiral centres.

Although all the chiroptical techniques are inherently different, they are quite similar when it comes to their practical application. Indeed, all chiroptical spectra of enantiomers are mirror images, but no conclusions on the AC can be drawn just looking at the spectra. Therefore, one needs to simulate these spectra for a molecule of a given AC using quantum chemical calculations. This simulated spectrum can then be used as a reference for the interpretation of the experiment. If the signs of the bands are equal in both spectra, the sample has the same AC as the calculated species. If the obtained spectra are mirror images, the sample is the enantiomer of the calculated molecule. Also, these chiroptical properties depend on the molecular geometry. Therefore, a Boltzmann averaged spectrum must be calculated by adding the spectra for each conformer with its respective Boltzmann weight.

The main focus of this thesis lies on VCD spectroscopy. Therefore, the theory of vibrational circular dichroism is discussed in Chapter 2 in some detail. Stephens' equations of VCD are discussed, since these are the expressions incorporated in the available quantum chemical software packages. The other techniques are discussed briefly to achieve a basic understanding of the physical properties involved, and of how these phenomena are related.

In Chapter 3, the experimental set-up of VCD spectroscopy is described. The difference in absorption of left and right CPL is about 4 orders of magnitude smaller than the absorption of unpolarized light. Therefore, one cannot simply subtract the absorption spectra of left and right CPL. To resolve this, a dual modulation technique is used to obtain differential absorption spectra with an acceptable signal-to-noise ratio (S/N): not only is the linearly polarized light Fourier transformed (as is the case for conventional FT–IR spectroscopy), a second modulation is added by transforming the linearly polarized light to sinusoidally varying left and right circularly polarized states. Using a lock-in amplifier (LIA), this high frequency polarization modulated signal can be extracted from the slower Fourier modulation. It is shown how by dividing these Fourier transformed signals one obtains the VCD signal. Linear birefringence in the optical path of the spectrometer makes the baseline deviate from zero. Although this is for a large part resolved by using a dual PEM set-up, all spectra in this thesis are shown after subtracting the solvent baseline.

10.2 Results

Chapter 4 embodies the transition from the background information of this thesis to the results section. As explained before, the assignment of the AC is possible only by comparing the experimental VCD (or ROA) spectrum with the calculated one. Due to the many approximations made during simulation of these spectra, this comparison is not always straightforward. To quantify the validity of the AC assignment made, a method is proposed that ascribes a confidence level to the determination of the AC. We use a neighbourhood similarity algorithm that is extended to the use of VCD by considering the positive and the negative parts of the VCD spectra separately. By calculating the overlap between the theory and the experiment for both enantiomers, two quantities are measured. Σ is a measure for the similarity of each of the enantiomers with the experiment. By subtracting these Σ values for both enantiomers, the enantiomeric similarity index Δ is obtained, which is a measure for the discriminative power of the VCD analysis between both enantiomers. By comparing these two quantities to the values in a database of validated AC assignments, one can assign a level of confidence to the pending VCD analysis. As can be seen in the following chapters, this CompareVOA algorithm should be used as a quantification and validation of a manual AC assignment.

The first application of these methods is discussed in Chapter 5, in which the AC of 3-(1'-hydroxyethyl)-1-(3'-phenylpropanoyl)-azetidin-2-one, a medium-sized but quite flexible molecule with two chiral centers is assigned. At least in this case, it was found that VCD is able to distinguish not only between enantiomers, but between four possible diastereoisomers generated by the two stereogenic centers. This result was obtained by thorough band-to-band analysis of the IR and VCD spectra, allowing subtle differences to be identified. Due to their limited information richness, this result could not be obtained using ORD or ECD. It was also established that ORD is more sensitive to changes in approximate Boltzmann weights, which depend on the level of theory used for the DFT calculations. Finally, the concept of robust modes was studied in the case of conformationally flexible molecules. A normal mode of vibration is termed robust if the angle between the electric and magnetic dipole transition moment deviates sufficiently from 90°. However, little coherence was found for the robustness of normal modes between different conformers. Only normal modes involving carbonyl stretching seem to be consistently non-robust.

This mode of operation is continued in Chapter 6. Here, the stereochemical char-

acterization of 5-(3-bromophenyl)-4-hydroxy-5-methylhexan-2-one, a natural product building block, is done. Again, a conformational analysis was performed, and three chiroptical techniques were used to assign the AC. Since only one chiral center is involved in the molecule under study, a decisive conclusion is reached for each of the chiroptical methods. As before, VCD has the most detail, and shows almost perfect agreement with the experiment. Surprisingly, this excellent agreement is not reflected in a very high confidence level using the CompareVOA algorithm. The reason for this was found to be the value of the triangular weighting function l used in the calculation of the neighbourhood similarity. It was suggested that in cases where the frequency alignment of the theoretical and experimental spectra is nearly perfect, a smaller weighting function is used (20 $cm^{-1} \rightarrow 10$ cm^{-1}), significantly enhancing the discriminative power between both enantiomers.

In Chapter 7, VCD, ORD and ECD are combined again to assign the stereochemistry of all four diastereoisomers of tadalafil, a natural product useful in the treatment of erectile dysfunction, pulmonary arterial hypertension and benign prostatic hyperplasia. Using VCD, the complete stereochemical characterization of all 4 compounds can be done without prior knowledge of their relative configuration as opposed to ECD and ORD. Also, NMR experiments are combined with the calculation of NMR magnetic shielding constants to confirm the relative stereochemistry of tadalafil. These shielding constants are converted to chemical shifts using linear regression with the experimental data. Also, a level of confidence can be obtained for this NMR study using the CP3 method.

The complexity of molecules studied using chiroptical spectroscopy reaches a new level in Chapter 8. The structure of hemicalide, a marine natural product with 21 chiral centers is determined. The relative configuration of two subunits of hemicalide was established in previous studies, combining extended synthesis and NMR studies. For the final fragment, C36–C45, these methods were unable to determine the stereochemistry of one stereogenic center, C42. Therefore, attention was turned to chiroptical spectroscopy. Two model compounds, epimers in C42, were synthesized and only for one of those epimers the experimental NMR matches that of the natural product. Unfortunately, the relative configuration at C42 could not be established using conventional (2D-)NMR. First, an attempt was made to determine the relative configuration by combining NMR experiments of the two model compounds with calculated magnetic shielding constants using the CP3 analysis. To this end, slightly less flexible derivatives with the same stereochemistry for the 6 chiral centers were made of the model com-

pounds that serve as test molecules for both the VCD and NMR analysis. Different conclusions were reached based on the ^{1}H and ^{13}C data for the CP3 analysis which thus remains inconclusive. Therefore, we recommend the use of both NMR spectra in determining the relative configuration. A second attempt to determine the stereochemistry at C42 was made using VCD spectroscopy. In the conformational analysis, the abundance of 'folded' conformers, showing intramolecular hydrogen bonding, was heavily overestimated in solution state. This is probably due to basis set superposition error (BSSE), which could for a large part be resolved using a large enough basis set (aug-cc-pVDZ) that includes diffuse functions. Also, the 'unfolded' conformers were stabilized when a solvent sphere was added using a polarizable continuum model (PCM). Consistent with previous findings, VCD has superb sensitivity to chirality, and is able to distinguish between epimers for which five out of six chiral centers are equal. The discriminative power is enhanced even further when experimental and theoretical subtraction spectra of the epimers are considered.

In the final chapter, ROA is added as a final chiroptical technique to determine the AC of the natural Alzheimer drug galantamine. This molecule has three chiral centers and thus eight possible configurations, but has a rigid structure. This way, the sensitivity of all techniques to multiple chiral centers, rather than to conformational flexibility can be assessed. Two pathways are considered to obtain an AC assignment. First, calculated NMR spectra for the 4 possible relative configurations are compared to the experimental NMR of the natural product using the DP4 algorithm. The relative configuration could be determined this way with a high level of confidence. Using VCD and/or ROA, the AC was then determined. This time, a second algorithm, next to CompareVOA, was used to ascribe a level of confidence to the ROA or VCD analysis. The ACreliability method is independent of a database, and thus gives a value that is also of relevance for the ROA analysis. In the second pathway, VCD and ROA were evaluated as stand alone techniques, i.e. their potency to determine the AC out of 8 possible configurations, without prior knowledge of the relative configuration using NMR, is established. Although both methods indicate the same configuration as the one corresponding to galantmaine, the assignment using ROA is much more conclusive than that with VCD. From this, we can conclude that ROA is at least in the case of galantamine the preferable stand-alone technique. On the other hand, the addition of an NMR analysis requires little extra effort when VCD is considered, since NMR experiments are routinely available and NMR magnetic shielding constants are part of the output of VCD calculations.

10.3 Conclusion and Outlook

As a general conclusion of this dissertation, it can be stated that vibrational optical activity has an enormous potential as methodology for the stereochemical structure determination of large, flexible organic molecules and natural products. In order to make a confident AC assignment using these techniques, special attention needs to be paid to an extensive conformational analysis and consideration of possible solvent effects. In some cases only a combination of chiroptical techniques and NMR can yield the expected result. It was found consistently throughout this research that ORD and ECD do not have the same information richness as VOA methods, and thus have little added value in the structure determination. For cases with multiple chiral centers however, combination of NMR experiments with calculation of NMR magnetic shielding constants can significantly aid in the structure determination.

Therefore, the challenge is to apply this set of methods to increasingly complex molecules, with an increasing number of chiral centers. Molecules of the likes of hemicalide (or its subunits) could possibly be analysed using only chiral spectroscopy, without the need for extensive time-consuming syntheses. By increasing complexity, new challenges will most likely emerge, related to increasing conformational flexibility, solvent effects and functional groups leading to poor reproduction of chiroptical spectra. The use of solvent models for determining possible solvent effects, computational methods that allow for a correct description of challenging functional groups, such as sulfoxides, and localized modes to interpret features arising from complex, large molecules are first steps, yet to be thoroughly explored, towards expanding the range of applicability of the chiroptical methods used in this thesis.

Chapter 11

Samenvatting

11.1 Chiraliteit

Het onderzoek van dit doctoraat draait rond het begrip chiraliteit. Een voorwerp is chiraal wanneer zijn spiegelbeeld niet superponeerbaar is op het origineel. Een tastbaar voorbeeld hiervan zijn onze handen (in het Grieks '$\chi\epsilon\iota\rho$' of *cheir*). Deze zijn elkaars spiegelbeeld maar zijn niet superponeerbaar. Het verschil tussen de zogeheten enantiomeren uit zich vooral wanneer ze in contact worden gebracht met andere chirale voorwerpen, zoals onze handen met handschoenen. Op moleculair niveau speelt chiraliteit een erg belangrijke rol. Niet alleen zijn veel moleculen waarmee we in contact komen, zoals geneesmiddelen, voedings- en smaakstoffen, natuurlijke producten, ... chiraal, ook ons lichaam bestaat voor een belangrijk deel uit chirale moleculen. Zo zijn er eiwitten, die volledig zijn opgebouwd uit L-aminozuren, of koolhydraten die bestaan uit D-monosaccharides. Wanneer de chirale moleculen in contact komen met de chirale eiwitten en enzymen in ons lichaam, gaan deze bijgevolg verschillend interageren. Dit verschil in interactie worden we gewaar als bijvoorbeeld een verschillende geur van de twee spiegelbeelden (of enantiomeren) van de molecule limoneen: Sinaasappels halen hun geur van (*R*)-limoneen, terwijl de geur van citroenen veroorzaakt wordt door het andere enantiomeer van deze molecule, (*S*)-limoneen. De benaming van de absolute configuratie (AC) van deze moleculen volgt het principe van Cahn-Ingold-Prelog. Daarbij wordt aan elke chiraal centrum een *R* ('rectus') of *S* ('sinister') toegekend. Voor molecules met meerdere chirale centra, moet voor elk van de chirale

centra de configuratie bepaald worden. Molecules met meerdere chirale centra die isomeren zijn, maar geen enantiomeren (die dus verschillen in minstens 1, maar niet alle chirale centra) worden diastereoisomeren genoemd.

Wanneer het gaat over farmaceutische stoffen zijn de gevolgen van chiraliteit op het lichaam ingrijpender. Vaak is er een verschil in activiteit tussen beide enantiomeren van een farmaceutisch ingredient. Waar het ene enantiomeer de gewenste werking vertoont, kan het spiegelbeeld inactief zijn, of zelfs ongewenste tot dramatische effecten vertonen. In beide gevallen is het voordeliger om dus enkel het werkzame enantiomeer toe te dienen. Vandaar dat zowel de farmaceutische industrie als de regulerende instanties hun voorkeur uiten voor het toedienen van enkel het werkzame enantiomeer (enantiopuur), eerder dan het mengsel van beide enantiomeren (racemaat). Het is daarbij van groot belang (de absolute configuratie van) het werkzame enantiomeer te kunnen identificeren, en dit vormt het onderwerp van het huidig doctoraatsonderzoek.

11.2 Structuurbepaling

Dit onderzoek handelt over het bepalen van de stereochemie van chirale moleculen, in het bijzonder van farmaceutische en natuurlijke producten. Enkele technieken zijn hiervoor beschikbaar, allen met hun voor- en nadelen. In dit gedeelte wordt een kort overzicht van de bestaande technieken gegeven, met de focus op de technieken die gebruikt worden voor het onderzoek in deze thesis. Misschien de meest courante techniek is X-straal diffractie. Hierbij worden X-straal fotonen op een kristal van het te onderzoeken staal gericht, en het diffractiepatroon wordt geobserveerd. Hieruit kan dan de 3D-structuur van het onderzochte staal bepaald worden. Hoewel deze techniek gekend staat als betrouwbaar, is ze slechts toepasbaar op moleculen waarbij zware atomen (P,S,...) aanwezig zijn en waarvoor bovendien kristallen van goeie kwaliteit beschikbaar zijn.

Dit laatste vormt niet zelden een beperking van X-straal diffractie (XRD) en voor deze gevallen bieden chiroptische technieken, die in oplossing toegepast kunnen worden, een alternatief. Onder chiroptische technieken wordt een verzameling technieken verstaan die gebaseerd zijn op de verschillende interactie van chirale moleculen met links- of rechtsdraaiend circulair gepolariseerd licht. Voor deze technieken geldt dat de geobserveerde grootheid tegengesteld is van teken voor beide enantiomeren. Spijtig genoeg is uit het spectrum niet rechtstreeks op te maken welke AC het betrokken

staal heeft. Daarom worden de opgemeten spectra vergeleken met kwantumchemisch berekende spectra van een molecule van een gekende absolute configuratie.

Voor electronisch circulair dichroïsme (ECD) en optische rotatie dispersie (ORD) gaat het om circulair gepolariseerd licht uit het UV-Vis gebied van het spectrum. Hoewel voor beide technieken electronische excitaties van de molecule aan de basis van het fenomeen liggen, gaat het bij ECD om een verschil in absorptie van links en rechts circulair gepolariseerd licht en bij ORD over verschillende brekingsindices voor beide polarisatietoestanden. Het nadeel van beide technieken is dat er weinig signalen beschikbaar zijn voor de toewijzing van de absolute configuratie.

Dit probleem wordt verholpen wanneer circulair gepolariseerd licht uit het infrarood (IR) gebied van het spectrum gebruikt wordt. De energie van deze elektromagnetische straling veroorzaakt vibrationele transities in de molecule. Een molecule telt 3N-6 mogelijke vibrationele transities of normaalmodes (met N het aantal atomen in de molecule), waardoor de overeenkomstige spectra rijker zijn aan informatie. Twee technieken in het IR-gebied worden gebruikt in deze thesis, die samen vibrationele optische activeit (VOA) gedoopt werden. Een eerste techniek, Raman optische activiteit (ROA), steunt op het feit dat chirale moleculen een verschillende inelastische verstrooiing veroorzaken voor links en rechts circulair gepolariseerd licht. ROA wordt veelvuldig toegepast op grote biomoleculen zoals eiwitten, maar op het einde van deze onderzoeksthesis wordt ze toegepast op een farmaceutisch natuurproduct. De techniek die veruit de meeste aandacht geniet in dit onderzoek is vibrationeel circulair dichroïsme. VCD is volledig analoog aan ECD, met dat verschil dat het resulterende spectrum veer rijker is aan informatie en detail wegens de beschikbaarheid 3N-6 vibrationele overgangen in het IR-gebied.

11.3 Doelstelling

In dit onderzoek wordt bepaald in welke mate de chiroptische technieken geschikt zijn als alternatief voor bvb. XRD voor het bepalen van de absolute configuratie van relatief grote farmaceutische molecules en natuurproducten. Gedurende de startfase van het onderzoek was VCD al een vaak gebruikte techniek om de AC van relatief kleine, starre chirale moleculen te bepalen. Het doel van dit onderzoek was om te bestuderen in welke mate de techniek gebruikt kan worden voor de structuurbepaling van grotere, flexibele molecules, met meerdere chirale centra. In eerste instantie werd VCD hiertoe

aanzien als de basistechniek, die eventueel kan aangevuld worden met ECD of ORD. In een latere fase werden ook NMR en ROA toegevoegd aan dit pallet van technieken. Er wordt onderzocht of de bijkomstige technieken daadwerkelijk een toegevoegde waarde geven aan de VCD analyse, en welke methodologie of combinatie van technieken het beste overweg kan met meerdere chirale centra en een grote conformationele flexibiliteit. Bovendien werd onderzocht hoe het vergelijken van berekende spectra met het experimentele spectrum op een objectieve manier gekwantificeerd kan worden, en hoe een betrouwbaarheid kan worden toegekend aan een VCD analyse.

11.4 Resultaten en Conclusie

In deze thesis zijn enkele resultaten ondergebracht in 5 verschillende hoofdstukken. In het eerste daarvan, hoofdstuk 4, wordt een algoritme besproken om een maat van overeenkomst tussen het berekende en experimentele VCD spectrum bekomen. Immers, door de vele benaderingen gebruikt in de berekening van de spectra, en mogelijk ook door artifacten in de metingen, is er niet altijd een perfecte overeenkomst tussen beide spectra. Om de geldigheid van een VCD (of ROA) analyse te beoordelen, wordt daarom een methode voorgesteld dat een betrouwbaarheidsniveau toekent aan de analyse, op basis van de similariteit Σ van het berekende spectrum met het experiment enerzijds, en het spiegelbeeld van dat experimentele spectrum anderzijds. Het verschil tussen deze twee similariteiten, Δ, is een maat voor de kracht van de analyse om een onderscheid te maken tussen beide enantiomeren. Door deze Σ en Δ waarde vervolgens te vergelijken met de waarden van vorige, onafhankelijk gevalideerde analyses, kan een betrouwbaarheid toegekend worden aan de lopende VCD analyse. Dit algoritme ligt ook aan de basis van het CompareVOA softwarepakket, en wordt doorheen de rest van het onderzoek veelvuldig gebruikt voor het kwantificeren van de onderzoeksresultaten.

Daarna worden vier *case studies* gebruikt om het gebruik van chiroptische technieken voor de structuurbepaling van organische moleculen te beoordelen. In het eerste geval wordt een vrij grote en vooral flexibele molecule, 3-(1'-hydroxyethyl)-1-(3'-phenylpropanoyl)-azetidin-2-one, bestudeerd. Deze molecule heeft met zijn twee chirale centra dus vier mogelijke configuraties. Het bleek dat met een zorgvuldige analyse van het VCD spectrum, in combinatie met zijn bijhorend IR spectrum, men in staat is om met grote betrouwbaarheid de AC van de molecule volledig toe te wijzen. ECD en ORD daarentegen blijken weinig toegevoegde waarde te hebben. Het concept

van robuuste modes wordt ook getest op flexibele molecules. Een vibrationele normaal mode is robuust in VCD spectroscopie wanneer de hoek tussen het elektrisch en het magnetisch dipooltransitiemoment minstens 30° afwijkt van 90°. Dit concept is echter niet waardevol voor dergelijke molecules, gezien geen consistentie werd gevonden voor een bepaalde normaalmode over de verschillende conformeren.

In hoofdstuk 6 gaan we op hetzelfde stramien verder. Hier wordt de structuurbepaling van 5-(3-bromophenyl)-4-hydroxy-5-methylhexan-2-one aangepakt, een precursor voor de synthese van natuurproducten met 1 chiraal centrum. Opnieuw blijkt dat VCD veruit de krachtigste techniek is, en wordt er een sterke overeenkomst gevonden tussen theorie en experiment. Vreemd genoeg leidde dit niet tot een hoog betrouwbaarheidsniveau volgens de CompareVOA analyse. Uit onderzoek bleek dit veroorzaakt te worden door een bijna perfecte overeenkomst tussen de berekende en experimentele frequenties. Hierdoor wordt, door het in rekening nemen van de omgevingspunten van elk punt van het experimenteel spectrum, een artificieel hoge similariteit verkregen voor het verkeerde enantiomeer, wat op zijn beurt aanleiding geeft tot een relatief lage Δ waarde. Het verkleinen van de breedte van de driehoeks weegfunctie l tot 10 cm^{-1}, biedt hiervoor een oplossing.

Daarna, in hoofdstuk 7, wordt voor het eerst ook gebruik gemaakt van NMR experimenten met bijhorende berekeningen. Dit wordt toegepast op tadalafil, een natuurproduct met twee chirale centra en dus vier mogelijke configuraties. Opnieuw is enkel VCD in staat om op een correcte en betrouwbare manier de AC toe te wijzen. Met de NMR berekeningen en de CP3 methode, kunnen we nu bovendien de relatieve configuratie valideren, wat zorgt voor een toegevoegde betrouwbaarheid van de analyse.

In hoofdstuk 8 bereikt de complexiteit van de bestudeerde molecule een nieuw hoogtepunt. Het marien natuurproduct hemicalide heeft niet minder dan 21 chirale centra. De molecule wordt opgesplitst in drie onderdelen. Van de eerste twee wordt met behulp van synthese methodes en experimentele NMR studies de relatieve configuratie bepaald. Dit blijkt echter niet mogelijk voor het derde en laatste fragment: het C36–C45 fragment. Immers, voor chiraal centrum C42 blijkt geen enkele tot dan gebruikte *conventionele* methode afdoende informatie aan te leveren om de configuratie te bepalen. Daarom werden van beide modelstructuren twee derivaten bereid, een voor elke configuratie ter hoogte van C42. Deze werden op hun beurt onderworpen aan een VCD studie. Tijdens de conformationele analyse werd een overschatting van de hoeveelheid *opgevouwen* conformeren vastgesteld. Dit kwam door een overschatting van

de stabilisatie-energie van intramoleculaire waterstofbruggen. Aan de oorzaak hiervan lag vermoedelijk *Basis Set Superposition Error* of BSSE, wat grotendeels opgelost kan worden door gebruik van voldoende grote basis sets met diffuse functies, in combinatie met een *Polarizable Continuum Model* solvent modelering. Eerst werd geprobeerd om met behulp van NMR berekeningen en de DP4 methode toch de relatieve configuratie te bepalen van C42, maar dit bleek ook nu niet mogelijk, gezien de tegenstrijdige resultaten voor de ^{1}H NMR analyse enerzijds en de ^{13}C analyse anderzijds. Dit duidt ook op het belang van het gebruik van beide NMR spectra in dergelijke NMR analyse. Met VCD daarentegen, waren we in staat om onderscheid te maken tussen twee epimeren waarvoor 5 van de 6 chirale centra gelijk waren. Een extra hulp voor deze VCD analyse was het gebruik van *subtraction* spectra, waarbij enerzijds experimentele VCD spectra van beide derivaten afgetrokken worden, en anderzijds de berekende spectra van beide model structuren. Vergelijking van deze subtractie spectra levert een erg betrouwbare VCD analyse op.

In het laatste hoofdstuk wordt de absolute configuratie van galantamine, een stof werkzaam tegen de ziekte van Alzheimer, bepaald. Deze molecule heeft drie dicht gelegen chirale centra maar is toch relatief star, waardoor de gevoeligheid van de gebruikte technieken aan stereochemie, eerder dan aan conformationele flexibiliteit bestudeerd kan worden. Naast de gebruikelijke chiroptische technieken en NMR, wordt voor deze analyse ook beroep gedaan op ROA spectroscopie. Voor de volledige structuurbepaling worden twee werkwijzes gehanteerd. In de eerste werkwijze wordt eerst de relatieve configuratie bepaald met NMR experimenten en berekenigen, gecombineerd met een DP4 analyse. Daarna werd de AC bepaald met VCD en/of ROA, met overtuigend resultaat. Daarnaast werd getest of VCD en/of ROA in staat zijn om zonder voorkennis van de relatieve configuratie de correctie absolute configuratie te onderscheiden uit de acht mogelijke configuraties. Hieruit blijkt dat, hoewel beide methodes de correcte configuratie aanduiden, de ROA analyse een veel duidelijkere conclusie verschaft. Daarom lijkt, op zijn minst in dit geval, dat ROA de te verkiezen *stand-alone* techniek is. Anderzijds zijn NMR berekeningen een onderdeel van VCD berekeningen, waardoor het toevoegen van een NMR analyse aan een VCD berekening slechts een kleine extra moeite vergt.

Als algemeen besluit kunnen we stellen dat vibrationele optische activiteit, met name VCD en ROA, een groot potentieel hebben voor de structuurbepaling van grote, flexibele molecules met meerdere chirale centra. Een zorgvuldige conformationele analyse en nauwkeurige visuele interpretatie van de spectra, in combinatie met het Com-

pareVOA algoritme zorgen steevast voor een betrouwbare toewijzing van de absolute configuratie. Voor moeilijke gevallen zorgt combinatie van deze technieken, eventueel met een bijkomstige NMR analyse, zonder meer voor een toegevoegde waarde. Het gebrek aan detail in ORD en ECD spectra daarentegen zorgen voor weinig extra informatie in vergelijking met de VOA methodes.

Bibliography

[1] E. Debie, E. De Gussem, R. Dukor, W. Herrebout, L. Nafie, and P. Bultinck. "A Confidence Level Algorithm for the Determination of Absolute Configuration Using Vibrational Circular Dichroism or Raman Optical Activity". In: *Chemphyschem* 12.8 (2011), pp. 1542–1549.

[2] E. De Gussem, P. Bultinck, M. Feledziak, J. Marchand-Brynaert, C. V. Stevens, and W. Herrebout. "Vibrational Circular Dichroism versus Optical Rotation Dispersion and Electronic Circular Dichroism for diastereomers: the stereochemistry of 3-(1 '-hydroxyethyl)-1-(3 '-phenylpropanoyl)-azetidin-2-one". In: *Physical Chemistry Chemical Physics* 14.24 (2012), pp. 8562–8571.

[3] F. Cherblanc, Y. P. Lo, E. De Gussem, L. Alcazar-Fuoli, E. Bignell, Y. A. He, N. Chapman-Rothe, P. Bultinck, W. A. Herrebout, R. Brown, H. S. Rzepa, and M. J. Fuchter. "On the Determination of the Stereochemistry of Semisynthetic Natural Product Analogues using Chiroptical Spectroscopy: Desulfurization of Epidithiodioxopiperazine Fungal Metabolites". In: *Chemistry-A European Journal* 17.42 (2011), pp. 11868–11875.

[4] E. De Gussem, J. Cornelus, S. Pieters, D. Van den Bossche, J. Van der Eycken, W. Herrebout, and P. Bultinck. "Synthesis of the Natural Product Building Block 5-(3-Bromophenyl)-4-hydroxy-5-methylhexan-2-one and its Chiral Characterization by Using Chiroptical Spectroscopy". In: *ChemPhysChem* 14.14 (2013), pp. 3255–3262.

[5] S. Qiu, E. De Gussem, K. A. Tehrani, S. Sergeyev, P. Bultinck, and W. Herrebout. "Stereochemistry of the Tadalafil Diastereoisomers: A Critical Assess-

ment of Vibrational Circular Dichroism, Electronic Circular Dichroism, and Optical Rotatory Dispersion". In: *Journal of Medicinal Chemistry* 56.21 (2013), pp. 8903–8914.

[6] E. De Gussem, W. Herrebout, S. Specklin, C. Meyer, J. Cossy, and P. Bultinck. "Strength by Joining Methods: Combining Synthesis with NMR, IR, and Vibrational Circular Dichroism Spectroscopy for the Determination of the Relative Configuration in Hemicalide". In: *Chemistry A European Journal* (2014).

[7] L. D. Barron. "Chemistry: Chirality, magnetism and light". In: *Nature* 405.6789 (2000), pp. 895–896.

[8] W. Kelvin. *The Molecular Tactics of a Crystal*. Robert Boyle lecture. Clarendon Press, 1894.

[9] H. D. Flack. "Louis Pasteur's discovery of molecular chirality and spontaneous resolution in 1848, together with a complete review of his crystallographic and chemical work". In: *Acta Crystallographica Section A* 65.5 (2009), pp. 371–389.

[10] L. A. Nafie. *Vibrational Optical Activity: Principles and Applications*. 1st. Wiley, 2011, p. 398.

[11] R. S. Cahn, C. K. Ingold, and V. Prelog. "Specification of molecular chirality". In: *Angewandte Chemie-International Edition* 5 (1966), pp. 385–415.

[12] C. Mathews, K. Van Holde, and K. Ahern. *Biochemistry*. Addison-Wesley world student series. Benjamin Cummings, 2000.

[13] J. C. Leffingwell. *Chirality & Odour Perception*. 2002. URL: `http://www.leffingwell.com/chirality/chirality.htm`.

[14] R. Crossley. *Chirality and Biological Activity of Drugs*. New Directions in Organic & Biological Chemistry. Taylor & Francis, 1995.

[15] H. Caner, E. Groner, L. Levy, and I. Agranat. "Trends in the development of chiral drugs". In: *Drug discovery today* 9.3 (2004), pp. 105–110.

[16] C. Tian, P. Xiu, Y. Meng, W. Zhao, Z. Wang, and R. Zhou. "Enantiomerization Mechanism of Thalidomide and the Role of Water and Hydroxide Ions". In: *Chemistry A European Journal* 18.45 (2012), pp. 14305–14313.

[17] H. Izumi, S. Futamura, N. Tokita, and Y. Hamada. "Fliplike motion in the thalidomide dimer: Conformational analysis of (R)-thalidomide using vibrational circular dichroism spectroscopy". In: *Journal of Organic Chemistry* 72.1 (2007), pp. 277–279.

[18] P. Mansfield, D. Henry, and A. Tonkin. "Single-enantiomer drugs: elegant science, disappointing effects". In: *Clin Pharmacokinet* 43.5 (2004), pp. 287–90.

[19] "FDA'S policy statement for the development of new stereoisomeric drugs". In: *Chirality* 4.5 (1992), pp. 338–340.

[20] H. D. Flack. "The use of X-ray Crystallography to Determine Absolute Configuration (II)". In: *Acta Chimica Slovenica* 55.4 (2008), pp. 689–691.

[21] H. D. Flack and G. Bernardinelli. "Absolute structure and absolute configuration". In: *Acta Crystallographica Section A* 55 (1999), pp. 908–915.

[22] L.-Y. Kong and P. Wang. "Determination of the absolute configuration of natural products". In: *Chinese Journal of Natural Medicines* 11.3 (2013), pp. 193–198.

[23] N. Berova, P. L. Polavarapu, K. Nakanishi, and R. W. Woody. *Comprehensive Chiroptical Spectroscopy*. John Wiley & Sons, 2012.

[24] P. Stephens. "Vibrational Circular Dichroism Spectroscopy: A New Tool for the Stereochemical Characterization of Chiral Molecules". In: *Computational Medicinal Chemistry for Drug Discovery*. Vol. 26. New York: Marcel Dekker Inc., 2004, pp. 699–725.

[25] D. J. Newman and G. M. Cragg. "Natural products as sources of new drugs over the last 25 years". In: *Journal of natural products* 70.3 (2007), pp. 461–477.

[26] P. L. Polavarapu. "Why is it important to simultaneously use more than one chiroptical spectroscopic method for determining the structures of chiral molecules?" In: *Chirality* 20.5 (2008), pp. 664–672.

[27] S. Allenmark and J. Gawronski. "Determination of absolute configuration - an overview related to this special issue". In: *Chirality* 20.5 (2008), pp. 606–608.

[28] R. Feynman, R. Leighton, and M. Sands. *The Feynman Lectures on Physics, Desktop Edition Volume III*. v. 1. Basic Books, 2013.

[29] L. D. Barron. *Molecular Light Scattering and Optical Acticity*. 2nd. Cambridge University Press, 2004.

[30] D. Craig and T. Thirunamachandran. *Molecular Quantum Electrodynamics*. Dover Books on Chemistry. Dover Publications, 2012.

[31] I. Levine. *Molecular spectroscopy*. A Wiley-Interscience publication. Wiley, 1975.

[32] J. A. Schellman. "Circular Dichroism and Optical Rotation". In: *Chemical Reviews* 75(3) (1975), pp. 323–331.

[33] F. Levin. *An Introduction to Quantum Theory*. Cambridge, UK: Cambridge University Press, 2002.

[34] P. Stephens, F. Devlin, and J. Cheeseman. *VCD Spectroscopy for Organic Chemists*. Taylor & Francis, 2012.

[35] B. Bransden and C. Joachain. *Quantum Mechanics*. Prentice Hall, 2000.

[36] M. Boas. *Mathematical Methods in the Physical Sciences*. Wiley, 2006.

[37] P. Atkins and R. Friedman. *Molecular Quantum Mechanics*. Oxford, UK: Oxford University Press, 2005.

[38] D. Harris and M. Bertolucci. *Symmetry and Spectroscopy: An Introduction to Vibrational and Electronic Spectroscopy*. Dover Books on Chemistry Series. Dover Publications, 1978.

[39] G. Joos and I. Freeman. *Theoretical Physics*. Dover Books on Physics. Dover Publications, 2013.

[40] L. Landau, J. Bell, J. Kearsley, L. Pitaevskii, E. Lifshitz, and J. Sykes. *Electrodynamics of Continuous Media*. Course of Theoretical Physics. Elsevier Science, 1984.

[41] A. Rauk. "Vibrational Circular Dichroism Intensities: Ab Initio Calculations". In: *New Developments in Molecular Chirality*. Kluwer Academic Publishers, 1991, pp. 57–92.

[42] P. J. Stephens. "Theory of vibrational circular dichroism". In: *The Journal of Physical Chemistry* 89.5 (1985), pp. 748–752.

[43] L. A. Nafie and T. B. Freedman. "Vibronic coupling theory of infrared vibrational transitions". In: *Journal of Chemical Physics* (1983), pp. 7108–7116.

[44] L. D. Barron and A. D. Buckingham. "Vibrational Optical Activity". In: *Chemical Physics Letters* 492 (2010), pp. 199–213.

[45] A. D. Buckingham, P. W. Fowler, and P. A. Galwas. "Velocity-dependent property surfaces and the theory of vibrational circular dichroism". In: *Chemical Physics* 112.1 (1987), pp. 1–14.

[46] G. Arfken and H. Weber. *Mathematical Methods For Physicists International Student Edition*. Elsevier Science, 2005.

[47] V. P. Nicu. "Implementation, Calculation and Interpretation of Vibrational Circular Dichroism Spectra". Thesis. 2009.

[48] E. Wilson, J. Decius, and P. Cross. *Molecular Vibrations: The Theory of Infrared and Raman Vibrational Spectra*. Dover Books on Chemistry. Dover Publications, 2012.

[49] A. Szabo and N. Ostlund. *Modern Quantum Chemistry*. New York: McGraw-Hill, Inc., 1989.

[50] F. Jensen. *Introduction to Computational Chemistry*. Wiley, 2013.

[51] R. Amos, N. Handy, K. Jalkanen, and P. Stephens. "Efficient calculation of vibrational magnetic dipole transition moments and rotational strengths". In: *Chemical Physics Letters* 133.1 (1987), pp. 21 –26.

[52] L. Rosenfeld. "Quantenmechanische Theorie der natürlichen optischen Aktivität von Flüssigkeiten und Gasen". German. In: *Zeitschrift für Physik* 52.3-4 (1929), pp. 161–174.

[53] A. Buckingham. "Permanent and induced molecular moments and long-range intermolecular forces". In: *Adv. Chem. Phys* 12 (1967), pp. 107–142.

[54] P. L. Polavarapu. "Ab initio molecular optical rotations and absolute configurations". In: *Molecular Physics* 91.3 (1997), pp. 551–554.

[55] P. L. Polavarapu and C. Zhao. "A comparison of ab initio optical rotations obtained with static and dynamic methods". In: *Chemical Physics Letters* 296 (1998), pp. 105–110.

[56] T. D. Crawford. "Ab initio calculation of molecular chiroptical properties". In: *Theoretical Chemistry Accounts* 115.4 (2006), pp. 227–245.

[57] P. J. Stephens, F. J. Devlin, J. R. Cheeseman, and M. J. Frisch. "Calculation of optical rotation using density functional theory". In: *Journal of Physical Chemistry A* 105.22 (2001), pp. 5356–5371.

[58] A. D. Buckingham. "Introductory lecture. The theoretical background to vibrational optical activity". In: *Faraday Discussions* 99 (1994), pp. 1–12.

[59] T. Helgaker, K. Ruud, K. L. Bak, P. Jorgensen, and J. Olsen. "Vibrational Raman Optical Activity Calculations using London Atomic Orbitals". In: *Faraday Discussions* 99 (1994), pp. 165–180.

[60] J. C. Facelli. "Calculations of chemical shieldings: Theory and applications". In: *Concepts in Magnetic Resonance Part A* 20A.1 (2004), pp. 42–69.

[61] J. R. Cheeseman, G. W. Trucks, T. A. Keith, and M. J. Frisch. "A comparison of models for calculating nuclear magnetic resonance shielding tensors". In: *Journal of Chemical Physics* 104.14 (1996), pp. 5497–5509.

[62] T. Helgaker, M. Jaszunski, and K. Ruud. "Ab Initio Methods for the Calculation of NMR Shielding and Indirect Spin-Spin Coupling Constants". In: *Chemical Reviews* 99.1 (1999), pp. 293–352.

[63] W. Kutzelnigg. "Ab initio calculation of molecular properties". In: *Journal of Molecular Structure: THEOCHEM* 202.0 (1989), pp. 11 –61.

[64] M. J. Frisch, G. W. Trucks, H. B. Schlegel, G. E. Scuseria, M. A. Robb, J. R. Cheeseman, G. Scalmani, V. Barone, B. Mennucci, G. A. Petersson, H. Nakatsuji, M. Caricato, X. Li, H. P. Hratchian, A. F. Izmaylov, J. Bloino, G. Zheng, J. L. Sonnenberg, M. Hada, M. Ehara, K. Toyota, R. Fukuda, J. Hasegawa, M. Ishida, T. Nakajima, Y. Honda, O. Kitao, H. Nakai, T. Vreven, J. A. Montgomery Jr., J. E. Peralta, F. Ogliaro, M. Bearpark, J. J. Heyd, E. Brothers, K. N. Kudin, V. N. Staroverov, R. Kobayashi, J. Normand, K. Raghavachari, A. Rendell, J. C. Burant, S. S. Iyengar, J. Tomasi, M. Cossi, N. Rega, J. M. Millam, M. Klene, J. E. Knox, J. B. Cross, V. Bakken, C. Adamo, J. Jaramillo, R. Gomperts, R. E. Stratmann, O. Yazyev, A. J. Austin, R. Cammi, C. Pomelli, J. W. Ochterski, R. L. Martin, K. Morokuma, V. G. Zakrzewski, G. A. Voth, P. Salvador, J. J. Dannenberg, S. Dapprich, A. D. Daniels, . Farkas, J. B. Foresman, J. V. Ortiz, J. Cioslowski, and D. J. Fox. *Gaussian 09 Revision D.01*. Gaussian Inc. Wallingford CT 2009.

[65] M. W. Lodewyk, M. R. Siebert, and D. J. Tantillo. "Computational Prediction of ^{1}H and ^{13}C Chemical Shifts: A Useful Tool for Natural Product, Mechanistic, and Synthetic Organic Chemistry". In: *Chemical Reviews* 112.3 (2011), pp. 1839–1862.

[66] J. Mandel. *The Statistical Analysis of Experimental Data*. Dover Books on Mathematics. Dover Publications, 2012.

[67] G. Bifulco, P. Dambruoso, L. Gomez-Paloma, and R. Riccio. "Determination of relative configuration in organic compounds by NMR spectroscopy and computational methods". In: *Chemical Reviews* 107.9 (2007), pp. 3744–3779.

[68] S. G. Smith and J. M. Goodman. "Assigning the Stereochemistry of Pairs of Diastereoisomers Using GIAO NMR Shift Calculation". In: *Journal of Organic Chemistry* 74.12 (2009), pp. 4597–4607.

[69] S. G. Smith and J. M. Goodman. "Assigning Stereochemistry to Single Diastereoisomers by GIAO NMR Calculation: The DP4 Probability". In: *Journal of the American Chemical Society* 132.37 (2010), pp. 12946–12959.

[70] M. Dogruel. URL: `http://newton.physics.metu.edu.tr/~mdogruel/pro443.htm`.

[71] P. Griffiths. *Chemical Infrared Fourier Transform Spectroscopy*. John Wiley & Sons, 1975.

[72] J. Hilario, D. Drapcho, R. Curbelo, and T. A. Keiderling. "Polarization modulation Fourier transform infrared spectroscopy with digital signal processing: Comparison of vibrational circular dichroism methods". In: *Applied Spectroscopy* 55.11 (2001), pp. 1435–1447.

[73] L. A. Nafie. "Dual polarization modulation: A real-time, spectral-multiplex separation of circular dichroism from linear birefringence spectral intensities". In: *Applied Spectroscopy* 54.11 (2000), pp. 1634–1645.

[74] B. Wang and J. List. "Basic Optical Properties Of The Photoelastic Modulator Part I: Useful Aperture and Acceptance Angle". In: *SPIE Proceedings* 5888 (2005).

[75] HindsInstruments. URL: `http://www.hindsinstruments.com`.

[76] G. Holzwart, E. C. Hsu, H. S. Mosher, T. R. Faulkner, and A. Moscowit. "Infrared circular-dichroism of carbon-hydrogen and carbon-deuterium stretching modes - observations". In: *Journal of the American Chemical Society* 96.1 (1974), pp. 251–252.

[77] L. A. Nafie, T. A. Keiderling, and P. J. Stephens. "Vibrational circular-dichroism". In: *Journal of the American Chemical Society* 98.10 (1976), pp. 2715–2723.

[78] J. Gal. "Chiral drugs from a historical point of view". In: *Chirality in Drug Research*. Ed. by E. Francotte, W. Lindner, R. Mannhold, H. Kubinyi, and G. Folkers. Methods and Principles in Medicinal Chemistry. Wiley, 2007.

[79] F. J. Devlin, P. J. Stephens, J. R. Cheeseman, and M. J. Frisch. "Ab initio prediction of vibrational absorption and circular dichroism spectra of chiral natural products using density functional theory: alpha-pinene". In: *Journal of Physical Chemistry A* 101.51 (1997), pp. 9912–9924.

[80] L. A. Nafie. "Vibrational optical activity". In: *Applied Spectroscopy* 50.5 (1996), A14–A26.

[81] T. Kuppens, W. Herrebout, B. van der Veken, and P. Bultinck. "Intermolecular association of tetrahydrofuran-2-carboxylic acid in solution: A vibrational circular dichroism study". In: *Journal of Physical Chemistry A* 110.34 (2006), pp. 10191–10200.

[82] T. Buffeteau, D. Cavagnat, A. Bouchet, and T. Brotin. "Vibrational absorption and circular dichroism studies of (-)-camphanic acid". In: *Journal of Physical Chemistry A* 111.6 (2007), pp. 1045–1051.

[83] C. Cappelli, S. Monti, and A. Rizzo. "Effect of the environment on vibrational infrared and circular dichroism spectra of (S)-proline". In: *International Journal of Quantum Chemistry* 104.5 (2005), pp. 744–757.

[84] E. Debie, L. Jaspers, P. Bultinck, W. Herrebout, and B. van der Veken. "Induced Solvent Chirality: A VCD study of camphor in $CDCl_3$". In: *Chemical Physics Letters* 450 (2008), pp. 426–430.

[85] E. Debie, P. Bultinck, W. Herrebout, and B. van der Veken. "Solvent effects on IR and VCD spectra of natural products: an experimental and theoretical VCD study of pulegone". In: *Physical Chemistry Chemical Physics* (2008), pp. 3948–3508.

[86] A. M. Rouhi. "A Dream Realized. Spectroscopic tool championed by two chemists makes it easier to determine absolute configuration". In: *Science & Technology* (2005).

[87] T. Kuppens, K. Vandyck, J. van der Eycken, W. Herrebout, B. van der Veken, and P. Bultinck. "A DFT conformational analysis and VCD study on methyl tetrahydrofuran-2-carboxylate". In: *Spectrochimica acta. Part A, Molecular and biomolecular spectroscopy* 67.2 (2007), pp. 402–411.

[88] T. Kuppens, W. Langenaeker, J. P. Tollenaere, and P. Bultinck. "Determination of the stereochemistry of 3-hydroxymethyl-2,3-dihydro-[1,4]dioxino[2,3-b]pyridine by vibrational circular dichroism and the effect of DFT integration grids". In: *Journal of Physical Chemistry A* 107.4 (2003), pp. 542–553.

[89] T. Kuppens, K. Vandyck, J. Van der Eycken, W. Herrebout, B. J. van der Veken, and P. Bultinck. "Determination of the absolute configuration of three as-hydrindacene compounds by vibrational circular dichroism". In: *Journal of Organic Chemistry* 70.23 (2005), pp. 9103–9114.

[90] T. Kuppens. *Development of methodology to assign absolute configurations using vibrational circular dichroism*. PhD Thesis. 2006.

[91] R. De Gelder, R. Wehrens, and J. A. Hageman. "A generalized expression for the similarity of spectra: Application to powder diffraction pattern classification". In: *Journal of Computational Chemistry* 22.3 (2001), pp. 273–289.

[92] J. Shen, C. Zhu, S. Reiling, and R. Vaz. "A novel computational method for comparing vibrational circular dichroism spectra". In: *Spectrochimica Acta Part A-Molecular and Biomolecular Spectroscopy* 76 (2010), pp. 418–422.

[93] I. M. Alecu, J. Zheng, Y. Zhao, and D. G. Truhlar. "Computational Thermochemistry: Scale Factor Databases and Scale Factors for Vibrational Frequencies Obtained from Electronic Model Chemistries". In: *Journal of Chemical Theory and Computation* 6.9 (2010), pp. 2872–2887.

[94] P. Pulay, G. Fogarasi, G. Pongor, J. E. Boggs, and A. Vargha. "Combination of theoretical ab initio and experimental information to obtain reliable harmonic force-constants - scaled quantum-mechanical (sqm) force-fields for glyoxal, acrolein, butadiene, formaldehyde, and ethylene". In: *Journal of the American Chemical Society* 105.24 (1983), pp. 7037–7047.

[95] A. D. Becke. "Density-functional thermochemistry 3. The role of exact exchange". In: *Journal of Chemical Physics* 98.7 (1993), pp. 5648–5652.

[96] C. T. Lee, W. T. Yang, and R. G. Parr. "Development of the colle-salvetti correlation-energy formula into a functional of the electron-density". In: *Physical Review B-Condensed Matter* 37.2 (1988), pp. 785–789.

[97] W. J. Hehre, L. Radom, P. R. Schleyer, and J. A. Pople. *Ab initio molecular orbital theory*. Wiley, 1986.

[98] M. J. Frisch, G. W. Trucks, H. B. Schlegel, G. E. Scuseria, M. A. Robb, J. R. Cheeseman, J. A. Montgomery Jr, T. Vreven, K. N. Kudin, J. C. Burant, J. M. Millam, S. S. Iyengar, J. Tomasi, V. Barone, B. Mennucci, M. Cossi, G. Scalmani, N. Rega, G. A. Petersson, H. Nakatsuji, M. Hada, M. Ehara, K. Toyota, R. Fukuda, J. Hasegawa, M. Ishida, T. Nakajima, Y. Honda, O. Kitao, H. Nakai, M. Klene, X. Li, J. E. Knox, H. P. Hratchian, J. B. Cross, V. Bakken, C. Adamo, J. Jaramillo, R. Gomperts, R. E. Stratmann, O. Yazyev, A. J. Austin, R. Cammi, C. Pomelli, J. W. Ochterski, P. Y. Ayala, K. Morokuma, G. A. Voth, P. Salvador, J. J. Dannenberg, V. G. Zakrewski, S. Dapprich, A. D. Daniels, M. C. Strain, O. Farkas, D. K. Malick, A. D. Rabuck, K. Raghavachari, J. B. Foresman, J. V. Ortiz, Q. Cui, A. G. Baboul, S. Clifford, J. Ciolowski, B. B. Stefanov, G. Liu, A. Liashenko, P. Piskorz, I. Komaromi, R. L. Martin, D. J. Fox, T. Keith, M. A. Al-laham, C. Y. Peng, A. Nanayakkara, M. Challacombe, P. M. W. Gill, B. Johnson, W. Chen, M. W. Wong, C. Gonzalez, and J. A. Pople. *Gaussian 03*. Computer Program. 2004.

[99] C. N. Guo, R. D. Shah, R. K. Dukor, T. B. Freedman, X. L. Cao, and L. A. Nafie. "Fourier transform vibrational circular dichroism from 800 to 10,000 cm^{-1}: Near-IR-VCD spectral standards for terpenes and related molecules". In: *Vibrational Spectroscopy* 42.2 (2006), pp. 254–272.

[100] F. J. Devlin and P. J. Stephens. "Ab initio density functional theory study of the structure and vibrational spectra of cyclohexanone and its isotopomers". In: *Journal of Physical Chemistry A* 103.4 (1999), pp. 527–538.

[101] F. J. Devlin and P. J. Stephens. "Conformational analysis using ab initio vibrational spectroscopy: 3-methylcyclohexanone". In: *Journal of the American Chemical Society* 121.32 (1999), pp. 7413–7414.

[102] E. Debie, P. Bultinck, L. Nafie, and R. Dukor. *CompareVOA: Confidence Level Algorithm For Comparing VCD & ROA Spectra*. Computer Program. 2010.

[103] A. J. Hutt and J. O'Grady. "Drug chirality: a consideration of the significance of the stereochemistry of antimicrobial agents". In: *Journal of Antimicrobial Chemotherapy* 37 (1996), pp. 7–32.

[104] G. Magyarfalvi, G. Tarczay, and E. Vass. "Vibrational circular dichroism". In: *Wiley Interdisciplinary Reviews-Computational Molecular Science* 1.3 (2011), pp. 403–425.

[105] P. J. Stephens, F. J. Devlin, C. F. Chabalowski, and M. J. Frisch. "Ab Initio Calculation of Vibrational Absorption and Circular Dichroism Spectra Using Density Functional Force Fields". In: *The Journal of Physical Chemistry* 98.45 (1994), pp. 11623–11627.

[106] E. Baerends, T. Ziegler, J. Autschbach, D. Bashford, A. Brces, F. Bickelhaupt, C. Bo, P. Boerrigter, L. Cavallo, D. Chong, L. Deng, R. Dickson, D. Ellis, M. van Faassen, L. Fan, T. Fischer, C. F. Guerra, A. Ghysels, A. Giammona, S. van Gisbergen, A. Gtz, J. Groeneveld, O. Gritsenko, M. Grning, S. Gusarov, F. Harris, P. van den Hoek, C. Jacob, H. Jacobsen, L. Jensen, J. Kaminski, G. van Kessel, F. Kootstra, A. Kovalenko, M. Krykunov, E. van Lenthe, D. McCormack, A. Michalak, M. Mitoraj, J. Neugebauer, V. Nicu, L. Noodleman, V. Osinga, S. Patchkovskii, P. Philipsen, D. Post, C. Pye, W. Ravenek, J. Rodrguez, P. Ros, P. Schipper, G. Schreckenbach, J. Seldenthuis, M. Seth, J. Snijders, M. Sol, M. Swart, D. Swerhone, G. te Velde, P. Vernooijs, L. Versluis, L. Visscher, O. Visser, F. Wang, T. Wesolowski, E. van Wezenbeek, G. Wiesenekker, S. Wolff, T. Woo, and A. Yakovlev. *ADF2010*.

[107] DALTON. *A molecular electronic structure program, http://daltonprogram.org/*. Computer Program. Release 2011.

[108] Schrödinger. *Jaguar*. Computer Program. 2011.

[109] M. Muñoz, O. Muñoz, and P. Joseph Nathan. "Absolute configuration of natural diastereoisomers of 6 beta-hydroxyhyoscyamine by vibrational circular dichroism". In: *Journal of Natural Products* 69.9 (2006), pp. 1335–1340.

[110] M. A. Muñoz, O. Muñoz, and P. Joseph-Nathan. "Absolute configuration determination and conformational analysis of (-)-(3S,6S)-3a,6β-diacetoxytropane using vibrational circular dichroism and DFT techniques". In: *Chirality* 22.2 (2010), pp. 234–241.

[111] M. Muñoz, C. Chamy, A. Carrasco, J. Rovirosa, A. Martin, and P. Joseph Nathan. "Diastereoisomeric Assignment in a Pacifenol Derivative Using Vibrational Circular Dichroism". In: *Chirality* 21.1E (2009), E208–E214.

[112] E. Debie, T. Kuppens, K. Vandyck, J. Van der Eycken, B. van der Veken, W. Herrebout, and P. Bultinck. "Vibrational circular dichroism DFT study on bicyclo[3.3.0]octane derivatives". In: *Tetrahedron-Asymmetry* 17.23 (2006), pp. 3203–3218.

[113] D. Yang, H. Tran, E. Fan, W. Shi, T. L. Lowary, and Y. Xu. "Determination of the Absolute Configurations of Synthetic Daunorubicin Analogues Using Vibrational Circular Dichroism Spectroscopy and Density Functional Theory". In: *Chirality* 22 (2010), pp. 734–743.

[114] G. Longhi, S. Abbate, P. Scafato, and C. Rosini. "A vibrational circular dichroism approach to the determination of the absolute configuration of flexible and transparent molecules: fluorenone ketals of 1,n-diols". In: *Physical Chemistry Chemical Physics* 12 (2010), pp. 4725–4732.

[115] B. Gordillo-Roman, J. Camacho-ruiz, M. A. Bucio, and P. Joseph-Nathan. "Chiral recognition of diastereomeric 6-cedrols by vibrational circular dichroism". In: *Chirality* 24.2 (2012), pp. 147–154.

[116] J. M. Batista, A. N. L. Batista, J. S. Mota, Q. B. Cass, M. J. Kato, V. S. Bolzani, T. B. Freedman, S. N. Lopez, M. Furlan, and L. A. Nafie. "Structure Elucidation and Absolute Stereochemistry of Isomeric Monoterpene Chromane Esters". In: *Journal of Organic Chemistry* 76.8 (2011), pp. 2603–2612.

[117] J. M. Batista, A. N. L. Batista, D. Rinaldo, W. Vilegas, Q. B. Cass, V. S. Bolzani, M. J. Kato, S. N. Lopez, M. Furlan, and L. A. Nafie. "Absolute configuration reassignment of two chromanes from Peperomia obtusifolia (Piperaceae) using VCD and DFT calculations". In: *Tetrahedron-Asymmetry* 21.19 (2010), pp. 2402–2407.

[118] V. Nicu, J. Neugebauer, and E. Baerends. "Effects of complex formation on vibrational circular dichroism spectra". In: *The journal of physical chemistry. A* 112.30 (2008), pp. 6978–6991.

[119] S. Gobi and G. Magyarfalvi. "Reliability of computed signs and intensities for vibrational circular dichroism spectra". In: *Physical Chemistry Chemical Physics* 13.36 (2011), pp. 16130–16133.

[120] M. Feledziak, C. Michaux, A. Urbach, G. Labar, G. Muccioli, and D. Lambert. "β-Lactams Derived from a Carbapenem Chiron Are Selective Inhibitors of Human Fatty Acid Amide Hydrolase versus Human Monoacylglycerol Lipase". In: *Journal of Medicinal Chemistry* 52.22 (2009), pp. 7054–7068.

[121] T. A. Halgren. "Merck molecular force field 1. Basis, form, scope, parameterization, and performance of MMFF94". In: *Journal of Computational Chemistry* 17.5-6 (1996), pp. 490–519.

[122] T. A. Halgren. "MMFF VII. Characterization of MMFF94, MMFF94s, and other widely available force fields for conformational energies and for intermolecular-interaction energies and geometries". In: *Journal of Computational Chemistry* 20.7 (1999), pp. 730–748.

[123] M. Clark, R. D. Cramer, and N. Van Opdenbosch. "Validation of the general purpose tripos 5.2 force field". In: *Journal of Computational Chemistry* 10.8 (1989), pp. 982–1012.

[124] Wavefunction. *Spartan '08*. Computer Program. 2008.

[125] *CONFLEX Program*. Computer Program.

[126] H. Goto and E. Osawa. "Corner Flapping - A simple and fast algorithm for exhaustive generation of ring conformations". In: *Journal of the American Chemical Society* 111.24 (1989), pp. 8950–8951.

[127] H. Goto and E. Osawa. "An efficient algorithm for searching low-energy conformers of cyclic and acyclic molecules". In: *Journal of the Chemical Society-Perkin Transactions 2* (1993), pp. 187–198.

[128] A. D. Becke. "A new mixing of Hartree–Fock and local density-functional theories". In: *The Journal of Chemical Physics* 98.2 (1993), pp. 1372–1377.

[129] T. Dunning. "Gaussian-basis sets for use in correlated molecular calculations 1. The atoms boron through neon and hydrogen". In: *The Journal of Chemical Physics* 90.2 (1989), pp. 1007–1023.

[130] J. Tomasi, R. Cammi, and B. Mennucci. "Medium effects on the properties of chemical systems: An overview of recent formulations in the polarizable continuum model (PCM)". In: *International Journal of Quantum Chemistry* 75.4-5 (1999), pp. 783–803.

[131] J. Tomasi, B. Mennucci, and R. Cammi. "Quantum mechanical continuum solvation models". In: *Chemical Reviews* 105.8 (2005), pp. 2999–3093.

[132] P. J. Stephens and N. Harada. "ECD cotton effect approximated by the Gaussian curve and other methods". In: *Chirality* 22.2 (2010), pp. 229–233.

[133] V. Nicu, E. Debie, W. Herrebout, P. Bultinck, and E. Baerends. "A VCD Robust Mode Analysis of Induced Chirality: The Case of Pulegone in Chloroform". In: *Chirality* 21.1E (2009), E287–E297.

[134] V. Nicu and E. Baerends. "On the origin dependence of the angle made by the electric and magnetic vibrational transition dipole moment vectors". In: *PCCP. Physical Chemistry Chemical Physics* 13.36 (2011), pp. 16126–16129.

[135] P. Polavarapu, G. Scalmani, E. Hawkins, C. Rizzo, N. Jeirath, and I. Ibnusaud. "Importance of Solvation in Understanding the Chiroptical Spectra of Natural Products in Solution Phase: Garcinia Acid Dimethyl Ester". In: *Journal of Natural Products* 74.3 (2011), pp. 321–328.

[136] J. W. Finley and P. J. Stephens. "Density functional theory calculations of molecular structures and harmonic vibrational frequencies using hybrid density functionals". In: *Journal of Molecular Structure: THEOCHEM* 357.3 (1995), pp. 225–235.

[137] P. Stephens, F. Devlin, F. Gasparrini, A. Ciogli, D. Spinelli, and B. Cosimelli. "Determination of the absolute configuration of a chiral oxadiazol-3-one calcium channel blocker, resolved using chiral chromatography, via concerted density functional theory calculations of its vibrational circular dichroism, electronic circular dichroism, and optical rotation". In: *Journal of Organic Chemistry* 72.13 (2007), pp. 4707–4715.

[138] P. J. Stephens, A. Aamouche, F. J. Devlin, S. Superchi, M. I. Donnoli, and C. Rosini. "Determination of absolute configuration using vibrational circular dichroism spectroscopy: The chiral sulfoxide 1-(2-methylnaphthyl) methyl sulfoxide". In: *Journal of Organic Chemistry* 66.11 (2001), pp. 3671–3677.

[139] P. J. Stephens, F. J. Devlin, J. R. Cheeseman, M. J. Frisch, B. Mennucci, and J. Tomasi. "Prediction of optical rotation using density functional theory: 6,8-dioxabicyclo[3.2.1]octanes". In: *Tetrahedron-Asymmetry* 11.12 (2000), pp. 2443–2448.

[140] T. Kuppens, W. Herrebout, B. van der Veken, D. Corens, A. De Groot, J. Doyon, G. Van Lommen, and P. Bultinck. "Elucidation of the absolute configuration of JNJ-27553292, a CCR2 receptor antagonist, by vibrational circular dichroism analysis of two precursors". In: *Chirality* 18.8 (2006), pp. 609–620.

[141] V. P. Nicu and E. J. Baerends. "Robust normal modes in vibrational circular dichroism spectra". In: *Physical Chemistry Chemical Physics* 11.29 (2009), pp. 6107–6118.

[142] D. J. Caldwell and H. Eyring. "Optical Rotation". In: *Reviews of Modern Physics* 35.3 (1963), pp. 577–586.

[143] R. Kondru, P. Wipf, and D. Beratan. "Structural and conformational dependence of optical rotation angles". In: *The Journal of Physical Chemistry A* 103.33 (1999), pp. 6603–6611.

[144] W. W. Wood, W. Fickett, and J. G. Kirkwood. "The Absolute Configuration of Optically Active Molecules". In: *The Journal of Chemical Physics* 20.4 (1952), pp. 561–568.

[145] P. Polavarapu, E. Donahue, G. Shanmugam, G. Scalmani, E. Hawkins, and C. Rizzo. "A Single Chiroptical Spectroscopic Method May Not Be Able To Establish the Absolute Configurations of Diastereomers: Dimethylesters of Hibiscus and Garcinia Acids". In: *The journal of Physical Chemistry A* 115.22 (2011), pp. 5665–5673.

[146] R. K. Dukor. "Use of Vibrational Circular Dichroism in the Synthesis and Analysis of Chiral Pharmaceuticals". In: *Technology & Services* (2005).

[147] T. B. Freedman, X. L. Cao, R. K. Dukor, and L. A. Nafie. "Absolute configuration determination of chiral molecules in the solution state using vibrational circular dichroism". In: *Chirality* 15.9 (2003), pp. 743–758.

[148] L. A. Nafie and R. K. Dukor. "Applications of Vibrational Optical Activity in the Pharmaceutical Industry". In: *Applications of Vibrational Spectroscopy in Pharmaceutical Research and Development*. John Wiley & Sons, 2007.

[149] J. M. Batista Jr, A. N. L. Batista, M. J. Kato, V. S. Bolzani, S. N. Lpez, L. A. Nafie, and M. Furlan. "Further monoterpene chromane esters from Peperomia obtusifolia: VCD determination of the absolute configuration of a new diastereomeric mixture". In: *Tetrahedron Letters* 53.45 (2012), pp. 6051–6054.

[150] E. Burgueno-Tapia, C. Ordaz-Pichardo, A. I. Buendia-Trujillo, F. J. Chargoy-Antonio, and P. Joseph-Nathan. "Structure and absolute configuration of a visamminol derivative using IR and vibrational circular dichroism". In: *Phytochemistry Letters* 5.4 (2012), pp. 804–808.

[151] M. A. Muñoz, A. Urzua, J. Echeverria, M. A. Bucio, A. Hernandez-Barragan, and P. Joseph-Nathan. "Determination of absolute configuration of salvic acid, an ent-labdane from Eupatorium salvia, by vibrational circular dichroism". In: *Phytochemistry* 80 (2012), pp. 109–114.

[152] J. M. Batista, A. N. L. Batista, V. S. Bolzani, M. J. Kato, L. A. Nafie, S. N. Lopez, and M. Furlan. "Absolute configuration determination of complex chiral natural product molecules using vibrational circular dichroism (VCD)): A case study". In: *Pharmaceutical Biology* 50.5 (2012), pp. 587–587.

[153] F. J. Devlin, P. J. Stephens, J. R. Cheeseman, and M. J. Frisch. "Ab initio prediction of vibrational absorption and circular dichroism spectra of chiral natural products using density functional theory: Camphor and Fenchone". In: *Journal of Physical Chemistry A* 101.35 (1997), pp. 6322–6333.

[154] R. K. Kondru, P. Wipf, and D. N. Beratan. "Theory-Assisted Determination of Absolute Stereochemistry for Complex Natural Products via Computation of Molar Rotation Angles". In: *Journal of the American Chemical Society* 120 (1998), pp. 2204–2205.

[155] P. J. Stephens, J. J. Pan, F. J. Devlin, K. Krohn, and T. Kurtan. "Determination of the absolute configurations of natural products via density functional theory calculations of vibrational circular dichroism, electronic circular dichroism, and optical rotation: The iridoids plumericin and isoplumericin". In: *Journal of Organic Chemistry* 72.9 (2007), pp. 3521–3536.

[156] D. B. Ramachary and R. Sakthidevi. "Direct Catalytic Asymmetric Synthesis of Highly Functionalized 2-Methylchroman-2,4-diols via Barbas-List Aldol Reaction". In: *Chemistry-A European Journal* 15.18 (2009), pp. 4516–4522.

[157] P. Singh, A. Bhardwaj, S. Kaur, and S. Kumar. "Design, synthesis and evaluation of tetrahydropyran based COX-1/-2 inhibitors". In: *European Journal of Medicinal Chemistry* 44.3 (2009), pp. 1278–1287.

[158] B. Alcaide, P. Almendros, A. Luna, and M. R. Torres. "Proline-catalyzed diastereoselective direct aldol reaction between 4-oxoazetidine-2-carbaldehydes and ketones". In: *Journal of Organic Chemistry* 71.13 (2006), pp. 4818–4822.

[159] F. Calderon, E. G. Doyaguez, and A. Fernandez-Mayoralas. "Synthesis of azasugars through a proline-catalyzed reaction". In: *Journal of Organic Chemistry* 71.16 (2006), pp. 6258–6261.

[160] B. Alcaide, P. Almendros, A. Luna, and T. Martinez del Campo. "Synthesis of novel enantiopure 4-hydroxypipecolic acid derivatives with a bicyclic beta-lactam structure from a common 3-azido-4-oxoazetidine-2-carbaldehyde precursor". In: *Journal of Organic Chemistry* 73.4 (2008), pp. 1635–1638.

[161] R. Tello-Aburto, T. D. Newar, and W. A. Maio. "Evolution of a Protecting-Group-Free Total Synthesis: Studies en Route to the Neuroactive Marine Macrolide (-)-Palmyrolide A". In: *Journal of Organic Chemistry* 77.14 (2012), pp. 6271–6289.

[162] S. Ma, S. Zhang, W. Duan, and W. Wang. "An enantioselective synthesis of (+)-(S)-n-gingerols via the L-proline-catalyzed aldol reaction". In: *Bioorganic & Medicinal Chemistry Letters* 19.14 (2009), pp. 3909–3911.

[163] A. M. Bernard, A. Frongia, R. Guillot, P. P. Piras, F. Secci, and M. Spiga. "L-proline-catalyzed direct intermolecular asymmetric aldol reactions of 1-phenylthiocycloalkyl carboxaldehydes with ketones. Easy access to spiro- and fused-cyclobutyl tetrahydrofurans and cyclopentanones". In: *Organic Letters* 9.3 (2007), pp. 541–544.

[164] S. Y. Wang, P. Song, L. Y. Chan, and T. P. Loh. "Total Synthesis of Phytophthora Mating Hormone alpha 1". In: *Organic Letters* 12.22 (2010), pp. 5166–5169.

[165] L. Z. Peng, H. W. Liu, T. Zhang, F. Z. Zhang, T. S. Mei, Y. Li, and Y. L. Li. "Novel construction of the brassinolide side chain". In: *Tetrahedron Letters* 44.27 (2003), pp. 5107–5108.

[166] F. Secci, E. Cadoni, C. Fattuoni, A. Frongia, G. Bruno, and F. Nicolo. "Enantioselective organocatalyzed functionalization of benzothiophene and thiophenecarbaldehyde derivatives". In: *Tetrahedron* 68.24 (2012), pp. 4773–4781.

[167] I. Kumar and C. V. Rode. "Stereoselective synthesis of 2-amino-1,3,5-hexane triols using L-proline catalyzed aldol reaction". In: *Tetrahedron-Asymmetry* 17.5 (2006), pp. 763–766.

[168] Y. Fukazawa, Y. Takeda, S. Usui, and M. Kodama. "Synthesis and Conformation of 1,1,10,10-tetramethyl 3.3 metacyclophane". In: *Journal of the American Chemical Society* 110.23 (1988), pp. 7842–7847.

[169] M. Yamashita, Y. Ono, and H. Tawada. "A convenient ring formation of 3-aryl-2,2-dialkyl-2,3-dihydrobenzofurans from phenols and 2-aryl-2,2-dialkylacetaldehydes". In: *Tetrahedron* 60.12 (2004), pp. 2843–2849.

[170] T. A. Halgren. "Merck molecular force field .2. MMFF94 van der Waals and electrostatic parameters for intermolecular interactions". In: *Journal of Computational Chemistry* 17.5-6 (1996), pp. 520–552.

[171] T. A. Halgren. "Merck molecular force field. I. Basis, form, scope, parameterization, and performance of MMFF94". In: *Journal of Computational Chemistry* 17.5-6 (1996), pp. 490–519.

[172] N. L. Allinger, Y. H. Yuh, and J. H. Lii. "Molecular Mechanics - the MM3 Force-Field for Hydrocarbons". In: *Journal of the American Chemical Society* 111.23 (1989), pp. 8551–8566.

[173] P. L. Polavarapu. "Molecular optical rotations and structures". In: *Tetrahedron-Asymmetry* 8.20 (1997), pp. 3397–3401.

[174] A. E. Hansen and K. L. Bak. "Ab-initio calculations of electronic circular dichroism". In: *Enantiomer* 4.5 (1999), p. 455.

[175] T. Yanai, D. P. Tew, and N. C. Handy. "A new hybrid exchangecorrelation functional using the Coulomb-attenuating method (CAM-B3LYP)". In: *Chemical Physics Letters* 393.13 (2004), pp. 51–57.

[176] P. U. Biedermann, J. R. Cheeseman, M. J. Frisch, V. Schurig, I. Gutman, and I. Agranat. "Conformational spaces and absolute configurations of chiral fluorinated inhalation anaesthetics. A theoretical study". In: *Journal of Organic Chemistry* 64.11 (1999), pp. 3878–3884.

[177] F. Wang and P. L. Polavarapu. "Vibrational circular dichroism, predominant conformations, and hydrogen bonding in (S)-(-)-3-butyn-2-ol". In: *Journal of Physical Chemistry A* 104.9 (2000), pp. 1822–1826.

[178] P. Bour, J. Kubelka, and T. A. Keiderling. "Simulations of oligopeptide vibrational CD: Effects of isotopic labeling". In: *Biopolymers* 53.5 (2000), pp. 380–395.

[179] G. A. Guirgis, Y. D. Hsu, A. C. Vlaservich, H. D. Stidham, and J. R. Durig. "Vibrational spectrum, ab initio calculations, assignments of fundamentals, barriers to internal rotation and stabilities of conformers of 1,2-dichloropropane". In: *Journal of Molecular Structure* 378.2 (1996), pp. 83–102.

[180] A. P. Scott and L. Radom. "Harmonic vibrational frequencies: An evaluation of Hartree- Fock, Moller-Plesset, quadratic configuration interaction, density functional theory, and semiempirical scale factors". In: *Journal of Physical Chemistry* 100.41 (1996), pp. 16502–16513.

[181] G. Shanmugam, P. L. Polavarapu, A. Kendall, and G. Stubbs. "Structures of plant viruses from vibrational circular dichroism". In: *Journal of General Virology* 86.8 (2005), pp. 2371–2377.

[182] N. Harada. "Determination of absolute configurations by X-ray crystallography and 1H NMR anisotropy". In: *Chirality* 20.5 (2008), pp. 691–723.

[183] T. J. Wenzel. *Discrimination of Chiral Compounds Using NMR Spectroscopy*. Electronic Book. 2007.

[184] J. M. Seco, E. Quinoa, and R. Riguera. "Assignment of the Absolute Configuration of Polyfunctional Compounds by NMR Using Chiral Derivatizing Agents". In: *Chemical Reviews* 112.8 (2012), pp. 4603–4641.

[185] K. C. Nicolaou and S. A. Snyder. "Chasing Molecules That Were Never There: Misassigned Natural Products and the Role of Chemical Synthesis in Modern Structure Elucidation". In: *Angewandte Chemie International Edition* 44.7 (2005), pp. 1012–1044.

[186] V. Liégeois, K. Ruud, and B. Champagne. "An analytical derivative procedure for the calculation of vibrational Raman optical activity spectra". In: *The Journal of Chemical Physics* 127.20, 204105 (2007).

[187] M. Pecul. "New applications and challenges for computational ROA spectroscopy". In: *Chirality* 21.1E (2009), E98–E104.

[188] R. Bast, U. Ekstrom, B. Gao, T. Helgaker, K. Ruud, and A. J. Thorvaldsen. "The ab initio calculation of molecular electric, magnetic and geometric properties". In: *Phys. Chem. Chem. Phys.* 13 (7 2011), pp. 2627–2651.

[189] J. R. Cheeseman and M. J. Frisch. "Basis Set Dependence of Vibrational Raman and Raman Optical Activity Intensities". In: *Journal of Chemical Theory and Computation* 7.10 (2011), pp. 3323–3334.

[190] T. Weymuth, M. P. Haag, K. Kiewisch, S. Luber, S. Schenk, C. R. Jacob, C. Herrmann, J. Neugebauer, and M. Reiher. "MOVIPAC: Vibrational spectroscopy with a robust meta-program for massively parallel standard and inverse calculations". In: *Journal of Computational Chemistry* 33.27 (2012), pp. 2186–2198.

[191] W. Hug and G. Hangartner. "A novel high-throughput Raman spectrometer for polarization difference measurements". In: *Journal of Raman Spectroscopy* 30.9 (1999), pp. 841–852.

[192] W. Hug. "Virtual enantiomers as the solution of optical activity's deterministic offset problem". In: *Appl Spectrosc* 57.1 (2003), pp. 1–13.

[193] P. J. Stephens, F. J. Devlin, and J. R. Cheeseman. *VCD Spectroscopy for Organic Chemists*. CRC Press, 2012, p. 370.

[194] G. Pescitelli, L. Di Bari, and N. Berova. "Conformational aspects in the studies of organic compounds by electronic circular dichroism". In: *Chemical Society Reviews* 40.9 (2011), pp. 4603–4625.

[195] P. Butz, R. T. Kroemer, N. A. Macleod, and J. P. Simons. "Conformational Preferences of Neurotransmitters: Ephedrine and Its Diastereoisomer, Pseudoephedrine". In: *The Journal of Physical Chemistry A* 105.3 (2001), pp. 544–551.

[196] U. Gresser and C. H. Gleiter. "Erectile dysfunction: comparison of efficacy and side effects of the PDE-5 inhibitors sildenafil, vardenafil and tadalafil review of the literature". In: *European Journal of Medical Research* 7 (2002), pp. 435–446.

[197] A. Daugan, P. Grondin, C. Ruault, A.-C. Le Monnier de Gouville, H. Coste, J. M. Linget, J. Kirilovsky, F. Hyafil, and R. Labaudinire. "The Discovery of Tadalafil: A Novel and Highly Selective PDE5 Inhibitor. 2: 2,3,6,7,12,12a-hexahydropyrazino[1,2:1,6]pyrido[3,4-b]indole-1,4-dione Analogues". In: *Journal of Medicinal Chemistry* 46.21 (2003), pp. 4533–4542.

[198] *FDA approves Cialis to treat benign prostatic hyperplasia*. 2011. URL: `http://www.fda.gov/NewsEvents/Newsroom/PressAnnouncements/ucm274642.htm`.

[199] J.-D. Chai and M. Head-Gordon. "Long-range corrected hybrid density functionals with damped atom-atom dispersion corrections". In: *Physical Chemistry Chemical Physics* 10.44 (2008), pp. 6615–6620.

[200] M. W. Lodewyk, M. R. Siebert, D. J. Tantillo, P. R. Rablen, and T Bally. *Chemical Shift Repository*. URL: `http://cheshirenmr.info/`.

[201] J. Autschbach. "Computing chiroptical properties with first-principles theoretical methods: Background and illustrative examples". In: *Chirality* 21.1E (2009), E116–E152.

[202] T. B. Freedman, X. L. Ca, Z. Luz, H. Zimmermann, R. Poupko, and L. A. Nafie. "Isotopic difference spectra as an aide in determining absolute configuration using vibrational optical activity: Vibrational circular dichroism of C-13- and H-2-labelled nonamethoxy cyclotriveratrylene". In: *Chirality* 20.5 (2008), pp. 673–680.

[203] G. Barone, D. Duca, A. Silvestri, L. Gomez-Paloma, R. Riccio, and G. Bifulco. "Determination of the Relative Stereochemistry of Flexible Organic Compounds by Ab Initio Methods: Conformational Analysis and Boltzmann-Averaged GIAO 13C NMR Chemical Shifts". In: *Chemistry A European Journal* 8.14 (2002), pp. 3240–3245.

[204] M. W. Lodewyk, M. R. Siebert, and D. J. Tantillo. "Computational Prediction of H-1 and C-13 Chemical Shifts: A Useful Tool for Natural Product, Mechanistic, and Synthetic Organic Chemistry". In: *Chemical Reviews* 112.3 (2012), pp. 1839–1862.

[205] D. J. Tantillo. "Walking in the woods with quantum chemistry - applications of quantum chemical calculations in natural products research". In: *Natural Product Reports* 30.8 (2013), pp. 1079–1086.

[206] J. W. Blunt, B. R. Copp, R. A. Keyzers, M. H. G. Munro, and M. R. Prinsep. "Marine natural products". In: *Natural Product Reports* 30.2 (2013), pp. 237–323.

[207] I. Carletti, G. Massiot, and C. Debitus. *Patent, WO 2011/051380A1*. Patent. 2011.

[208] E. Fleury, M. I. Lannou, O. Bistri, F. Sautel, G. Massiot, A. Pancrazi, and J. Ardisson. "Relative Stereochemical Determination and Synthesis of the C1-C17 Fragment of a New Natural Polyketide". In: *Journal of Organic Chemistry* 74.18 (2009), pp. 7034–7045.

[209] E. Fleury, G. Sorin, E. Prost, A. Pancrazi, F. Sautel, G. Massiot, M. I. Lannou, and J. Ardisson. "Relative Stereochemical Determination and Synthesis of the C17-C25 δ-Lactone Fragment of Hemicalide". In: *Journal of Organic Chemistry* 78.3 (2013), pp. 855–864.

[210] Y. He, B. Wang, R. K. Dukor, and L. A. Nafie. "Determination of Absolute Configuration of Chiral Molecules Using Vibrational Optical Activity: A Review". In: *Applied Spectroscopy* 65.7 (2011), pp. 699–723.

[211] L. A. Nafie. "Infrared and Raman vibrational optical activity: Theoretical and experimental aspects". In: *Annual Review of Physical Chemistry* 48 (1997), pp. 357–386.

[212] J. C. Cedron, A. Estevez-Braun, A. G. Ravelo, D. Gutierrez, N. Flores, M. A. Bucio, N. Perez-Hernandez, and P. Joseph-Nathan. "Bioactive Montanine Derivatives from Halide-induced Rearrangements of Haemanthamine-type Alkaloids. Absolute Configuration by VCD". In: *Organic Letters* 11.7 (2009), pp. 1491–1494.

[213] B. Gordillo-Roman, M. Reina, L. Ruiz-Mesia, W. Ruiz-Mesia, and P. Joseph-Nathan. "Absolute configuration of indoline alkaloids from Geissospermum reticulatum". In: *Tetrahedron Letters* 54.13 (2013), pp. 1693–1696.

[214] P. J. Stephens, J. J. Pan, F. J. Devlin, M. Urbanova, O. Julinek, and J. Hajicek. "Determination of the absolute configurations of natural products via density functional theory calculations of vibrational circular dichroism, electronic circular dichroism, and optical rotation: The iso-schizozygane alkaloids isoschizogaline and isoschizogamine". In: *Chirality* 20.3-4 (2008), pp. 454–470.

[215] F. J. Devlin, P. J. Stephens, J. R. Cheeseman, and M. J. Frisch. "Prediction of vibrational circular dichroism spectra using density functional theory: Camphor and fenchone". In: *Journal of the American Chemical Society* 118.26 (1996), pp. 6327–6328.

[216] C. S. Ashvar, P. J. Stephens, T. Eggimann, and H. Wieser. "Vibrational circular dichroism spectroscopy of chiral pheromones: frontalin (1,5-dimethyl-6,8-dioxabicyclo[3.2.1]octane)". In: *Tetrahedron-Asymmetry* 9.7 (1998), pp. 1107–1110.

[217] B. Simmen, T. Weymuth, and M. Reiher. "How Many Chiral Centers Can Raman Optical Activity Spectroscopy Distinguish in a Molecule?" In: *Journal of Physical Chemistry A* 116.22 (2012), pp. 5410–5419.

[218] M. Reina, E. Burgueno-Tapia, M. A. Bucio, and P. Joseph-Nathan. "Absolute configuration of tropane alkaloids from Schizanthus species by vibrational circular dichroism". In: *Phytochemistry* 71.7 (2010), pp. 810–815.

[219] M. A. Muñoz, O. Muñoz, and P. Joseph-Nathan. "Absolute Configuration Determination and Conformational Analysis of (-)-(3S,6S)-3 alpha,6 beta-Diacetoxytropane Using Vibrational Circular Dichroism and DFT Techniques". In: *Chirality* 22.2 (2010), pp. 234–241.

[220] G. Uray, P. Verdino, F. Belaj, C. O. Kappe, and W. M. F. Fabian. "Absolute configuration in 4-alkyl- and 4-aryl-3,4-dihydro- 2(1H)-pyrimidones: A combined theoretical and experimental investigation". In: *Journal of Organic Chemistry* 66.20 (2001), pp. 6685–6694.

[221] X. J. Li, K. H. Hopmann, J. Hudecova, J. Isaksson, J. Novotna, W. Stensen, V. Andrushchenko, M. Urbanova, J. S. Svendsen, P. Bour, and K. Ruud. "Determination of Absolute Configuration and Conformation of a Cyclic Dipeptide by NMR and Chiral Spectroscopic Methods". In: *Journal of Physical Chemistry A* 117.8 (2013), pp. 1721–1736.

[222] K. H. Hopmann, J. Sebestik, J. Novotna, W. Stensen, M. Urbanova, J. Svenson, J. S. Svendsen, P. Bour, and K. Ruud. "Determining the Absolute Configuration of Two Marine Compounds Using Vibrational Chiroptical Spectroscopy". In: *Journal of Organic Chemistry* 77.2 (2012), pp. 858–869.

[223] T. Taniguchi, C. L. Martin, K. Monde, K. Nakanishi, N. Berova, and L. E. Overman. "Absolute Configuration of Actinophyllic Acid As Determined through Chiroptical Data". In: *Journal of natural products* 72.3 (2009), pp. 430–432.

[224] H. Goto, K. Ohta, T. Kamakura, S. Obata, N. Nakayama, T. Matsumoto, and E. Osawa. *Conflex*. Computer Program. 2004.

[225] BioTools. *ComputeVOA*. Computer Program. 2013.

[226] T. H. Dunning. "Gaussian Basis Functions for Use in Molecular Calculations. III. Contraction of (10s6p) Atomic Basis Sets for the First - Row Atoms". In: *The Journal of Chemical Physics* 55.2 (1971), pp. 716–723.

[227] F. Jensen. *Computational Chemistry*. Chichester: John Wiley & Sons Ltd., 1999.

[228] S. Lilienfeld. "Galantamine–a novel cholinergic drug with a unique dual mode of action for the treatment of patients with Alzheimer's disease". In: *CNS Drug Rev* 8.2 (2002), pp. 159–76.

[229] J. Marco-Contelles, M. D. Carreiras, C. Rodriguez, M. Villarroya, and A. G. Garcia. "Synthesis and pharmacology of galantamine". In: *Chemical Reviews* 106.1 (2006), pp. 116–133.

[230] P. Bultinck, H. De Winter, W. Langenaeker, and J. P. Tollenaere. *Computational medicinal chemistry for drugs discovery*. New York: Marcel Dekker, Inc, 2004.

[231] L. D. Barron and A. D. Buckingham. "Rayleigh and Raman Scattering from optically active molecules". In: *Molecular Physics* 20.6 (1971), pp. 1111–1118.

[232] L. D. Barron, F. Zhu, L. Hecht, G. E. Tranter, and N. W. Isaacs. "Raman Optical activity: An incisive probe of molecular chirality and biomolecular structure". In: *Journal of Molecular Structure* 834-836 (2007), pp. 7–16.

[233] T. Mugishima, M. Tsuda, Y. Kasai, H. Ishiyama, E. Fukushi, J. Kawabata, M. Watanabe, K. Akao, and J. Kobayashi. "Absolute stereochemistry of citrinadins A and B from marine-derived fungus". In: *Journal of Organic Chemistry* 70.23 (2005), pp. 9430–9435.

[234] S. Qiu, G. N. Li, S. M. Lu, B. K. Huang, Z. C. Feng, and C. Li. "Chiral Sulfur Compounds Studied by Raman Optical Activity: tert-Butanesulfinamide and its Precursor tert-Butyl tert-Butanethiosulfinate". In: *Chirality* 24.9 (2012), pp. 731–740.

[235] B. Nieto-Ortega, J. Casado, E. W. Blanch, J. T. L. Navarrete, A. R. Quesada, and F. J. Ramirez. "Raman Optical Activity Spectra and Conformational Elucidation of Chiral Drugs. The Case of the Antiangiogenic Aeroplysinin-1". In: *Journal of Physical Chemistry A* 115.13 (2011), pp. 2752–2755.

[236] M. A. Lovchika, G. Frater, A. Goeke, and W. Hug. "Total synthesis of juniouone, a natural monoterpenoid from Juniperus communis L., and determination of the absolute configuration of the naturally occurring enantiomer by ROA spectroscopy". In: *Chemistry & Biodiversity* 5.1 (2008), pp. 126–139.

[237] R. Matusch, M. Kreh, and U. Muller. "Formation, X-ray crystal-structure, and absolute-configuration of (-)-N-chloremethyl Galanthaminium chloride". In: *Helvetica Chimica Acta* 77.6 (1994), pp. 1611–1615.

[238] J. Vandenbussche, P. Bultinck, A. K. Przybyl, and W. A. Herrebout. "Statistical Validation of Absolute Configuration Assignment in Vibrational Optical Activity". In: *Journal of Chemical Theory and Computation* 9.12 (2013), pp. 5504–5512.

[239] P. Chen, X. Bao, L. F. Zhang, M. Ding, X. J. Han, J. Li, G. B. Zhang, Y. Q. Tu, and C. A. Fan. "Asymmetric Synthesis of Bioactive Hydrodibenzofuran Alkaloids: (-)-Lycoramine, (-)-Galanthamine, and (+)-Lunarine". In: *Angewandte Chemie-International Edition* 50.35 (2011), pp. 8161–8166.

Dankwoord

Zo, hier zijn we dan. Na het kleuter en lager in Kachtem, humaniora in het Roeselaarse college en mijn opleiding als Bio-ir. in Gent sta ik op het punt de 'hoogste academische graad' te bereiken: Doctor in de Wetenschappen. Enkele mensen speelden hierin een belangrijke rol, en hen wil ik bij deze van harte bedanken.

Mijn eerste 'bedankt' richt ik aan Patrick en Wouter. Patrick slaagde erin om me te boeien voor de wondere wereld van de kwantumchemie, een onbekend terrein voor een bio-ingenieur in opleiding. Die interesse werd geconcretiseerd in een masterthesis, waardoor ik ook in contact ben gekomen met Wouter. Aan Wouter ben ik extra dankbaarheid verschuldigd, om hemel en aarde te verzetten om me ondanks alles toch een plaats te geven na mijn laatste jaar. Ik wens jullie tot slot ook te bedanken voor de vrijheid mezelf te ontplooien, en dit in beide deelgebieden waarin jullie gespecialiseerd zijn.

De collega's, zowel uit Antwerpen als uit Gent, waren altijd paraat voor wat afleiding tijdens de soms wel lange dagen als doctorandus. In het bijzonder vermeld ik graag mijn collega *nerd* Sam (aka sjacobs1) voor de doorgedreven brainstorm sessies, resonantiestudies, maar ook voor de vele aangename babbels. Nick, die nog steeds moet bekomen van zijn talrijke basketbal nederlagen, Liene voor de vrouwelijke toets, Shi voor de vele geureffecten en de *anciens* Johan, Bart en Dieter: merci. Ook in Gent was ik steeds welkom, waarvoor ik de GQCG-leden moet bedanken: Sofie, mijn VCD-companion Jelle, Dieter en Guillaume. En Elke natuurlijk, die me met een blitzcursus VCD lanceerde voor de voorbije 4 jaar.

At the beginning of my PhD period I got the chance to visit the leading VCD-instrument company, BioTools, Inc. I want to thank Rina for this amazing experience

and her hospitality and Larry Nafie for his patience in introducing me to VCD spectroscopy. The drive and passion you share for what you do is an example for everyone. Also thanks to all other, sometimes exotic, colleagues and friends I crossed paths with in the past 4 years. I recently noticed that besides chiral spectroscopy, we all share an interest in beer. No further comment.

Op het moment van schrijven ben ik reeds een jaar werkzaam in het Belgische chemiebedrijf Proviron. Ik wens de directie te bedanken om me de tijd en vrijheid te gunnen om alsnog dit doctoraat af te werken.

Mijn ouders wens ik te bedanken voor de grote steun, op alle gebieden, die ik doorheen de jaren heb genoten. Mijn talrijke broers en zussen ben ik dankbaar voor de vele leuke momenten, maar ook voor de nodige steun en begeleiding op de momenten dat belangrijke keuzes moesten gemaakt worden.

Tot slot bedank ik vanuit de grond van mijn hart mijn prachtige vrouw Liesbeth. In het voorbije jaar, waaarin ik een voltijdse job combineerde met het schrijven van dit doctoraat, kwam veel druk op haar schouders te liggen. Toch vond ze de tijd en energie om mezelf en onze twee lieve dochters Esther en Suzanne in de watten te leggen en ons alles te geven om gelukkig te zijn.

Aan allen: bedankt!